

AL A 11 2619

DTIC FILE COPY

①
Bulletin 45
(Part 3 of 5 Parts)

THE SHOCK AND VIBRATION BULLETIN

Part 3
Aerospace Vehicles, Vibro-acoustics

JUNE 1975

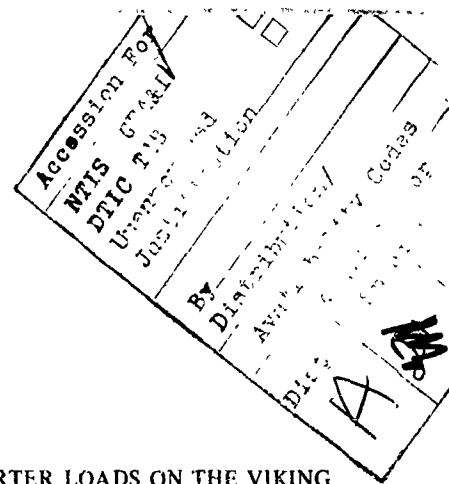
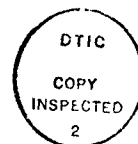
A Publication of
THE SHOCK AND VIBRATION
INFORMATION CENTER
Naval Research Laboratory, Washington, D.C.



Office of
The Director of Defense
Research and Engineering

Approved for public release; distribution unlimited.

82 03 26 073



CONTENTS

PAPERS APPEARING IN PART 3

Aerospace Vehicles

- AN EXPERIMENTAL/ANALYTICAL DETERMINATION OF TRANSPORTER LOADS ON THE VIKING SPACECRAFT 1
G. Kachadourian, General Electric Company, Hampton, Virginia
- DETERMINATION OF PROPELLANT EFFECTIVE MASS PROPERTIES USING MODAL TEST DATA . . . 15
J. C. Chen and J. A. Garba, Jet Propulsion Laboratory, Pasadena, California
- UNIQUE FLIGHT INSTRUMENTATION/DATA REDUCTION TECHNIQUES EMPLOYED ON THE VIKING DYNAMIC SIMULATOR 25
F. D. Day, Martin Marietta Aerospace, Denver, Colorado and B. K. Wada, The Jet Propulsion Laboratory, Pasadena, California
- ANALYTICAL PREDICTION AND CORRELATION FOR THE ORBITER DURING THE VIKING SPACECRAFT SINUSOIDAL VIBRATION TEST 37
G. R. Brownlee and J. A. Garba, Jet Propulsion Laboratory, Pasadena, California, and F. D. Day, III, Martin Marietta Aerospace, Denver, Colorado
- FAIL SAFE FORCED VIBRATION TESTING OF THE VIKING 1975 DEVELOPMENTAL SPACECRAFT . . 59
J. W. Fortenberry, Jet Propulsion Laboratory, Pasadena, California, and P. Rader, Martin Marietta Corporation, Denver, Colorado
- A METHOD FOR DETERMINING TACTICAL MISSILE JOINT COMPLIANCES FROM DYNAMIC TEST DATA 75
J. G. Maloney and M. T. Shelton, General Dynamics Corporation, Pomona, California

Vibro-Acoustics

- DYNAMIC STRAIN MEASUREMENT TECHNIQUES AT ELEVATED TEMPERATURES 89
R. C. Taylor, Air Force Flight Dynamics Laboratory, Wright-Patterson Air Force Base, Ohio
- AN ACTIVE LINEAR BRIDGE FOR STRAIN MEASUREMENT 95
P. T. JaQuay, Air Force Flight Dynamics Laboratory, Wright-Patterson Air Force Base, Ohio
- VIKING DYNAMIC SIMULATOR VIBRATION TESTING AND ANALYSIS METHOD 103
A. F. Leondis, General Dynamics Corporation, San Diego, California
- ANALYSIS AND FLIGHT TEST CORRELATION OF VIBROACOUSTIC ENVIRONMENTS ON A REMOTELY PILOTED VEHICLE 115
S. Zurnacian and P. Boeckemohle, Northrop Corporation Electronics Division, Hawthorne, California
- AERO-ACOUSTIC ENVIRONMENT OF RECTANGULAR CAVITIES WITH LENGTH TO DEPTH RATIOS IN THE RANGE OF FOUR TO SEVEN 137
L. L. Shaw and D. L. Smith, Air Force Flight Dynamics Laboratory, Wright-Patterson Air Force Base, Ohio
- PREDICTION OF ACOUSTICALLY INDUCED VIBRATION IN TRANSPORT AIRCRAFT 149
H. W. Bartel, Lockheed-Georgia Company, Marietta, Georgia

SIMPLIFIED TECHNIQUES FOR PREDICTING VIBRO-ACOUSTIC ENVIRONMENTS/	167
K. Y. Chang and G. C. Kao, Wyle Laboratories, Huntsville, Alabama	
USE OF A SEMI-PERIODIC STRUCTURAL CONFIGURATION FOR IMPROVING THE SONIC FATIGUE LIFE OF STIFFENED STRUCTURES,	183
G. Sengupta, Boeing Commercial Airplane Company, Seattle, Washington	

PAPERS APPEARING IN PART 2

ADDRESS OF WELCOME

Dr. D. Zonais, Chief Scientist, Air Force Flight Dynamics Laboratory, Wright-Patterson Air Force Base, Ohio

ADDRESS OF WELCOME

Mr. George Peterson, Director, Air Force Materials Laboratory, Wright-Patterson Air Force Base, Ohio

KEYNOTE ADDRESS

Lt. General James L. Stewart, Commander, Aeronautical Systems Division, Wright-Patterson Air Force Base, Ohio

Invited Papers

STANDARDIZING THE DYNAMICS OF MAN

Dr. H. E. Von Gierke, Aerospace Medical Research Laboratory, Wright-Patterson Air Force Base, Ohio

THE RIVET GYRO STORY

Mr. John E. Short, Aeronautical Systems Division, Wright-Patterson Air Force Base, Ohio

AVIONICS RELIABILITY

Lt. Colonel Ben H. Swett, Headquarters, Air Force Systems Command, Andrews Air Force Base, Washington, D.C.

Panel Sessions

MIL-STD-810C

TEST OR ANALYZE?

Seismic

SEISMIC SIMULATOR FOR SILO CONSTRAINED MISSILE GUIDANCE PLATFORM

R. L. Felker, Rockwell International Corporation, Anaheim, California

EARTHQUAKE RESPONSE OF COMMUNICATIONS EQUIPMENT IN SMALL BUILDINGS

N. J. DeCapua and F. X. Prendergast, Bell Laboratories, Whippany, New Jersey

SEISMIC ANALYSIS OF MOTORS FOR NUCLEAR POWER PLANTS

L. J. Taylor, Westinghouse Electric Corporation, Buffalo, New York and N. M. Isada, State University of New York at Buffalo, New York

Special Problems

EXTENSION OF CONTROL TECHNIQUES FOR DIGITAL CONTROL OF RANDOM VIBRATION TESTS

J. D. Tebbs and D. O. Smallwood, Sandia Laboratories, Albuquerque, New Mexico

VIBRATION-INDUCED DOPPLER EFFECTS ON AN AIRBORNE SHF COMMUNICATION SYSTEM

J. Pearson and R. E. Thaller, Air Force Flight Dynamics Laboratory, Wright-Patterson Air Force Base, Ohio

FATIGUE DAMAGE EQUIVALENCE OF FIELD AND SIMULATED VIBRATIONAL ENVIRONMENTS

D. D. Kana and D. C. Scheidt, Southwest Research Institute, San Antonio, Texas

AN EVALUATION OF SHOCK RESPONSE TECHNIQUES FOR A SHIPBOARD GAS TURBINE

J. R. Manceau and E. Nelson, AiResearch Manufacturing Company of Arizona, Phoenix, Arizona

THE DEVELOPMENT OF A WATER PARTICLE VELOCITY METER

J. D. Gordon, Naval Ship Research and Development Center, Underwater Explosions Research Division, Portsmouth, Virginia

PAPERS APPEARING IN PART 4

Impact

EXPLOSIVELY PROPELLED ROTATING PLATES FOR OBLIQUE IMPACT EXPERIMENTS

F. H. Mathews, Sandia Laboratories, Albuquerque, New Mexico

IMPACT TESTING USING A VARIABLE ANGLE ROCKET LAUNCHER

H. W. Nunez, Sandia Laboratories, Albuquerque, New Mexico

EVALUATION OF THE SHOCK PULSE TECHNIQUE TO THE UH-1 SERIES HELICOPTER

J. A. George, T. C. Mayer and E. F. Covill, Parks College of St. Louis University, Cahokia, Illinois

STRUCTURAL RESPONSE MODELING OF A FREE-FALL MINE AT WATER ENTRY

R. H. Waser, G. L. Matteson and J. W. Honaker, Naval Surface Weapons Center, White Oak Laboratory, Silver Spring, Maryland

PLASTIC DESIGN ANALYSIS OF SHIPBOARD EQUIPMENT SUBJECTED TO SHOCK MOTIONS

L. T. Butt, Naval Ship Research and Development Center, Underwater Explosions Research Division, Portsmouth, Virginia

Packaging and Shipping

HIGHWAY SHOCK INDEX (SI) PROCEDURE FOR DETERMINING SI

J. H. Grier, Military Traffic Management Command, Transportation Engineering Agency, Newport News, Virginia

THE DYNAMIC ENVIRONMENT ON FOUR INDUSTRIAL FORKLIFT TRUCKS

M. B. Gens, Sandia Laboratories, Albuquerque, New Mexico

A STATISTICALLY BASED PROCEDURE FOR TEMPERATURE SENSITIVE DYNAMIC CUSHIONING CURVE DEVELOPMENT AND VALIDATION

D. McDaniel, U.S. Army Missile Command, Redstone Arsenal, Alabama, R. M. Wyskida and M. R. Wilhelm, The University of Alabama, Huntsville, Alabama

A DAVIS GUN PENETRATOR LAUNCH SYSTEM

L. O. Seamons, Sandia Laboratories, Albuquerque, New Mexico

Blast and Impulsive Loading

X-RAY SIMULATION WITH LIGHT-INITIATED EXPLOSIVE

R. A. Benham and F. H. Mathews, Sandia Laboratories, Albuquerque, New Mexico

STRUCTURAL DYNAMIC RESPONSE TO HEIGHT OF BURST AIR BLAST LOADING

H. F. Korman, N. Lipner and J. S. Chiu, TRW Systems Group, Redondo Beach, California

RESPONSE OF FLAT PLATES SUBJECTED TO MILD IMPULSIVE LOADINGS

C. A. Ross, University of Florida Graduate Engineering Center, Eglin Air Force Base, Florida and W. S. Strickland, U. S. Air Force Armament Laboratory, Eglin Air Force Base, Florida

A MATRIX STRUCTURAL DYNAMIC MODEL OF PARACHUTE THERMAL COVER EJECTION BY PYROTECHNIC DEVICES

A. E. Barniskis and R. A. Romanzi, General Electric Company, Philadelphia, Pennsylvania

STRUCTUREBORNE GUN BLAST SHOCK TEST USING AN ELECTROHYDRAULIC VIBRATION EXCITER

N. D. Nelson, Hughes Aircraft Company, Fullerton, California and R. L. Woodfin, Naval Weapons Center, China Lake, California

DYNAMIC PROPERTIES OF CONCRETE UNDER IMPACT LOADING

G. R. Griner, R. L. Sierakowski, and C. A. Ross, Department of Engineering Sciences, University of Florida, Gainesville, Florida

PREDICTING PLATE RESPONSE TO BLAST LOADING

Lt. Col. Robert O. Meitz and Lt. Philip B. Aitken-Cade, Air Force Institute of Technology, Wright-Patterson Air Force Base, Ohio

PAPERS APPEARING IN PART 5

Isolation and Damping

IMPACT ON COMPLEX MECHANICAL STRUCTURES

S. F. Jan, Bechtel Power Corporation, Houston, Texas and E. A. Ripperger, The University of Texas at Austin, Austin, Texas

ENERGY ABSORPTION AND PHASE EFFECTS IN SHOCK EXCITED COUPLED SYSTEMS

C. T. Morrow, Advanced Technology Center, Inc., Dallas, Texas

HIGH PERFORMANCE VIBRATION ISOLATION SYSTEM FOR THE DD963 GEARS

P. C. Warner, Westinghouse Electric Corporation, Sunnyvale, California and D. V. Wright, Westinghouse Electric Corporation, Pittsburgh, Pennsylvania

THE DESIGN AND MEASUREMENT OF A HIGH IMPEDANCE FOUNDATION TO 20 kHz AND USE OF THE DATA IN CORRECTING NOISE MEASUREMENTS

J. R. Hupton, Westinghouse Electric Corporation, Sunnyvale, California

RESPONSE OF THICK STRUCTURES DAMPED BY VISCOELASTIC MATERIAL WITH APPLICATION TO LAYERED BEAMS AND PLATES

M. Lalanne, M. Paulard and P. Trompette, Institut National des Sciences Appliquees, Villeurbanne, France

CONTROLLING THE DYNAMIC RESPONSE OF JET ENGINE COMPONENTS

D. I. G. Jones, Air Force Materials Laboratory, Wright-Patterson Air Force Base, Ohio and C. M. Cannon, M. L. Parin, University of Dayton, Dayton, Ohio

AN INVESTIGATION OF THE RESPONSE OF A DAMPED STRUCTURE USING DIGITAL TECHNIQUES

M. L. Drake, University of Dayton Research Institute, Dayton, Ohio and J. P. Henderson, Air Force Materials Laboratory, Wright-Patterson Air Force Base, Ohio

AN ALTERNATIVE SYSTEM FOR MEASURING COMPLEX DYNAMIC MODULI OF DAMPING MATERIALS

D. I. G. Jones, Air Force Materials Laboratory, Wright-Patterson Air Force Base, Ohio

Dynamic Analysis

NONLINEAR VIBRATION OF CYLINDRICAL SHELLS UNDER RADIAL LINE LOAD

S. S. Taug, Rockwell International Corporation, Los Angeles, California

DETERMINATION OF THE ELASTIC MODES AND FREQUENCIES WHEN RIGID BODY MODES EXIST

J. W. Straight, Christian Brothers College, Memphis, Tennessee

ON THE FORCED VIBRATION OF TRIANGULAR PLATES

H. M. Negm, S. Chander, and B. K. Donaldson, Department of Aerospace Engineering, University of Maryland, College Park, Maryland

EXPERIMENTAL DETERMINATION OF MULTIDIRECTIONAL MOBILITY DATA FOR BEAMS

D. J. Ewins, Imperial College of Science and Technology, London, England and P. T. Gleeson, Middlesex Polytechnic and Imperial College, London, England

A NEW STUDY OF THE HARMONIC OSCILLATOR WITH NON-LINEAR FLUID DAMPING

R. A. Eyman, Martin Marietta Aerospace, Orlando, Florida

MECHANICAL DESIGN, ANALYSIS, AND TEST OF THE STANDARD ELECTRONICS CABINET AND CONTROL DISPLAY CONSOLE FOR THE AN/BQQ-5 SONAR SET

R. E. Denver and J. M. Menichello, IBM Corporation, Owego, New York

SHOCK SPECTRA, RESIDUAL, INITIAL AND MAXIMAX AS CRITERIA OF SHOCK SEVERITY

C. T. Morrow, Advanced Technology Center, Inc., Dallas, Texas

AEROSPACE VEHICLES

AN EXPERIMENTAL/ANALYTICAL DETERMINATION OF TRANSPORTER LOADS ON THE VIKING SPACECRAFT

George Kachadourian
General Electric Re-entry & Environmental Systems Division
Viking Project Support Services
Hampton, Virginia

Transportation tests were performed at the Kennedy Space Center using a full scale Dynamic Simulator of the Viking Spacecraft. Loads in the Viking Dynamic Simulator were measured and compared with allowables. Analysis method for determining loads in transportation of flight articles was defined.

INTRODUCTION

The universal requirement for the design and operation of handling and transport equipment is that they shall not impose design load conditions on the space flight article. That launch site transportation loads are not critical for the Encapsulated Viking Spacecraft was demonstrated in November and December of 1973 during transportation of a Viking Dynamic Simulator. This paper presents the experimental and analytical methods used in this demonstration.

PROJECT DESCRIPTION

Two Viking spacecraft, each consisting of an orbiter and a sterilized lander capsule, will be separately launched by Titan/Centaur launch vehicles from the Air Force Eastern Test Range at Cape Kennedy during the 1975 Mars launch opportunity. The two spacecraft are to provide complementary data about Mars and perform complementary functions as well as provide redundancy.

The launch vehicle is made up of the Titan III E Booster Vehicle and the Centaur D-1T space vehicle with the Centaur Standard Shroud enclosing the entire Centaur and Viking Spacecraft (Figure 1). The first Titan/Centaur flight, TC-1, launched February 11, 1974, was a Proof Flight for this new launch vehicle configuration. The payload carried was a low frequency dynamic simulator of the Viking Spacecraft.

The primary objective of the TC-1 Proof Flight was to demonstrate the Titan/Centaur combination.

DESCRIPTION OF THE VIKING DYNAMIC SIMULATOR

The Viking Spacecraft is made up of two major assemblies, the Viking Lander Capsule and the Viking Orbiter as shown in Figure 2. The Viking Orbiter is itself made up of two large masses, the Orbiter Bus and the Orbiter Propulsion System. The total spacecraft is supported by a 12 member truss adapter and the Lander is supported off the Orbiter by a 6 member truss adapter.

The Viking Dynamic Simulator, pictured in Figure 3 uses the same truss adaptors as the Viking Spacecraft and three relatively rigid masses. The cylindrical body on top duplicates the weight, center of gravity and moments of inertia of the Viking Lander Capsule. The two mass Orbiter Dynamic Simulator duplicates the weight, center of gravity and moment of inertia properties of the Viking Orbiter.

The two Orbiter Simulator masses are connected by a set of flat beam springs. The mass proportionment and longitudinal stiffness are such as to duplicate the first longitudinal mode of the Viking Spacecraft both as to frequency and effective mass.

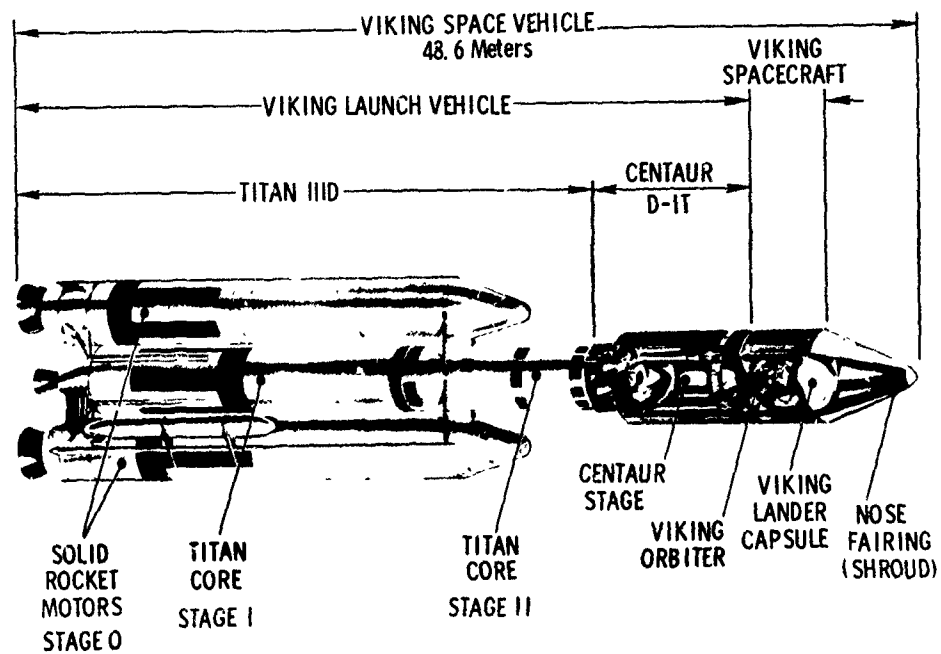


FIGURE 1. VIKING SPACE VEHICLE CONFIGURATION

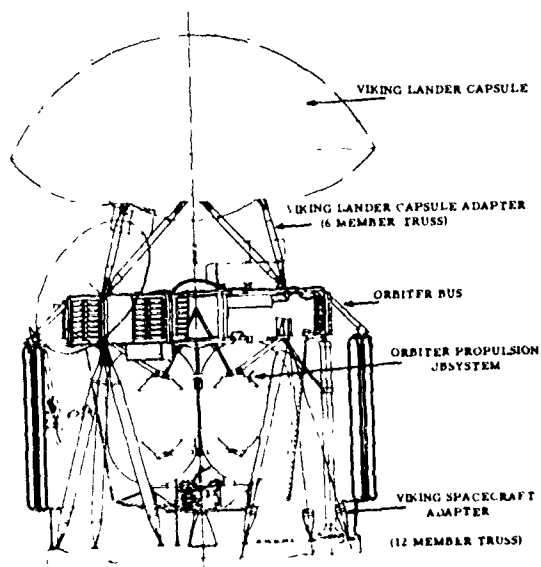


FIGURE 2. VIKING SPACECRAFT CONFIGURATION



FIGURE 3. VIKING DYNAMIC SIMULATOR

Table 1 and Figure 4 show a comparison of the Viking Spacecraft and Viking Dynamic Simulator modal frequencies and effective masses. The comparison shows excellent agreement in view of the simplicity of the simulation.

The Viking Dynamic Simulator was not intended to be an exact simulation but only as close as possible within directed cost objectives. Its primary intended usage was to verify dynamic analysis methods used in predicting Viking Spacecraft loads. This was accomplished through measurements of response loads and accelerations during launch flight and comparison to analytically predicted responses for the Proof Flight configuration.

VIKING DYNAMIC SIMULATOR MODAL CHARACTERISTICS AND TRANSPORTATION LOAD LIMIT CRITERIA

A comprehensive experimental and analytical program was performed to determine the modal characteristics of the VDS. The details of this work are described in Reference 1. In addition to frequencies and mode shapes, the work of Reference 1 also resulted in the definition of modal force coefficients for the 18 members of the lander and spacecraft adapters. The force coefficients for a given mode indicate the modal force in each member for normalized amplitude of the eigenvector solution.

Table 1 contains a summary of the characteristic frequencies of the Viking Dynamic Simulator with a comparison of experimental and analytic results. The comparison shows the math model to be a good one. In Reference 1 comparison is also made of other parameters (mode shape, modal effective mass, generalized mass and force coefficient data) with the same general conclusion of good correlation between experimental results and math model results.

Given the modal characteristics of a configuration it is theoretically possible to define a limit load criteria referenced to one parameter. That is the limit value for that parameter can be defined for each mode which will preclude the exceedance of load limits throughout the configuration. The practical limitation is that any given parameter is not equally sensitive to all modes and will probably have very poor sensitivity to some modes.

For the Viking Spacecraft configuration the two truss adapters (Viking Lander Capsule Adapter and Viking Spacecraft Adapter) are convenient structures for indicating the response levels of the basic structural modes (i. e. low frequency). For the Viking Dynamic Simulator (VDS) they are also the critically loaded elements. A definition of allowable loads in these adapters is consequently sufficient for the total VDS. It was therefore decided that, for the VDS transportation test, loads in the six Lander Adapter struts would be monitored. The load limits in each of the six struts were defined so that the load limits of all 18 struts would not be exceeded.

The matrix of modal force coefficients shown in Table 2 was developed for this purpose with the VDS math model cantilevered at the base of the Viking Spacecraft Adapter. Load limits for the adapter members were taken as 50% of design limit reduced by 1 g loads. The 50% margin was felt to be needed for two reasons: first to cover for loads uncertainties and second to cover for fatigue effects. Loads uncertainties are due primarily to the fact that there was no VDS loads prediction for the transportation configuration and because the load limit criteria is based on a math model which uses approximate boundary conditions, (i. e. cantilevered at the transporter interface.)

The resulting limit strain criteria is shown here in Table 3. The use of this criteria requires that the measured strain data be frequency analyzed. That is the transient vibration induced in transportation will be composites of several frequencies. The analysis must identify each frequency and its amplitude.

ASSEMBLY AND TRANSPORTATION

The Viking Spacecraft will be assembled and encapsulated in the Spacecraft Assembly and Encapsulation Building (SAEB No. 2) clean room. Assembly will be on the transporter. Encapsulation will be with the forward portion of the Centaur Standard Shroud.

When ready for assembly to the Launch Vehicle the Encapsulated Spacecraft will be transported to Launch Complex 41 in the train configuration shown in Figure 5. Transportation will be over either of the two routes shown in Figure 6. The two routes are about equal with respect to road roughness and

TABLE 1. COMPARISON OF VIKING DYNAMIC SIMULATOR
AND VIKING SPACECRAFT RESONANT MODES

Description of Mode (VDS Coordinates)	Viking Space- craft Analysis		Viking Dynamic Simulator		
	No.	Hz	No.	Test Hz	Anal. Hz
X Bending	1	4.32	1	4.48	4.41
Y Bending	2	4.40	2	4.66	4.57
Θ_z (torsion)	-	-	3	6.83	6.78
Coupled Modes	3	6.93			
	4	7.03			
	5	9.04	4	9.44	9.43
	6	9.67	5	9.77	9.57
	7	10.34			
	8	10.70			
	9	12.05			
	10	13.04			
	11	13.18			
	12	13.40			
Z Translation	13	14.55	6	13.41	13.45
Z Translation	14	14.86			
Coupled Modes	15	15.67	7	13.96	13.74
	16	15.86			
	17	16.25			
	18	16.45			
Z Translation	19	17.19			
Coupled Modes	20	17.60			
	21	18.23	8	18.37	20.21

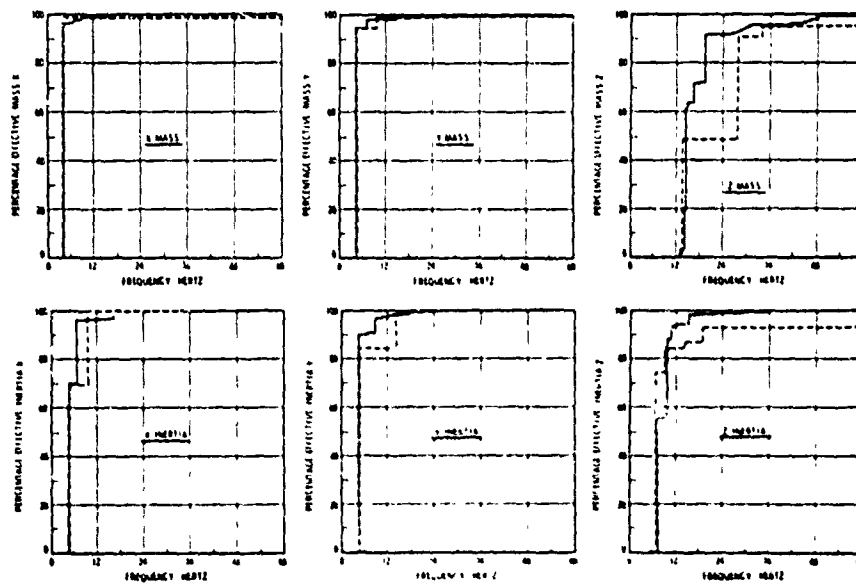


FIGURE 4. COMPARISON OF EFFECTIVE MODAL MASS

— Viking Spacecraft
- - - Viking Dynamic Simulator

TABLE 2 MODEL FORCE COEFFICIENTS ADAPTER MEMBERS (POUNDS)

Mode No.	1	2	3	4	5	6	7	8	9	10	11	Limit Load
Freq. (Hz)	7.01	7.46	7.59	10.25	11.45	13.79	16.49	23.39	30.82	35.18	40.72	
1	-646	-1415	157	-7094	7868	-484	11533	22706	-15810	-27141	-9427	2245
2	608	-1114	-711	6930	8286	-391	-11777	-21382	-18245	-28264	-23607	
3	-2394	982	892	-8347	-5596	-103	-3180	-3189	-2228	-25472	11901	3960
4	2427	1327	-381	8435	-5289	-139	3359	1567	-2423	-23217	34065	
5	-1931	572	111	-1844	-5836	-298	-8666	14652	-32435	27426	6085	3690
6	1942	526	125	1942	-5643	-352	9116	-13511	-31473	26062	-15879	
7	-3701	4650	-1081	5682	-3422	-1861	4354	10524	-5605	-9123	-16507	
8	-4409	-4545	1412	-152	3464	-1965	10671	-8259	-11683	-2160	11904	3475
9	4307	-3506	-3143	251	3444	-1868	-10544	8482	-11203	-2984	3527	
10	3801	3412	2824	-5770	-3663	-1880	-4223	-10221	-6496	-7298	-2095	
11	942	1169	-166	1446	-3908	-1845	4798	3833	-6144	-8356	-10717	
12	540	-1176	149	-904	3857	-1935	6485	328	-11076	-3023	5943	2175
13	-573	-932	-595	816	3863	-1861	-6297	-221	-11003	-2739	5979	
14	-913	954	615	-1359	-3989	-1788	-4730	-3405	-6455	-7461	-4272	
15	-3996	4397	2728	-5	5427	-2197	-3111	-10810	-12631	-3103	8940	
16	4069	-5195	400	-2270	-5567	-2176	7384	-4485	-8138	-8767	-3908	3562
17	4096	5113	-655	-474	5446	-2263	3464	10683	-12137	-4802	-1836	
18	-4178	-4296	-2480	2682	-5511	-2104	-7435	5258	-7813	-8954	-6711	

TRUSS ELEMENT NO.

TABLE 3. TRANSPORTATION STRAIN LIMITS BY MODES
FOR LANDER CAPSULE ADAPTER MEMBERS

Mode No.	1	2	3	4	5	6	7	8	9	10
Frequency, Hz	7.01	7.46	7.59	10.25	11.45	13.79	16.49	23.39	30.82	35.18
Strain, μ in./in.										
1-(209)	- 81	-154	33	-357	339	- 86	349	357	-286	-343
2-(210)	76	-121	-148	349	357	- 70	-357	-336	-330	-357
3-(211)	-300	107	185	-420	-241	- 18	- 96	- 50	- 40	-321
4-(214)	304	145	- 79	425	-228	- 25	102	25	- 44	-293
5-(212)	-242	62	23	- 93	-251	- 53	-263	230	-587	346
6-(213)	243	57	26	98	-243	- 63	283	-212	-569	329

distance (about 13 miles). One notable difference is the drawbridge on the south route.

Assembly, encapsulation, transportation and erection of the Viking Dynamic Simulator (VDS) on the Proof Flight Launch Vehicle duplicated to the extent possible the planned Viking procedures. Since environmental controls were not required for the VDS the associated lines, ducts and GSE on the trailer were mass simulated. The trailer was also used to carry instrument conditioning and recording equipment.

VIKING DYNAMIC SIMULATOR TRANSPORTATION TEST

Transportation tests were performed using the basic train configuration shown in Figure 5. The north route shown in Figure 6 was traveled in going from SAEB No. 2 to Launch Complex 41 and the south route was used in return.

Instrumentation for the VDS transportation test consisted of eight accelerometers, six strain gages, and transporter speed. Location and notation on the accelerometers and strain gages are shown in Figures 7 and 8. All data was displayed in real time on two Brush Recorders

Tape recordings were also made on two magnetic tape recorders. Both tape recorders also recorded time and voice. All four recorders were carried on the support trailer. Instruments and recording system were chosen to provide flat frequency response from 0 to 50 Hertz.

Three of the eight accelerometers were mounted to provide a measure of transporter vibration (A₁, A₂ and A₃). The other five were located on the frame adapter which interfaces the Viking Spacecraft Adapter. These five accelerometers were located so that five degree of freedom motion of the spacecraft support plane can be defined. (Rotational motion about the roll axis of the spacecraft was not measured). Full scale recording range was set at $\pm 1.0g$ peak for the vertical accelerometers and $\pm 0.5g$ peak for the horizontal accelerometers.

The six strain gage measurements were the flight gages located one on each of the six members of the PFLA. Strain gage channels were calibrated for full scale of $\pm 100 \mu$ in./in. Conversion factors between strain and load had been obtained from laboratory testing of the adapter members prior to assembly.

TRANSPORTATION TEST RESULTS

The basic procedure followed in the analysis of test results was to compare measured Lander Adapter strut loads (strains) to allowables. This was done first without regard to frequency content. If the maximum strain measured in each strut was less than the lowest modal strain limit no further analysis was necessary. If on the other hand the strain limit was exceeded it was necessary to frequency analyze the test data in order to make a mode by mode comparison of measured strain to strain limit.

This procedure was carried out in two phases. The first was a real time monitor of strain readings displayed on the Brush

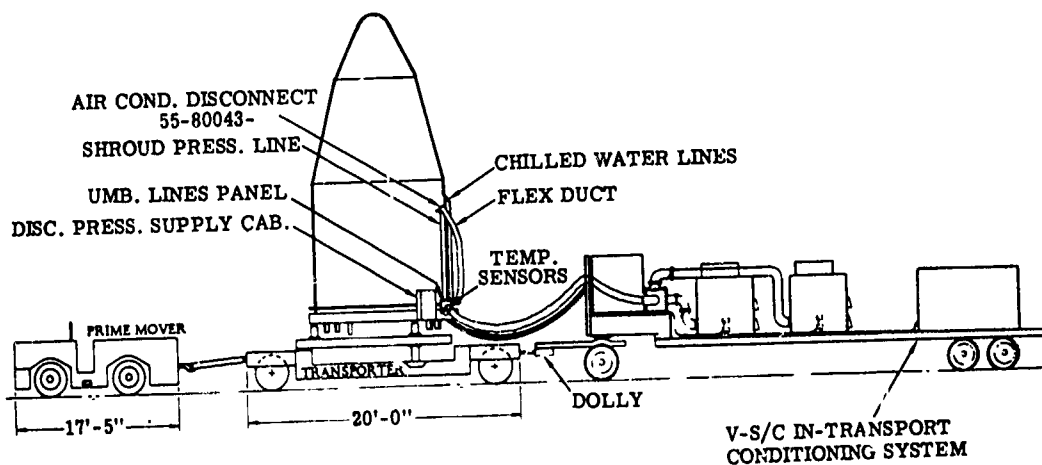


FIGURE 5. ENCAPSULATED VIKING SPACECRAFT IN TRANSPORTER TRAIN

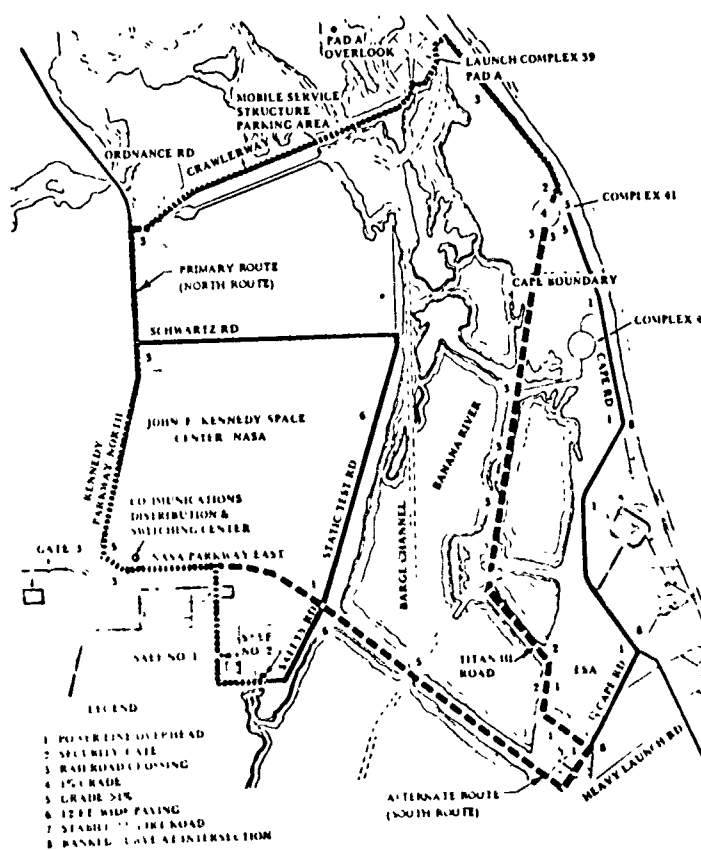


FIGURE 6. TRANSPORTATION ROUTES BETWEEN SAEB AND LAUNCH COMPLEX 41

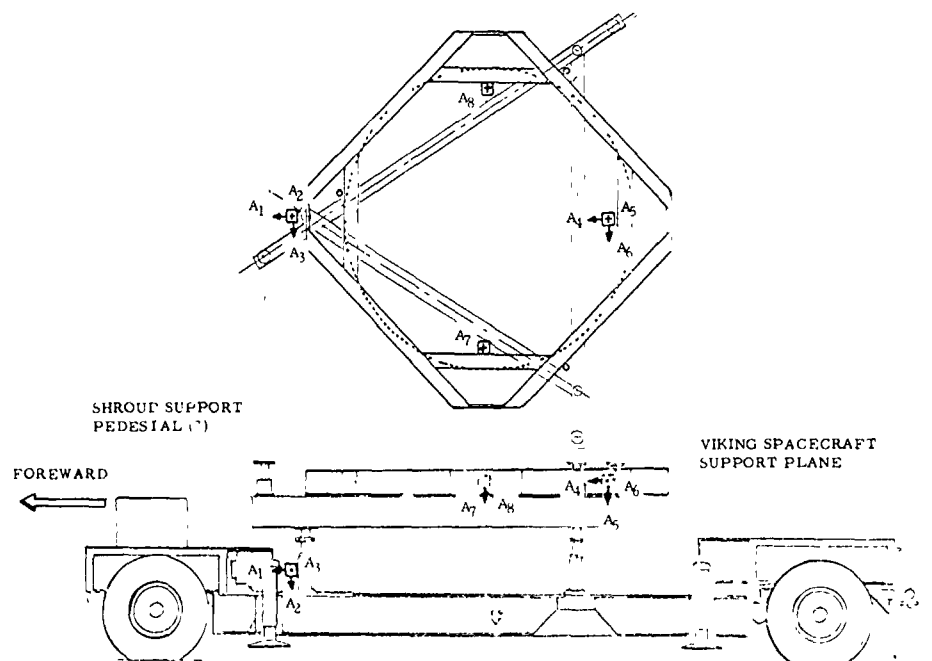


FIGURE 7. ACCELEROMETER LOCATIONS ON VIKING TRANSPORTER

Recorders. The second phase was performed at the NASA Langley Research Center following completion of the test. The real time analysis was necessarily cursory with frequency analysis being limited primarily to identification of the transporter low frequency modes. Oscillograph records were made at Langley for the second phase effort with blow up as to both time and amplitude. There were 23 time segments identified as including all significant loadings over the total test and detailed analysis was concentrated on these time segments. Maximum values of each strain gage and accelerometer were read for each of the 23 time segments. These readings are contained in Tables 4a and 4b. The accelerometer data shows to be very low, the maximum out of 184 reading being ± 0.13 g peak.

The strain readings are also low valued but generally exceed the lowest allowable modal strain (18 micro inch/inch). A detailed frequency analysis was then made of the strain data to show that on a modal comparison basis load limits were not exceeded.

Three methods of frequency analysis were considered: Fourier, narrow band filter and manual ("eyeball"). The Fourier analysis was not suitable since the highest loadings occurred during transient conditions and the non-stationary nature of the responses could not be properly analyzed by Fourier methods. The narrow band filter analysis method was better suited but problems in obtaining proper filter characteristics were anticipated (i. e. bandwidth, roll off characteristics and damping). The manual method was chosen for use for several reasons. First, the strain data showed that generally the maximum responses in any time segment was in identifiable and separable frequencies so that manual frequency analysis was in most cases easily done. The analysis could be done quickly. Finally it appeared that there would be large margins between measured loads and load limits which would permit the relative inaccuracy of the manual analysis.

The frequency analysis of the 23 time segments showed the total responses to be made up of 7 discernable frequencies. These

TABLE 4a. VDS TRANSPORTATION TEST - PEAK STRAIN DATA

EVENT	(Speed: MPH)	PEAK STRAINS - $\pm \mu$ IN./IN.					
		211	214	213	212	210	209
1	NASA Causeway East of Relief Bridge (5.3)	24	21	18	22	26	25
2	Same (5.1)	27	31	29	26	29	29
3	NASA Causeway, Crossing Relief Bridge (6.7)	24	28	19	16	29	22
4	NASA Causeway, East of Draw Bridge (8.0)	24	36	25	24	31	33
5	NASA Causeway East, Downshift (2.0)	30	32	27	25	31	32
6	Upramp NASA Causeway Draw Bridge (1.5)	16	16	11	13	19	19
7	NASA Causeway Draw Bridge Grating (2.5)	21	22	17	20	29	20
8	Causeway Bridge Down Ramp, Braking (3.0 - 3.5)	18	25	15	16	24	19
9	NASA Causeway, West of Draw Bridge (5.6)	26	26	26	26	33	30
10	Ave. E, Pipe Trench (5.2 - 4.0)	21	32	30	24	28	27
11	Avenue E (3.5)	22	24	27	21	25	29
12	Upshift, Ave. E, Northbound (3.7 - 4.6)	34	42	32	29	29	34
13	Ave. E, Northbound (5.5)	26	26	23	24	33	39
14	NASA Causeway, Westbound from Ave. E, Upshift (3.0 - 4.0)	38	34	30	32	39	31
15	NASA Causeway, Westbound from Ave. E (6.0)	13	14	12	21	22	19
16	NASA Causeway Westbound, Upshift (3.9 - 5.1)	21	34	23	20	20	28
17	Kennedy Parkway (8.0)	33	25	22	23	43	30
18	R.R. Crossing, VAB (1.3)	31	36	29	26	31	27
19	Pothole & Downshift (7.5 - 6.0)	46	57	41	37	43	50
20	Cape Road (7.0)	31	29	20	22	34	29
21	Beach Road, Upshift (7.2 - 7.5)	49	31	30	31	48	38
22	Maneuvering Transient at Cx 41 ~ 0	44	29	19	30	33	29
23	NASA Causeway Crossover (Lane divider reflectors) (5.7)	56	42	30	34	45	53

TABLE 4b. VDS TRANSPORTATION TEST ACCELEROMETER DATA

EVENT	(Speed, MPH)	ACCELEROMETER DATA - PEAK \pm G'S							
		A1	A2	A3	A5	A6	A4	A7	A8
1	NASA Causeway East of Relief Bridge (5.3)	.02	.01	0	.06	.024	.059	.058	.038
2	Same (5.1)	.06	.03	.02	.07	.030	.044	.080	.061
3	NASA Causeway, Crossing Relief Bridge (6.7)	.03	.02	.02	.03	.017	.035	.036	.030
4	NASA Causeway, East of Drawbridge (8.0)	.06	.03	.04	.09	.028	.059	.087	.091
5	NASA Causeway, East, Downshift (2.0)	.05	.02	.10	.09	.033	.123	.073	.053
6	Upramp NASA Causeway Drawbridge (1.5)	.05	.02	.01	.06	.005	.020	.036	.038
7	NASA Causeway Drawbridge Grating (2.5)	.02	.02	.02	.05	.012	.028	.044	.045
8	Causeway Bridge Down Ramp (Braking) (3.0 - 3.5)	.03	.02	.02	.03	.019	.037	.044	.038
9	NASA Causeway, West of Drawbridge (5.6)	.03	.02	.02	.05	.044	.037	.073	.091
10	Ave. E, Pipe Trench (5.2 - 4.0)	.03	.02	.03	.05	.026	.052	.073	.045
11	Ave. E (5.5)	.02	.01	0	.04	.025	.037	.051	.045
12	Upshift Ave. E Northbound (3.7 - 4.6)	.05	.02	.12	.09	.037	.130	.073	.076
13	Ave. E, Northbound (5.5)	.04	.02	.02	.05	.032	.037	.044	.045
14	NASA Causeway, Westbound from Ave. E, Upshift (3.0 - 4.0)	.05	0	.09	.06	.032	.100	.065	.061
15	NASA Causeway, Westbound from Ave. E (6.0)	.02	.01	0	.03	.028	.018	.036	.038
16	NASA Causeway, Westbound Upshift (3.9 - 5.1)	.02	.01	.05	.04	.021	.066	.036	.038
17	Kennedy Parkway (8.0)	.02	.01	.01	.03	.026	.024	.044	.053
18	RR Crossing, VAB (1.3)	.07	.03	.02	.03	.017	.040	.065	.076
19	Pothole & Downshift (7.5 - 6.0)	.07	.04	.05	.09	.034	.088	.087	.106
20	Cape Road (7.0)	.03	.02	.02	.04	.028	.028	.044	.045
21	Beach Road, Upshift (7.2 - 7.5)	.02	.02	.02	.06	.036	.072	.073	.076
22	Maneuvering Transient at Cx 41 (~ 0)	.04	.08	.06	.04	.036	.074	.036	.038
23	NASA Causeway Crossover (5.7)	.03	.03	.02	.06	.05	.04	.09	.09

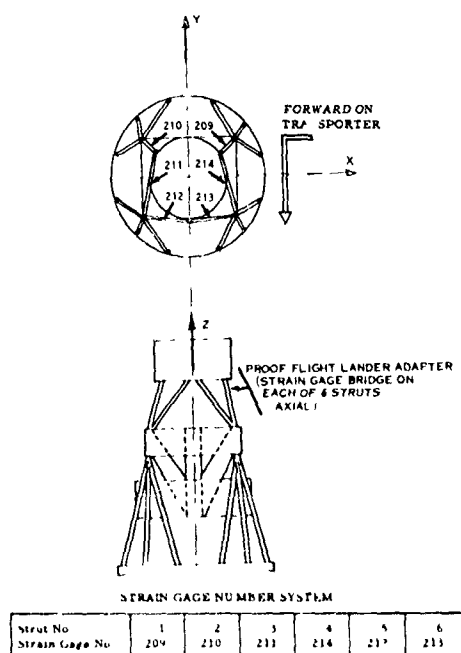


FIGURE 8. STRAIN GAGE LOCATIONS ON VIKING DYNAMIC SIMULATOR

TABLE 5. MODAL IDENTIFICATION OF RESPONSE DATA VIKING DYNAMIC SIMULATOR TRANSPORTATION

VDS MODE NO.	CANTILEVER ANALYSIS FREQ. (HZ)	DESCRIPTION OF MODE	TRANSPORTATION DATA	
			FREQ. (HZ)	OCCURRENCE
0	--	Transporter Rocking	1.2	Infrequent (low level)
0	--	Transporter Vertical	2-2.5	Predominant
1	7.01	X	5.9-6.2	Frequent
2	7.40	Y	--	Not Discernable
3	7.59	Θ_z	--	Not Discernable
4	10.25	X & Y	10-11	Frequent
5	11.45	Y	--	(See Discussion)
6	13.79	Z	--	Not Discernable
7	16.49	Θ_y & Θ_z	16-17	Frequent
8	23.39	Θ_y & X	19-22	Infrequent (low level)
9	30.82	Z	--	Not Discernable
10	35.18	Coupled	35-36	Frequent

frequencies are listed and identified as to mode in Table 5. The Mode 1 identification was made on the basis of frequency and mode shape. Although Modes 1, 2 and 3 are all between 7.0 to 7.6 Hertz, the motion of each have basic and easily discerned differences and the measured frequency of about 6 Hertz was identified with Mode 1 mode shape. The difference in frequency is attributable to the fact that the 7.0 Hertz was obtained with a cantilevered math model. The 10-11 Hertz measured response could have been identified with either mode 4 (10.25 Hz) or Mode 5 (11.45 Hz) based on frequency. Identification by mode shape could not be made in this case because of difficulty in reliably determining phase relationships. However further identification was academic since load limits were not exceeded in either case.

Comparison of measured loads against allowables are summarized in the plots of Figures 9, 10 and 11. In each Figure the curves at the top of the plot are the limit strain envelopes. Each dot represents a frequency/strain level reading from the 23 time samples analyzed. The plots show that comfortably large margins exist between the measured modal strains and the strain limits.

The method used to compare transportation loads to allowable considers loads in each mode separately where in the actual case there may be response in more than one mode occurring at the same time. The margins between loads and allowables were large enough that further analysis was felt to be unnecessary.

The most noteworthy factor in the accelerometer data was that the levels were very low. Maximum values were generally less than ± 0.10 g's. The highest value seen in the total, 26 mile circuit, was ± 0.13 g. This was accelerometer No. A4, spacecraft/transporter interface in the fore and aft direction and was caused by gear shift transient. In reviewing the results it became obvious that accelerometer measurements on the transporter is insufficient data to evaluate the severity of the transport environment and can actually be misleading by seeming to be very low.

Although there was a comfortable margin between loads experienced in transportation and allowables, the loads were large enough to emphasize adherence to the transportation

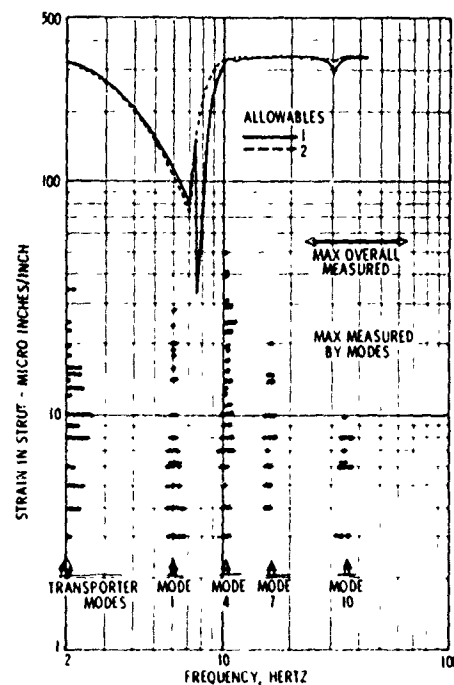


FIGURE 9.

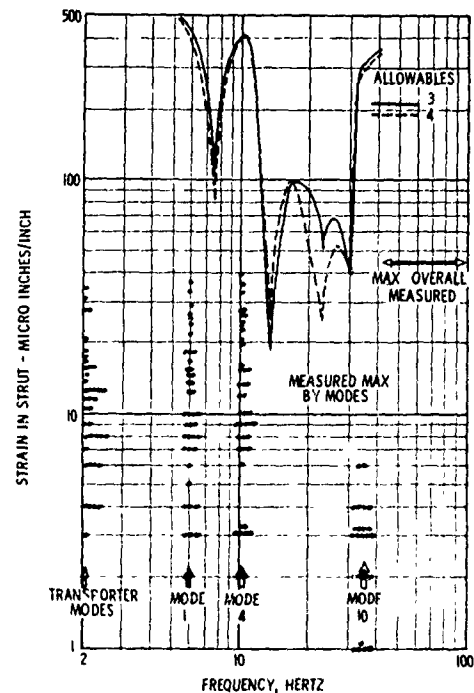


FIGURE 10.

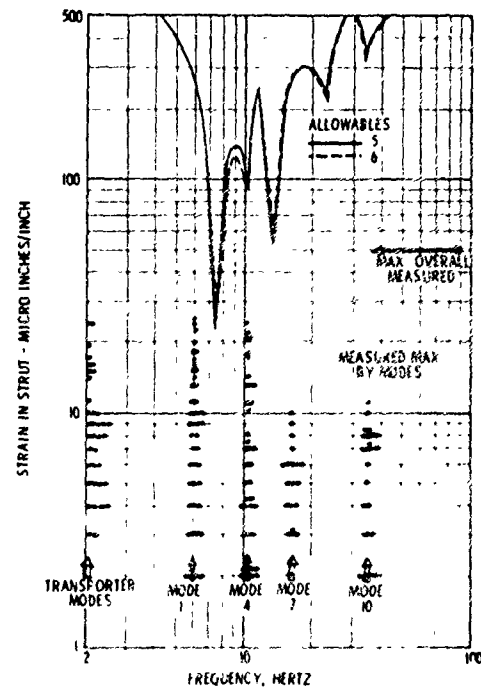


FIGURE 11

procedures specified. These procedures, originally outlined in Reference 2, contain the following pertinent points:

1. Transporter tire pressure should be maintained at 70 psig
2. Transporter speeds should be limited to the following maxima: 8 mph over smooth road; 5 mph over minor bumps; 2.5 mph over railroad tracks and other similar road roughness
3. Sudden hard application of brakes must be avoided
4. Proper use of tug gears is essential to minimize gear shift transient loads.

ANALYTIC SOLUTION OF TRANSPORTATION LOADS

Analytic solutions have been performed which use the accelerometer data at the Spacecraft/Transporter interface as input forcing functions using the math model of the VDS discussed earlier in this report. Preliminary results of this analysis, which is in progress at this writing, show reasonably good correlation of measured and calculated strut loads.

When the Viking Spacecraft is transported there will be accelerometers at the same Spacecraft/Transporter interface locations as for VDS testing with the addition of a 6th accelerometer to provide 6 degree of freedom data. Dynamic loads analysis will be performed only if something unexpected occurs. These dynamic response analysis will be performed using the measured interface motion as input forcing functions to show what loads were experienced by the Viking spacecraft.

CONCLUSIONS

It was shown by conducting transportation tests of the Viking Dynamic Simulator according to prescribed transport procedures, that loads in the spacecraft would be within specification allowables.

It was also shown that in the event of unexpected occurrences during transportation, accelerometer measurements at the Spacecraft/Transporter interface could be used in a dynamic loads analysis to define the loads internal to the spacecraft.

It was found that road roughness and transporter speed were the two most influential parameters in transportation loads. Eight miles per hour was found to be a safe limit speed for smooth road. Lower speeds were required depending on road roughness.

It was found that technique in operating the tug had significant effect on loads generated. Specifically a large transient could be generated at the point where the tug shifted gears. Highest loads were experienced when the train was being slowed down in the approach to a bump in the roadway and the tug down shifted simultaneous with the transporter's traversal of the bump. Proper operation would have reached constant speed operation before bump encounter. Proper tug operating technique can also minimize the transient at gear shift.

Finally it was found that measurement of transporter vibration g levels is insufficient in itself to be assured that spacecraft loads are not exceeded. That is even very low vibration levels (less than ± 0.1 g's) at critical frequencies can cause allowable loads to be exceeded.

ACKNOWLEDGEMENTS

Transportation testing of the Viking Dynamic Simulator was the net result of the coordinated efforts of many people and many agencies. The agencies involved included General Dynamics Convair Aerospace Division, Jet Propulsion Laboratory, Martin Marietta Corporation, NASA Kennedy Space Center, NASA Lewis Research Center, NASA Langley Research Center and the General Electric Company in support of the Viking Project Office at Langley. Floyd Curlington of NASA Kennedy Space Center, Fred Day for the Jet Propulsion Laboratory, Alex Leondis for General Dynamics Convair, Tom Jones of NASA Langley Research Center and Hal Baber of the Viking Project Office contributed to the success of this test program.

REFERENCES

1. A. F. Leondis, Viking Dynamic Simulator Vibration Testing and Analysis Modeling, 45th Shock and Vibration Symposium.
2. J. S. Gacho, Test Report for Viking Transporter Roadability Test, GDCA Report BNZ 72-030, 9 October 1972.

DETERMINATION OF PROPELLANT EFFECTIVE MASS PROPERTIES USING MODAL TEST DATA*

Jay C. Chen and John A. Garba
Jet Propulsion Laboratory
Pasadena, California

Abstract

In the development of a mathematical dynamic model of structural systems, the mass properties of the structure must be represented accurately. For a structural system involving large quantities of fluid mass, special considerations must be taken to obtain the fluid mass properties. Modal vibration testing is required on most spacecraft projects as a means of verification of the mathematical model. This paper presents a method for the evaluation of the effective mass of the fluid from modal test results. Overall cost is reduced by elimination of a special effective mass test and substitution of a slight extension of a required modal test. This method is demonstrated first by a computer simulation and then by the actual modal test data of the Viking Orbiter Propulsion Module.

1. INTRODUCTION

The development of finite element models for dynamic analyses of spacecraft and launch vehicle system requires proper dynamic representation of fluid masses.

Proper mass representation is required for the prediction of loads in structural members as well as in the data reduction for the modal test. A limited number of effective propellant mass properties can be obtained analytically from the derivation of fluid slosh models using classical fluid mechanics (Ref. 1). Full scale propellant tank testing provides a means for obtaining complete fluid mass properties accounting for such effects as geometric tank irregularities, baffles, and propellant management devices. Due to requirements of elaborate fixturing and instrumentation such testing tends to be expensive. During the course of Viking Orbiter structural dynamic analysis, such a test has been conducted (Ref. 2). Figure 1 shows the test set up and Figs. 2 and 3 show the typical measured effective mass properties as a function of the Viking Orbiter propellant tank ullage condition.

Modal vibration testing is required on most spacecraft projects as a means of verification

of the mathematical model. This paper presents a method for the evaluation of the effective mass of the fluid from modal test results. Overall cost is reduced by elimination of a special effective mass test and substitution of a slight extension of a required modal test.

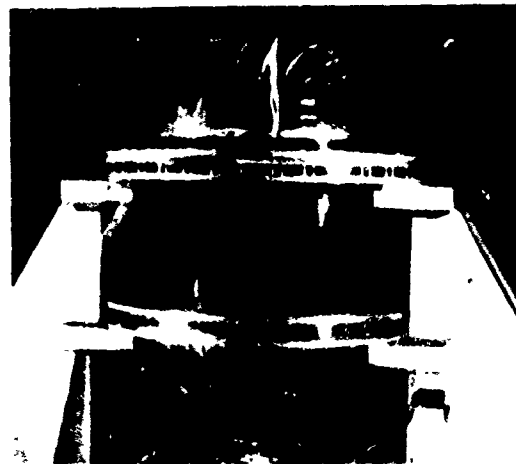


Figure 1 Propellant Tank Effective Weight Test

*This paper presents the results of one phase of research carried out at the Jet Propulsion Laboratory, California Institute of Technology, under Contract No. NAS 7-100, sponsored by the National Aeronautics and Space Administration.

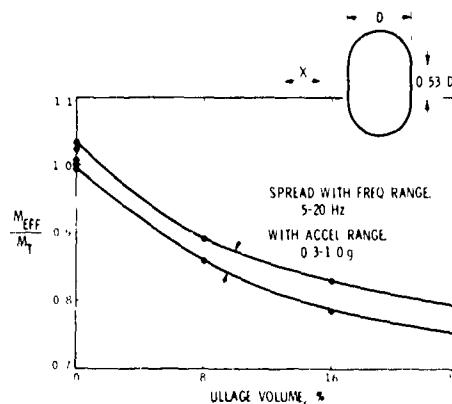


Figure 2 Effective Mass Ratio - PMD In

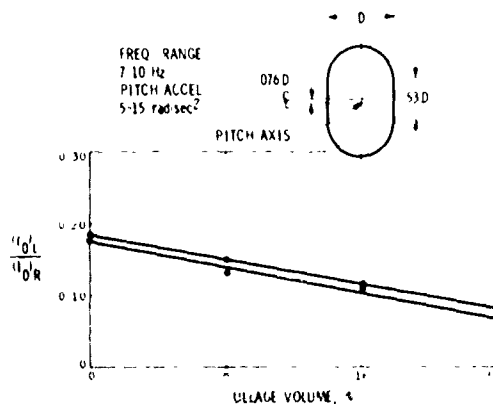


Figure 3. Effective Moment-of-Inertia Ratio - No PMD

First, a relationship between the effective mass matrices of the fluids and the measured mode shapes and system frequencies will be derived. While the derivation is intended for the determination of effective fluid mass the method is equally applicable to other unknown masses.

Next the procedure is demonstrated by computer simulation. Feasibility of the method is established by applying it to an example problem wherein analytical data is presumed to be derived from modal test. The fluid effective mass matrix is thus reconstructed and compared to known results. The agreement is found to be very good.

To further illustrate the feasibility of the method it is applied to the Viking Orbiter. In using Viking modal data it was found that the required modal matrix formulated from test data can be ill-conditioned if inaccuracies exist in the data. This ill-conditioned modal matrix violated certain assumptions made in the derivation of the method. Based on the past experiences, it is likely that the inaccuracies existed in the mode shape measurements rather than the natural frequency measurements. Therefore, a perturbation technique was developed to "treat" the raw test data to avoid this ill-conditioning and perturb the data to result in a solution with physical reality. The results of the fluid effective mass obtained by this method are compared to that obtained from the full scale tank tests.

II. DESCRIPTION OF THE PROBLEM

In the finite-element representation of a structural system, the continuous structure is discretized into individual degrees of freedom which are interconnected by linear springs. These springs represent the stiffness of the elements. For the dynamic problem, a certain amount of mass will be attached to all or some of the degrees-of-freedom. These masses represent the inertia properties of the structural system. Then the equation of motion governing this discretized structural system can be written in the matrix form

$$[M]\{\ddot{x}\} + [C]\{\dot{x}\} + [K]\{x\} = \{f(t)\} \quad (1)$$

where

$[M]$ mass matrix

$[C]$ damping matrix

$[K]$ stiffness matrix

$\{x\}$ displacement vector of each degree-of-freedom

$\{f(t)\}$ forcing function vector

The loads due to the dynamic environments can be calculated by

$$\{P\} = [S]\{x\} \quad (2)$$

where

$\{P\}$ member loads vector

$[S]$ stress coefficient matrix

Here $\{x\}$ is the solution from eq. (1).

Based on the geometric configuration and material properties of the individual element, the stiffness matrix $[K]$ and stress coefficient

matrix $[S]$ can be constructed. The mass matrix $[M]$ usually is constructed by concentrating nonstructural and structural masses onto each degree-of-freedom. The distribution of the masses among all the degrees-of-freedom is dependent solely on the analyst's engineering judgement. The damping matrix $[C]$ is estimated from the test. To predict the responses and loads accurately, the parameters such as the stiffness matrix $[K]$ and mass matrix $[M]$ must be realistically representative of the actual structural system. The state-of-the-art of analytical modeling is quite advanced. The stiffness matrix $[K]$ can be accurately constructed once the geometric dimensions and material properties of discretized elements are determined. The mass matrix $[M]$ can be constructed with relative ease by distributing the physical mass to the degree-of-freedom. The analyst's experienced intuition is usually adequate for determining the mass matrix. Also the total mass of all the degrees-of-freedom must be equal to the total weight of the structure. However, for fluid masses, the mass matrix cannot be accurately determined short of a full scale effectiveness test. Since the "effective mass" is involved, the mass representing the fluid may or may not be equal to the total weight of the fluid.

In a process of structural analysis, the mathematical model formulated by analysis is often verified by certain tests. Usually a modal test is conducted for this purpose. During the modal test, the natural frequencies and the normal modes of the structural system are measured. These correspond to the eigenvalues and eigenvectors of the modal analysis which can be expressed as follows:

$$[M]\{\ddot{x}\} + [K]\{x\} = 0 \quad (3)$$

Let

$$\{x\} = [\phi]\{q\} \quad (4)$$

such that

$$\left. \begin{aligned} [\phi]^T [M] [\phi] &= [M_G] \\ [\phi]^T [K] [\phi] &= [M_G] [\lambda] \end{aligned} \right\} \quad (5)$$

Here $[\phi]$ is the eigenvector matrix and $[\lambda]$ is the eigenvalue. The measured normal modes and natural frequencies are compared to these values. Equation (5) is referred to as the orthogonality condition.

Since the eigenvector $[\phi]$ and the eigenvalue $[\lambda]$ are functions of the mass matrix $[M]$ and the stiffness matrix $[K]$, it is possible that part of the mass matrix which involves the fluid can be identified by using measured $[\phi]$ and $[\lambda]$. Unlike the effective mass obtained by full scale tank test which is constrained in uniaxial motion, the fluid mass properties determined in this fashion have the advantage of being realistic in the fluid motion. In addition the resulting fluid mass matrix shows good correlation with the system being tested. To verify the validity of other parameters modal tests of several different mass configurations can be tested such as an empty configuration or a configuration with known added masses. In the following the relationship between the test measured normal modes, natural frequencies and the unknown fluid mass will be derived.

III. DERIVATION

In principle, the mass matrix $[M]$ and the stiffness matrix $[K]$ can be calculated as a function of the measured normal modes $[\phi]$ and natural frequencies $[\lambda]$ from the orthogonality conditions expressed in Eq. (5) if $[\phi]^{-1}$ exists. However in practice, the number of modes measured during the test are much less than the number of degrees-of-freedom in the analytical model. Therefore, $[\phi]$ will be a rectangular matrix and $[\phi]^{-1}$ does not exist. There are other conditions which must be imposed to calculate the mass matrix.

First, let the number of degrees-of-freedom of the analytical model be n , then the total mass matrix can be written as

$$n \times n \quad [M] = \begin{bmatrix} M_1 & \\ & M_2 \end{bmatrix} \quad (6)$$

where

$m \times m$
 $[M_1]$ = mass matrix associated with fluid mass

m = number of degrees-of-freedom representing the unknown fluid mass

$[M_2]$ = mass matrix representing the mass distribution other than the fluid mass

Further, it is assumed that the stiffness matrix $[K]$ and mass matrix $[M_2]$ constructed by the analyst are correct. These parameters can in practice be verified by tests excluding $[M_1]$, so only the mass matrix $[M_1]$ which is

representing the fluid mass are to be determined.

A pre-test modal analysis with the same stiffness matrix $[K]$ and an estimated mass matrix $[M_F]$ will be performed. The matrix $[M_F]$ will be of the form of

$$[M_F] = \begin{bmatrix} M_{F1} & \\ & M_2 \end{bmatrix} \quad (7)$$

Here $[M_{F1}]$ is estimated.

The modal analysis

$$[M_F]\{\ddot{x}\} + [K]\{x\} = 0 \quad (8)$$

yields the normal mode matrix $[\phi_F]$ and eigenvalues $[\lambda_F]$ which satisfy the following orthogonality condition:

$$\left. \begin{aligned} [\phi_F]^T [M_F] [\phi_F] &= [I] \text{ identity matrix} \\ [\phi_F]^T [K] [\phi_F] &= [\lambda_F] \end{aligned} \right\} \quad (9)$$

Only m number of modes are required, therefore matrix $[\phi_F]$ is of the order $n \times m$.

Now, let the test measured normal modes $[\phi]$ and the pre-test analytical modes $[\phi_F]$ be related by a transformation matrix $[T]$ as follows:

$$[\phi] = [\phi_F][\phi]^T [T] \quad (10)$$

Pre-multiplying Eq. (10) by $[\phi_F]^T [M_F]$ and using Eq. (9), one obtains

$$[M] = [\phi]^T [T] \quad (11)$$

where

$$[M] = [\phi_F]^T [M_F] [\phi] \quad (12)$$

From Eqs. (10) and (11), one obtains

$$[\phi] = [\phi_F][\bar{M}] \quad (13)$$

Here the $[M]$ is a square matrix of order m .

Now substituting Eq. (13) into Eqs. (5) and using Eqs. (9), one may obtain

$$[\bar{M}]^T [\lambda_F] [\bar{M}] = [\lambda] [M_G] \quad (14)$$

$$[\bar{M}] = [\lambda_F] [\bar{M}] [\lambda] [\bar{M}]^{-1} \quad (15)$$

where

$$[\bar{M}] = [\phi_F]^T [M] [\phi_F] \quad (16)$$

The normal mode matrices $[\phi]$ and $[\phi_F]$ can be partitioned into two parts, one is for all the degrees-of-freedom associated with fluid mass and the other is for the rest of the degrees-of-freedom.

$$[\phi_F] = \begin{bmatrix} \phi_{F1} \\ \phi_{F2} \end{bmatrix} \quad (17)$$

where

$$\begin{bmatrix} \phi_{F1} \end{bmatrix}_{m \times m} = \text{Mode shape associated with } [M_{F1}] \text{ degrees-of-freedom.}$$

$$\begin{bmatrix} \phi_{F2} \end{bmatrix}_{(n-m) \times m} = \text{Mode shape associated with other degrees-of-freedom.}$$

Substituting Eqs. (7) and (17) into the orthogonality condition as expressed by Eq. (9), gives

$$\begin{aligned} [\phi_F]^T [M_F] [\phi_F] &= \begin{bmatrix} \phi_{F1} \end{bmatrix}^T \begin{bmatrix} M_{F1} \end{bmatrix} \begin{bmatrix} \phi_{F2} \end{bmatrix}^T \\ &+ \begin{bmatrix} \phi_{F2} \end{bmatrix}^T [M_2] \begin{bmatrix} \phi_{F2} \end{bmatrix} \\ &= [I] \end{aligned} \quad (18)$$

Similarly, Eq. (16) can be expanded as

$$\begin{aligned} [\phi_F]^T [M] [\phi_F] &= \begin{bmatrix} \phi_{F1} \end{bmatrix}^T [M_1] \begin{bmatrix} \phi_{F1} \end{bmatrix} \\ &+ \begin{bmatrix} \phi_{F2} \end{bmatrix}^T [M_2] \begin{bmatrix} \phi_{F2} \end{bmatrix} = [\bar{M}] \end{aligned} \quad (19)$$

Subtracting Eq. (18) from Eq. (19), gives

$$\begin{aligned} [\phi_{F1}]^T [M_1] [\phi_{F1}] &= [\tilde{M}] - [I] \\ &+ [\phi_{F1}]^T [M_{F1}] [\phi_{F1}] \end{aligned} \quad (20)$$

Since $[\phi_{F1}]$ is a square matrix of order m , it can be inverted. Therefore, the unknown fluid mass matrix $[M_1]$ can be calculated as

$$[M_1] = [\phi_{F1}]^{-1} [\tilde{M} - [I] - [\phi_{F1}]^T [M_{F1}] [\phi_{F1}]] [\phi_{F1}]^{-1} \quad (21)$$

In the following, the procedure will be summarized:

1. Collect the test measured normal modes $[\phi]$ and natural frequencies $[\lambda]$.
2. Perform the pre-test analysis based on the estimated unknown fluid mass $[M_{F1}]$ and obtain the normal modes $[\phi_F]$ and eigenvalues $[\lambda_F]$.
3. Calculate $[\tilde{M}] = [\phi_F]^T [M_F] [\phi_F]$

4. Calculate

$$[M] = [\lambda_F]^{-1} [\tilde{M}] [\lambda_F]^{-1} [\tilde{M}]^{-1}$$

5. Calculate the unknown fluid mass $[M_1]$ from Eq. (21).

IV. COMPUTER SIMULATION

To demonstrate the feasibility of this procedure, a computer simulation has been performed. The analytical model of the Viking Orbiter Propulsion Module (Fig. 4) is chosen for this purpose. The Viking Orbiter Propulsion Module consists mainly of two large propellant tanks, a pressurant tank, a rocket engine, a propellant control assembly and support structural members. The propellant tanks carry approximately 8000 pounds of liquid fuel and oxidizer, each different, and the total weight of the other components is less than 200 pounds. Each of the fuel and oxidizer mass is represented by a single mass point located at its center of gravity with six degrees-of-freedom. Thus, the total fluid mass of the structural system is represented by 12 degrees-of-freedom. The values in this

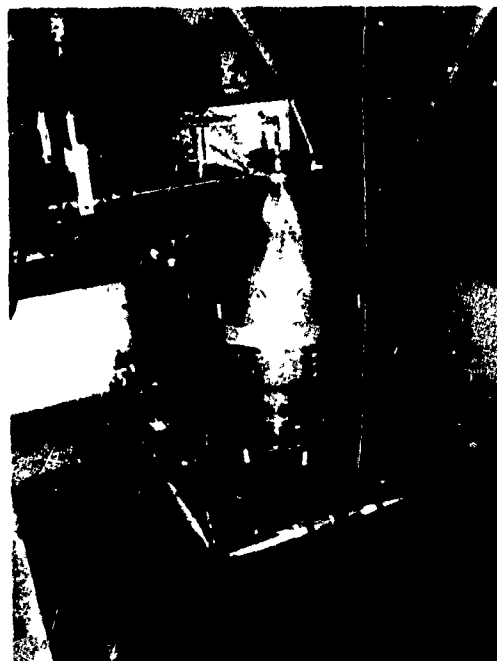


Figure 4. Viking Orbiter Propulsion Module Modal Test

fluid mass matrix have been estimated based on the full scale single tank slosh test in which the effective mass is measured under the actual ullage condition. The analytical model of the structural system consists of 702 elastic degrees-of-freedom and 33 dynamic degrees-of-freedom. Figure 5 shows a schematic drawing of the finite element model. The calculated normal modes and eigenvalues are presumed to be derived from the modal test. The purpose is to apply these data to the above mentioned method and to reconstruct the fluid mass matrix. The pre-test analysis is performed by assuming that both the fuel and oxidizer tanks are full and the corresponding fluid mass matrix is used. The calculated fluid mass matrix compares very well with the original fluid mass matrix. A new modal analysis is performed based on this reconstructed fluid mass matrix. Table i shows the comparison of eigenvalues between the results of the original fluid mass matrix and calculated fluid mass matrix. The excellent agreement is obvious. This establishes the feasibility of the method. Next, instead of computer simulated test data, actual test data will be used to reconstruct the fluid mass matrix.

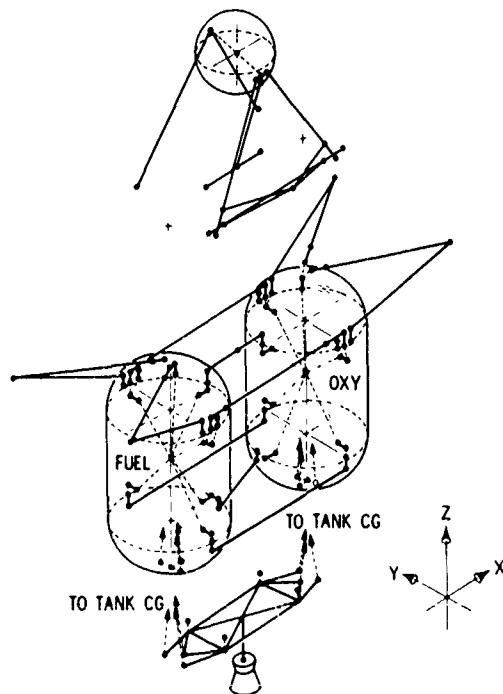


Figure 5. Schematic Drawing of VO'75 Propulsion Module Finite Element Model

V. PERTURBATION TECHNIQUE FOR TREATMENT OF TEST DATA

Data from the modal test of the Viking Orbiter Propulsion Subsystem are used in this method to calculate the fluid mass matrix. The results fail to reconstruct a physically meaningful mass matrix. After careful examination, it is found that the test data does not satisfy some of the assumptions made in this method. One of the assumptions is that the stiffness matrix $[K]$ is assumed to be correct. Therefore, the orthogonality condition expressed in the second equation of Eq. (5) must be satisfied by the test measured modes $[\phi]$. This orthogonality condition is also expressed in an alternative form in Eq. (14). Using test measured normal modes, the triple product does not yield a diagonal matrix. It is concluded that the inaccuracies in the test mode shape measurement are the causes. Therefore, the raw test data must be treated such that Eq. (14) will be satisfied. Assuming that the test measured modes are deviated from the true modes such that

$$[\phi] = [\phi'] + [\epsilon] \quad (22)$$

where

$[\phi']$ test measured normal modes.

Table I. Frequency Comparison

Mode No.	Frequency based on original mass (CPS)	Frequency based on calculated mass (CPS)
1	15.945	15.919
2	18.903	18.895
3	22.174	22.151
4	29.657	29.630
5	30.866	30.768
6	35.596	35.514
7	42.119	42.117
8	47.899	47.855
9	52.481	52.468
10	52.909	52.900
11	61.011	60.998
12	64.602	63.900
13	71.930	65.201
14	73.837	73.815
15	79.559	79.518
16	96.993	90.375
17	118.86	97.854
18	121.65	114.65
19	125.19	121.73
20	138.02	126.50
21	141.06	136.70
22	156.71	156.58
23	194.86	159.90
24	199.95	187.27

$[\epsilon]$ = deviation of measured modes from "true" modes.

Substituting Eq. (22) into Eq. (12), gives

$$[\bar{M}] = [\phi_F]^T [M_F] [\phi'] + [\phi_F]^T [M_F] [\epsilon] \quad (23)$$

Defining

$$[\bar{M}_1] = [\phi_F]^T [M_F] [\phi'] \quad (24)$$

$$[\epsilon] = [\phi_F]^T [M_F] [\epsilon]$$

Equation (23) can be rewritten as

$$[\bar{M}] = [\bar{M}_1] + [\epsilon] \quad (25)$$

Substituting Eq. (25) into Eq. (14), gives

$$[\lambda] = \left[[\bar{M}_1]^T + [\delta]^T \right] [\lambda_F] \left[[\bar{M}_1] + [\delta] \right] \quad (26)$$

Here the generalized mass $[\bar{M}_G]$ is normalized to unity.

Equation (26) can be expanded as follows

$$\begin{aligned} [\bar{M}_1]^T [\lambda_F] [\delta] + [\delta]^T [\lambda_F] [\bar{M}_1] \\ + [\delta]^T [\lambda_F] [\delta] = [\lambda] - [\lambda'] \end{aligned} \quad (27)$$

where

$$[\lambda'] = [\bar{M}_1]^T [\lambda_F] [\bar{M}_1] \quad (28)$$

It may be noted that $[\lambda']$ is not a diagonal matrix.

If the deviation of test measured modes is small, it is reasonable to assume that

$$\left| [\delta]^T [\lambda_F] [\delta] \right| \ll \left| [\lambda'] \right| \quad (29)$$

Then Eq. (27) can be approximated as

$$[\bar{M}_1]^T [\lambda_F] [\delta] + [\delta]^T [\lambda_F] [\bar{M}_1] = [\lambda] - [\lambda'] \quad (30)$$

Equation (30) can be used for solving $[\delta]$ and consequently $[\bar{M}]$ can be calculated from Eq. (25). The new calculated $[\bar{M}]$ is then substituted into Eq. (14). If Eq. (14) is still not satisfied within reasonable accuracy, the entire procedure can be repeated to calculate another new $[\bar{M}]$. This is the iteration procedure for treating the raw test data.

The method takes advantage of correcting the solution to impose known conditions during the calculation to prevent small errors to propagate and result in large errors in the final solution. It is similar to procedures used in finite element method where the stiffness matrix of substructures or subsets of finite element are corrected to represent rigid body motion. Often small computer roundoff errors result in stiffness matrices that do not satisfy zero forces during rigid body motion. (Ref. 4).

Two sets of test data have been used to calculate the fluid mass matrix. One is for the full

tank configuration and the other configuration is for the tanks having ullage. In both cases the pre-test analysis is performed by using the effective mass for the fluid mass matrix obtained from a full scale tank slosh test. Three iterations have been used in both cases to calculate $[\bar{M}]$. The final reconstructed fluid mass matrices closely resemble the effective mass matrix based on the full scale tank slosh test. Based on these reconstructed fluid mass matrices, modal analyses for both configurations are performed. Table II shows the frequency comparison between the results of pre-test analysis and analysis based on the reconstructed fluid mass matrix (post-test) together with test-measured frequencies for the full tank configuration. Table III shows the similar comparison for the ullage configuration. In both cases, the pre-test analytical frequencies and post-test analytical frequencies are in good agreement with test measured frequencies, the post-test frequencies having a slightly better agreement.

Table IV shows the reconstructed fluid mass matrix comparing it to the effective mass matrix based on the full scale tank slosh test for the ullage configuration. As mentioned before, the slosh test is a uni-axial test in which the inertia coupling effects such as I_{xy} , I_{yz} , I_{zx} cannot be measured. The small amounts of inertia couplings shown in the test-measured effective mass matrix are due to the CG shift for the ullage configuration. The

Table II. VO'75 Propulsion Subsystem
Modal Test - Full Configuration
Frequency Comparison

Mode No.	Pre-Test	Test	Post-Test
1	12.37 (CPS)	12.99	13.06
2	15.86	17.66	17.58
3	19.37	20.80	21.11
4	26.49	22.97	23.13
5	27.90	28.33	28.53
6	34.19	32.76	32.69

Table III. VO'75 Propulsion Subsystem
Modal Test - Ullage Configuration
Frequency Comparison

Mode No.	Pre-Test	Test	Post-Test
1	15.95 (CPS)	16.57	16.71
2	18.90	20.00	20.09
3	22.17	24.08	24.63
4	29.66	30.77	31.58
5	30.87	28.48	29.00

Table IV. Oxidizer Tank Fluid Mass Matrix Comparison of Ullage Configuration

	M_x	M_y	M_z	I_x	I_y	I_z
M_x	1797.40 (1836.80)	0.0 (-38.46)	0.0 (6.40)	0.0 (-1130.40)	12693.17 (13128.00)	0.0 (-1168.60)
M_y	0.0 (-38.46)	1797.40 (1772.60)	0.0 (-26.59)	-12693.17 (-13048.00)	0.0 (-1263.20)	-50.48 (9.12)
M_z	0.0 (6.40)	0.0 (-26.59)	2229.13 (2225.10)	0.0 (-473.63)	50.48 (539.87)	0.0 (-679.47)
I_x	0.0 (-1130.40)	-12693.17 (-13048.00)	0.0 (-473.62)	153040.10 (149740.00)	0.0 (-21968.00)	117.40 (2247.50)
I_y	12693.17 (13128.00)	0.0 (-1263.20)	50.48 (539.87)	0.0 (-21968.00)	152958.80 (163250.00)	0.0 (-60404.00)
I_z	0.0 (-1168.60)	-50.48 (9.12)	0.0 (-679.47)	117.40 (2247.50)	0.0 (-60404.00)	36487.43 (36677.00)

Fuel Tank Fluid Mass Matrix Comparison of Ullage Configuration

	M_x	M_y	M_z	I_x	I_y	I_z
M_x	1088.43 (1274.10)	0.0 (-6.69)	0.0 (-36.92)	0.0 (-2065.40)	3593.58 (3484.70)	0.0 (-2452.90)
M_y	0.0 (-6.69)	1088.43 (1106.00)	0.0 (10.97)	-3593.58 (-3307.60)	0.0 (-916.81)	-50.48 (251.02)
M_z	0.0 (-36.92)	0.0 (10.97)	1252.13 (1263.20)	0.0 (334.80)	50.48 (-899.56)	0.0 (442.97)
I_x	0.0 (-2065.40)	-3593.58 (-3307.60)	0.0 (334.80)	112827.80 (136020.00)	0.0 (-12674.00)	1.50 (23927.00)
I_y	3593.58 (3484.70)	0.0 (-916.81)	50.48 (-899.56)	0.0 (-12674.00)	112746.50 (117870.00)	0.0 (-21052.00)
I_z	0.0 (-2452.90)	-50.48 (251.02)	0.0 (442.97)	1.50 (23927.00)	0.0 (-21052.00)	33525.03 (31564.00)

NOTE: 1. Numbers without parentheses are obtained from full scale tank slosh test.
 2. Numbers with parentheses are calculated from modal test results.
 3. Unit of M is lb.
 4. Unit of I is lb-in.².

reconstructed fluid mass matrix based on the modal test data is a full matrix with every inertia coupling term presented. The diagonal terms of the two matrices are in good agreement. It is difficult to attach a physical meaning to translational inertia coupling terms such as M_{xy} , M_{yz} , M_{zx} which appear in the reconstructed fluid mass matrix. Nevertheless, these terms are of small quantities compared to the diagonal terms.

VI. CONCLUDING REMARKS

Throughout the derivation of the method, it appears that the number of test-measured modes must be equal to the number of degrees-of-freedom of the fluid mass matrix to be reconstructed. In the case of Viking Orbiter

Propulsion Module, the fluid mass matrix has 12 degrees-of-freedom but only 6 test-measured modes are available. A careful examination of the test-measured modes reveal that only the first 5 normal modes are predominantly involved with the fluid motion. From the 6th mode on, very little fluid motion was involved. They are high frequency modes and primarily local modes. The amount of participation of fluid motion in each mode can be determined by examining the local kinetic energy distribution of each mode (Ref. 3). For instance, the 6th mode is a pressurant tank mode, more than 80% of the kinetic energy is concentrated on the pressurant tank, very little motion is found in other degrees-of-freedom. This leads to a conclusion that the dynamic characteristics

of the fluid mass can be represented by the first 5 modes. Also, it can be found that the higher frequency local modes are relatively independent of the dynamic characteristics of the fluid mass. Therefore, one may substitute the test-measured modes by the corresponding analytical modes without losing the dynamic characteristics of the fluid mass.

The feasibility of the method has been demonstrated by both a computer simulation and by actual modal test data. The results are in good agreement with the results of a full scale tank slosh test. The advantages of the method are the elimination of a full scale fluid tank slosh test and the ability of obtaining the cross-product of the inertia which, in general, are not measured from the full scale slosh test.

This method is relatively simple to implement once the test-measured modal data are reduced into the form which is compatible with the analysis. The Viking Orbiter modal test has been performed with automatic data acquisition and reduction (Ref. 5). Therefore the test data is readily available immediately after the completion of the test. Utilization of the test data for parameter identification such as reconstruction of fluid mass matrix can be performed before the complete dismantling of the test set-up.

This method is still in its preliminary state. Many of the details lack the rigorous mathematical proof such as the convergence of the iteration procedure. Also the conditions for which the final results converge to the true solution have yet to be established. However, these are the same problems which still plague the "system identification", i.e. using the results of dynamic testing to identify the parameters in the equations of motion (Ref. 6). Definitely, more work needs to be done in this area.

Although the method has been developed for identifying the dynamic characteristics of the fluid mass, it can also be applied to other unknown masses and stiffness terms. This

information might be of value to future projects such as the Space Shuttle.

References

1. Abramson, N. H., et al, "The Dynamic Behavior of Liquids in Moving Containers," NASA SP-106, 1966.
2. Gayman, W. H., "Measurements of Propellant Fluid Dynamics," Jet Propulsion Laboratory, presented at the Aerospace Flutter and Dynamics Council, Seattle, Washington, May, 1973, to be published as a Jet Propulsion Laboratory report.
3. Wada, B., Garba, J., and Chen, J., "Development and Correlation, Viking Orbiter Analytical Dynamic Model with Modal Test," Jet Propulsion Laboratory, presented at the 44th Shock and Vibration Symposium, Houston, Texas, Dec. 1973; also published in the Bulletin.
4. Bamford, R., Wada, B., Garba, J., and Chisholm, J., "Dynamic Analysis of Large Structural Systems," presented at the Winter Annual Meeting of the ASME, Washington, D. C., Nov. 30, 1971; also published in "Synthesis of Vibrating Systems," ASME, New York, 1971, pp. 57-71.
5. Leppert, L., Miyakawa, R., and Wada, B., "Modal Test Results of the Viking Orbiter," Jet Propulsion Laboratory, presented at the 44th Shock and Vibration Symposium, Houston, Texas, Dec. 1973; also published in the Bulletin.
6. Flannely, W. and Berman, A., "The State of the Art of System Identification of Aerospace Structures," published in "Systems Identification of Vibrating Structures," ASME, New York, 1972, pp. 121-132.

UNIQUE FLIGHT INSTRUMENTATION/DATA REDUCTION TECHNIQUES EMPLOYED ON THE VIKING DYNAMIC SIMULATOR*

F. D. Day
Martin Marietta Aerospace
Denver, Colorado

and

B. K. Wada
The Jet Propulsion Laboratory
Pasadena, California

The incorporation of strain-gauged truss members calibrated as load cells in the spacecraft primary structure and the use of low frequency accelerometers for extracting the six degree-of-freedom motion of a rigid inertia simulator are discussed. The post flight processing of the data with a modified ground station and analog computers, greatly expanding the capability for detailing structural response information from the limited number of transducers, is presented and the success of these techniques discussed.

INTRODUCTION

The Viking Spacecraft will be launched aboard a new launch vehicle system, the Titan IIIE/Centaur, in August 1975. The Jet Propulsion Laboratory (JPL) is responsible for the Viking Orbiter System, which is part of the overall Viking Project managed by the Viking Project Office at Langley Research Center (LRC) for NASA.

Although the Viking Spacecraft is not the first hardware designed to fly aboard a new launch vehicle system, areas do exist where somewhat unique approaches have been taken to familiar engineering problems. These areas include the basic approach to design of the primary structure; the methods employed in the verification of the design, in particular the flight of a dynamic simulation of the Viking Spacecraft (referred to as the Viking Dynamic Simulator (VDS)); and the flight instrumentation and data reduction techniques employed.

This paper will emphasize the somewhat unique aspects of flight instrumentation and post-flight reduction techniques used on the VDS data obtained in February 1974. The Viking Spacecraft design approach is briefly discussed.

VIKING SPACECRAFT DESIGN APPROACH

The Viking Spacecraft is one of the few projects in which, from inception, the basic design

philosophy has been to use predicted transient flight loads to design the primary load carrying structure.⁽¹⁾ This approach influenced both the test and the analytical aspects of the program. The structural testing has been directed towards verification of the analytical models and techniques through extensive modal test programs,^(2,3) the use of structural response limitations for high level tests (based on the predicted flight induced loads)^(4,5), and static test for structural qualification of the primary structure based upon predicted flight member loads. This differs from the conservative approach of designing and testing to test specifications that simulate flight environments. The analytical aspects emphasized the coupled launch vehicle/spacecraft dynamic model and its responses to external transient forcing functions. The importance of the analytical effort to establish design and qualification loads provided impetus to verify the accuracy of the analyses.

VDS CONFIGURATION

The proof flight of the new launch vehicle system provided the unusual opportunity of flying a dynamic simulation of the spacecraft, the VDS. The main objectives of the VDS were to verify the mathematical modeling techniques, the methodology employed in coupling the spacecraft and launch vehicle models, the loads prediction techniques, and the flight instrumentation. To best meet the objectives, the VDS flight instrumentation design consisted of accelerometers, strain gauges, a specially designed data reduction facility with sets

* This paper presents the results of one phase of research carried out at the Jet Propulsion Laboratory, California Institute of Technology, under Contract No. NAS 7-100, sponsored by the National Aeronautics and Space Administration.

of phase and amplitude matched filters, and analog computers. Similar instrumentation is planned for the two Viking Spacecrafts.

The Viking Dynamic Simulator (VDS) is shown in Figure 1. It consisted of inertia simulations of the major components of the Viking Spacecraft. The Viking Lander Dynamic Simulator (VLDS), and the Viking Orbiter Dynamic Simulator (VODS), were supported by flight-type trusses. The composite VDS payload simulated the inertia properties of the Viking Spacecraft and provided limited simulation of the dynamic characteristics of the spacecraft. A thorough modal survey, including modal force data, was performed to verify the VDS mathematical model. (6)

VDS FLIGHT INSTRUMENTATION

Most spacecraft flight instrumentation to obtain dynamic environmental data has consisted of accelerometers located in critical areas to measure important local input or response data. Less often, accelerometers were used to measure the six degree-of-freedom motion across a "rigid" interface, as was attempted on the Mariner 6 and 7 spacecraft. This type of information is more

effective because it can be used as a unique forcing function to be applied to a model to obtain estimates of responses at many locations above the interface. However, since accelerometers will only measure the local accelerations for a flexible structure, the six degree-of-freedom motion across an interface cannot be determined. The VDS instrumentation approach differed primarily in the use of six channels of strain-gauge data to determine the force time history across an interface. Additionally six channels of accelerometers on the "rigid" simulation of the Viking Orbiter bus provided its complete motion time history. These sets of special measurements, augmented by two additional strain gauge transducers and one additional accelerometer, made it possible to generate over thirty response parameters, when processed by the specialized playback equipment.

The VDS was also instrumented with a microphone for acoustic measurements, and a high frequency crystal accelerometer to correlate predicted and measured local environments. The channel assignments and measurement numbers are listed in Table I. The locations of the various transducers are shown in Figure 2.

The VDS response measurements were broadcast as continuous data via an FM/FM standard IRIG proportional bandwidth multiplexed telemetry system with a carrier frequency of 2215.5 MHz.

Strain Gauge Data

The six pin-ended struts, referred to as the Proof Flight Lander Adapter (PFLA), were instrumented with temperature compensative strain gauge bridges. These struts were individually loaded prior to assembly and calibrated as axial load cells. The flight data obtained from the six struts were used to (1) provide direct load data for verification of the loads prediction techniques, (2) provide a complete time history of the forces and moments across an interface, and (3), completely define the accelerations of the structure above the PFLA.

The individual truss member full scale ranges and zero load bias values are presented in Table II. The channels were biased to provide approximately 60% of the range as compression, 40% as tension. The effective cut-off frequencies listed in Table II for channels 12 through 17 resulted from employment of non-standard discriminator output filters. These were required for proper phase matching during analog computer processing to determine VLDS rigid body motions. The normal output filters could not provide phase matching of the truss loads while maintaining a constant amplitude response.

Additionally two of the twelve V-S/C-A truss tubes were instrumented and monitored during flight.

Low Frequency Accelerometers

The six strain measurements on the PFLA were used to determine the rigid body motions of the VLDS. The motion of the rigid VODS bus was determined from six properly placed DC to 50 Hz accelerometers (See Figures 1 and 2). Again, non-standard filters were necessary to insure

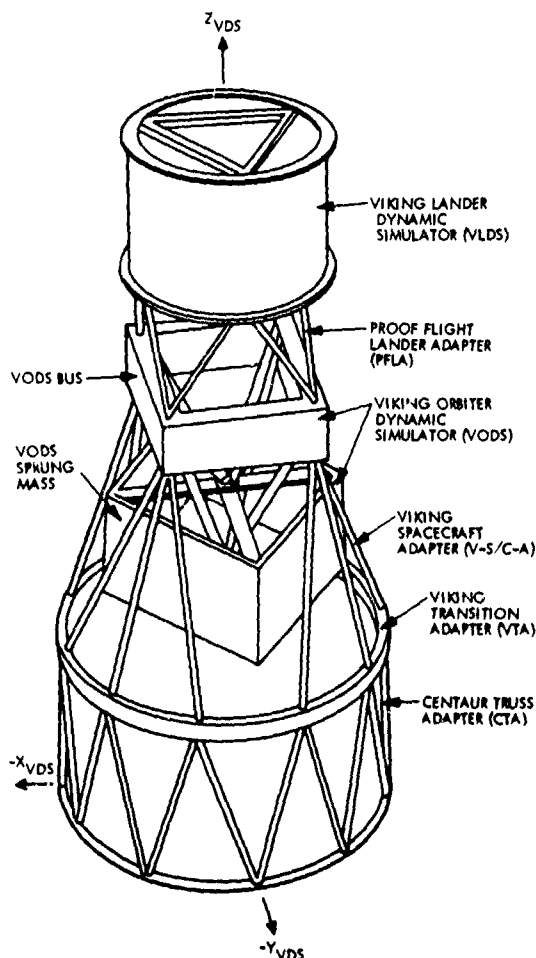


Figure 1. Viking Dynamic Simulator Configuration

Table 1. VDS Measurement List

Number	Measurement Number	Description
3	CY216-S	V-S/C-A Axial Load Transducer
4	CY215-S	V-S/C-A Axial Load Transducer
5	CY208-φ	VODS Sprung Mass Z-Axis Accelerometer
6	CY207-φ	VODS Bus X-Axis Accelerometer
7	CY206-φ	VODS Bus Y-Axis Accelerometer
8	CY205-φ	VODS Bus Y-Axis Accelerometer
9	CY204-φ	VODS Bus Z-Axis Accelerometer
10	CY203-φ	VODS Bus Z-Axis Accelerometer
11	CY202-φ	VODS Bus Z-Axis Accelerometer
12	CY214-S	PFLA Truss Axial Load, Member 202
13	CY213-S	PFLA Truss Axial Load, Member 203
14	CY212-S	PFLA Truss Axial Load, Member 204
15	CY211-S	PFLA Truss Axial Load, Member 205
16	CY210-S	PFLA Truss Axial Load, Member 206
17	CY209-S	PFLA Truss Axial Load, Member 201
18	CY201-φ	Piezoelectric Accelerometer, Z-Axis
19	CY217-Y	Acoustic Microphone

proper phase and gain characteristics on the post-flight processing. The cut-off frequencies listed in Table II for the VODS accelerometers (channels 6 through 11) are indicative of the filters purchased for this task.

Additionally, a single accelerometer was placed on the PSS simulation, or "sprung mass", sensitive in the longitudinal axis. This DC-50Hz accelerometer was incorporated primarily as a "Pogo" accelerometer to determine possible adverse coupling with launch vehicle axial modes.

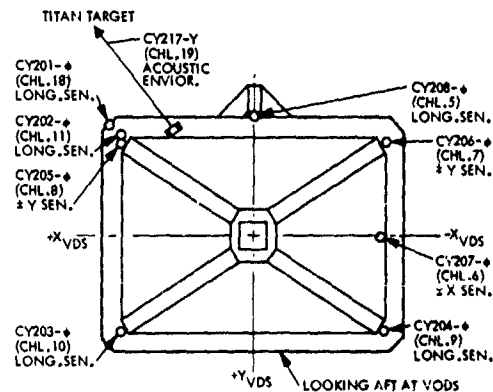
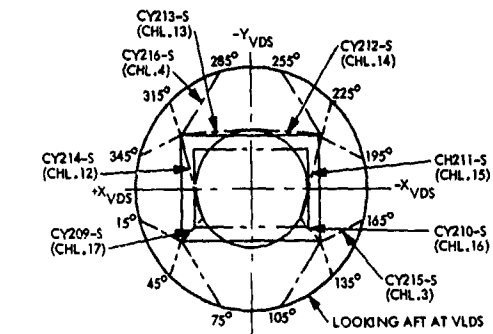


Figure 2. VDS Instrumentation Locations

Crystal Accelerometer and Microphone

Both the crystal accelerometer and microphone measurements are primarily high frequency in nature and therefore used the highest frequency IRIG channels (Table I). While the standard IRIG frequency responses were extended upward by the use of non-standard modulation indexes in playback, both measurements were intended to be single point or localized measurements as opposed to transducers grouped for more general response information.

DATA REDUCTION PROCESS

In general, the reduction of VDS flight data took the form of time history oscillographs, power spectral density (PSD) plots, and shock response spectrum plots. The special processing consisted of analog computer manipulations performed on the PFLA loads data and the VODS accelerometer data.

The particular flight events of interest were processed for spectral information either as PSD's if the data were predominantly steady-state random, or as shock response spectrum plots if the data were dominated by a relatively short duration transient event.

Table II. VDS Instrumentation Characteristics

Channel Number	Measurement Number	Zero Load Bias	Full Scale Range	Data Cutoff Frequency
19	CY217-Y		150.0 dB	1400.0 Hz
18	CY201-φ		40.0 g's	1050.0
17	CY209-S	61.6%	27319 lbs	200.0
16	CY210-S	60.1%	27175 lbs	204.0
15	CY211-S	59.2%	26636 lbs	210.0
14	CY212-S	61.1%	27157 lbs	220.0
13	CY213-S	61.0%	27192 lbs	239.0
12	CY214-S	59.6%	27177 lbs	265.0
11	CY202-φ	0.0	20.00 g's	41.7
10	CY203-φ	0.0	19.98 g's	43.4
9	CY204-φ	0.0	20.00 g's	46.2
8	CY205-φ	0.0	10.01 g's	49.7
7	CY206-φ	0.0	9.99 g's	55.0
6	CY207-φ	0.0	10.00 g's	65.8
5	CY208-φ	20%	10.01 g's	20.0
4	CY215-S	59%	25331 lbs	14.0
3	CY216-S	59%	25342 lbs	11.0

Loads Data Processing

The strain-gauging and calibration of the PFLA truss tubes as axial load cells created unique post-flight data processing capabilities. The six channels of data were reduced directly as load information, phase correlated and manipulated to provide the complete force and moment history across the interface with the VDS, and phase correlated and manipulated to provide the complete description of motion for the center of mass of the Viking Lander Dynamic Simulator.

The reduction of the PFLA data as loads information was performed for the events listed in Table III. This table also indicates the type of data analysis performed. For all analyses the flight data was demultiplexed by the modified IRIG proportional bandwidth system which included the special discriminator output filters. The special filters were purchased to phase match the six channels of data with no amplitude attenuation, to at least 100 Hz. The filters and channel selectors were calibrated and the phase/amplitude characteristics verified prior to reduction of the flight data.

All spectral analyses, either in PSD or shock response spectra form, were generated with the use of digital computer programs. The six

channels of data were digitized simultaneously at a rate of 1066 samples/sec for each channel. This rate allowed generation of PSD's with an effective resolution of just over 2.0 Hz. The PSD analysis bandwidth was limited to 533 Hz. The shock response spectra plots were generated for a frequency range of 1.0 to 100.0 Hz, with the spectra defined by forty points per decade. Shock response plots were generated for three values of gain (Q), 10, 20, and 50.

The two Viking Spacecraft Adapter truss members which had been calibrated as load cells were reduced directly as loads information. The channels assigned were of low frequency response capability, and standard IRIG filters were used for discriminator output.

Low Frequency Accelerometer Data

The basic servo-accelerometer telemetry data was reduced employing the modified IRIG proportional bandwidth demultiplexing equipment, with special discriminator output filters. These filters were used to provide phase correlation with no amplitude attenuation to at least 25 Hz. The seventh servo-accelerometer, measurement CY208 on telemetry channel 5, was reduced with the normal IRIG filter, set for constant amplitude response.

Table III. Summary of VDS Data Reduction Effort

Event	Ref Time*	Ambient					Lift Off					Transonic							
		47-50	48-01	48-01	48-01	48-01	48-01	48-01	48-01	48-01	48-01	48-01	48-01	48-01	48-01	48-01	48-01	48-01	48-01
Analysis Time**		0 5-2 5	0 2-2 2	2 2-4 2	1 2-3 2	0 2-1 2	0 0-3 0	0-2	2-4	4-6	6-8	8-10	10-12	12-14					
IRIG No.	Meas No																		
19	CY217-Y	A	A	A	A	A	A	A	A	A	A	A	A	A					
18	CY201-Ø	P S	P		P	P													
17	CY209-S	P	P	P	P	P	S	P	P	P	P	P	P	P					
16	CY210-S	P	P	P	P	P	S	P	P	P	P	P	P	P					
15	CY211-S	P	P	P	P	P	S	P	P	P	P	P	P	P					
14	CY212-S	P	P	P	P	P	S	P	P	P	P	P	P	P					
13	CY213-S	P	P	P	P	P	S	P	P	P	P	P	P	P					
12	CY214-S	P	P	P	P	P	S	P	P	P	P	P	P	P					
11	CY202-Ø	P	P	P	P	P	S	P	P	P	P	P	P	P					
10	CY203-Ø	P	P	P	P	P	S	P	P	P	P	P	P	P					
9	CY204-Ø	P	P	P	P	P	S	P	P	P	P	P	P	P					
8	CY205-Ø	P	P	P	P	P	S	P	P	P	P	P	P	P					
7	CY206-Ø	P	P	P	P	P	S	P	P	P	P	P	P	P					
6	CY207-Ø	P	P	P	P	P	S	P	P	P	P	P	P	P					
5	CY208-Ø	P	P	P	P	P	S	P	P	P	P	P	P	P					
4	CY215-S	P	P	P	P	P		P	P	P	P	P	P	P					
3	CY216-S	P	P	P	P	P		P	P	P	P	P	P	P					
Analog System 1		P	P	P	P	P		P	P	P	P	P	P	P					
Analog System 2		P S	P	P	P	P	S	P	P	P	P	P	P	P					
Analog System 3		P S	P	P	P	P	S	P	P	P	P	P	P	P					

*GMT Time Ref 042 13.00.00

**Times listed as even sec for convenience

KEY: P = Power spectral density analysis
 S = Shock response spectra analysis
 F = Fourier transform analysis
 A = Acoustic analysis, sound pressure spectrum level and sound pressure level plots

Event	FBR St 1 IGN		Stage 1 Oscillation					Stage 1 B/O	Shroud	Stage 2	Stage 2 B/O
Ref Time	49:41.2	49:56.5	51:30	51:50	51:58	52:10	52:22	52:22	52:35.2	55:00	55:50.5
Analysis Time	0 0-2 0	0 0-2 0	0-2	0-2	0-2	0-2	0-2	2 0-3 25	0 0-2 0	0 0-2 0	0 0-2 0
IRIG No	Meas No										
19	CY217-Y										
18	CY201-Ø	S	S	S	S	S	S	F	F	F	F
17	CY209-S	S	S	P	P	P	P	S	S	P	S
16	CY210-S	S	S	P	P	P	F	P	S	P	S
15	CY211-S	S	S	P	P	P	P	P	S	P	S
14	CY212-S	S	S	P	P	P	P	P	S	P	S
13	CY213-S	S	S	P	P	P	P	P	S	P	S
12	CY214-S	S	S	P	P	P	P	P	S	P	S
11	CY202-Ø	S	S	P	P	P	P	P	S	P	S
10	CY203-Ø	S	S	P	P	P	P	P	S	P	S
9	CY204-O	S	S	P	P	P	P	P	S	P	S
8	CY205-Ø	S	S	P	P	P	P	P	S	P	S
7	CY206-Ø	S	S	P	P	P	P	P	S	P	S
6	CY207-Ø	S	S	P	P	P	P	P	S	P	S
5	CY208-Ø		S	P	P	P	P	P	S	P	S
4	CY215-S		S	P	P	P	P	P	S	P	S
3	CY216-S		S	P	P	P	P	P	S	P	S
Analog System 1		S	S*	P	P	P	P	P	S	P	S**
Analog System 2		S	S	P	P	P	P	F	S	P	
Analog System 3		S	S	P	P	P	P	P	S	P	S

*Time slice is 0 0-2 3, Ref 49:56 2

**Time slice is 0 0-1 4, Ref 55:50 2

KEY: P = Power spectral density analysis
 S = Shock response spectra analysis
 F = Fourier transform analysis
 A = Acoustic analysis, sound pressure spectrum level and sound pressure level plots

The spectral analyses performed on the low frequency accelerometer data were similar to the processing done on the PFLA loads data.

In addition, the accelerometer data was processed through an analog computer to provide the rigid body motion of the VODS bus.

Analog Processing of PFLA Loads Data

The data was reduced directly as individual member loads, Figures 3 - 8, combined to give resultant forces and moments across an interface, Figures 9 - 11, and also displayed as the resultant accelerations at the center of mass of the VLDS, Figure 12 - 14. The last two forms of data reduction incorporated analog computer processing of the phase matched, demultiplexed data.

The standard data reduction system is shown in block diagram form in Figure 15. The composite signal was processed through a ground station consisting of a demultiplexing unit (in this case an IRIG proportional bandwidth system) to obtain individual measurement signals; those

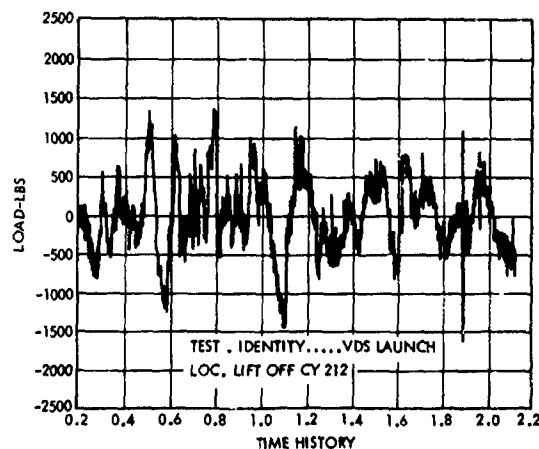


Figure 5. PFLA Load Measurement CY212: Liftoff

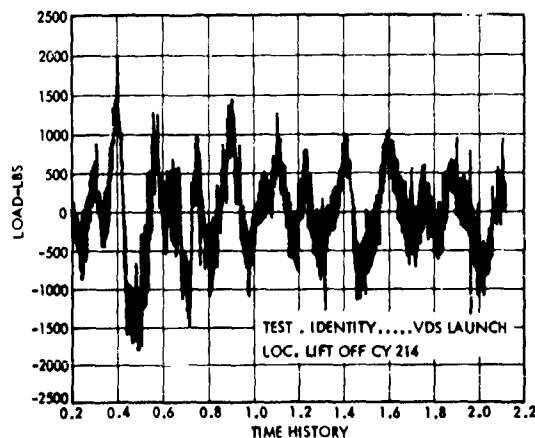


Figure 3. PFLA Load Measurement CY214: Liftoff

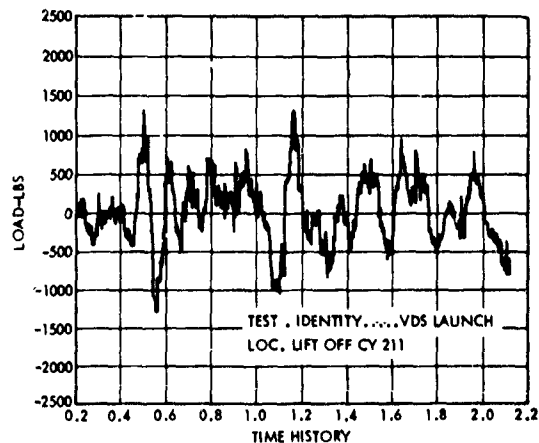


Figure 6. PFLA Load Measurement CY211: Liftoff

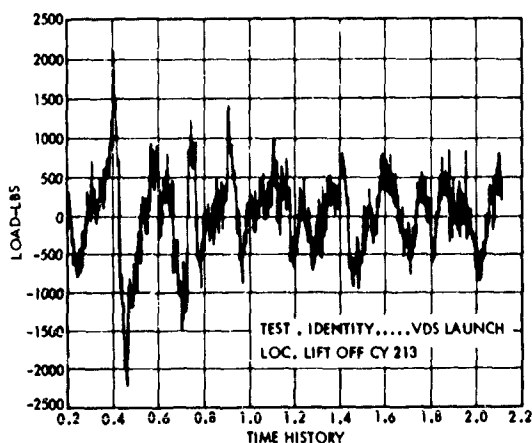


Figure 4. PFLA Load Measurement CY213: Liftoff

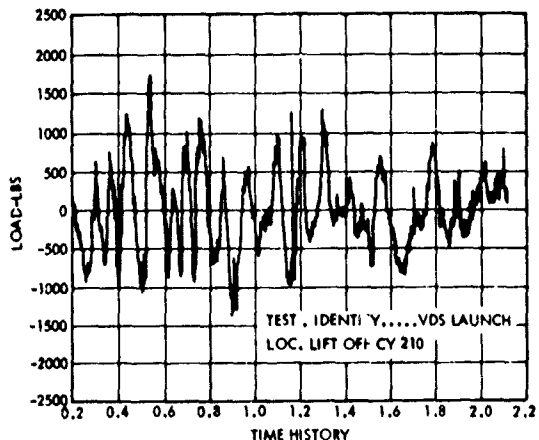


Figure 7. PFLA Load Measurement CY210: Liftoff

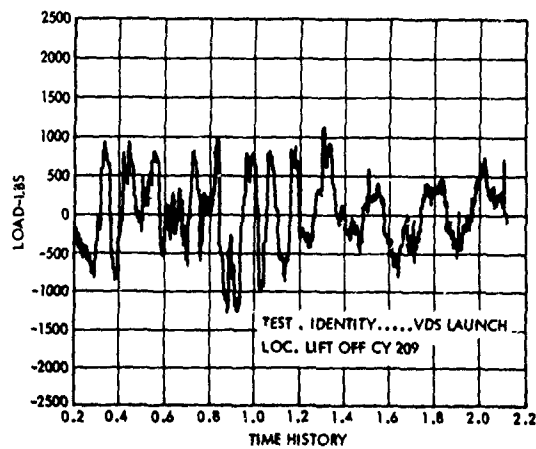


Figure 8. PFLA Load Measurement CY209:
Liftoff

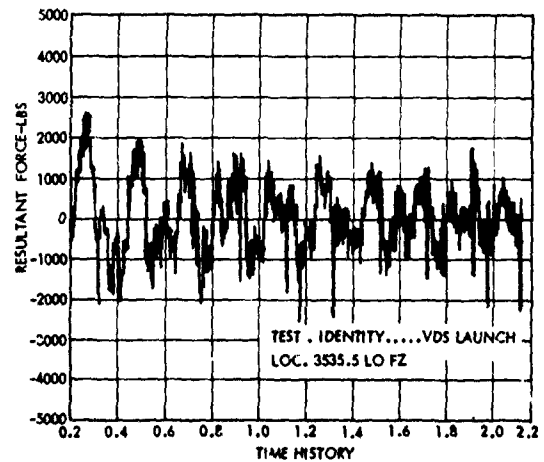


Figure 11. Resultant PFLA Force F_z ,
Liftoff

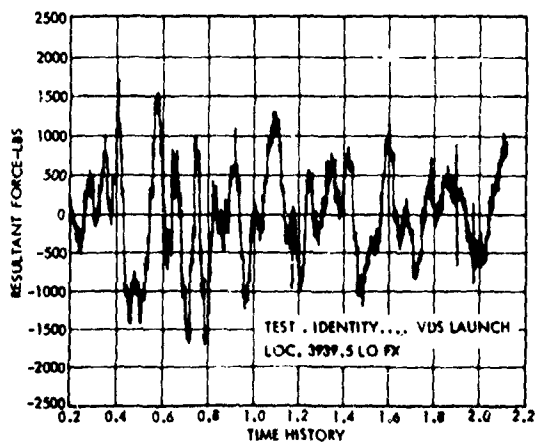


Figure 9. Resultant PFLA Force F_x ,
Liftoff

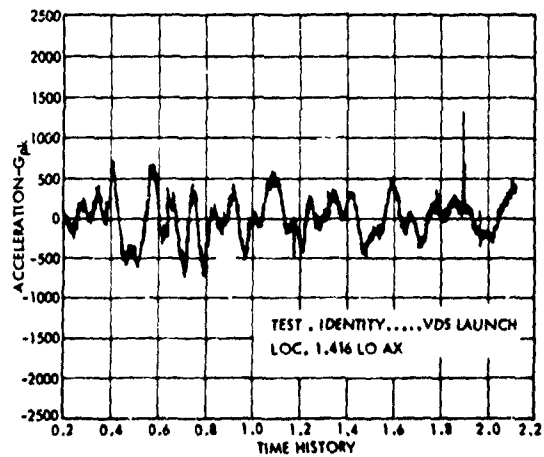


Figure 12. VLDS c.g. Acceleration \ddot{x} ,
Liftoff

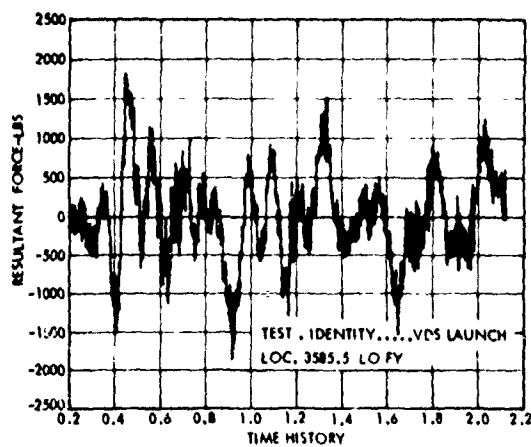


Figure 10. Resultant PFLA Force F_y ,
Liftoff

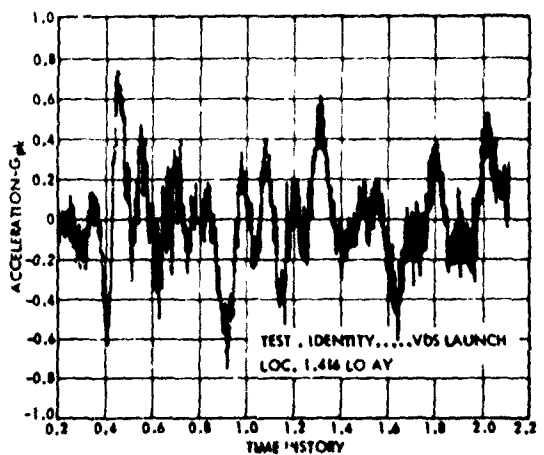


Figure 13. VLDS c.g. Acceleration \ddot{y} ,
Liftoff

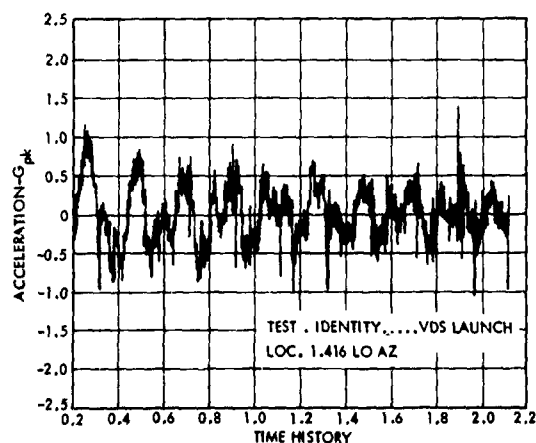


Figure 14. VLDS c. g. Acceleration \ddot{z} ,
Liftoff

individual signals were then recorded on oscillograph paper, digitized for spectral analysis, or otherwise displayed as engineering data. The block diagram of Figure 15 shows the processing performed on the strain measurements as individual channels of data.

The unique aspects of the VDS strain data processing are shown in the block diagrams of Figures 16 and 17. The demultiplexing unit was modified by incorporating special filters for the six channels of strain data to provide phase and amplitude correlation. The phase correlated channels were then processed by an analog computer to provide either resultant forces and moments across the PFLA interface, or resultant accelerations at the center of gravity of the rigid VLDS.

Figure 16 shows in block diagram form the processing for resultant forces and moments. The geometric properties of the truss, scale factors, and conversion factors to obtain engineering units were incorporated in the analog program along with the necessary coordinate transformations. The resultant accelerations at the center of gravity of the rigid VLDS were obtained in a similar manner. With the forces and moments across the PFLA interface known, the resultant

accelerations were computed using the VLDS inertia properties. The block diagram of Figure 17 shows the processing employed in obtaining engineering data in terms of these accelerations.

The truss identification as used in the analog processing is shown in Figure 18. For the resultant forces/moments, the analog computer output was low-pass filtered at 500 Hz to suppress noise inherent in the particular analog computer used. The resultant VLDS accelerations were not filtered as a different analog computer, with better noise characteristics, was employed.

Analog Processing of VODS Accelerometer Data

The locations of the six servo-accelerometers mounted on the upper plane of the VODS bus are shown in Figure 19. The equations for the six degree-of-freedom motion of the point on the centerline of the VODS, in the plane of the accelerometers, were based on geometry and are as follows:

$$\begin{aligned}\ddot{X}_{VDS} &= a_6 \\ \ddot{Y}_{VDS} &= 0.5(a_7 + a_8) \\ \ddot{Z}_{VDS} &= 0.5(a_9 + a_{11}) \\ \ddot{\theta}_{xVDS} &= 16.29(a_{10} - a_{11}) \\ \ddot{\theta}_{yVDS} &= 11.39(a_9 - a_{10}) \\ \ddot{\theta}_{zVDS} &= 11.39(a_8 - a_7)\end{aligned}\quad (1)$$

where \ddot{X} , \ddot{Y} , \ddot{Z} are accelerations in g's, $\ddot{\theta}_x$, $\ddot{\theta}_y$, $\ddot{\theta}_z$ are rotational accelerations in rad/sec² and a_6 , a_7 , ..., a_{11} , are accelerations in g's per Figure 19.

Equations (1), with appropriate scale factors, were implemented on the analog computer used previously for generation of the VLDS center-of-mass accelerations. The flight data was reduced in a manner similar to that employed for the strain data, using the special phase/amplitude matched filters purchased for IRIG channels six through eleven. There were no additional low-pass filters following the analog processing.

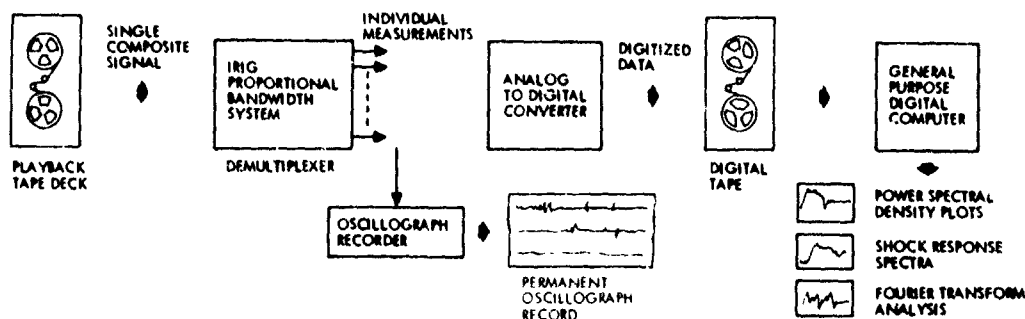


Figure 15. Standard Flight Data Processing System

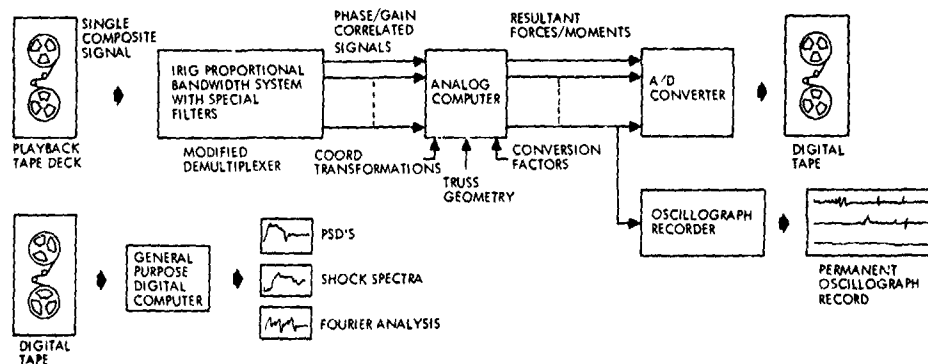


Figure 16. Strain Processing for Resultant Forces/Moments

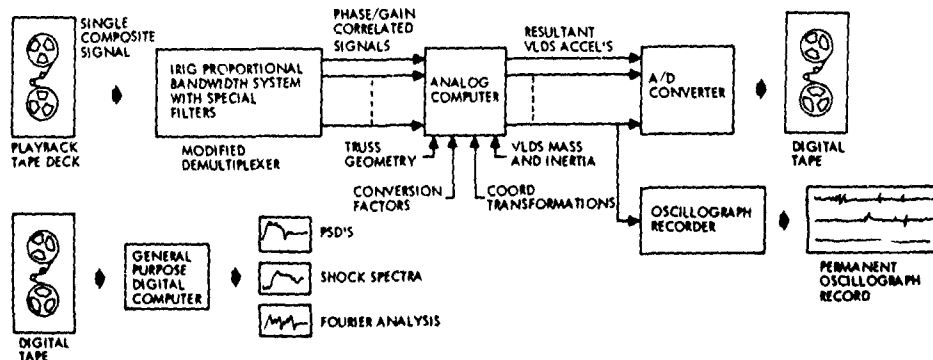


Figure 17. Strain Processing for Resultant VLDS Accelerations

SUMMARY OF FLIGHT DATA

The use of the special filters slightly decreased the signal to noise ratio for channels 12 and 13. The major problem was noise signal at approximately 5.0 Hz which was apparently caused by one of the tape recorders employed by ETR in producing the duplicate tape. This noise signal is clearly seen in the time history plots for the resultant force in the Z-axis, Figure 20. The signal can be found on all the channels to some extent, and the sharp spike at the discontinuity is seen on the PFLA channels. A second duplicate tape was received from ETR after this noise problem was identified and the source determined. The second tape is cleaner. The majority of the data were not redigitized because of schedule and cost considerations. Otherwise, the data obtained from the PFLA strain-gauged struts were good and proved useful in post-flight reconstruction of the various events.

The PFLA data, processed through the analog computer, provided useful data for post-flight reconstruction and correlation with Viking Lander tests and analyses. Significant noise at 5 Hz was evident in the resultant force in the longitudinal direction (F_z) and the resultant longitudinal acceleration (A_z). These terms sum all six PFLA measurements in phase, thus accentuating any noise common to the telemetry/playback system. Reference PSD's and shock response spectra have been provided for most data channels to facilitate identification of the noise characteristics. These reference spectral analyses were generated for a time slice approximately ten seconds prior to launch.

The data obtained from the seven low-frequency accelerometers were good. The VLDS bus data is limited to 25 Hz by the special filters purchased for phase/amplitude correlation. Amplitude information for individual channels can

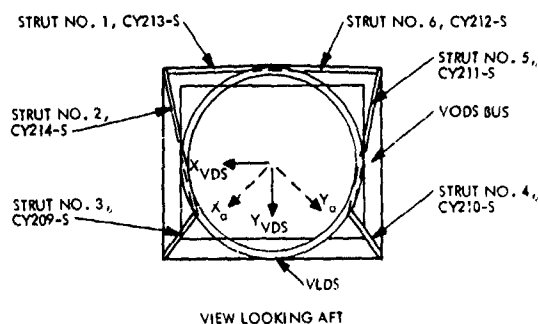


Figure 18. PFLA Truss Numbering for Analog Programs

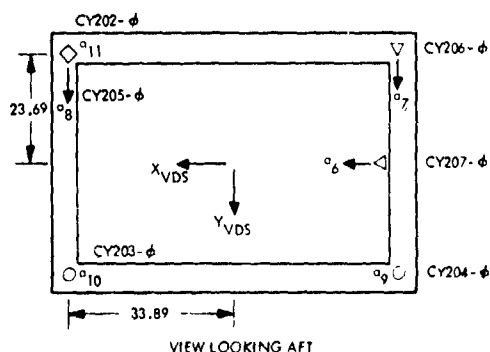


Figure 19. VODS Accelerometer Numbering for Analog Program

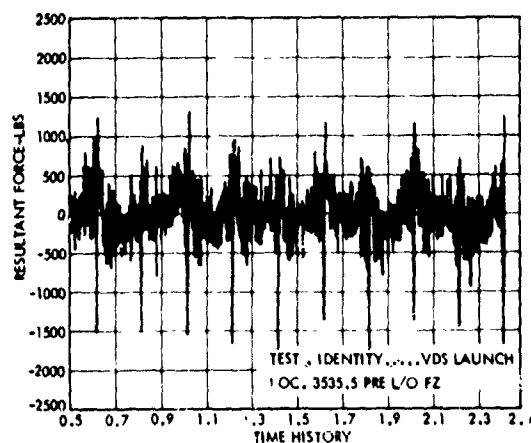


Figure 20. Resultant Force F_z , Pre-liftoff Ambient

be obtained above 25 Hz, but the filters have a gradual roll-off to achieve -3dB gain at the cut-off frequencies listed in Table II. Again, the penalty incurred by using the special filters is a decrease in the signal to noise ratio for channels 6, 7 and 8. This is especially noticable with channel 6, both as an individual measurement and as a resultant acceleration output from the analog computer. The

approximately 5 Hz noise from tape recorder processing at ETR can also be seen periodically in the low frequency accelerometer data.

The analog processing of the VODS bus accelerometer data along analyses coordinate was useful in post-flight reconstruction and investigation of the VDS launch.

CONCLUSION

The use of calibrated load cells which are an integral part of the primary spacecraft structure was demonstrated as a feasible approach to flight instrumentation on the VDS. The advantage of using load cells was that a complete force time history was obtained across an interface. From this, the complete acceleration time history of the structure above the interface was derived through specialized post-flight processing. In the past, attempts to determine a complete acceleration time history across an interface, with accelerometers, resulted in limited success because of "local" resonances. The force time history was used as an input to the VLDS to calculate the acceleration time history. Similar data from the Viking Spacecraft flight will allow calculation of the complete acceleration and force on any part of the Viking Lander Capsule. In addition, the complete acceleration time history of the rigid Viking Orbiter Bus Dynamic Simulator was achieved through use of servo-accelerometers and specialized post-flight processing. This was possible because of the rigidity of the VODS bus within the frequency limitations of the instrumentation/telemetry system. This technique would not be as easily adapted to lightweight flight hardware.

The VDS results should be of interest to engineers selecting flight instrumentation and reduction of data for verification of spacecraft loads and environments. A set of load cell instrumentation similar to that used on the VDS will be employed as the primary response transducers on two Viking Spacecraft to be launched in 1975.

REFERENCES

1. Wada, B. K., "Viking Orbiter - Dynamics Overview", paper presented at the 44th Shock and Vibration Symposium, December 4-7, 1973, Houston, Texas.
2. Wada, B. K., Garba, J. A., and Chen, J. C., "Development and Correlation: Viking Orbiter Analytical Dynamic Model with Modal Test", paper presented at the 44th Shock and Vibration Symposium, December 4-7, 1973, Houston, Texas. Also published as JPL TM 33-690, June 1974.
3. Leppert, E. L., Wada, B. K., and Miyakawa, R., "Modal Test Results of the Viking Orbiter", paper presented at the 44th Shock and Vibration Symposium, December 4-7, 1973, Houston, Texas. Also published as JPL TM 33-688, June 1974.
4. Fortenberry, J. W. and Rader, P., "Fail Safe Forced Vibration Testing of the Viking 1975 Developmental Spacecraft", paper to be presented at the 45th Shock and Vibration Symposium.

5. Fortenberry, J. and Brownlee, G., "Viking 75 Lander Dynamic Test Model/Orbiter Developmental Test Model Forced Vibration Test Summary Report", JPL TM 33-689, June 1974.

6. Leondis, A., "Viking Dynamic Simulator-Vibration Testing and Analysis Modeling", paper presented at the 45th Shock and Vibration Symposium, October 1974, Dayton, Ohio.

ANALYTICAL PREDICTION AND CORRELATION FOR THE
ORBITER DURING THE VIKING SPACECRAFT
SINUSOIDAL VIBRATION TEST*

Gerald R. Brownlee
Jet Propulsion Laboratory
Pasadena, California

Fred D. Day III
Martin-Marietta Aerospace
Denver, Colorado
(Assigned to the Jet Propulsion Laboratory)

John A. Garba
Jet Propulsion Laboratory
Pasadena, California

Analyses were performed to simulate the sinusoidal testing of the Viking Spacecraft Dynamic Test Model. The complex nature of the spacecraft test hardware and response control techniques employed to safeguard the structure required an extensive series of analyses to predict dynamic responses and test capabilities. Representative analytical predictions and their correlation with test results are presented.

INTRODUCTION

The Viking Spacecraft will be launched on a Titan III/Centaur launch vehicle in August 1975. Managed for NASA by the Viking Project Office at the Langley Research Center, the Viking consists of an Orbiter system (the responsibility of the Jet Propulsion Laboratory, (JPL)), and a Lander Capsule (built by Martin Marietta Aerospace). The purpose of the Viking mission is the scientific exploration of Mars.

The Viking Orbiter (VO) structure was designed for analytically derived flight loads through an approach referred to as Loads Analysis. [1] The primary structure design loads are generated analytically as responses to the various transient Launch Vehicle events anticipated during the boost phase of the mission. This design approach, by necessity, had significant influence on the VO structural qualification test program.

The loads and the associated test programs were subdivided into three categories: the low frequency range, 0 to (20/30) Hz, middle frequency range, (20/30) to 200 Hz, and the

high frequency range, above 200 Hz. In the low frequency range, the member forces are predicted by analysis and the structural integrity of the VO system was verified primarily by static tests. In addition, a controlled sine vibration test, from 10 to 200 Hz, was employed to satisfy requirements for the low frequency as well as the middle frequency range. Acoustic excitation and pyrotechnic device firings were used for qualification in the high frequency range.

In order to simplify the operational, contractual and analytical interfaces, formal qualification testing of the Proof Test Orbiter was performed using an inertia simulation of the Viking Lander Capsule. The Proof Test Lander Capsule was qualified separately by the Martin Marietta Company in Denver, Colorado. However, representative hardware for both the Orbiter and Lander Capsule were combined for a developmental sine test program performed at JPL prior to the structure qualification tests.

The objectives of this development test were (1) evaluate the effect of Orbiter/Lander Capsule interactions on the responses at

This paper presents the results of one phase of spacecraft development carried out at the Jet Propulsion Laboratory, California Institute of Technology, under Contract No. NAS 7-100; sponsored by the National Aeronautics and Space Administration.

subsystem and component locations to determine the adequacy of component sinusoidal test levels, (2) evaluate the adequacy of the V-S/C secondary structure, (3) serve as a precursor to the Proof-Test Orbiter (PTO) qualification test, (4) evaluate the adequacy of the Proof Test Capsule (PTC) qualification test levels, and (5) obtain data for comparison with analytical results.

All VO testing was subject to the constraint imposed by the VO structural design criteria, namely: "Tests Other Than Static Qualification Tests Shall Not Result in Member Loads Greater Than Limit Loads Established by Flight Loads Analysis." Thus the excitation levels of the VO/VLC development vibration test were limited by strain gauged member responses and accelerations through a closed loop control system.

The complete sinusoidal test program consisted of separate excitations along 3 orthogonal axes. In the two lateral configurations the test specimen was cantilevered at its base and the excitation was provided by four pendulously suspended 150 lb. modal shakers. For the longitudinal excitation the test specimen was mounted on a fixture attached to one Ling A-249 exciter. The discussion herein is limited to the longitudinal configuration with the elastic VLC since it presented the most challenging engineering problems.

The emphasis in this paper is on the analysis and its correlation with test results. The implementation of the test procedure is the subject of another paper.^[2] The analytical work is divided into three areas:

- (1) Test feasibility studies. These consisted of computer simulations to determine fixture characteristics and to verify the restraint system's capability for limiting shaker armature rotations. Excessive armature rotation would automatically abort the test.
- (2) Response prediction studies. These studies were aimed at identifying critical structural members and aiding in the selection of strain gauge and accelerometer channels for use in the test control.
- (3) Correlation studies. These studies compare the predicted responses to the test responses after each has been renormalized to a common input base.

TEST CONFIGURATION

The test configuration was consistent with other large spacecraft vertical vibration test programs. A large electromagnetic shaker provided the excitation through a bowl-type test fixture upon which the spacecraft Dynamic Test Model (DTM) was mounted. (See Fig. 1 and Fig. 2.)

Test Specimen

Hardware responsibility for the test specimen rested with three separate organizations. The Lander developmental test model (LDTM) was built by Martin Marietta Aerospace. The Viking Transition Adapter (VTA) was the responsibility of General Dynamics/Convair Astronautics. The Orbiter developmental test model (ODTM) was built by JPL. Each organization was responsible for ensuring that the test hardware was representative of the flight configuration.

The ODTM consisted of the Viking Lander Capsule Adapter (VLCA); octagonal bus structure with flight type bays and simulated electronics, cabling, and cable trough; four solar panels with dampers; scan platform with simulated science, antennae (high and low gain and relay); propulsion module; and Viking Spacecraft Adapter (V-S/C-A). All simulated hardware consisted of accurate representations with respect to interface requirements, inertial properties, stiffness and damping for the frequency range from 0 to 200 Hz.

Test Facility

The large size and weight of the Viking Spacecraft as compared to previous spacecraft tested at JPL required some special test hardware and special fixturing.

A magnesium fixture weighing 3000 lb. was used as a transition between the 12 spacecraft adapter members and the shaker head. In addition, an airbag suspension system was required to react the spacecraft-fixture dead weight and protect the Ling A-249 shaker armature flexures. Due to the large spacecraft height and non-symmetric mass configuration a lateral support was required. This support was provided by three pairs of hydrostatic bearings and a set of three reaction piers. The lateral supports were attached to the test fixture as shown schematically in Fig. 1.

Test Control

Of the thirty-six channels available for control during the test, twelve were input controls and twenty-four were response controls or response limiters. The input controls (accelerometers on the Orbiter bus) were employed in defining a nominal test vibration level. This nominal control level was automatically suppressed at any frequency by a response control (either accelerometer or strain-gauge) reaching a preset level. The control system would ideally allow the maximum response, up to the nominal control level, so long as none of the twenty-four response controls exceeded its preset level. In this way the restriction on exceedance of flight derived limit loads would be adhered to. In addition, a total of 59 channels were monitored during the test for emergency abort. The test was

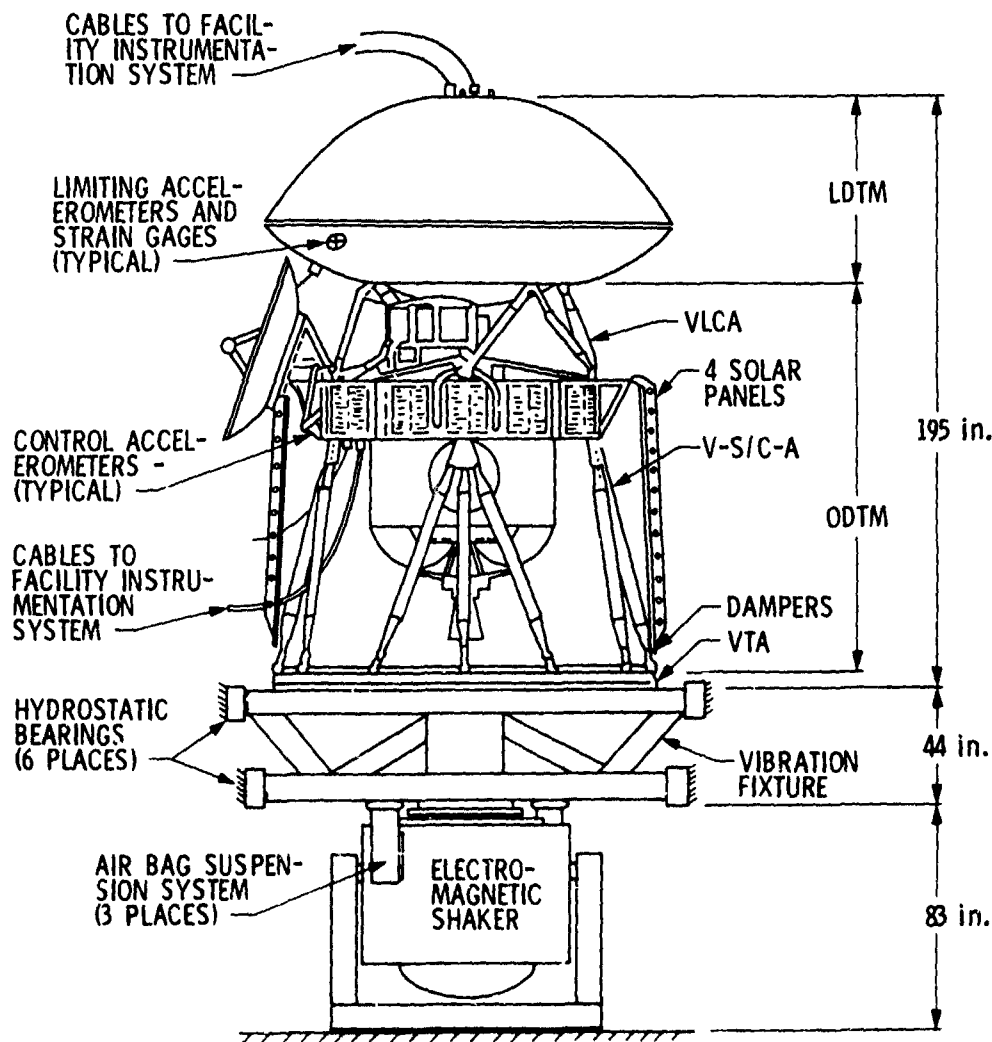


Figure 1. Longitudinal Axis Test Installation

automatically terminated by any one of these measurements reaching a preset value.

TEST FEASIBILITY STUDIES

The test feasibility studies were concerned with two related areas, the dynamic characteristics of the test fixture and the capability of the shaker/restraint system to provide adequate force and moment reactions.

Fixture Analyses

For the more common base-input-controlled sine tests, fixture resonances within

the test frequency range can be a serious problem. Since the Viking developmental sine test used response controls and response limiting, fixture resonances were not automatically considered as detrimental to the program. The possibility of designing a test fixture of the size and weight required for Viking, without having resonances below 200 Hz, was small to start with. However, a fixture which is rigid throughout the frequency range of the analytic simulation would greatly simplify the mathematical models required and significantly reduce costs. Analyses of the fixture design with a simplified spacecraft model, were performed to determine the extent of elastic

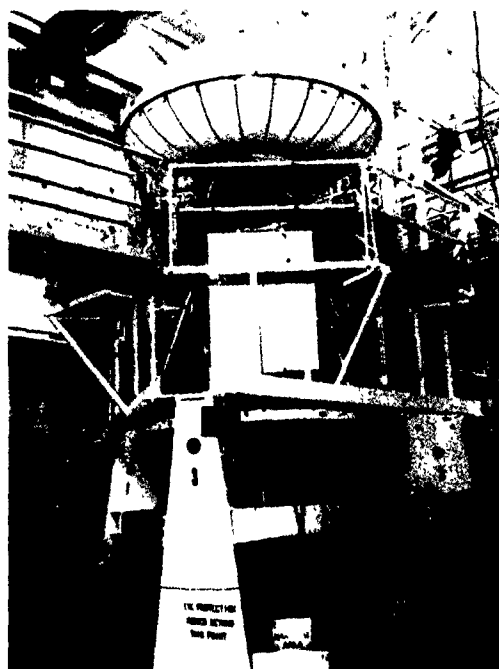


Figure 2. Viking Spacecraft in the Test Facility

participation by the fixture in normal modes below 200 Hz, and evaluate the accuracy of assuming a rigid fixture for the 0-40 Hz frequency range simulated by analysis. The spacecraft model consisted of a rigid lander and rigid orbiter supported by representative truss members.

As a result of these studies the original fixture concept was modified to provide additional torsional stiffness and include the external restraint system. These changes resulted in a first mode frequency of 109 Hz.

Shaker Capability Studies

Early in the planning of the Viking Spacecraft developmental sine test an analysis was performed to obtain an estimate of the requirements to be imposed on the shaker. This analysis employed a detailed elastic model of the Orbiter and a rigid inertia model of the Lander. The spacecraft model was fixed at the base of the spacecraft adapter and base motion input forcing functions applied. A determination of the reactions at the cantilever interface gave estimates of the required shaker force and the moments and shears which would be applied to the shaker if no other restraint system were

used. This study indicated that the shaker force capability was sufficient, but that additional external moment restraints were required.

At a later time, a refined elastic model of the Orbiter, with a rigid simulation of the Lander, was coupled to the shaker/restraint system model and a test simulation was performed. This analysis was performed as a check of the facility model and used the rigid lander representation since it was readily available. The results indicated that the test was feasible, the shaker force capability was sufficient, the armature relative rotation was within acceptable limits, the fixture stresses were acceptable, and the restraint system performance was adequate. This conclusion was confirmed by the detailed test simulation analysis and the test results themselves.

RESPONSE PREDICTION STUDIES

Once the test facility configuration was fixed and verified by analysis the response prediction analyses were initiated. The objectives of the response prediction studies were to identify critical structural members for use in selecting the response control channels, determine facility reaction loads for the restraint system, provide responses for numerous transducers for quick look comparison with test data, and indicate potential problem areas for test control.

Analytical Model

The total spacecraft model was generated using modal synthesis or modal coupling techniques. [3, 4] The Viking Orbiter was divided into the following subsystems for analysis, the bus, including the spacecraft adapter and lander adapter trusses; the cable trough; the scan platform; the propulsion subsystem; and the four solar panels. The subsystem models were verified by extensive modal testing. [5] The composite Orbiter model was also verified by system level modal tests employing an inertial simulation of the Lander. [6]

The flexible Lander model was generated by Martin Marietta Aerospace and supplied to JPL as a normal mode model. The total spacecraft dynamic model was then produced by coupling the Lander modes with the composite Orbiter model.

The test facility was represented by a discrete coordinate model of the shaker, fixture, and restraint system. A schematic of the test facility model is given in Fig. 3. The pertinent facility parameters are listed in Table 1. In modeling the test facility the following assumptions were made:

1. Since the fixture analyses indicated a first mode resonance at 109 Hz and the response analysis was to be limited to 40 Hz, the fixture was assumed rigid.

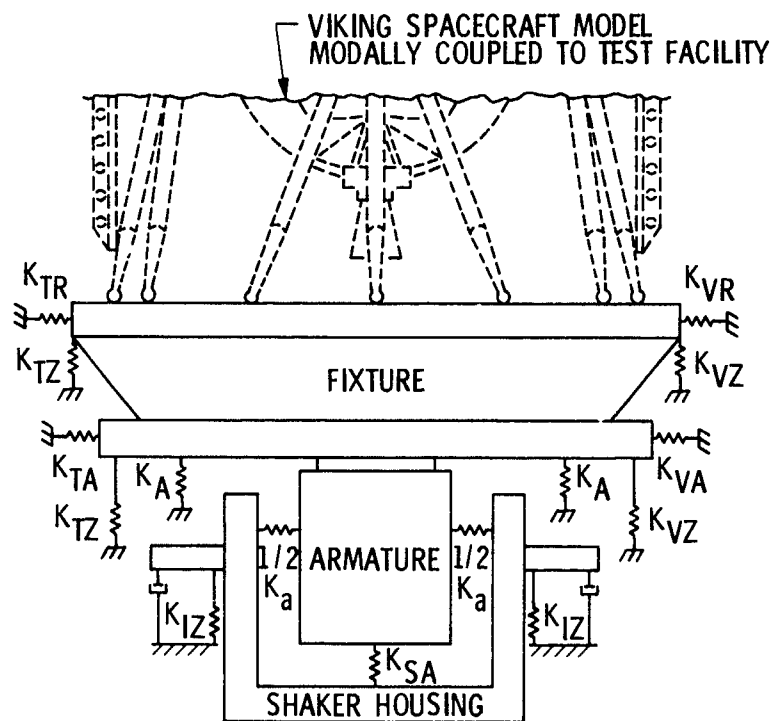


Figure 3(a). Facility Model, Schematic

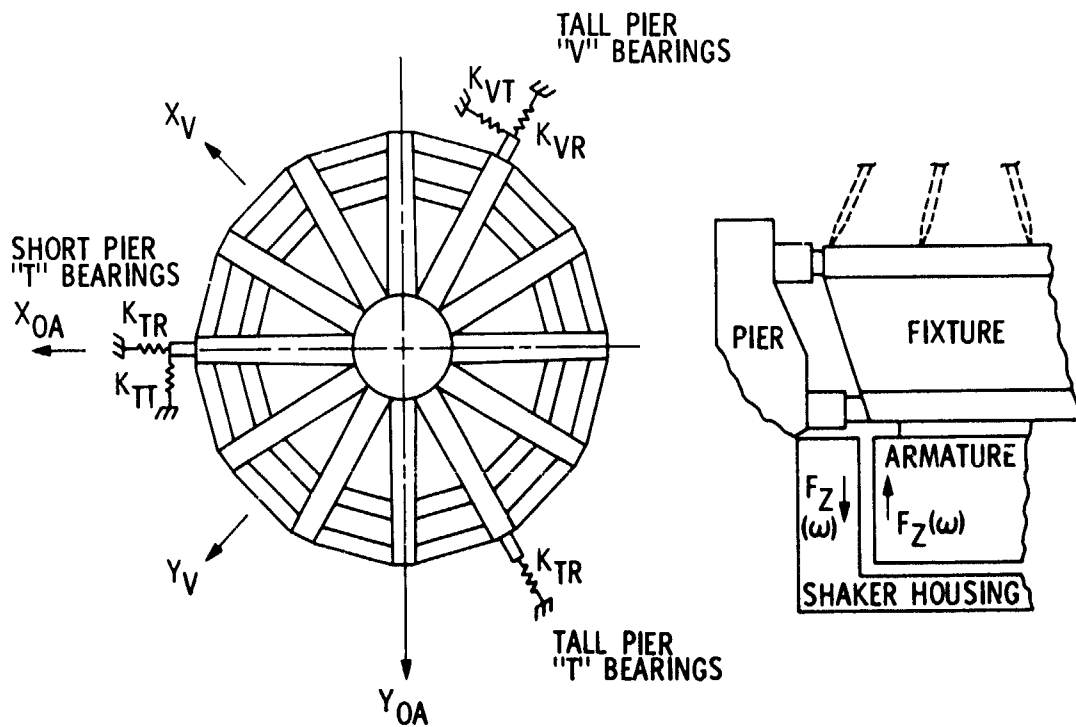


Figure 3(b). Facility Model, Schematic
Team Bearing Model

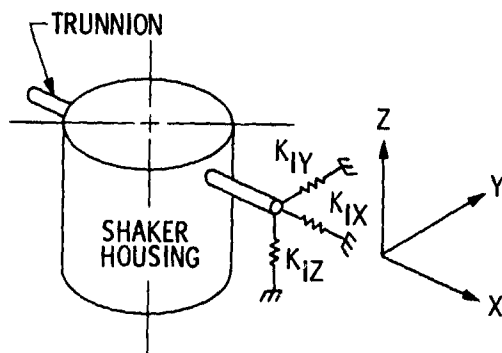


Figure 3(c). Facility Model, Schematic Isomode Pad Model

2. The shaker armature and the shaker housing were each assumed to be rigid masses.
3. The three reaction piers were treated as rigid supports for the hydrostatic bearings. However, the local flexibility of the piers at the lower plane of bearings was included in determining their effective spring rates.
4. The airbag spring rate was neglected as its effects were only evident below the frequency range of interest.

The facility model was formulated to provide response data in terms of armature-shaker housing relative motion, housing displacements and reactions at the shaker supports, loads on the reaction piers and

TABLE 1
Facility Parameters

A. LING 249 SHAKER PROPERTIES		
1. Inertial Properties		
Armature Weight	396 lbs.	
Housing Weight	29,000 lbs.	
Armature C. G.	13.2" below head surface, axi-symmetric	
Housing C. G.	27.75" below head surface, axi-symmetric	
2. Armature Stiffness Properties		
Effective Lateral Spring Constant		$(K_{SL}) = 1.6 \times 10^6$ lb/in.
Effective Axial Spring Constant		$(K_{SA}) = 1.6 \times 10^4$ lb/in.
3. Isomode Stiffness Properties		
Effective Spring Constant Along Trunnion Axis		$(K_{IX}) = .42 \times 10^6$ lb/in.
Effective Spring Constant Perpendicular to Trunnion Axis		$(K_{IY}) = .21 \times 10^6$ lb/in.
Effective Longitudinal Spring Constant		$(K_{Iz}) = .35 \times 10^6$ lb/in.
B. HYDROSTATIC BEARING STIFFNESS PROPERTIES		
1. "T" Type, Model Team 1830T-8		
Effective Tangential Spring Constant		$(K_{TT}) = 0$ lb/in.
Effective Radial Spring Constant		$(K_{TR}) = 8 \times 10^6$ lb/in.
Effective Longitudinal Spring Constant		$(K_{TZ}) = 0$ lb/in.
2. "V" Type, Model Team 1830V-8		
Effective Tangential Spring Constant		$(K_{VT}) = 1 \times 10^6$ lb/in.
Effective Radial Spring Constant		$(K_{VR}) = 8 \times 10^6$ lb/in.
Effective Longitudinal Spring Constant		$(K_{VZ}) = 0$ lb/in.
C. AIRBAG STIFFNESS PROPERTIES		
K_A	0 lb/in.	

fixture, and shaker force requirements. The resultant facility model consisted of twelve dynamic degrees of freedom, six for the armature/fixture mass and six for the shaker housing.

The system modes for the test simulation were produced by coupling the composite spacecraft cantilever model to the test facility model. Transformations were maintained such that accelerations, displacements, and internal loads for the subsystems could be generated from the composite system modal responses. Table 2 lists the frequencies and modal damping values employed for the first fifty modes of the complete system. A total of 109 system modes were employed in the response or test simulation analyses. The mathematical details of the

system modeling techniques will not be described extensively as they are well documented elsewhere and consistent with practices throughout industry. The derivation of the system damping, however, is not well defined elsewhere and methods vary considerably from company to company. The technique employed for this study will therefore be dealt with in some detail.

In general, subsystem modal damping values were obtained from test data wherever possible. The Viking Lander damping was supplied to JPL by Martin Marietta Aerospace as a diagonal modal damping matrix. Damping values varied from $c/c_c = 0.005$ to $c/c_c = 0.055$ depending on the mode (C_c = critical damping value).

TABLE 2
Composite Model

Mode No.	Frequency Hz	Damping Ratio c/c_c	Identification or Predominant Motion
1	3.60	.018	Rigid S/C on Armature, Longitudinal
2	5.61	.697	Solar Panel RB Mode
3	5.67	.698	Solar Panel RB Mode
4	5.70	.712	Solar Panel RB Mode
5	5.70	.734	Solar Panel RB Mode
6	5.89	.068	1st Spacecraft Bending Mode
7	6.02	.026	1st Spacecraft Bending Mode
8	7.08	.072	Housing Lateral X
9	7.42	.011	S/C 7th Mode, Lateral
10	7.77	.010	Orbiter Torsion Mode
11	9.74	.025	S/C 9th Mode, Lateral
12	10.36	.052	S/C 10th Mode
13	10.49	.036	S/C 11th Mode, Torsion
14	11.13	.100	Housing Longitudinal Z
15	12.02	.007	S/C 12th Mode, Torsion
16	12.80	.006	S/C 13th Mode, Torsion
17	13.63	.010	S/C 14th Mode
18	13.73	.010	S/C 15th Mode
19	14.64	.020	S/C 16th Mode
20	15.24	.016	S/C Longitudinal Mode
21	15.69	.056	Housing Lateral Y

TABLE 2
Composite Model (Continued)

Mode No.	Frequency Hz	Damping Ratio c/c_c	Identification or Predominant Motion
22	15.75	.024	Housing Torsion
23	16.26	.019	
24	16.46	.012	
25	17.23	.021	
26	18.17	.028	
27	18.43	.016	
28	19.03	.019	
29	20.52	.011	
30	20.96	.010	
31	21.41	.010	
32	21.47	.010	
33	21.67	.010	
34	22.36	.015	
35	23.05	.020	
36	23.33	.010	
37	23.94	.010	
38	23.95	.010	
39	23.95	.012	
40	24.75	.020	
41	25.11	.019	
42	25.68	.017	
43	25.84	.015	
44	25.93	.015	
45	26.12	.019	
46	27.01	.021	
47	29.04	.014	
48	29.53	.016	
49	29.94	.016	
50	30.12	.020	

The Orbiter damping was determined from subsystem and Orbiter system-level modal test data. Expressing the equations of motion for the Orbiter model in matrix form yields

$$[M] \begin{Bmatrix} \{\ddot{u}\}_R \\ \{\ddot{u}\}_B \\ \{\ddot{q}\}_1 \\ \vdots \\ \{\ddot{q}\}_i \end{Bmatrix} + [C] \begin{Bmatrix} \{\dot{u}\}_R \\ \{\dot{u}\}_B \\ \{\dot{q}\}_1 \\ \vdots \\ \{\dot{q}\}_i \end{Bmatrix} + [K] \begin{Bmatrix} \{u\}_R \\ \{u\}_B \\ \{q\}_1 \\ \vdots \\ \{q\}_i \end{Bmatrix} = \{0\} \quad (1)$$

where

$\{u\}_B$ = real displacement of the VO bus

$\{u\}_R$ = rigid body degrees of freedom of the VO

$\{q\}_i$ = modal displacements of i th substructure

$[M]$ = system mass matrix including the rigid VLC

$[C]$ = system damping matrix

$[K]$ = system stiffness matrix

The subsystem damping data was introduced in the matrix $[C]$ of Equation (1) as diagonal modal damping. Since Equation (1) contains a mixture of real and generalized coordinates, the Orbiter damping matrix,

$$[C_o] = [\Phi_o]^T [C] [\Phi_o] \quad (2)$$

where $[\Phi_o]$ = Orbiter system-level normal modes, lacks the damping contribution of the bus real coordinates. The matrix $[C_o]$ does contain the effect of the Solar Panel point dampers, as well as all subsystem damping. The ODTM modal test provided damping information for the Orbiter system less Solar Panels. The Solar Panels were left off the modal test specimen intentionally. The damping ratios for the ODTM as well as the subsystems are given in References 3 and 4.

Past experiences at JPL have shown that the use of measured modal damping to analytically predict spacecraft responses for a sinusoidal vibration test yielded responses higher than the sine test measurements. This is attributed to the increase in damping with excitation level. All Viking modal testing was done at several levels of excitation in order to study the nonlinearity of damping with amplitude. For the analysis the highest damping measured in the modal test was used. The procedure for obtaining a valid Orbiter damping matrix was as follows:

1. Identify the Orbiter normal modes using kinetic energy distribution and effective weight. Classify the normal modes as to overall system modes or subsystem modes.
2. Examine the diagonal terms of $[C_o]$, Equation (2) and estimate a damping ratio for each mode, neglecting the off-diagonal coupling terms.
3. For normal modes with appreciable subsystem contributions either use the damping in $[C_o]$ or augment it using subsystem test data.
4. For overall Orbiter normal modes such as system bending, longitudinal or torsional modes use the ODTM modal test data to augment the diagonal terms in $[C_o]$.

The above procedure produces two augmented Orbiter damping matrices, $[C_o^*]$ wherein the off-diagonal terms have been neglected and $[C_o']$ wherein the off-diagonal terms have been retained.

The above procedure is clearly based on engineering judgement, wherein all available test data is utilized to generate an estimate of Orbiter damping.

The total system normal mode damping is then generated by including effects for the facility and Lander damping.

No experimentally determined damping data was available for the test facility. The damping values were estimated based on modal test data of a similar shaker configuration. For the armature the damping ratio c/c_c was assumed to be .02. For the trunnion isomode pads a damping ratio of $c/c_c = 0.10$ was picked. Identifying the diagonal Lander damping matrix as $[C_L]$, and the spacecraft normal modes as $[\Phi_{sc}]$, the spacecraft combined damping is obtained by following basically the same procedure used for the Orbiter, thus the spacecraft damping matrix is generated as

$$[C_{sc}^*] = [\Phi_{sc}]^T \begin{bmatrix} [C_o^*] & 0 \\ 0 & [C_L] \end{bmatrix} [\Phi_{sc}] \quad (3)$$

using the diagonal Orbiter damping or

$$[C_{sc}'] = [\Phi_{sc}]^T \begin{bmatrix} [C_o'] & 0 \\ 0 & [C_L] \end{bmatrix} [\Phi_{sc}] \quad (4)$$

using the full Orbiter damping matrix. The diagonal terms of $[C_{sc}^*]$ and $[C_{sc}^i]$ are now examined and compared to see if the damping value reflects the expected damping for the identified mode. It was found that for most modes the diagonal terms of $[C_{sc}^*]$ and $[C_{sc}^i]$ were of similar magnitude. $[C_{sc}^*]$ and $[C_{sc}^i]$ can now be further diagonalized to produce two more matrices $[C_{sc}^{**}]$ and $[C_{sc}^{''}]$.

The composite system damping can now be determined from

$$[C_c^i] = [\phi_c]^T \begin{bmatrix} [C_{sc}^i] & 0 \\ 0 & [C_F] \end{bmatrix} [\phi_c] \quad (5)$$

where

$[C_F]$ represents the test facility discrete damping values

$[\phi_c]$ is the matrix of 109 composite system normal modes,

and $[C_{sc}^i]$ is taken as either $[C_{sc}^*]$, $[C_{sc}^{**}]$, $[C_{sc}^i]$ or $[C_{sc}^{''}]$.

The procedure used for estimating Orbiter damping was now applied to the above matrices to generate a diagonal damping matrix $[C_c]$ for the composite system. For most modes the diagonal element was used.

Ideally at least two response solutions for the composite can be generated, one by using $[C_c]$ for the composite damping and another by using the consistently coupled damping matrix, $[C_c^i]$ evaluated with $[C_{sc}^i]$.

The latter solution leads to either a complex eigenvalue solution or an integration of a large number of coupled differential equations. This was not attempted due to prohibitive cost. Instead the matrix $[C_c]$ was used in the response solution for the system.

Although four matrices in Equation (5) were generated and used for a qualitative assessment of the damping, diagonalization of the damping matrix at each level of the processing was favored. The diagonalization gives a better

insight at each level since it represents modal damping, while the effect of the off-diagonal terms are not fully understood.

Response Program

To predict the controlled responses of the spacecraft a digital computer program was developed wherein the equations of motion were solved such that none of the controls were exceeded, yet one of the controls always reached its limit. The equation of motion of the composite in generalized coordinates is expressed as

$$[M_c]\{\ddot{\xi}\} + [C_c]\{\dot{\xi}\} + [K_c]\{\xi\} = [\phi_c]^T \{f\} \quad (6)$$

where $[M_c]$, $[C_c]$ and $[K_c]$ are the generalized mass, damping and stiffness of the composite respectively, and $\{f\}$ is the forcing function.

Equation (6) is solved as a function of frequency for a unit force $\{f_{ZI}(\omega)\}$ excitation on the shaker in the Z (longitudinal) direction yielding a solution vector $\{\xi_I(\omega)\}$.

Responses for a set of control inember forces $\{f_l\}$ and accelerations $\{\ddot{u}_l\}$ are computed using the solution $\{\xi_I(\omega)\}$. These responses are now compared to the allowable forces $\{f_a\}$ and accelerations $\{\ddot{u}_a\}$ and a factor R is found such that none of the controls are exceeded yet one of the forces or accelerations reaches its allowable value. The response for the rest of the structure is now computed using R $\{\xi_I(\omega)\}$ as a solution to Equation (6).

In addition to calculating spacecraft member forces and accelerations throughout the structure, the program also provided information on armature rotation, shaker force requirement, and reaction forces on the facility. The responses were calculated as steady-state solutions in the frequency domain. The servo-control system for the shaker was not represented in the analysis.

Results

The response predictions were initially generated for a unit force applied by the shaker with no response controls or limiters. This produced transfer function data useful in evaluating the severity of an uncontrolled test, aided in the selection of control parameters, and

provided reference data for evaluation of subsystem environments.

The full response prediction program was then run to provide estimates of the controlled test conditions. These results were used to select the initial response control channels, select the peak limit parameters which would automatically terminate the test if preset values were exceeded, and provide indications of potential problem areas for test control. The results showed a potential problem in the region of the shaker housing vertical resonance. At this frequency, approximately 12 Hz, the housing accelerations and resultant reactions induced were severe. As a result of this study, it was decided to run the test from approximately 20 Hz to 200 Hz with the shaker housing supported by the isomode pads on the trunion. Below approximately 20 Hz the housing would be rigidly supported, eliminating the resonance problem. The analysis results also indicated a few areas where the controlling parameter for response switched rapidly (i.e., within a narrow frequency range) from one measurement to another. Because of the reaction speed of the shaker servo-system, overshoots and undershoots in control level would be anticipated in these frequency regions.

CORRELATION STUDIES

The correlation studies were performed to indicate the accuracy and validity of the analysis techniques employed. Test data and analytical predictions were compared for both acceleration measurements and structural loads.

Low Level Tests

Two series of low level tests were conducted from 7 Hz to 200 Hz to 7 Hz at 2 oct/min sweep rate using the 12 input control accelerometers and the 12 response controls indicated by the pretest analysis. The input controls were set at .5 G and the Orbiter response loads were set at 1/3 design limit load adjusted for 1 G static condition. Two series were necessary to obtain response measurements on all primary structure. The purpose of these tests was:

1. To verify the proper Orbiter response control members.
2. To investigate the control system performance, in particular the control channel switching capability and any resulting overshoots.
3. To provide data for use in checking the linearity of the system.

The results of these test runs indicated the following:

1. Some of the Orbiter structure loads did not develop as indicated by the

analysis. In one case it was because of a minor deficiency in the analytical model, and in another case the model was apparently conservative in the development of bending moments. This resulted in the pretest analysis indicating a load control which did not occur in the test and hence, the analytical load predictions in that control frequency range were suppressed. It was obvious that different structure would have controlled the test if it had been in the control system and hence, a revision to the Orbiter response controls was necessary for higher level tests.

2. Considerable overshoot occurred in the control channels. A survey of all control channels indicated an average overshoot of about 30%.

High Level Tests

The higher level tests were subsequently conducted using the Orbiter response controls revised on the basis of the low level tests. The response control levels were adjusted such that with a 30% overshoot design limit loads would not be exceeded. The input control acceleration levels were unchanged since structural protection was provided by the reduction in response control levels.

Post Test Analysis

As discussed above, the pretest analysis utilized a significantly different control set than what was eventually implemented in the tests and hence would not be sufficient for correlation with test data. A post test analysis was conducted for the purpose of correlation. This analysis utilized the actual test control set and levels for both the low level and the full level tests with the following exceptions. For the low level analysis those controls that did not occur due to model inaccuracies were eliminated, and for both low level and full level runs the Lander strain gage limits could not be used because no direct correlation existed between the strain gage readings and modal degrees of freedom. This post test analysis is the basis for correlation in this paper. All test data shown was taken from the 200 Hz to 7 Hz downsweeps.

Control Sequence Comparisons

Comparisons of the analytically predicted and recorded test control sequences were performed for the low level test. However, the exact frequency at which a switch in control occurs was not easily ascertained in either the analysis or test data. A shift of 1/2 to 1 Hz either up or down was within the accuracy of the measurements. Also, the control on the Lander strain gages which occurred in the test was not possible to include in the analysis.

Input Control Comparisons

Comparison of the analytically predicted and measured input accelerometer controls in the low level down-sweep are shown in Fig. 4 through Fig. 8. For brevity only those accelerometers that contributed to test control are shown. Each figure contains a plot of the prediction and two plots of the test data, filtered and unfiltered. It should be noted that the test control system operated on wide band 800 Hz low pass filtered test data. The plots refer to the wideband data as unfiltered, while the data labeled as filtered has been processed through a 5 Hz tracking filter.

Response Control Comparisons

Comparisons of the predicted and measured response controls for the low level down-sweep are shown in Fig. 9 and Fig. 10 for the Lander accelerometers and Fig. 11 and 12 for the Orbiter structural loads. Note again that it was not possible to compare the Lander strain gage controls. Again the accelerometer plots show predicted, filtered and unfiltered test data. The load plots show the predicted load and the test load as reduced from strain gage test data.

Structural Load Comparisons

Fig. 13 through 18 show plots of predicted and measured loads on typical members of the Orbiter primary structure. They are included here to show the accuracy of the analytical prediction in structure not controlling the test. Fig. 13 and 14 show two typical members in the spacecraft adapter, Fig. 15 is a typical member of the bus main longerons, Fig. 16 and 17 are two typical members of the propulsion system support truss, and Fig. 18 is a typical member of the Viking Lander Capsule Adapter. For brevity only, some typical members of primary structure have been shown.

Discussion

All of the measured data, input control, response control, and primary structure loads agree quite well with the analytical predictions. The control system overshoot is readily apparent in Fig. 6, 8, 9, 10, 11, and 12. The effects of the overshoot on other structural loads is evident in Fig. 16 and 17.

Evaluation of the comparisons made show that where the analysis and test data do not

agree it is mainly because of the following reasons:

1. The model failed to predict the control for a particular frequency.
2. The Lander strain gage controls could not be included in the model.
3. The test control system was not capable of switching controls as fast as the analysis and inherently allowed overshoots and undershoots while settling on the control level.
4. The test data had high frequency noise superimposed. The test was controlled on essentially an unfiltered signal while the analysis was valid only for a clean sine wave.

Conclusions

The above data illustrate how a complex structural system was analyzed to predict the dynamic behavior during a response controlled sinusoidal vibration test. The relative success of the correlation between test and analysis is attributed to:

1. A refined structural model, wherein each subsystem was verified by modal test.
2. Extensive feasibility studies of the fixturing and test facility configuration.
3. Proper planning of analytical and test efforts to meet project schedules.
4. Careful modeling of the test facility dynamic properties.
5. Development of special computer programs for controlled response predictions.
6. Data reduction techniques to obtain quick turnaround for the evaluation of response parameters.

For purposes of evaluating the adequacy of the modelling techniques of the system a better correlation between analysis and test could be achieved by analytically eliminating the effect of the overshoot from the test data. This was not done since the data as shown compare real test data with realistically attainable analytical predictions in a more meaningful way.

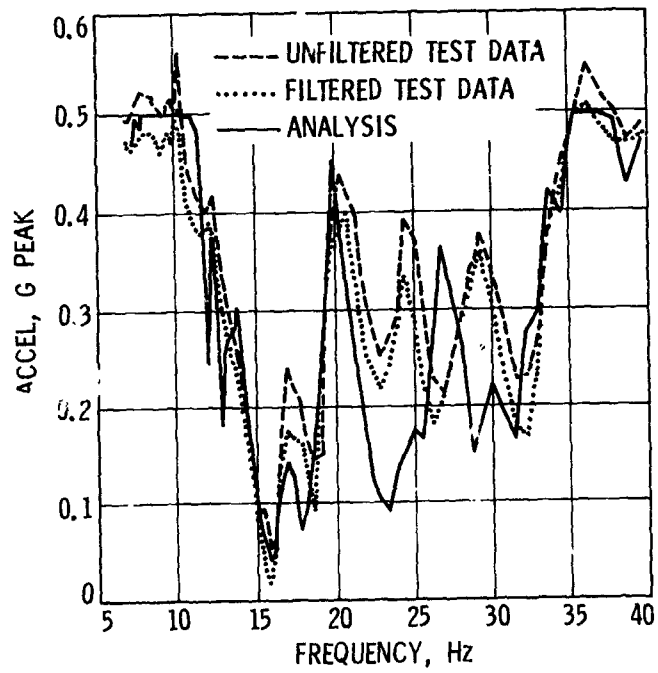


Figure 4. Orbiter Acceleration Input Control, Longitudinal (DOF 593)

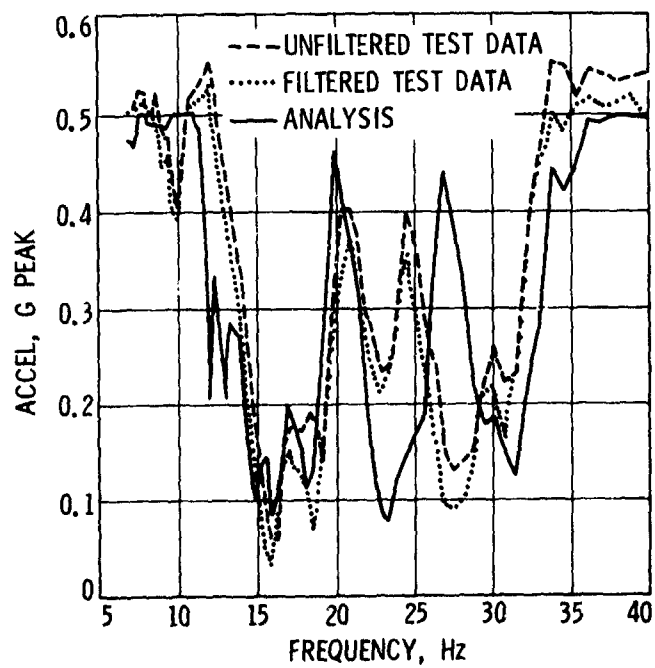


Figure 5. Orbiter Acceleration Input Control, Longitudinal (DOF 2493)

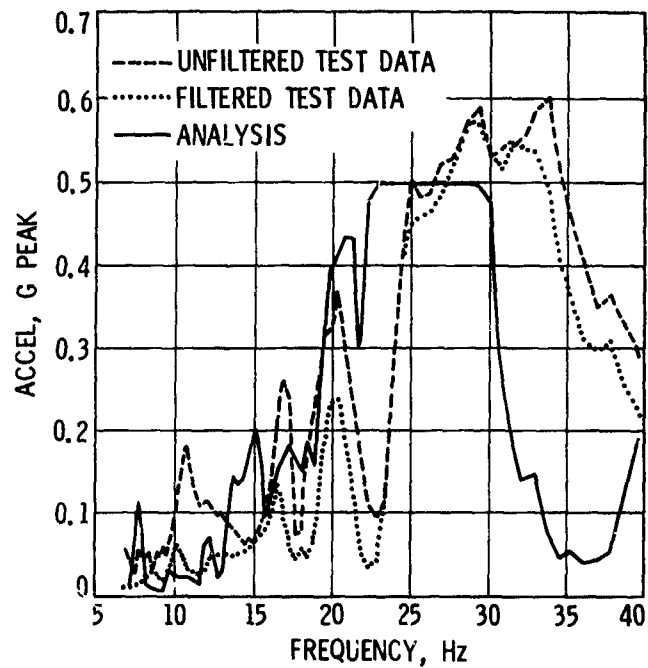


Figure 6. Orbiter Acceleration Input Control, Lateral (DOF 2492)

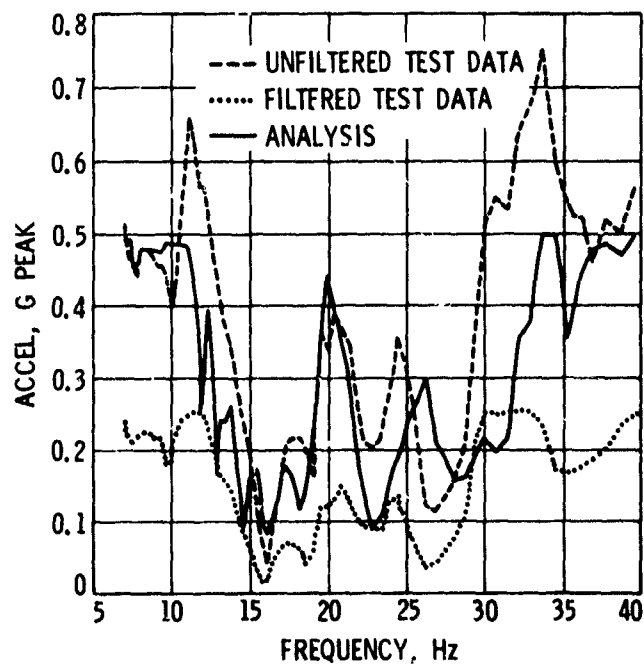


Figure 7. Orbiter Acceleration Input Control, Longitudinal (DOF 3993)

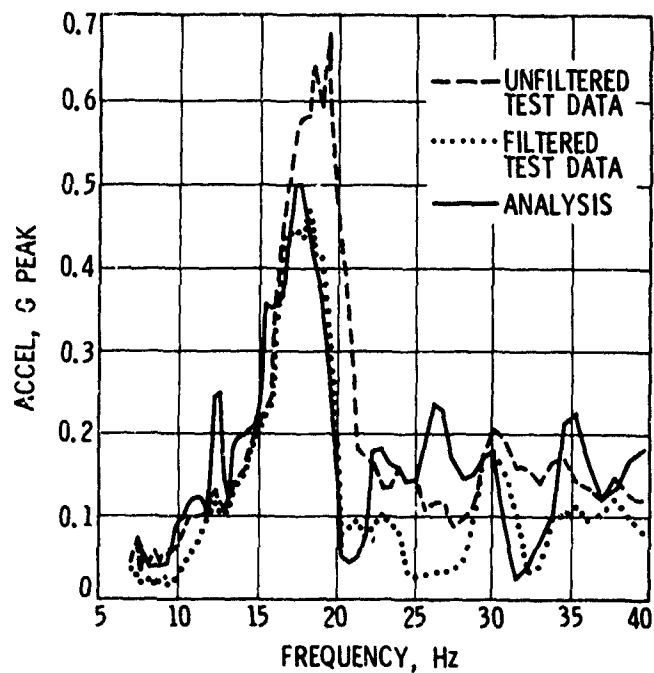


Figure 8. Orbiter Acceleration Input Control, Lateral (DCF 3971)

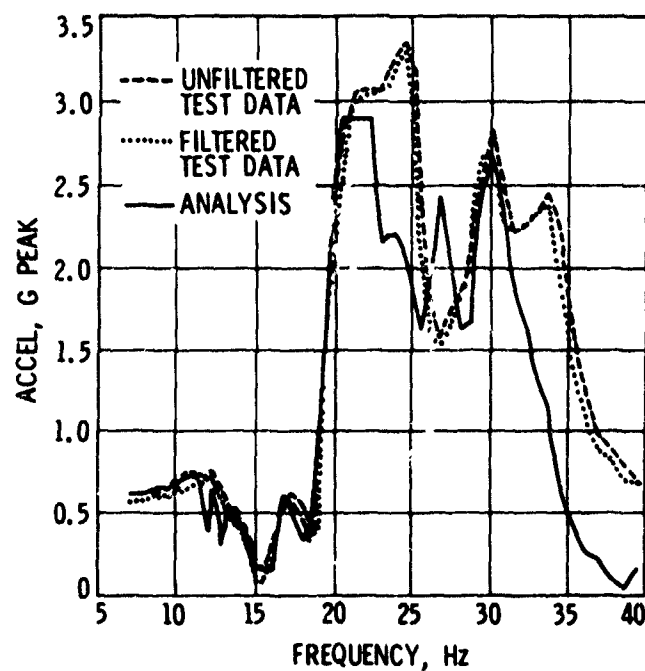


Figure 9. Lander Acceleration Response Control (DOF 3052)

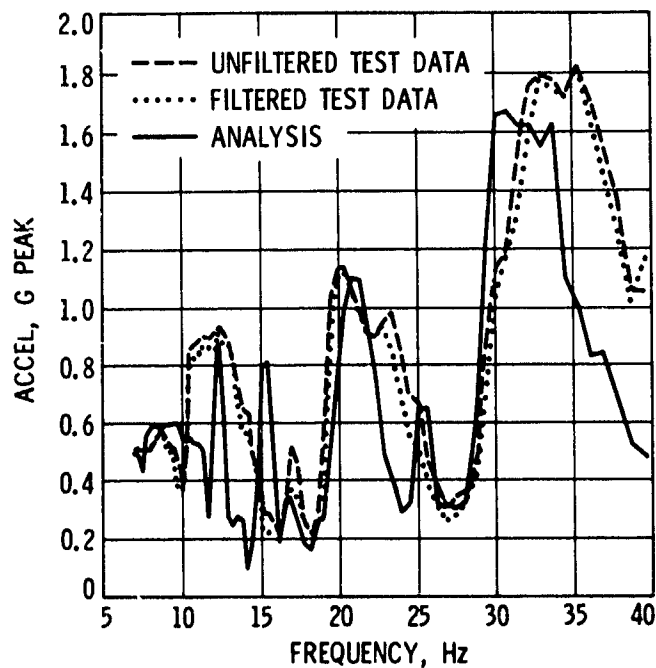


Figure 10. Lander Acceleration Response Control (DOF 3073)

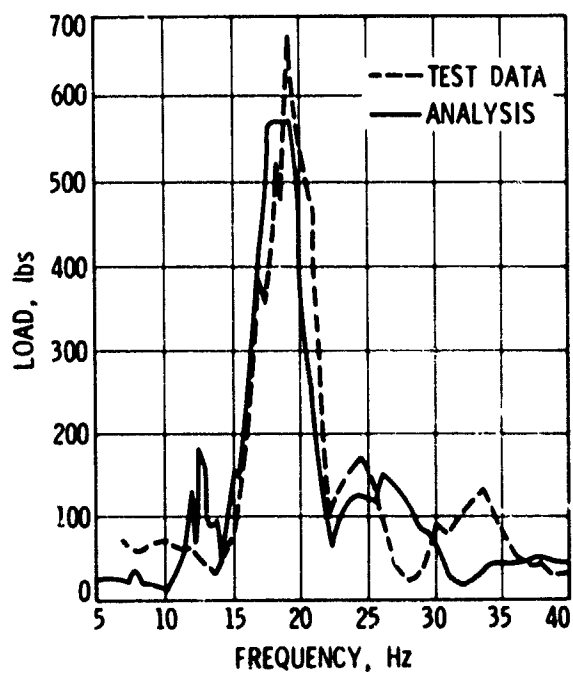


Figure 11. Orbiter Member No. 660 Response Control

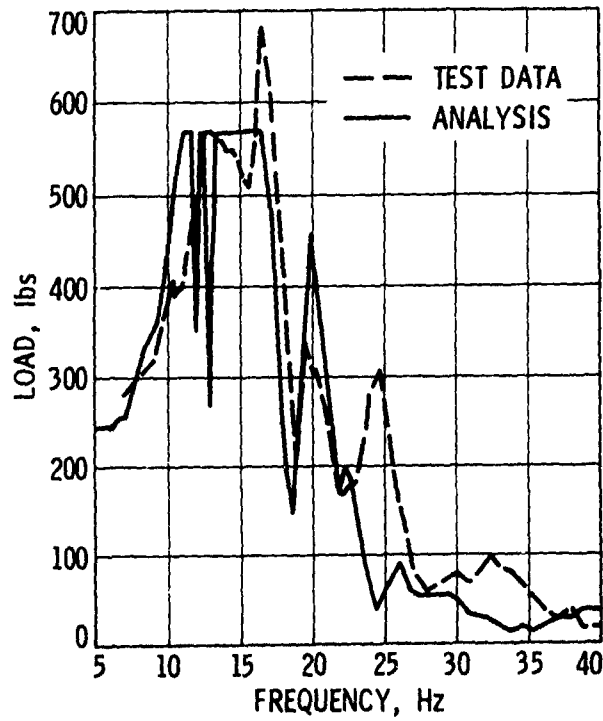


Figure 12. Orbiter Member No. 664 Response Control

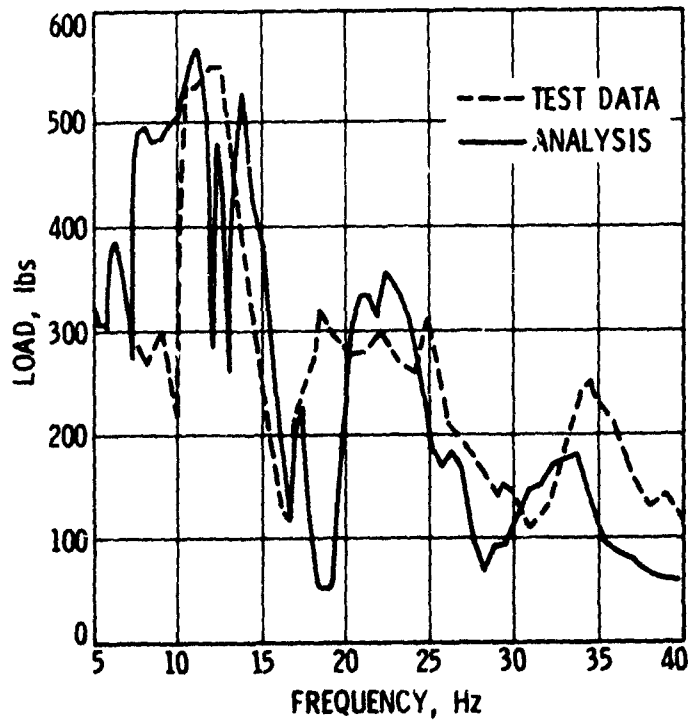


Figure 13. Orbiter Member No. 687 Response

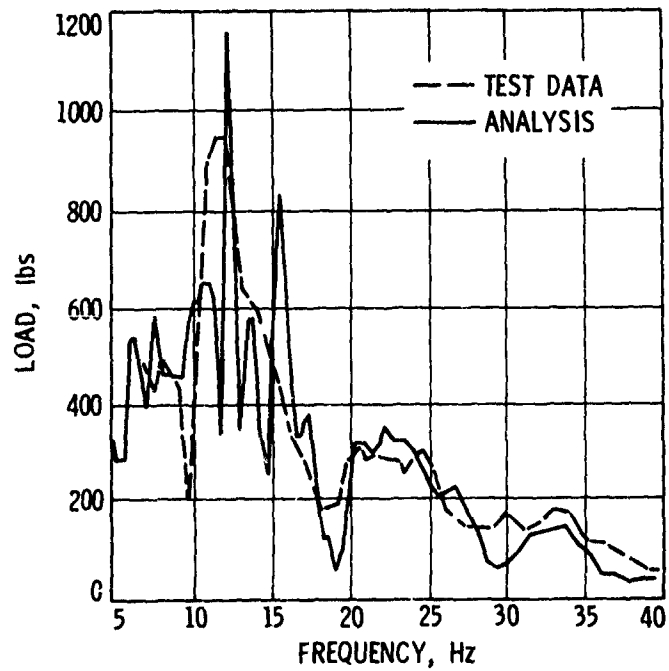


Figure 14. Orbiter Member No. 680 Response

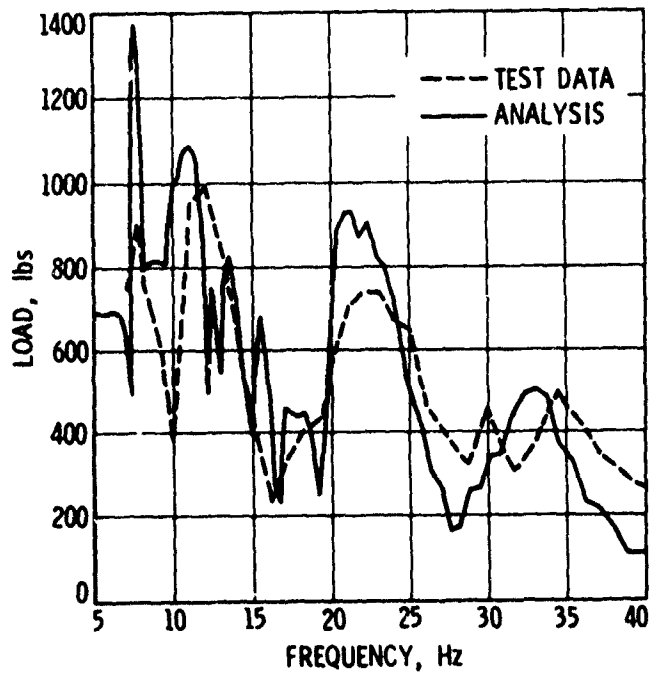


Figure 15. Orbiter Member No. 816 Response

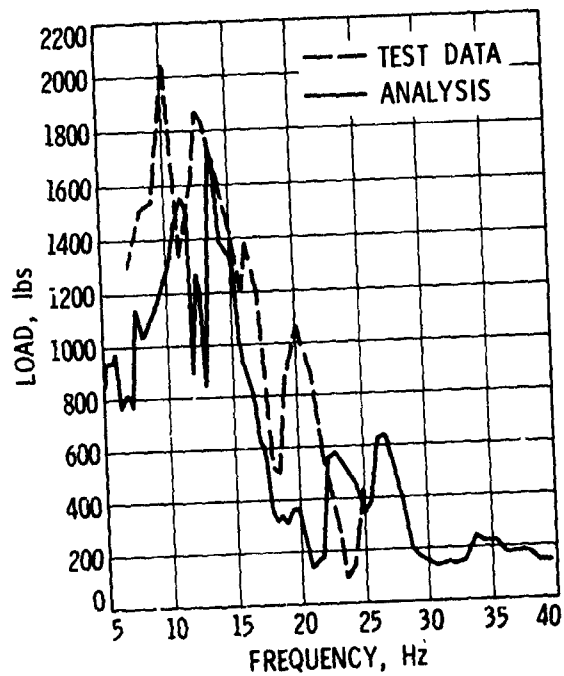


Figure 16. Orbiter Member No. 36 Response

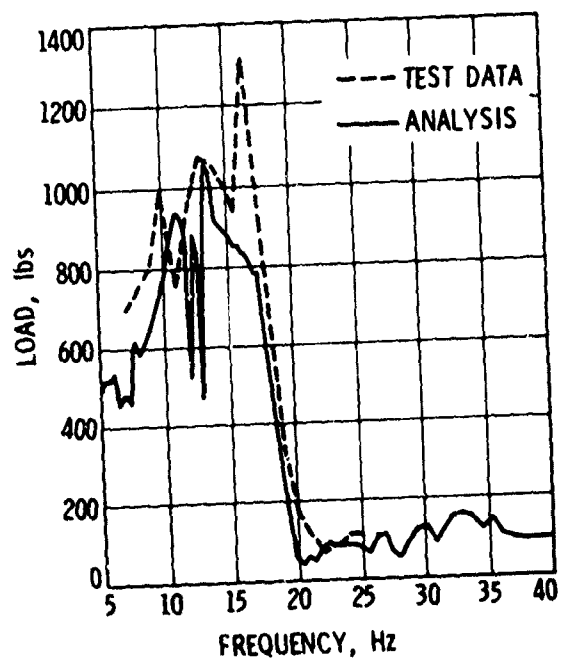


Figure 17. Orbiter Member No. 40 Response

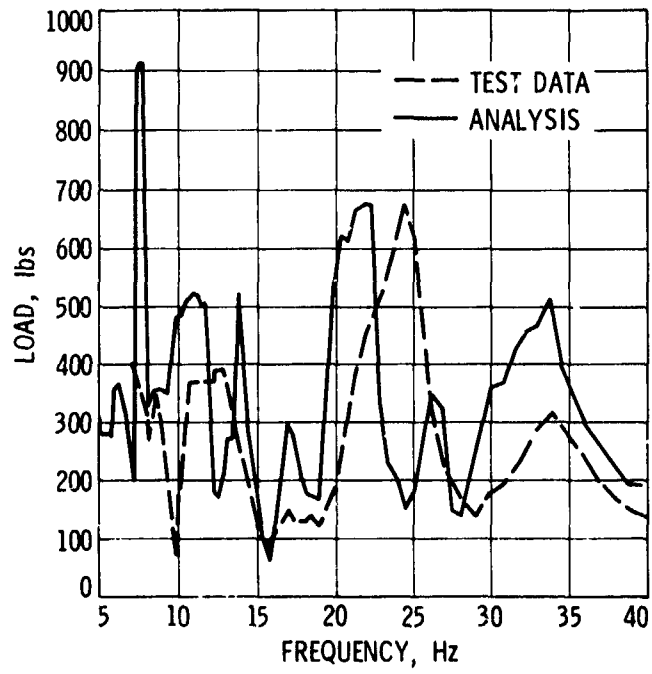


Figure 18. Orbiter Member No. 753 Response

REFERENCES

1. Wada, B.K., "Viking Orbiter - Dynamics Overview", paper presented at the 44th Shock and Vibration Symposium, December 4-7, 1973, Houston, Texas.
2. Fortenberry, J.W. and Rader, P., "Fail Safe Forced Vibration Testing of the Viking 1975 Developmental Spacecraft", paper presented at the 45th Shock and Vibration Symposium. Also published as JPL Technical Memorandum No. 33-689.
3. W. C. Hurty: Dynamic Analysis of Structural Systems by Component Mode Synthesis. Technical Report 32-350, Jet Propulsion Laboratory, Pasadena, California, January 15, 1964.
4. W. A. Benfield and R. F. Hrudá, "Vibration Analyses of Structures by Component Mode Substitution". AIAA J. Vol. 9, No. 7, July 1971, pp. 1255-1261.
5. Wada, B.K., Garba, J. A., and Chen, J. C., "Development and Correlation: Viking Orbiter Analytical Dynamic Model with Modal Test", paper presented at the 44th Shock and Vibration Symposium, December 4-7, 1973, Houston, Texas. Also published as JPL Technical Memorandum No. 33-690.
6. Leppert, E. L., Wada, B.K., and Miyakawa, R., "Modal Test Results of the Viking Orbiter", paper presented at the 44th Shock and Vibration Symposium, December 4-7, 1973, Houston, Texas. Also published as JPL Technical Memorandum No. 33-688.
7. Bamford, R. M., Wada, B.K., and Gayman, W. H., Equivalent Spring-Mass System for Normal Modes, Technical Memorandum 33-380, Jet Propulsion Laboratory, Pasadena, California, February 1971.
8. Wada, B.K., Bamford, R. M., and Garba, J. A., "Equivalent Spring Mass: A Physical Interpretation" Shock and Vibration Bulletin No. 42, Part 5, January 1972, pp. 215-225.

Fail Safe Forced Vibration Testing of the Viking 1975 Developmental Space Craft*

James W. Fortenberry
Jet Propulsion Laboratory
Pasadena, California

and

Paul Rader
Martin Marietta Corporation
Denver, Colorado

The vibration test program conducted on the Viking 1975 spacecraft represented a challenging, coordinated task for the analyst and the test engineer. To insure that test peculiar failures of the spacecraft would not occur, two main criteria were used:

- (1) Vibration input to the test specimen would be controlled so that loads in primary structure members would not exceed analytically predicted flight loads.
- (2) The number of loading cycles on selected primary structure would be monitored for cumulative damage ratios, a measure of possible fatigue damage to the structure.

To meet these criteria, a 36 channel control and 60 channel limit system were utilized along with over 200 other dynamic signals. Control system limitations, including switching capability and overshoot, are described. An analog/digital process was used for computation of member loading, bending moments, and cumulative damage ratios.

Considerable doubt existed as to the feasibility of mounting such a large structure on a shaker and maintaining adequate control of the test. The height of the spacecraft coupled with its C.G. offset would cause large overturning moments. In addition, control system limitations observed on previous testing of another spacecraft with similar response characteristics (narrow bands with high amplitudes) had resulted in damage to the structure. Accordingly, a response analysis of the entire test set-up and control system experiments preceded actual test implementation.

The effects of test philosophy on the development of the vibration control system are presented. Structural design of the spacecraft was accomplished using loads analyses based on statistical evaluation of previous Titan Booster flights. Since the Viking was "tailored" to meet a specific, limited launch environment, the standard practice of vibration testing the structure to a large number of loading cycles was rejected. This approach was reinforced by the fact that portions of the Orbiter structure were scheduled for static testing to ultimate load levels following the vibration test.

*This paper presents the results of one phase of research carried out at the Jet Propulsion Laboratory, California Institute of Technology, under Contract No. NAS 7-100, sponsored by the National Aeronautics and Space Administration. The Langley Research Center is Project Manager for the overall Viking Project; JPL is responsible for the Orbiter; MMA is responsible for the Lander.

SUMMARY

The Viking Mars Lander 1975 dynamic test model and Orbiter developmental test model were subjected to forced vibration sine tests in November - December, 1973, at JPL's dynamic test facility. Flight acceptance (FA) and type approval (TA) test levels were applied to the spacecraft structure in a longitudinal test configuration using a 30,000 -lb force shaker. Testing in the two lateral axes (x, y) was performed at lower levels using four 150 -lb force shakers.

The objectives of the stack* test series were to:

- (1) Evaluate the effect of Lander/Orbiter interaction on response at subsystem/component locations.
- (2) Evaluate the adequacy of the Viking Mars Lander 1975 dynamic test model (LDTM)/Orbiter developmental test model (ODTM) secondary structure.
- (3) Serve as a precursor to the proof test Orbiter (PTO) forced vibration test, and evaluate PTO test levels.
- (4) Evaluate component sinusoidal test levels.
- (5) Obtain data for comparison to analytical results.

Forced vibration qualification (TA) test levels were successfully imposed on the spacecraft at frequencies down to 10 Hz. JPL test equipment and methods have been adequately checked out for use on the proof test Orbiter.

Measured responses showed the same character as analytical predictions, and correlation was reasonably good. Because of control system test tolerances, Orbiter primary structure generally did not reach the design load limits attained in earlier static testing.

A post-test examination of critical spacecraft structure disclosed no apparent damage to the structure as a result of the test environment.

PRE-TEST ANALYSES

Significant analytical efforts were expended to provide assurance that test peculiar failures of primary structure should not occur, and to aid in test implementation since the complexity, scope, and tight schedule of the stack test left no time for surprises or emergencies.

The analyses were divided into four categories; test fixtures, overturning moment, response or test simulation, and fatigue damage.

*The mating of the Lander on the top of the Orbiter for vibration testing became popularly known as the "Stack Test".

TEST FIXTURE ANALYSIS

The predesign of the magnesium longitudinal axis test fixture (Figures 1, 2) was evaluated as a first step in the analysis of the stack test setup. The objective of this analysis was to determine characteristics of the basic fixture and to ascertain the level of fixture representation required for the response analysis.

The analytical configuration consisted of a simplified 12-degree-of-freedom (DOF) model of the spacecraft (6 DOF each for Lander and Orbiter) combined with a dynamic model of the test fixture. The Viking Lander Capsule Adapter (VLCA) and Viking Spacecraft Adapter (V-S/C-A) were elastically modeled. The fixture was considered fixed at the base of its core.

Two types of analyses were performed: static and modal. Static loads applied to the combined system yielded only a qualitative estimate of the fixture strength since boundary conditions were not represented in this analysis. Modal analysis was performed on the combined fixture/spacecraft model and also on the spacecraft model cantilevered from the base of the V-S/C-A. The comparison of combined system modes with cantilevered spacecraft modes gave an indication of fixture rigidity.

The first fixture mode (torsional) occurred at 36 Hz, with five additional modes between 100 and 200 Hz. Since a design goal was to keep fixture resonances close to 200 Hz, considerable changes were made to the proposed test setup. These modifications included a pair of V-type hydrostatic bearings at one location around the fixture. A further refinement of the analysis disclosed that the addition of torsional restraint flexures did not contribute enough stiffness to be cost-effective. The results are summarized in Table 1.

Overturning Moment

Early in the program, it became apparent that the longitudinal test buildup, its stack height coupled with the spacecraft C.G. offset, would be subject to large overturning moments. Estimates of these moments ranged from 500,000 to 1,000,000 lb-in applied to the Viking Transition Adapter (VTA)/test fixture interface.

For this analysis, the Orbiter elastic model was coupled to a rigid lander. This combination, in turn, was mated to a rigid longitudinal fixture model restrained at three locations by hydrostatic bearings of known stiffness. The results of the analysis offered the first positive indication that the stack test could be implemented. Angular deflection limits of the shaker armature, a source of concern, were shown to be no problem.

In addition, reaction forces on the hydrostatic bearings and the forces applied to the fixture were computed and used to perform a stress/fatigue analysis of the fixture and check the bearing adequacy. These same moment



Fig. 1. View from floor of Viking 75 LDTM/ODTM Longitudinal (Z) Axis Test Set-up

reaction forces were applied to the piers supporting the bearings to check their stability

Test Simulation, Responses Analysis

Response analysis of the test setup was required for the following reasons:

- (1) To obtain an estimate of the test environment, i.e., identify member loads and locate accelerometers at critical response points
- (2) To evaluate shaker force requirements and control levels

- (3) To provide reaction forces for fixture design.

- (4) To provide an estimate of the spacecraft fatigue capability

The analysis followed an evolutionary pattern and was accomplished in phases since both LDTM and ODTM elastic models were being revised and upgraded. A comparison of the characteristics of each phase is shown in Table 2 for longitudinal excitation.

Simulation of lateral axis excitation was noteworthy because of a change in test philosophy. Preliminary analysis had indicated

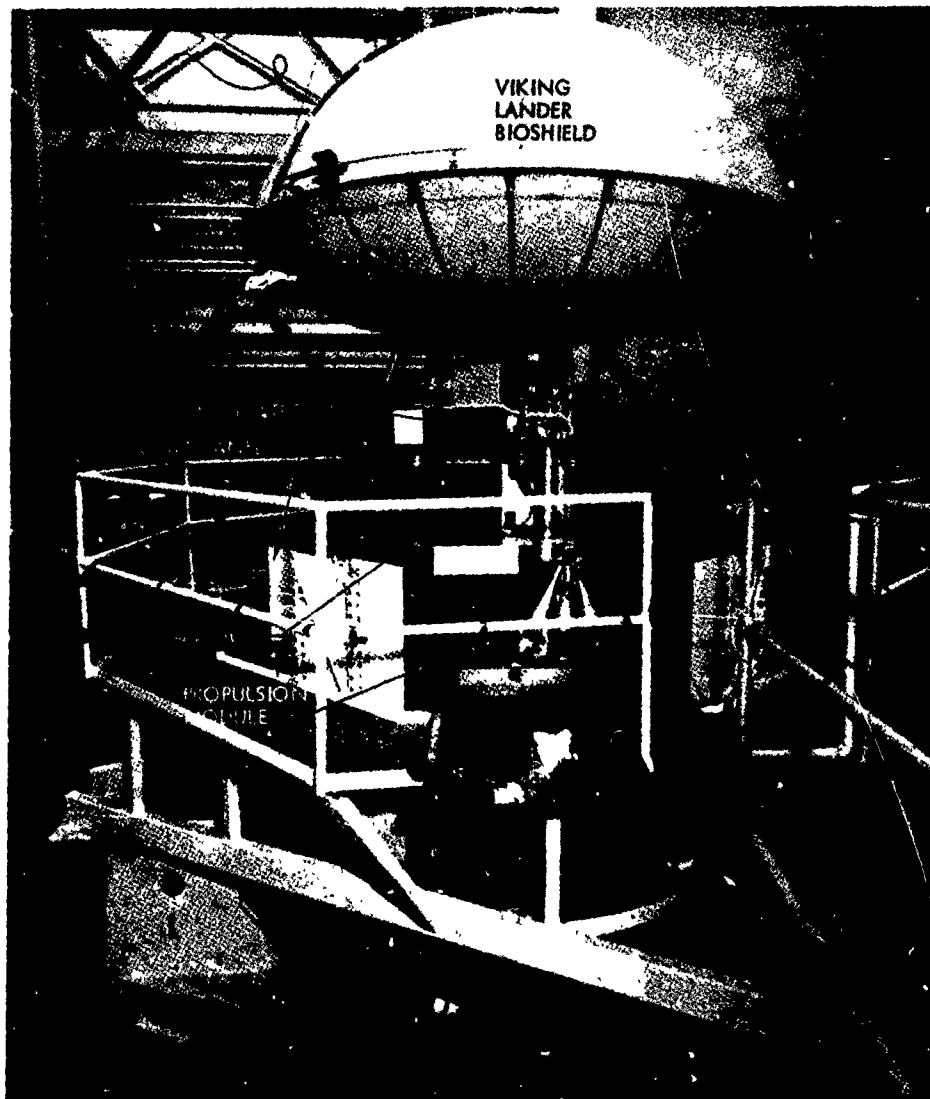


Fig. 2. View from balcony of Viking 75 LDTM/ODTM Longitudinal (Z) Axis Test Set-up

excessive coupling of the lateral and torsional modes of the spacecraft. This was due to the combination of spacecraft C.G. offset and the application of unrestrained driving forces at the bus main longerons. As a result, an intermediate analysis using restrained or guided input forces was performed; it appeared to solve the coupling problem at all but the lowest frequencies (5-10 Hz). In this bandwidth, analysis indicated that the driving forces required were so small that control might be difficult to achieve.

However, objections were raised over the restraint of spacecraft torsional motion due to the massive lateral test fixture connected to

the Ling 249 shaker. The fixture was to be constrained by hydrostatic bearings to move only in one plane. As a result, the test team was directed to seek a lateral driving scheme with minimum restraint. The final choice consisted of using four 150-lb shakers.

Estimate of Fatigue Damage

The objective of the fatigue analysis was to monitor and enable prediction of possible fatigue damage so that vibration test levels could be controlled to prevent cracks from forming in the ODTM primary structure.

Table 1. Test Fixture Modes as a Function of Design Iteration

Fixture Mode	Frequency, Hz		
	Initial Design	V-Bearing plus Lower Ring	Torsional Restraint Flexures
First Torsion	36	109	130
Lateral Translation	102	122	122
Second Torsion	147	177	183
Longitudinal Translation	199	209	209

Table 2. Comparison of Two Phases of Response Analysis (longitudinal)

Analysis Component	Phase I	Phase II
Lander	Rigid	Elastic Model
Fixture, Shaker	Not included, space-craft cantilevered at base of V-S/C-A	Shaker modeled, fixture assumed rigid (5-40 Hz), hydrostatic bearings included
Propellant tanks	Flight mass simulation	Test mass simulation (referee fluids)
Orbiter	Elastic model 7, no VTA, solar panel dampers	Elastic model 8, no VTA, solar panel dampers

The cumulative damage ratio (CDR) used to determine fatigue damage can be stated as

$$CDR = \frac{n}{N} \leq 0.20$$

where n = number of cycles experienced at a particular stress level and N = allowable number of cycles at that same stress level. The number of cycles n in any frequency bandwidth is given by the expression

$$N = \frac{6.0 \Delta f}{\lambda \ln 2}$$

where Δf = bandwidth (Hz) and λ = sweep rate (oct/min).

The CDR of 0.20 (failure is assumed at 1.00) was felt to be conservative yet generally consistent with prevailing practice in industry at present. Since the CDTM was scheduled for ultimate static testing following the vibration test, every effort had to be made to assure a healthy test structure. The analysis, performed in two phases, consisted of the following basic steps:

- (1) Identification of critical primary structure
- (2) Survey of parts for material, notch-sensitive areas.

- (3) Compilation of S/N curves, derivation of curve fitting equations.
- (4) Obtaining loading spectrum (predicted or test).
- (5) Computation of CDR's

Phase 1 of the analysis was designed to take computer-generated (response analysis) loads combined with geometric and material properties and compute the CDR. Phase 2 did the same but was designed to accept test data in digitized format. In addition, the contribution of each frequency interval to the total CDR for the member was to be output.

Phase I was accomplished as intended. Phase 2 fell prey to equipment limitations. Namely, reliable manipulated load data could not be provided in digitized format. The effort of converting the analog signals of the tapes to digital form was finally abandoned in favor of the analog setup shown in Figure 3.

The net result of the fatigue analysis was that the ODTM possessed substantial margin to withstand a moderate number of FA and TA level vibration sweeps without exceeding the CDR of 0.20. This provided considerable confidence in the conduct of the test since earlier approximate analyses had indicated potential problems in the VLCA and bus main longerons. This confi-

dence was borne out when a rigorous post-test dye-penetrant examination disclosed no apparent fatigue cracks.

TEST PROGRAM

TEST SPECIMEN

The test article consisted of the following major hardware assemblies:

- (1) LDTM
- (2) ODTM
- (3) Viking transition adapter (VTA).

Major assemblies of the LDTM/ODTM were of flight-configured hardware wherever possible. Mass mockups or simulators had inertial properties similar to the components being replaced. Thermal control hardware such as louvers and blankets was not used on the ODTM.

Pressurized systems on the LDTM consisted of the bioshield and propellant tanks. The bioshield was pressurized to 1.0 ± 0.9 in. of water during testing. The lander propellant tanks were filled with referee fluids and pressurized to 20 psig with gaseous nitrogen. This pressurization was maintained throughout the entire test series.

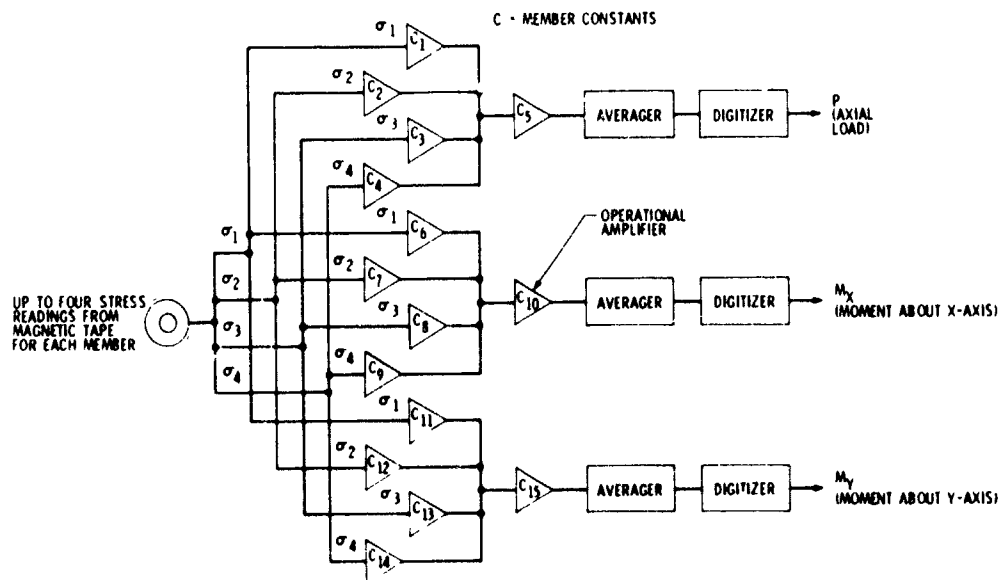


Fig. 3. Analog computation of loads

ODTM Propulsion Module Mass Configuration, 70° F

Tank	Referee Fluid	Fluid, Weight, lb	Ullage %	Pressure psia
Oxidizer	Freon TF	2,063	16.8	105
Fuel	Isopropyl Alcohol	1,112	10.1	105
Pressurant	-	-	-	Atmospheric

The only active pressurized subsystem on the ODTM was the propulsion module (PM), which was configured as shown above.

IMPLEMENTATION

1 Longitudinal Test Setup

The final longitudinal test configuration is shown in Figures 1 and 2. Excitation was provided by a Ling 249 30,000-lb force shaker. The interface between the shaker and the VTA was provided by the test fixture. The test fixture, a welded magnesium structure, was stabilized by a restraining system consisting of three steel piers on which hydrostatic bearings were mounted (Fig. 4). The bearings allowed vertical movement only, while the piers provided the reaction points for the spacecraft overturning moment predicted by response analysis.

The total weight of the reaction system was in excess of 43,000 pounds. The piers were structurally tied together by two twelve inch steel channels and a four by eight inch steel box section. As can be seen in Figures 1 and 2, the two channels were parallel and located near the lower bearing on each pier. The box section was used to tie the tops of the piers together. Thus, by virtue of the above members, a large triangular structure was formed with a reaction pier at each vertex.

Additionally, the piers were hard mounted to the floor. Four tabs were welded onto the base of each pier. These tabs were used to secure the piers to the concrete reaction mass with 3/4 inch screws.

The combined weights of the LDTM/ODTM and the test fixture (10,000 lb) would have caused excessive deflection of the shaker armature, preventing normal operation. Pneumatic springs with a resonant frequency of approximately 2 Hz (Barry Serva-Levels, Fig 5) were mounted on the shaker body at 120-deg intervals. A position control servo regulated the springs' air volume and positioned the shaker armature at the center of its stroke under static conditions.

Experimentation with the shaker indicated a trunnion resonance of approximately 12 Hz when the shaker was suspended on its isolation pads. Blocking the shaker or lifting the

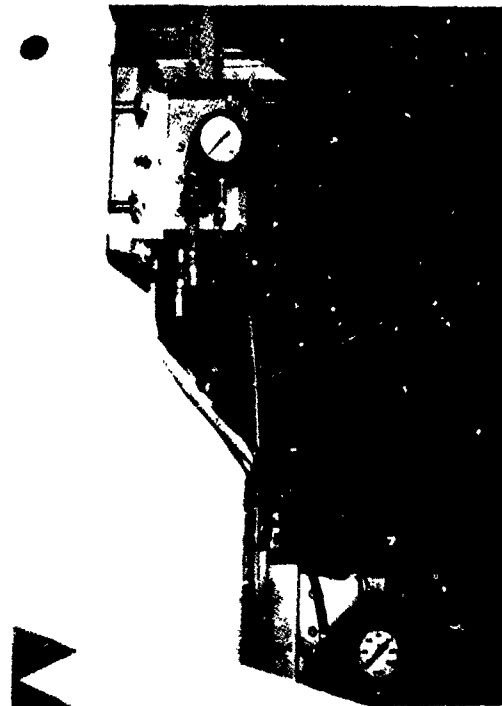


Fig. 4. Typical Hydrostatic Bearing Installation

trunnions off the isolation pads increased this frequency to 35 Hz. Further experimentation and analysis demonstrated the potential danger of sweeping through the trunnion resonance; i.e., undesirable coupling of the spacecraft and fixturing could occur. Therefore the shaker was blocked for all tests below 25 Hz by inserting shims between the shaker body and steel posts hard-mounted to the seismic mass (Figure 6). For testing above 25 Hz, the shims were removed.

2 Lateral Test Setup

Following longitudinal testing, the LDTM/VICA combination was demated from the ODTM.



Fig. 5. Pneumatic Spring Support System



Fig. 6. Shaker Body Blocking System

bus and set aside. The remainder of the test specimen, which included the ODTM, V-S/C-A, and VTA was then lifted as a unit and placed in the modal test tower, and the LDTM/VLCA was mated to the test assembly. The test setups for lateral excitation in the X- and Y- axes are illustrated in Figures 7 - 9.

Excitation of the LDTM/ODTM in each axis was accomplished with four Unholtz-Dickie electrodynamic shakers, each rated at 150-lb force. The shakers were pendulously supported

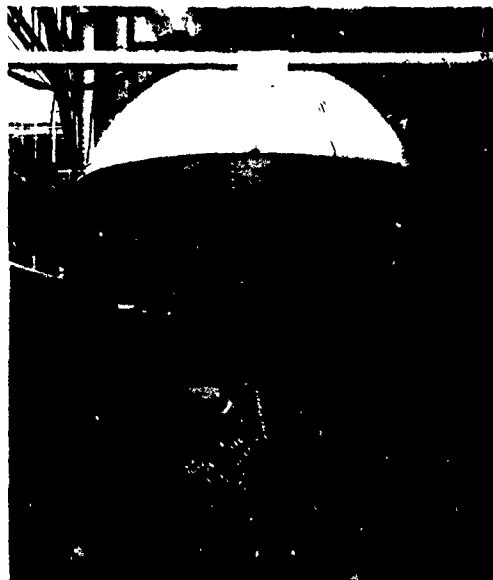


Fig. 7. Overall view of Viking 75 LDTM/ODTM Y Axis Lateral Test Set-up

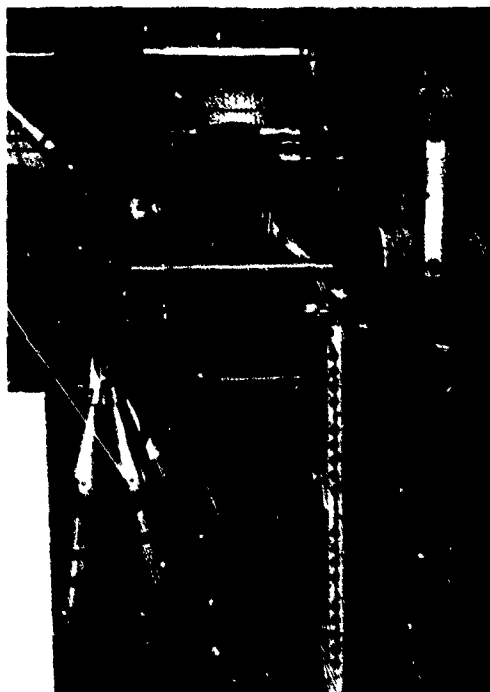


Fig. 8. Shaker No. 12, Stinger, Mechanical fuze, and ODTM Bus Longeron Attachment (Y Axis).

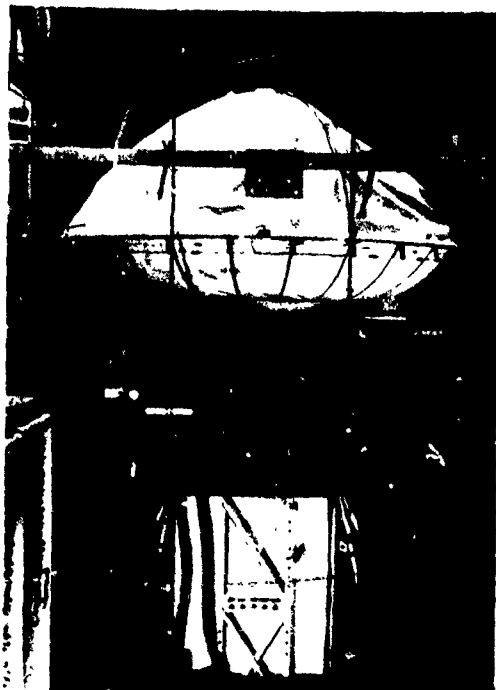


Fig. 9. Overall view of Viking '75 LDTM/ODTM X Axis Lateral Test Set-up

from crane hooks and chain and attached to the ODTM bus main longerons through adjustable "stingers" and mechanical fuses (flexures).

3. Test Levels

Low-level test runs were made prior to full-level testing. (Tables 3, 4). From these precursor runs, the responses of critical

structural elements or components were evaluated by analysis of O-graph plots, X-Y tracking filter plots, and the analog computer program that generated ODTM member loads. Comparison of these data with response analysis predictions provided confidence in the test structure to withstand full-level loading

4. Vibration Control

Control of the longitudinal vibration input to the LDTM/ODTM was accomplished with a 36-channel peak select system. The peak select control system continuously monitored the output signals of 12 input control accelerometers located on the ODTM bus structure main longerons (Fig. 10) plus a 24-channel mix of strain-gage/accelerometer response transducers. Bolted attachment was mandatory for the input control accelerometers.

The acceleration input to the test structure was controlled on the one transducer whose output signal matched its peak select setting. A functional diagram of the control system is shown in Figure 11.

A 59-channel peak limit system was used. This safety circuit terminated the output of the vibration exciter without transient if the instantaneous peak magnitude of any of the 59-peak limit settings exceeded a preset value. Because of test philosophy/hardware differences, the peak limited signals assigned to the LDTM were passed through a 200-Hz filter prior to reaching the protection module. Those channels used for ODTM peak limiting were conditioned with 800-Hz filters.

The control of the lateral axis testing, in which four separate shakers were used, was accomplished in a manner similar to the longitudinal test. The four Unholtz-Dickie Model 4 150-lb shakers and associated power supply were married to the peak select control system. Because the individual shakers were carefully matched with their transformers, it was decided to control the force input on all four shakers by connecting them together in series and using the

Table 3 Forced Vibration Test Levels, Longitudinal (Z) Axis

Level	Amplitude, g peak					
	25-7 Hz	22-8 Hz	22-10 Hz	200-20- 200 Hz	128-20- 128 Hz	200-128- 200 Hz
Precursor	0.5	-	-	0.5	-	-
Flight Acceptance	-	1.0	-	-	1.0	0.0012 in double amplitude
Type Approval	-	-	1.5	-	1.5	0.0018 in double amplitude

Table 4. Forced Vibration Test Levels, Lateral (X, Y) axes

Level	Test Axis	Amplitude - g peak	
		200-5-200 Hz	200-8-200 Hz
Precursor	Y	1.5 (70) ^a	-
Full	Y X	-	1.5 (125)
^a Numbers in parentheses indicate force level (lb) of each of the four Unholtz-Dickie Shakers			

armature current output signal from just one of the four shakers. This technique proved very successful.

5 Data Recording, Reduction

Control and response amplitude of the LDTM/ODTM were measured with strain gages and accelerometers (Figure 12)

274 output signals were recorded on electromagnetic tape for all test runs. In addition, approximately 48 channels of control and house-keeping data were recorded in real-time display on oscillographs for each test run. Following each test run, quick-look data reduction was accomplished and data review completed by the test team prior to proceeding to the next run.

A large number of static measurements were made on the ODTM during buildup and always following each test run. These strain measurements (approximately 140 to 175) were in printed paper tape format. Monitoring of dc offsets in this manner contributed greatly to test confidence where the integrity of ODTM structure was concerned.

6 Test Run Summary

A total of 44 separate test runs were made on the LDTM/ODTM during the period of November 5 through December 10, 1973 - a span of 24 days. Actual test runs were short - a matter of several minutes. Test preparation, control console setup, and trouble-shooting made the largest demands on the time budget.

DISCUSSION OF TEST RESULTS

DATA REDUCTION

The response characteristics of the test structure were derived from analysis of recorded test data. As originally planned, the bulk of ODTM test data on electromagnetic tape was to be reduced from analog to digitized format, manipulated by program, and output in a tab run form. During the initial test runs, it became apparent that the format specified could not be achieved because of equipment limitations in providing phase coherent digitized data.

Following a typical test run, the test team reviewed 48 channels of on-line oscillograph records. Anomalous or suspicious channels would then be patched in to an oscilloscope or high speed oscillograph for further examination. This phase of the data reduction process generally required 1 or 2 hours.

Once the test appeared acceptable, the tapes were secured and forwarded to the data analysis facility. First priority was to obtain X-Y plots of amplitude versus frequency for all control channels, followed by reduction of response channels.

The ODTM strain gage channels were run through an analog computer for derivation of member loads. These loads were averaged over several cycles to lessen transient effects and digitized to yield peak values at particular frequencies. To determine maximum stress, the axial loads and moments were added, assuming the worst combination of loading and phasing. Assessment of peak select levels and cumulative damage estimates were based on this process.

While the foregoing was being accomplished, the on-line oscillograph records were manually reduced. Control channels, peak amplitudes, and overshoot were determined and summarized for presentation to the test operations board.

Following completion of the testing, frequency vs amplitude plots were made for all LDTM/ODTM channels for FA and TA levels. This effort took over 2 months to complete.

TEST LEVELS/LOADS CONTROL

Because of control system and load limitations combined with the response characteristics of the LDTM/ODTM (narrow bands with high amplitudes), the servo control was unable to maintain a constant input acceleration at any one of the twelve control accelerometers. This was not unexpected since similar behavior had been observed in earlier spacecraft testing. In addition, studies conducted at the dynamic test facility using instrumented cantilevered beams and the proposed control hardware disclosed that control might be difficult at frequencies below 17 Hz. That is, during the switching from one control channel to another, overshoot

CONTROL ACCELEROMETERS MOUNTED ON MAIN LONGERONS			
ACC I.D.	UPPER RING	LOWER RING	DIRECTION
2-3 TOP L	✓		LONG. RADIAL
2-3 TOP R	✓		
2-3 BOT R		✓	
7-8 TOP L	✓		LONG. RADIAL
7-8 TOP R	✓		
7-8 BOT R		✓	
10-11 TOP L	✓		LONG. RADIAL
10-11 TOP R	✓		
10-11 BOT R		✓	
15-16 TOP L	✓		LONG. RADIAL
15-16 TOP R	✓		
15-16 BOT R		✓	

ADDITIONAL POSITIONS			
ACC I.D.	UPPER RING	LOWER RING	REMARKS
4-5 BOT TRI 15-15 BOT TRI 1-16 BOT TRI		✓ ✓ ✓	ACCEL TO BE MOUNTED ON BLOCKS ATTACHED TO CHASSIS FACE BY No. 8 SHEAR- PLATE FASTENERS

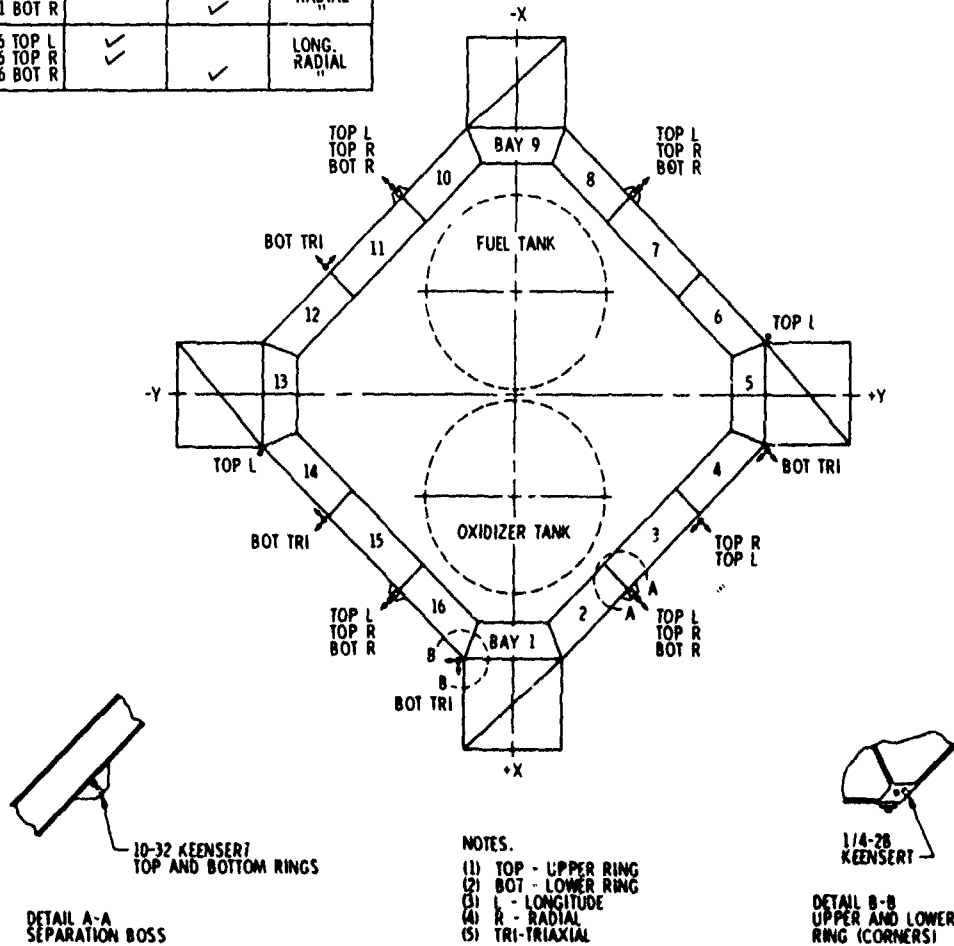


Fig. 10. Input Control Accelerometers

errors could occur resulting in a possible overshoot. Overshoot is defined as the maximum observed test amplitude greater than the desired peak select control level.

Two basic sources contribute to overshoot: RC time constant of ac to dc conversion and deadband. The time constant is simply the time required to convert the ac signal from the transducer into a dc voltage. This is done in two places; the ACS-6 (peak selector) and in the

servo. The time constant is a function of frequency and is longer at low frequency than high. Deadband may be defined as the amount that one signal must exceed another in order to cause a switch of the ACS-6 output from the latter to the former. Of the above two overshoot sources, the RC time constant was the more significant.

Although a definitive model of the control system capability is not available, the overshoot

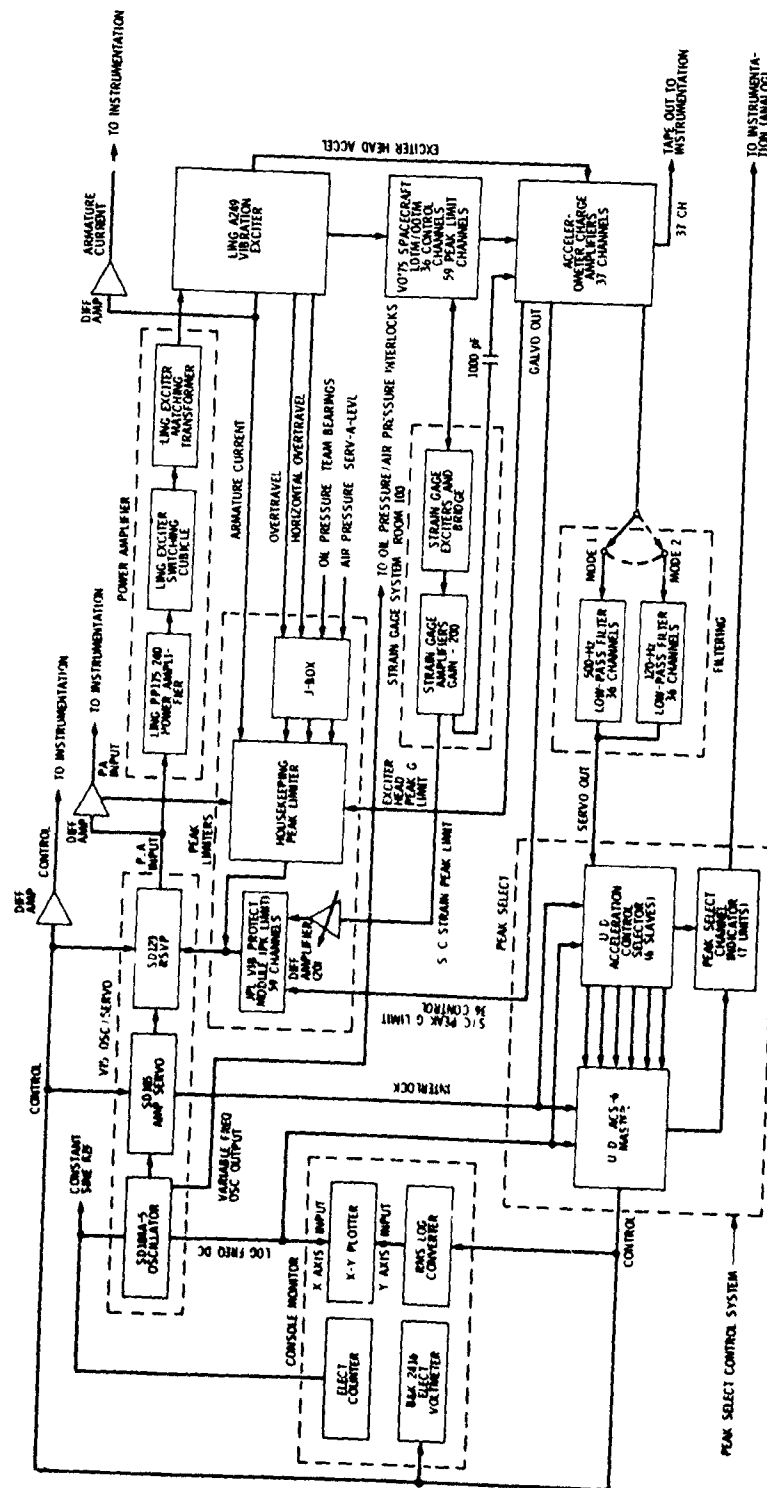


Fig. 11. Schematic of Longitudinal Axis Control System

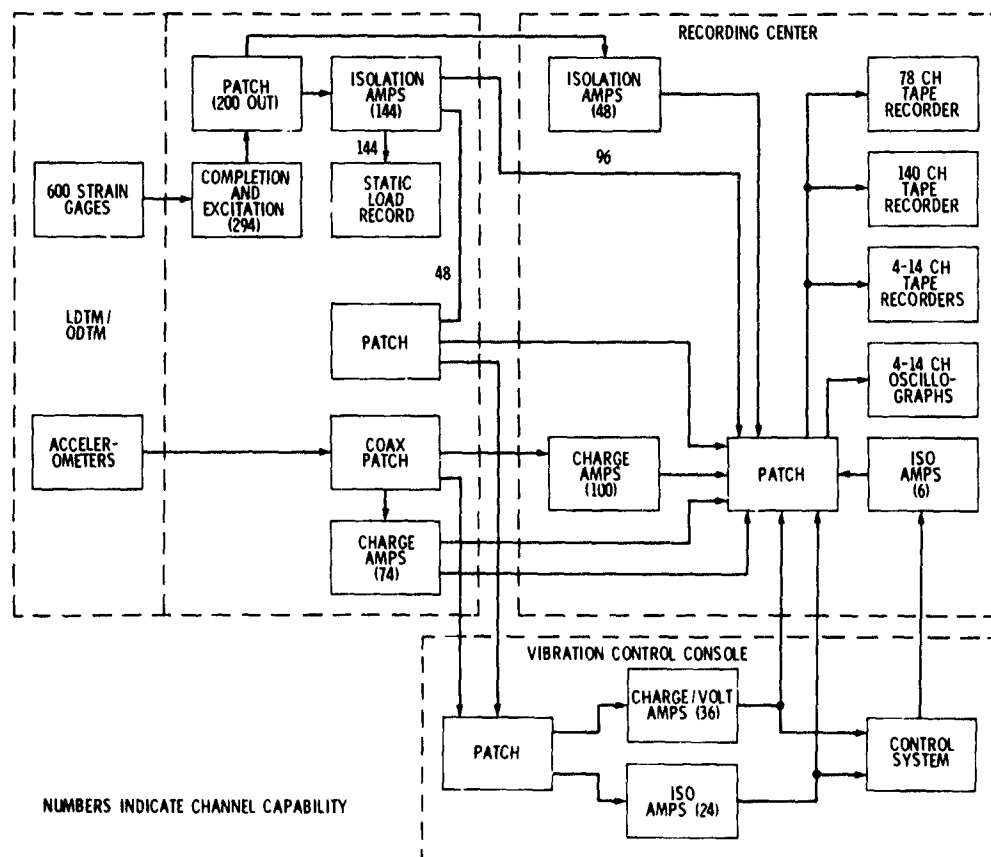


Fig. 12. Instrumentation Flow

appeared to be dependent on the following parameters:

- (1) Resonant frequency.
- (2) Slope or Q of the resonance.
- (3) Sweep rate.
- (4) Direction of sweep (up or down)

Significant overshoots were observed during the test runs. Low-level test runs were made and the peak select control levels carefully monitored to evaluate this phenomenon. Examination of on-line oscillograph records of response control strain gages disclosed initial amplitudes of 1.00 to 1.52 times the peak select level established for these transducers. The stress values from these low-level test runs were used to derive internal loads in the ODTM structural members. The peak limit and peak select load values were established based on these low-level runs and applied to full FA and TA test levels.

RESPONSE MEASUREMENTS

All forced vibration test runs on the LDTM/ODTM were controlled by ODTM bus input accelerometers or by various strain-gage/accelerometer response measurements. A typical run showing the effects of response control on the input levels at the ODTM bus is shown in Figure 13. Examples of comparisons of analytical and measured response values are shown in Figure 14 through 17.

The response analysis of the coupled LDTM/ODTM math models was very helpful in estimating potential response control channels. Examination of Table 5 gives an approximate indication of the actual versus predicted control channels. At first glance, it would appear that the correlation is not good. However, the agreement between analysis and test is better than casual observation indicates for the following reasons:

- (1) These frequencies marked (1) represent conditions where the terminal descent (TD) tank peak select levels

Table 5. LDTM/ODTM Forced Vibration Test Comparison of Control Channels for Longitudinal Axis Testing

Approximate f, Hz	FA Testing (40-8 Hz)			TA Testing (40-10 Hz)		
	Control	Predicted by Analysis		Control	Predicted by Analysis	
		Yes	No		Yes	No
40	140-S, upper plane truss	X		140-S, upper plane truss	X	
39	140-S, upper plane truss	X		140-X, upper plane truss	X	
38	DE-079 TD tank			DE-082 TD tank		(1)
37	DE-079 TD tank			DE-082 TD tank		(1)
36	DE-079 TD tank			DE-082 TD tank		(1)
35	DE-079 TD tank			DE-082 TD tank		(1)
34	128-S, upper plane truss	X		DE-082 TD tank		(1)
33	128-S, upper plane truss	X		128-S, upper plane truss	X	
32	128-S, upper plane truss	X		128-S, upper plane truss	X	
31	128-S, upper plane truss	X		128-S, upper plane truss	X	
30	Control No. 5			128-S, upper plane truss	X	
29	134-S, upper plane truss			Control No. 2	X	
28	134-S, upper plane truss			Control No. 2	X	
27	128-S, upper plane truss	X		128-S, upper plane truss		X
26	DE-052, equipment plate	X		128-S, upper plane truss		X
25	DS-330, payload adapter			DE-082 TD tank	X	
24	DS-333, payload adapter			DE-082 TD tank	X	
23	289-S, bedframe	X		Control No. 2	X	
22	DS-330 adapter			289-S, bedframe		X
21	DS-330, adapter	X		DE-082 TD tank	X	
20	DS-333 payload adapter			Control No. 4		(3)
19	288-S bedframe	X		289-S bedframe	X	
18	289-S bedframe	X		289-S bedframe	X	
17	289-S bedframe		X	Control No. 4	X	
16	295-S bedframe	X		295-S bedframe	X	
15	295-S bedframe	X		295-S bedframe	X	
14	295-S bedframe		X	295-S bedframe		X
13	295-S bedframe		X	295-S bedframe		X
12	295-S bedframe		X	295-S bedframe	X	
11	Control No. 4	X		Control No. 2	X	
10	Control No. 4	X		Control No. 2	X	
9	8-S, VLCA	X				
8	Control No. 1	X				
Total		8	14	11	14	6

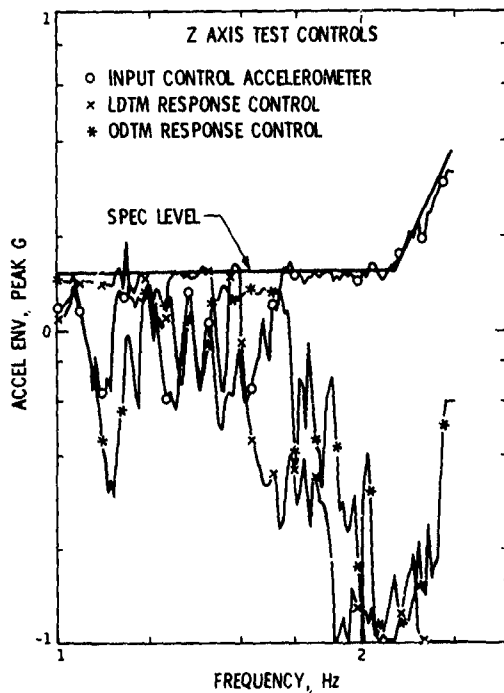


Fig. 13. LDTM/ODTM stack test, TA level downsweep controls

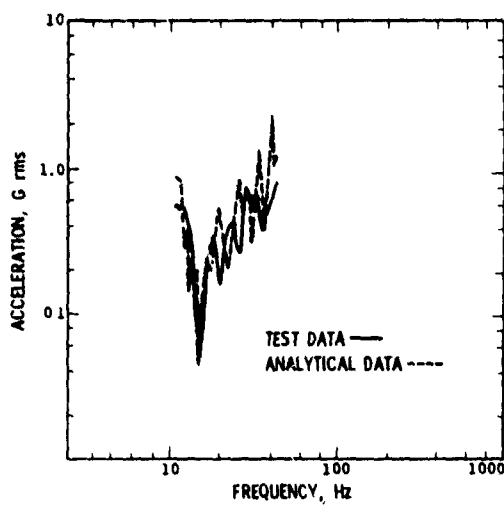


Fig. 14. Run 116-4 Down Sweep, 117-4 Down Sweep Measurement 111A (VTA Input) and DOF 1003

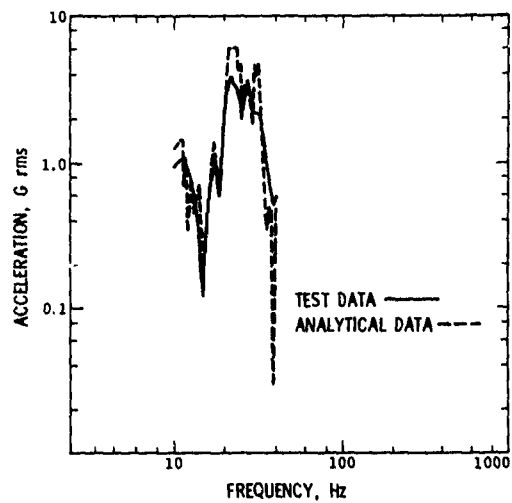


Fig. 15. Run 116-4 Down Sweep, 117-4 Down Sweep Measurement DE-052-LB-X (Equipment Plate) and DOF 97

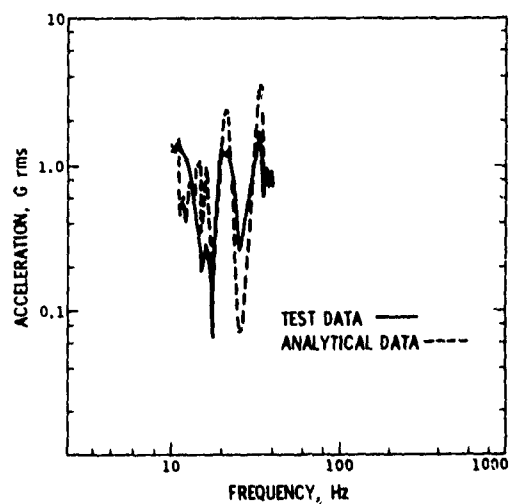


Fig. 16. Run 116-4 Down Sweep, 117-4 Down Sweep Measurement DE-061-LB-X (TD Engine 1) DOF 172

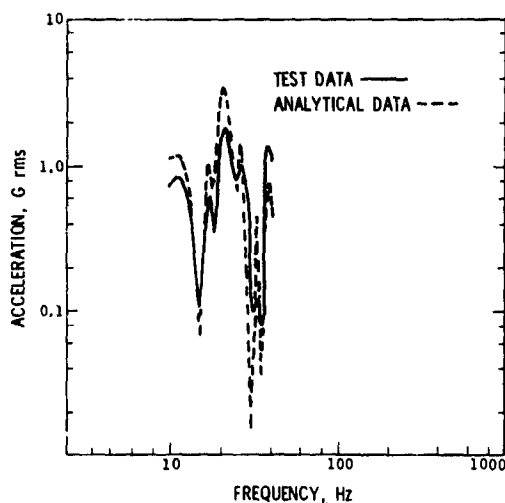


Fig. 17. Run 116-4 Down Sweep, 117-4 Down Sweep Measurement DE-064-LB-X (TD Engine 2) DOF 184

were set substantially lower than the values used in the analysis. Consequently, the TD tanks were biased to attain greater control during actual testing. The sensitivity of the control system to lower TD tank control levels is demonstrated by comparison of the FA and TA runs in the table. DE-079 used in the FA tests was replaced by DE-082, with a peak level setting approximately 80% of its initial TA level. This channel assumed control so effectively that no other Lander controls appeared in the TA switching sequence.

- (2) The (2) notation in FA testing represents Lander payload adapter strains that were never included in the response analysis.
- (3) Precision in determining exactly when a control accelerometer will take over (other than for rigid-body modes) is beyond the capability of present analysis. This is particularly true when the actual control system constraints are considered (i. e., overshoots, time constants, etc.).

- (4) The upper plane truss 134-S was shown by analysis to be at 80% of its limit.

Typical measured load values have been compared with their analytical counter parts. Based on that sample, 50% of the measured frequencies were higher than predicted and 50% lower. Approximately two thirds of the measured loads were somewhat lower than predicted values. This was not unexpected because of the tolerances used in establishing peak limit/select values; i. e., the analysis limits did not include test tolerances.

Examination of typical response accelerations reveals that measured frequencies were usually higher than those predicted by analysis. Amplitudes were generally lower than predicted by approximately that amount established by test tolerances.

CONCLUSIONS

The results of the Viking 75 LDTM/ODTM test are summarized as follows:

- (1) Test implementation went better than anticipated. This was due, in large part, to the pre-test analyses and careful preparation leading up to the test.
- (2) Forced vibration qualification levels were successfully imposed on the LDTM/ODTM structure. Load levels generally did not reach design load limits attained in static testing because of the control system test tolerances.
- (3) Test predictions based on the Viking mathematical model correlated reasonably well with the test data. In general, test frequencies were slightly higher than analytical predictions and amplitudes lower. This further demonstrates that the coupled Viking spacecraft mathematical model has no major errors.
- (4) JPL test equipment and methods have been checked out for use on the proof test Orbiter. The test was controllable down to 10 Hz at TA levels.

A METHOD FOR DETERMINING TACTICAL MISSILE
JOINT COMPLIANCES FROM DYNAMIC TEST DATA

John G. Maloney and Michael T. Shelton
General Dynamics Corporation
Pomona, California

This paper discusses a method for extracting joint compliances from measured tactical missile elastic mode test data. The method is based on varying the compliance values such that a quadratic function of the differences between theoretical and experimental eigenvalues and eigenvectors is minimized. An application of the method is presented in which the flexural compliance values of four joints are extracted from a set of measured tactical missile bending modes.

NOMENCLATURE

F	= Cost Function of Error Terms	k'	= Intermediate Spring Rate Used in Computing the Second Order Derivatives of F
N_e	= Number of Experimental Modes	r	= Intermediate Step Size Used to Obtain k'
\sum	= Summation on Index i	$\text{sgn}()$	= The Sign of $()$
ω	= Mode Frequency	ϵ	= Relative Error Size
x	= Mode Shape	λ	= ω^2 = Eigenvalue
w	= Weighting Factor	m	= Mass of Missile
$()^T$	= Transpose of $()$	e	= Experimental
K	= Stiffness Matrix	t	= Theoretical
M	= Mass Matrix	x	= Mode Shape
N	= Number of Internal Stations in Model	f	= Frequency
k	= Unknown Spring Components	i, j, l, m	= Indices or Counters
n	= Iteration Number		
θ	= Step Size		
∇F	= $\frac{\partial F}{\partial k}$ = Gradient of F		
S	= Step Size		
$[]^{-1}$	= Inverse of $[]$		
δ_{ij}	= Kronecker Delta $\begin{cases} = 1 & i = j \\ = 0 & i \neq j \end{cases}$		
K	= Matrix of Known Spring Elements		
N_j	= Number of Joints		
U	= Strain Energy		
x_j, x_j'	= Slope to the Left and Right of Joint j		

INTRODUCTION

The modular configuration approach commonly employed in designing tactical missiles results in the use of numerous separable airframe joints. The number of separable airframe joints that are used on a sampling of tactical missiles are shown below.

Missile	Number of Joints
Redeye	4
Sidewinder	4
Shrike	4
Standard	5
Sparrow	4

The compliance of these joints, and in particular the flexural compliances, play an important role in missile structural dynamic response characteristics. Exploitation of the modular missile design concept often results in the need to determine joint compliances for subsequent dynamic response modeling for new module combinations or module configurations. However, the behavior and complexity of most airframe joint designs is such that they are not amenable to simple analytical modeling techniques. Experimental determination of joint compliances is therefore commonly used. The experimental approach generally involves dynamic testing rather than static testing because the behavior under the small deflections associated with missile elastic mode response are of interest.

The method of determining compliances from dynamic test data that will be presented is referred to as the joint compliance extraction technique. This method has been applied to test data originating from two different test approaches. The first test approach utilizes special hardware embodying a single type of joint while the second test approach uses the actual tactical missile, with all of its airframe joints, for the test hardware. The two test techniques will be presented first followed by details of the joint compliance extraction technique. The material presented is drawn from a study entitled "Structural Dynamic Properties of Tactical Missile Joints" sponsored by the Naval Air Systems Command.

SINGLE JOINT TYPE TEST METHOD

The first test method approaches the problem by minimizing the number of unknowns and uncertainties. The method consists of fabricating special hardware that places a single type of joint at the midspan of the assembly. The remainder of the test assembly consists of tubular members with known physical properties. A sketch of an idealized test specimen is presented in Figure 1. The desirable attributes that this hardware embodies are known boundary conditions, known mass and stiffness distributions (except for the stiffness of the single joint), and high resolution on the effects of the joint compliance. A minor variation in the hardware configuration, that can be used if the joint happens to be located on either end of a long uniform section such as a rocket motor, places two joints of the same type near the midspan of the assembly. The motivation for this is that the only special hardware needed consists of a short adapter to join the two uniform sections.

The test approach embodying a single type of joint has been applied to three different joints. The three test assemblies utilizing a 2.75 inch diameter threaded coupling ring joint, a 5.0 inch diameter Marmon clamp joint and a 13.5 inch diameter shear bolt joint are illustrated in Figures 2, 3 and 4, respectively.

The measured mode shapes and frequencies are presented in Figures 5, 6 and 7. The theoretical mode shapes and frequencies produced by the joint compliance extraction technique (which will be presented later) are also compared with the measurements in Figures 5, 6 and 7. It is seen in every case that the theoretical mode shapes and frequencies agree well with the measurements.

The three flexural joint compliances that were extracted from these test data are presented in Figure 8, where they are compared with the joint rating system of Reference (1). The joint rating system is based on the premise that the flexural compliance of a joint varies inversely as the cube of the diameter. Four categories of increasing compliance "excellent, good, moderate and loose" are used. The three values of joint compliance extracted from the test data are seen to fall in the category of "good".

MISSILE LEVEL TEST METHOD

The second method of determining tactical missile joint compliances from dynamic test data embodies testing the entire missile. This eliminates the problem of designing and fabricating special hardware to represent each joint, but the problem with this method is the actual extraction of the airframe joint compliances from the measured mode shapes and frequencies. The extraction process can be a formidable undertaking when using trial and error procedures if the test specimen contains more than two or three joints of unknown stiffness. To simplify the extraction process, a method referred to as the joint compliance extraction technique has been developed. This technique is based upon the assumption that differences between theoretical and experimental mode shapes and frequencies are due totally to uncertainties in the airframe joint stiffnesses. The assumption that the airframe stiffness distribution (except in the local region of the joints) and the mass distribution are well defined is usually a reasonable assumption for tactical missiles.

The development of the joint compliance extraction technique and the associated computer program (JOINTS) were accomplished under a Naval Air Systems Command study contract, References (2) and (3). Originally the technique employed only first order gradient terms. It worked well for a small (two degree of freedom) system, but when the method was applied to larger systems the results were disappointing. Next a second order gradient method in which the second order terms were approximated by differences was tried and techniques were developed to improve convergence of the method. This technique is now presented.

JOINT COMPLIANCE EXTRACTION TECHNIQUE

The compliance extraction technique is an

application of a general method published by Hall, et al Reference (4). Our application of the method is restricted to the case of estimating joint compliances from measured tactical missile elastic mode data.

The joint compliance extraction technique is designed to determine mechanical joint compliances of an elastic missile structure by generating the "best" least square fit between a linear lumped parameter mathematical model and a given set of experimental modal data. A major assumption in the method is that the joint compliances constitute the principal unknowns in the lumped parameter system, with both distributed mass and stiffness being precisely defined. Weighting factors which involve mode number, shape, and frequency acknowledge the existence of accuracy limitations in the test data. The joint compliances yielding a best fit are found by minimizing a quadratic function of the differences between corresponding theoretical and experimental eigenvalues and eigenvectors. This function, referred to as the cost function, is expressed as follows:

$$F = \frac{1}{2} \sum_{i=1}^M \{ W_{ie} (\omega_{ie}^2 - \omega_{it}^2)^2 + (X_{ie} - X_{it})^T W_{ix} (X_{ie} - X_{it}) \} \quad (1)$$

The frequencies and mode shapes are denoted by ω and X , respectively. The weighting factor matrix is W and the index i is the mode number. If the mode shape slopes are used, they are treated as additional components of the X 's. The subscripts e and t denote experimental and theoretical values, respectively. The minimization of the cost function constitutes a nonlinear programming problem. Optimization problems not amenable to standard methods are more the rule than the exception. In this case the optimization is accomplished by a steepest descent method. Before proceeding with a detailed discussion of the method, the structural mathematical model utilized will be described.

The fundamental structural dynamic considerations of a tactical missile are often handled with a linear lumped parameter mathematical model. More expressly, the mathematical model simulates a beam-like body with a series of lumped masses connected by weightless beams. Discrete shear, compressive, torsional, and flexural springs may be included at any point in the model. The model can be used to analyze bending, torsion, and longitudinal motion. The model contains provisions for including appendages attached to the main body at arbitrary angles with arbitrary attachment springs. The appendages are modeled similarly to the main body. The boundary value problem that results from the representation can be expressed as an eigenvalue problem:

$$[K - \omega_{ie}^2 M] X_{ie} = 0 \quad i = 1, 2, \dots, N \quad (2)$$

where M and K are mass and stiffness matrices, respectively. The subroutine within the computer program which solves the eigenvalue problem uses the Holzer-Myklestad method. This numerical method utilizes transfer matrices from point to point on the model and finds the eigenvalues by satisfying the boundary conditions using an iterative procedure. A complete description of the method is found in Reference (5). Limitations of the method and economy preclude extraction of all N modes where N is typically 50 to 200. It will be seen later that the lack of a complete set of modes introduces approximations into the optimization method and necessitates modifications.

The "best" fit values of the joint compliances, defined in a least square error sense, are determined by minimizing the cost function which is accomplished with a modified steepest descent method. Steepest descent or gradient methods as they are also known, iteratively converge on the location of the minimum, since an analytical solution of the condition for an extremum, $\nabla F = 0$, is not possible. The successive estimates of the minimizing values of the independent variables, in this case a vector the components of which are the unknown spring rates of the structural joints k , are

$$k^{(n+1)} = k^{(n)} - \theta \nabla F|_{k^{(n)}} \quad (3)$$

The superscript indicates the number of the estimate. If the quantity θ is a constant, the algorithm is a first order method commonly referred to as the steepest descent method. It is based on the intuitive notion that if one proceeds in the direction of the steepest descent, which Equation (3), does, in small steps one must arrive at a local minimum. A very efficient second order method may be derived by applying the Newton-Raphson algorithm to the gradient of the cost function which yields the successive approximation,

$$k^{(n+1)} = k^{(n)} - S \left[\frac{\partial F}{\partial k_j \partial k_j} \right] \nabla F|_{k^{(n)}} \quad (4)$$

The matrix of second partial derivatives must be non-singular. Theoretically, the step size, S , is a scalar. However, it was necessary to generalize its definition. Equation (4) serves as the basis for the algorithm developed. The reasons for the modifications that were necessary will be explained as they are encountered.

The j th component of the gradient of the cost function is

$$\frac{\partial F}{\partial k_j} = \sum_{i=1}^M \{ W_{ie} (\omega_{ie}^2 - \omega_{it}^2) \frac{\partial \omega_{ie}^2}{\partial k_j} + (X_{ie} - X_{it})^T W_{ix} \frac{\partial X_{ie}}{\partial k_j} \} \quad (5)$$

where k_j is the j th unknown spring rate. In order to calculate the partial derivatives of the eigenvalues and eigenvectors with respect to the k_j 's, a departure was made from Reference (4). Here the modes were normalized to unity with respect to the generalized mass M ,

$$\mathbf{X}_{je}^T \mathbf{M} \mathbf{X}_{je} = \delta_{ij} \quad (6)$$

A joint compliance positioning matrix, \mathbf{K}^j , is introduced which locates the unknown spring rates within the full spring matrix

$$\mathbf{K} = \bar{\mathbf{K}} + \sum_{j=1}^N \mathbf{K}^j \mathbf{K}_j \quad (7)$$

$\bar{\mathbf{K}}$ is the matrix of known spring elements. Because of the peculiarities of the method used to solve the eigenvalue problem, the spring matrix, \mathbf{K} , is not directly available and so neither are the variable spring positioning matrices, the \mathbf{K}^j 's. However, they can be derived by considering the strain energy stored in the j th spring. For simplicity, assume that a separate spring rate is assigned to each joint. Then the strain energy associated with the j th spring is:

$$U_j = \frac{1}{2} k_j (x_j' - x_j'')^2 \quad (8)$$

where x_j' and x_j'' are the slopes to the left and to the right of the joint for the case of a rotational spring. The strain energy is also $U_j = 1/2 \mathbf{x}_j^T \mathbf{K}^j \mathbf{x}_j$. Equating the two expressions and then the coefficients of like terms, it can be deduced that the matrix, \mathbf{K}^j , must be the null matrix except for a submatrix,

$$\begin{pmatrix} 1 & -1 \\ -1 & 1 \end{pmatrix} \quad (9)$$

corresponding to the coordinates on either side of the joint. Then according to Reference (6) the partial derivatives are

$$\frac{\partial \omega_{je}^2}{\partial k_j} = \mathbf{X}_{je}^T \mathbf{K}^j \mathbf{X}_{je} \quad (10)$$

$$\frac{\partial \mathbf{X}_{je}}{\partial k_j} = \sum_{k \neq j} \frac{\mathbf{X}_{ke}^T \mathbf{K}^k \mathbf{X}_{je}}{\omega_{je}^2 - \omega_{ke}^2} \mathbf{X}_{ke} \quad (11)$$

Equations (10) and (11) can be expanded in terms of components of the normal coordinates by utilizing the strain energy relationship for each joint.

$$\begin{aligned} \frac{\partial \omega_{je}^2}{\partial k_j} &= X_{je, m_j} (X_{je, m_j} - X_{je, m_j+1}) \\ &\quad + X_{je, m_j+1} (-X_{je, m_j} + X_{je, m_j+1}) \\ &= (X_{je, m_j} - X_{je, m_j+1})^2 \end{aligned} \quad (12)$$

$$\begin{aligned} \frac{\partial \mathbf{X}_{je}}{\partial k_j} &= \sum_{k \neq j} (\omega_{je}^2 - \omega_{ke}^2)^{-1} \\ &\quad \{ X_{ke, m_j} (X_{je, m_j} - X_{je, m_j+1}) \\ &\quad + X_{ke, m_j+1} (-X_{je, m_j} + X_{je, m_j+1}) \} \mathbf{X}_{ke} \end{aligned} \quad (13)$$

where the indices m_j and m_j+1 refer to the components of the normal coordinates to the left and right of the j th joint respectively. The partial derivatives of the mode shapes were derived using the second formulation of Reference (6) which requires a complete set of theoretical modes. As pointed out previously the sum has to be truncated for reasons of

accuracy and economy. This is usually the case in dynamic problems. Here the justification is a posteriori. The number of theoretical modes used in the computation of their derivatives is an option to be selected by the user.

$$\frac{\partial \mathbf{X}_{je}}{\partial k_j} \approx \sum_{k \neq j} \frac{\mathbf{X}_{ke}^T \mathbf{K}^k \mathbf{X}_{je}}{\omega_{je}^2 - \omega_{ke}^2} \mathbf{X}_{ke} \quad (14)$$

It was felt that direct calculation of the second partial derivatives of the eigenvalues and eigenvectors was prohibitive because of computer memory size limits. It was subsequently realized that direct calculation of the second partial derivatives is very likely economically feasible since many of the terms are zero. However, since only a small number of unknown missile joints are assumed, the method employed in program JOINTS approximates the second partials by taking differences of the first partials. Such a numerical process tends to be accuracy sensitive and demands careful monitoring. Without resorting to double precision arithmetic, the step size must be large enough to yield a sufficient number of significant figures. On the other hand, too large a step size may enclose a region too large for the cost function to be represented by a quadratic. The procedure settled upon was the following. Using the current estimate $\mathbf{k}^{(n)}$, the gradient of the cost function is computed with Equations (5), (12) and (14). The current estimates of the unknown springs are incremented observing the sign of the gradient:

$$k_j^{(n+1)} = k_j^{(n)} \left[1 - r \cdot \text{SIGN} \left(\frac{\partial F}{\partial k_j} \right)_{\mathbf{k}^{(n)}} \right] \quad (15)$$

The relative increment, r , is the same for all the unknown spring rates and fixed for a particular problem. The gradient is calculated at $\mathbf{k}^{(n)}$ and the ratios of the difference of the respective components and the spring rate increments are computed. In order to improve the estimates of the second partial derivatives, corresponding off-diagonal estimates which theoretically should be equal are averaged as indicated below.

$$\begin{aligned} \frac{\partial^2 F^{(n)}}{\partial k_i \partial k_j} &= \frac{\partial^2 F^{(n)}}{\partial k_j \partial k_i} = \frac{1}{2} \left\{ \left(k_i^{(n)} - k_j^{(n)} \right)^{-1} \right. \\ &\quad \left[\frac{\partial F^{(n)}}{\partial k_j} \right]_{k_i} + \left(k_j^{(n)} - k_i^{(n)} \right)^{-1} \\ &\quad \left[\frac{\partial F^{(n)}}{\partial k_i} \right]_{k_j} \left. \right\} \quad (16) \end{aligned}$$

The Hessian, the matrix of second partial derivatives, is then inverted. The correction terms in Equation (4) are computed using a value of 1.0 for S . The sign and magnitude of each correction component are compared to those of the increment used to estimate the second partials. If the signs agree or if the magnitude

is less than 2-1/2% of the current spring rate, the second order correction is utilized. If not, equation (15) is used. If the new spring rates, $k(n+1)$, result in an increase in the cost function, the correction terms to $k(n)$ are halved repeatedly until a decrease in the cost function is obtained. In any case, each variable spring rate is kept within prespecified limits. These procedures which taken together may be considered a complicated method of selecting a varying step size, S , evolved heuristically. Modifications which can be made to improve them and put them on a more rigorous basis are possible.

Ideally the weighting in the cost function should reflect both the relative accuracy of the experimental data and the relative importance of the information to be obtained from applications of the mathematical model. Often for missiles constructed with thin cylindrical shells, the experimental data will diverge from beam behavior in progressively higher modes. For many dynamic analyses (such as dynamic loads analyses and autopilot elastic mode coupling analyses), the contribution of the higher modes is less significant than the lower modes. If the above conditions hold for any given problem, then the weighting factors should decrease in some way with increasing mode number.

A derivation of the weighting factors is now developed. The cost function (Equation 1) may be broken down into two terms (mode shape and frequency) for each mode

$$F_i = F_{if} + F_{ix} \quad (17)$$

where

$$F_{if} = \frac{1}{2} W_{if} (\omega_{ie}^2 - \omega_{ix}^2)^2 \quad (18)$$

$$F_{ix} = \frac{1}{2} (\chi_{ie} - \chi_{ix})^T W_{ix} (\chi_{ie} - \chi_{ix}) \quad (19)$$

Rewriting F_{ix} as a summation yields

$$F_{ix} = \frac{1}{2} W_{ix} \sum_n (\chi_{ie_n} - \chi_{ix_n})^2 \quad (20)$$

To see the size of terms produced in the cost function by an error in the eigenvalue or eigenvector, a relative error of size ϵ is assumed in each of the measured quantities. Then the cost function terms will be equated by proper selection of weighting factors. That is, an error of ϵ will be assumed in both ω^2 and χ , and weighting factors will then be found which give equal size terms in the cost function. If the theoretical eigenvalues and eigenvectors are assumed correct, then an error of ϵ in the eigenvalue can be written as

$$\omega_{ix}^2 = (1 + \epsilon) \omega_{ie}^2 \quad (21)$$

The frequency terms in the cost function become

$$F_{if} = \frac{1}{2} W_{if} \epsilon^2 \omega_{ie}^4 \quad (22)$$

This means that an error of ϵ in the eigenvalue will produce a residual term in the cost function proportional to the product of the fourth power of the frequency and the square of the error. Considering the same error applied to the mode shape contribution to the cost function yields

$$F_{ix} = \frac{1}{2} W_{ix} \sum_n \epsilon^2 \chi_{ie_n}^2 \quad (23)$$

The above equation shows that an error of ϵ in the eigenvector will produce a residual term in the cost function proportional to the product of the square of the eigenvector and the square of the error. Since the mode shapes are normalized to a unity generalized mass, then

$$1 = \sum_n m_n \chi_{ie_n}^2 \quad (24)$$

If assumptions are made that the test specimen is a slender beam with uniform mass and station distributions, then the above equation may be rewritten as

$$1 = M \sum_n \chi_{ie_n}^2 \quad (25)$$

and the mode shape portion of the cost function becomes inversely proportional to the mass

$$F_{ix} = \frac{1}{2} W_{ix} \epsilon^2 \frac{1}{M} \quad (26)$$

where $M = \frac{\text{mass of beam}}{\text{number of stations}}$

F_{ix} is independent of frequency, and is dependent upon the mass, number of beam stations, and the square of the error.

To equate the size of the frequency terms in the cost function with each other, the following weighting factors were selected

$$W_{if} = \frac{\omega_{N/e}^4}{\omega_{ie}^2} \quad (27)$$

where $\omega_{N/e}$ = highest experimental mode frequency.

Equating the mode shape and frequency terms of the cost function yields

$$W_{ix} \frac{1}{M} = \frac{\omega_{N/e}^4}{\omega_{ie}^2} \quad \omega_{ie}^4 = \omega_{N/e}^4 \quad (28)$$

$$W_{ix} = \omega_{N/e}^4 M$$

$$W_{ix} = \frac{\omega_{N/e}^4 m}{N} \quad (29)$$

where m = total mass of the missile
 N = number of internal stations.

The above weighting factors then approximately weight the mode shape and frequency errors equally.

APPLICATION OF THE METHOD

Here an application is presented to show the utility of the joint compliance extraction method. The example chosen consists of a set of measured bending modal data for a tactical missile. This set of modal data had previously been matched with a mathematical model by a trial and error method (which took approximately sixty computer runs). Previous test cases based on hypothetical models had shown that the method arrives at the correct joint compliances rapidly when an exact math model is used with no experimental errors in the input data. The results obtained for this application illustrate how well the program works when matching a lumped parameter model to actual measured data with its inherent experimental errors.

The set of weighting factors selected for this application were chosen to equate all three modes (both frequencies and mode shapes) equally. The first three joint compliances (which represent airframe joints) were started approximately 300% higher than the hand tuned values. The fourth joint compliance represented the attachment compliance for an internal appendage. The originally assumed value of the fourth compliance was started high by 30% over the hand tuned value.

Figure 9 shows the rate of convergence obtained by the method for the missile application. The program was run for a total of eight iteration cycles. However, the cost function did not improve significantly after the third cycle. The final (iteration cycle eight) joint compliances obtained agree quite well with the hand tuned values. Figure 10 presents a comparison of the experimental and theoretical modes. It is apparent from the figures that a good match has been obtained between the two sets of data.

Next, a new set of weighting factors was chosen to see what effect different weighting factors had on the solution. It should also be noted that the test data was represented well by the beam model in the above solution. The set of frequency weighting factor coefficients selected were 100, 10, and 1 for the first, second, and third modes respectively. The corresponding mode shape weighting factor coefficients were 1, 0.1, and 0.01. Figure 11 shows the solution (No. 2) obtained for this condition. Comparison of Figures 9 and 11 shows that both sets of compliances obtained are close to the hand tuned values. The following is a comparison of the experimental frequencies and the frequencies obtained for the two sets of weighting factors.

Mode No.	Experimental Frequency (Hz)	Theoretical Frequency (Hz)	
		Solution No. 1	Solution No. 2
1	59.3	59.5	59.3
2	116.	114.4	116.0
3	153.	154.2	153.6

As shown above, the case where the frequencies are weighted more heavily than the mode shapes (solution number 2) does in fact exhibit a better match between the experimental and theoretical frequencies.

The joint compliance extraction technique in its present format is believed to offer a useful, convenient, and reliable method for estimating effective compliances of missile joints from modal test data. The method presumes that the missile airframe distributed stiffness and mass properties are known, the modal characteristics can be adequately modeled as a lumped parameter beam, and that all discrepancies between modal analysis and modal test data can be attributed to uncertainties in the joint compliance values. As in any analytical method, additional refinements and areas for improvement will become evident as applications are further explored with actual test data.

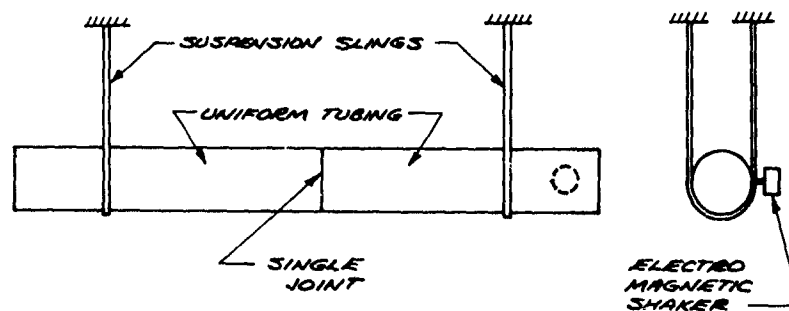
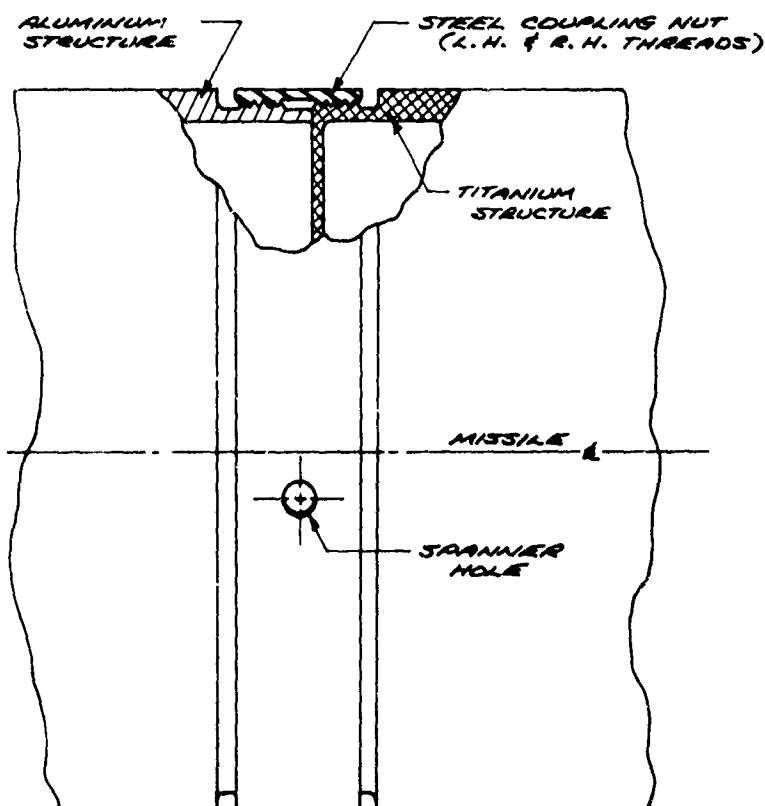


FIGURE 1

SKETCH OF IDEALIZED TEST SPECIMEN



JOINT LOCATION : 31% AIRFRAME LENGTH
JOINT DIAMETER : 2.75 INCHES

FIGURE 2

THREADED COUPLING RING JOINT

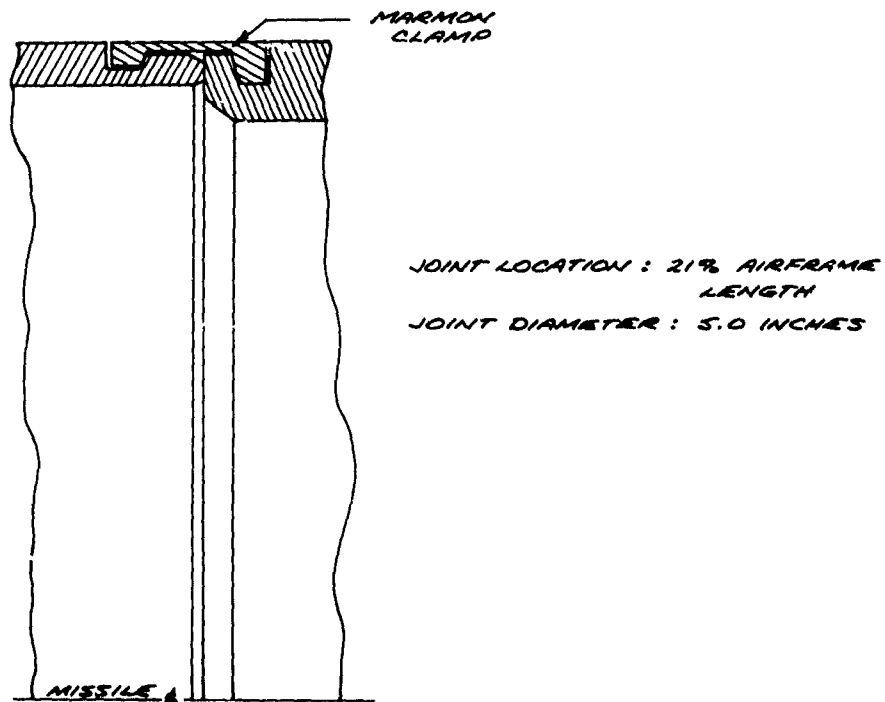


FIGURE 3
MARMON CLAMP JOINT

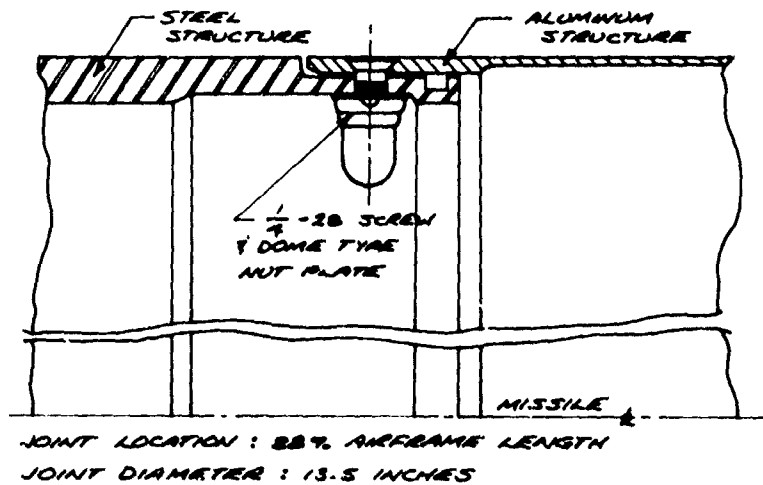


FIGURE 4
SHEAR BOLT JOINT

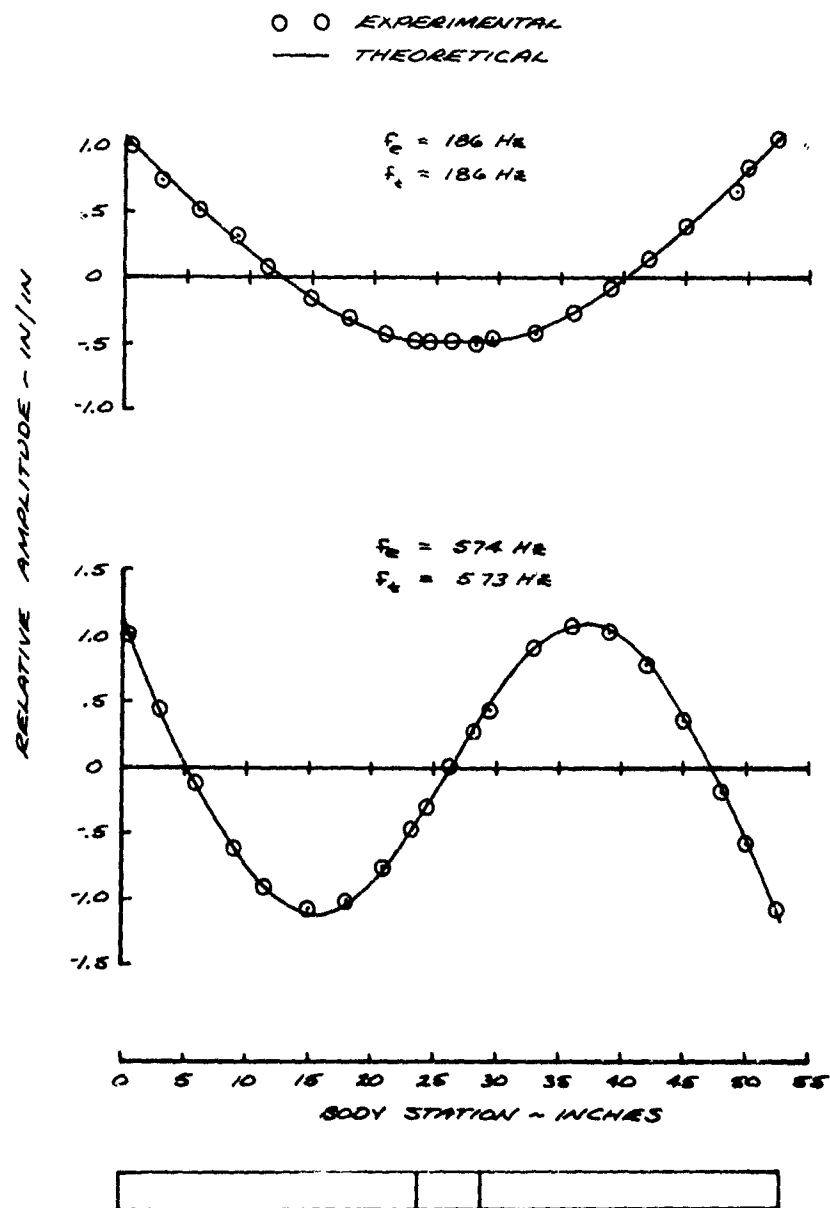


FIGURE 5
 THREADED COUPLING RING JOINT
 ANALYTICAL VERSUS EXPERIMENTAL MODES

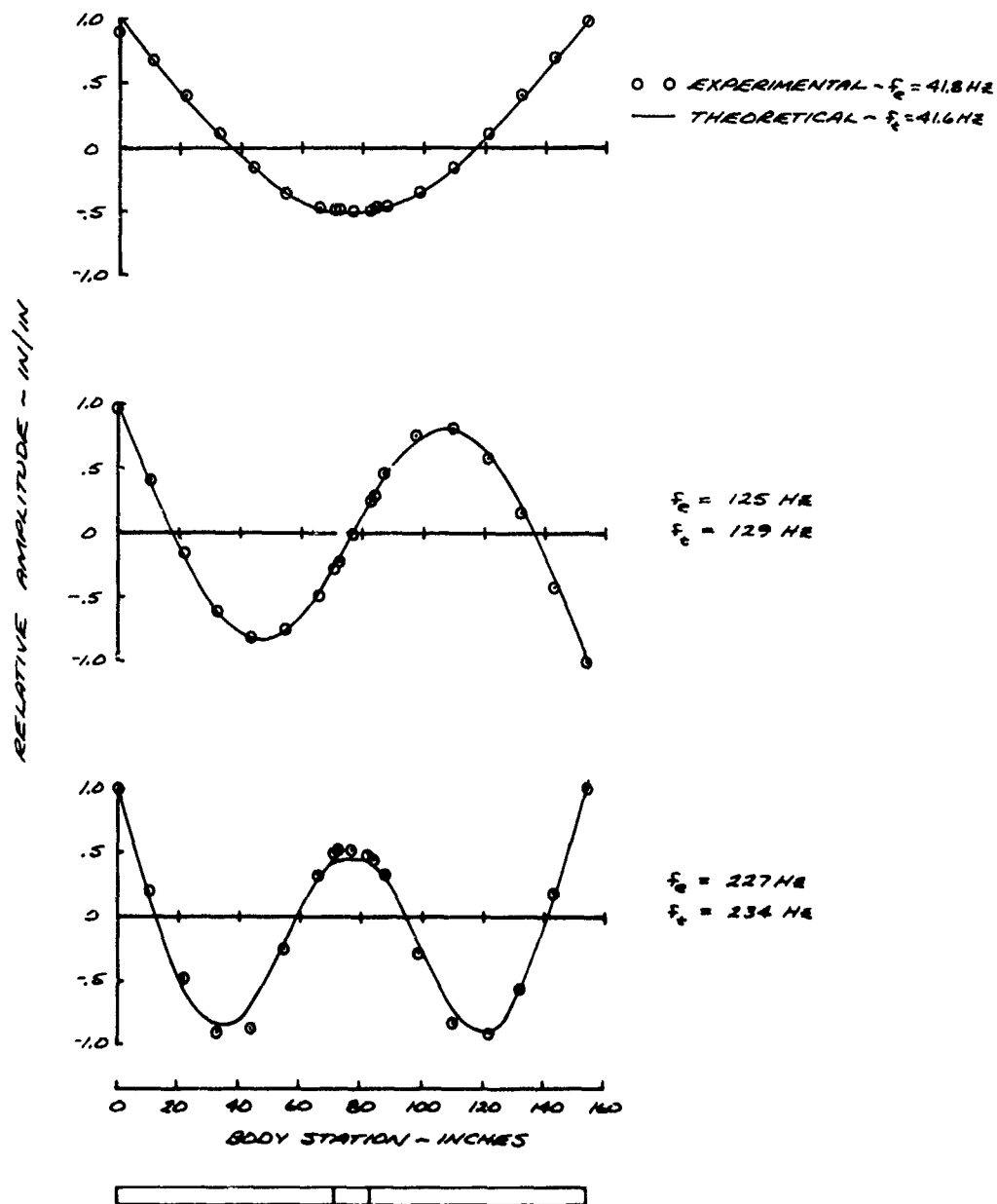


FIGURE 6
 MARION CLAMP JOINT
 ANALYTICAL VERSUS EXPERIMENTAL MODES

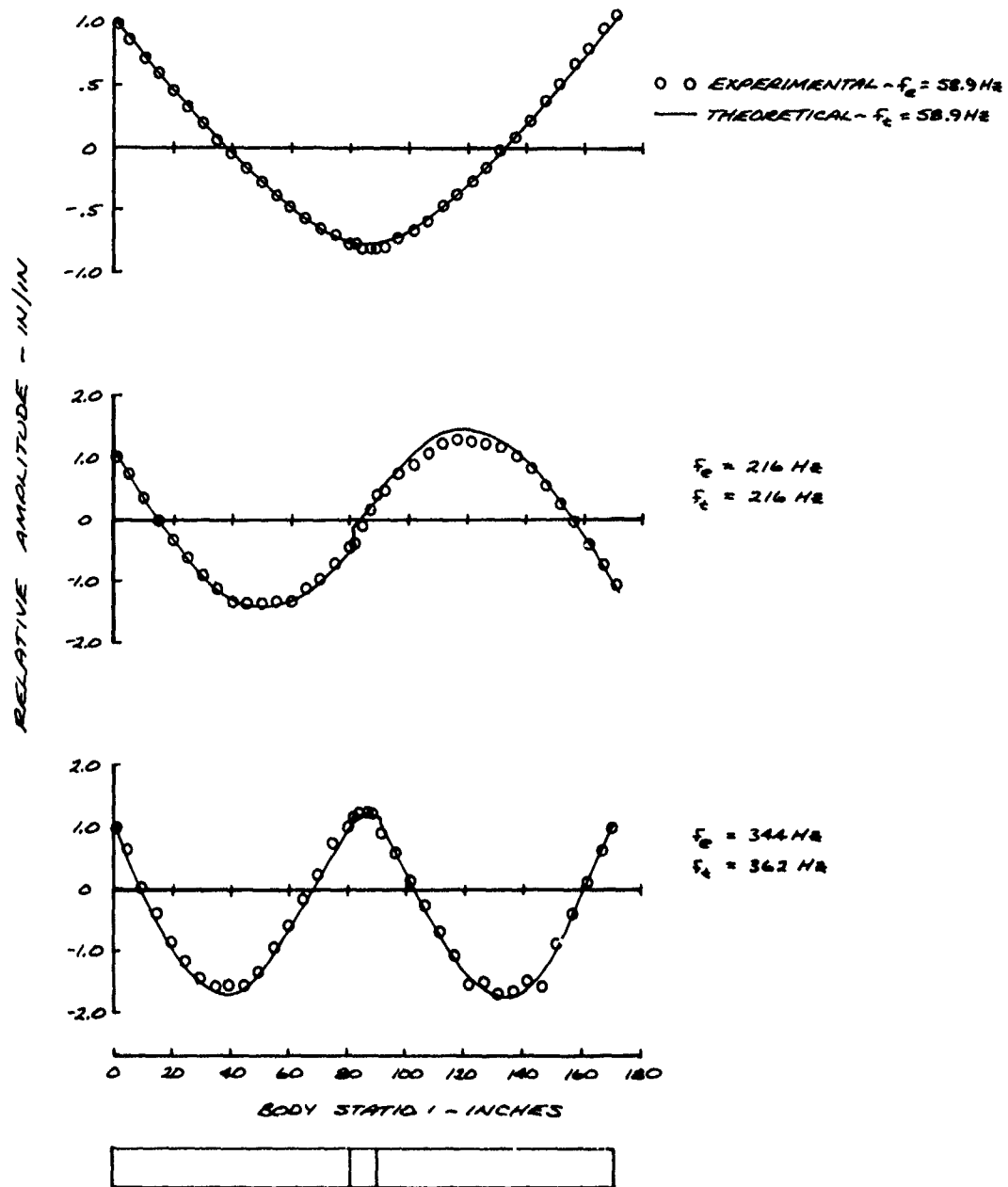


FIGURE 7
 13.5 INCH DIAMETER SHEAR BOLT JOINT
 TWELVE FASTENER CONFIGURATION
 ANALYTICAL VERSUS EXPERIMENTAL MODES

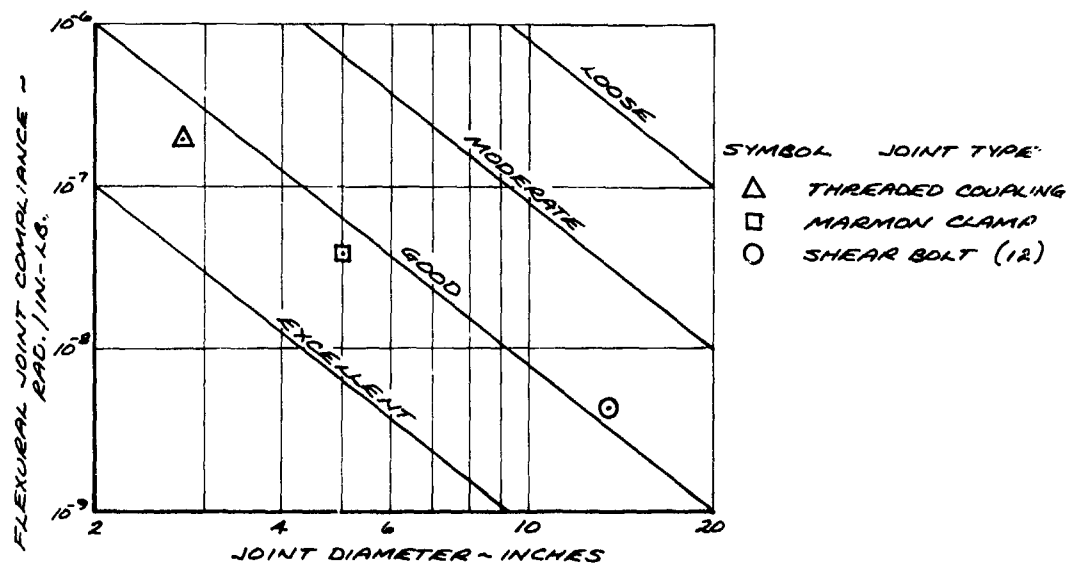


FIGURE 8
COMPARISON OF DERIVED JOINT COMPLIANCES
WITH RATING SYSTEM OF ALLEY AND LEADBETTER

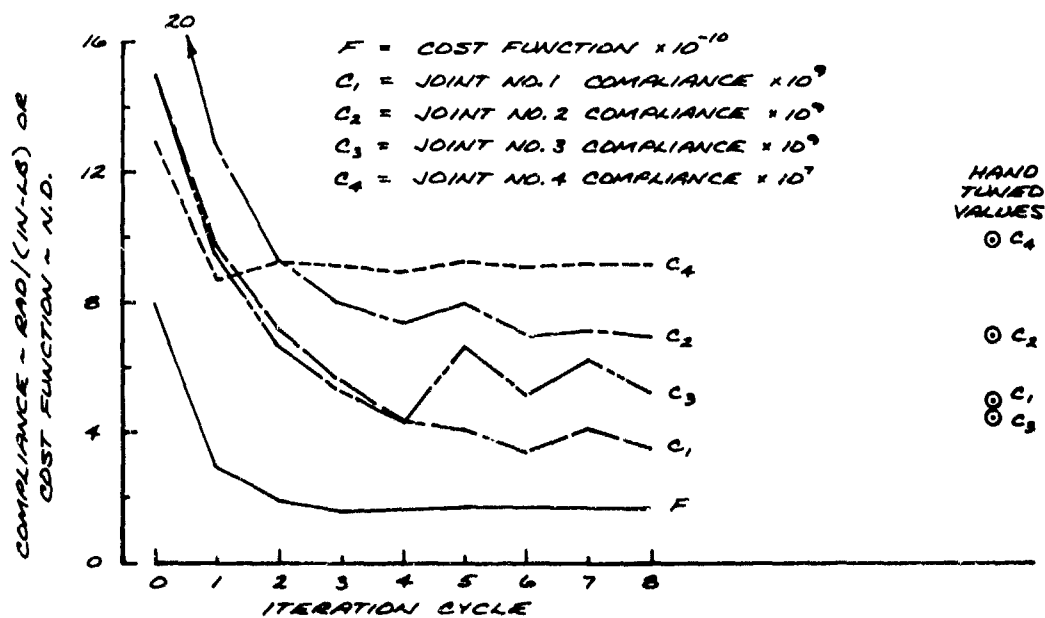


FIGURE 9
TACTICAL MISSILE APPLICATION SOLUTION NO. 1
EQUAL WEIGHTING FACTORS

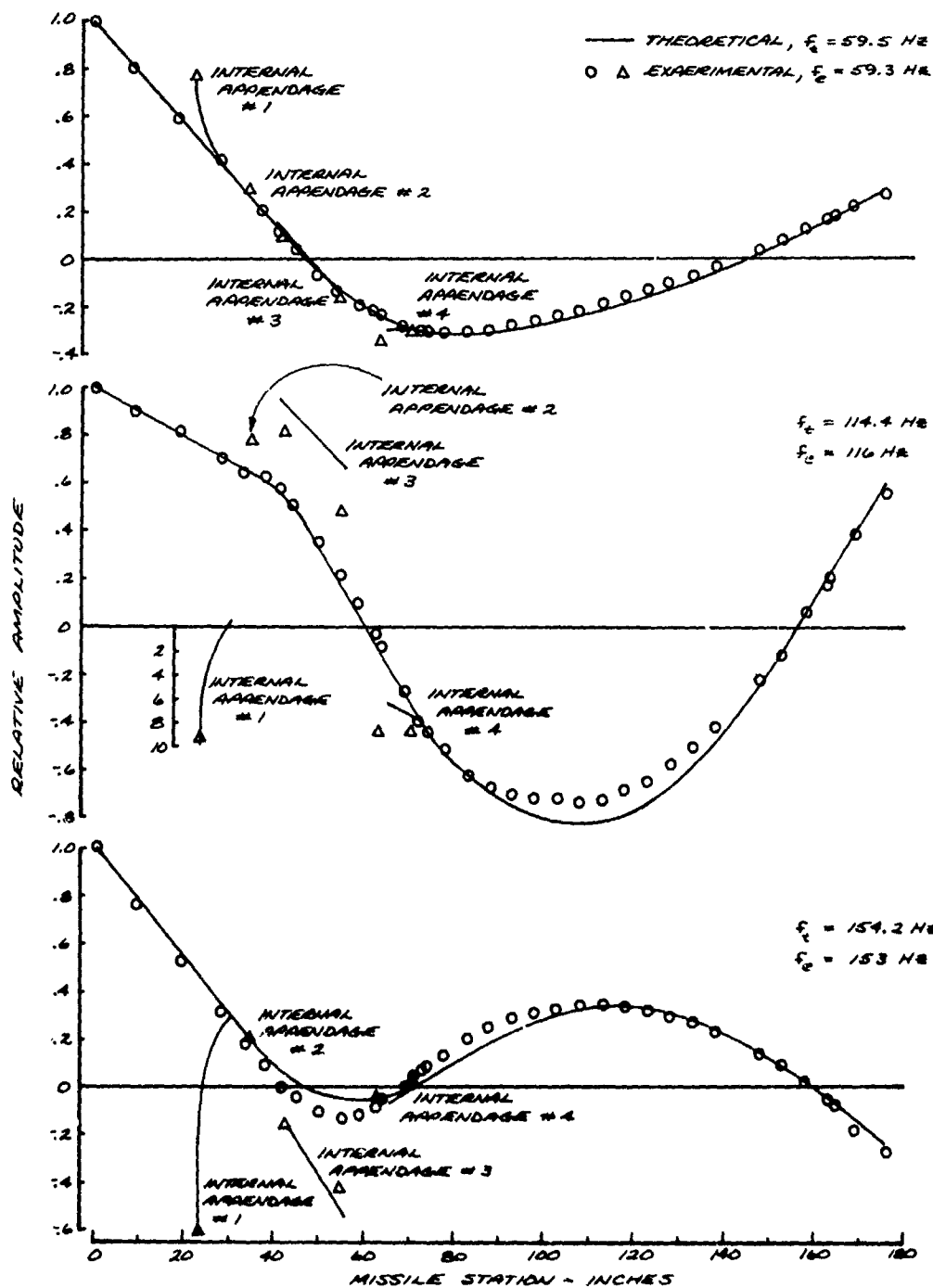


FIGURE 10
TACTICAL MISSILE APPLICATION
COMPARISON OF EXPERIMENTAL AND THEORETICAL MODES

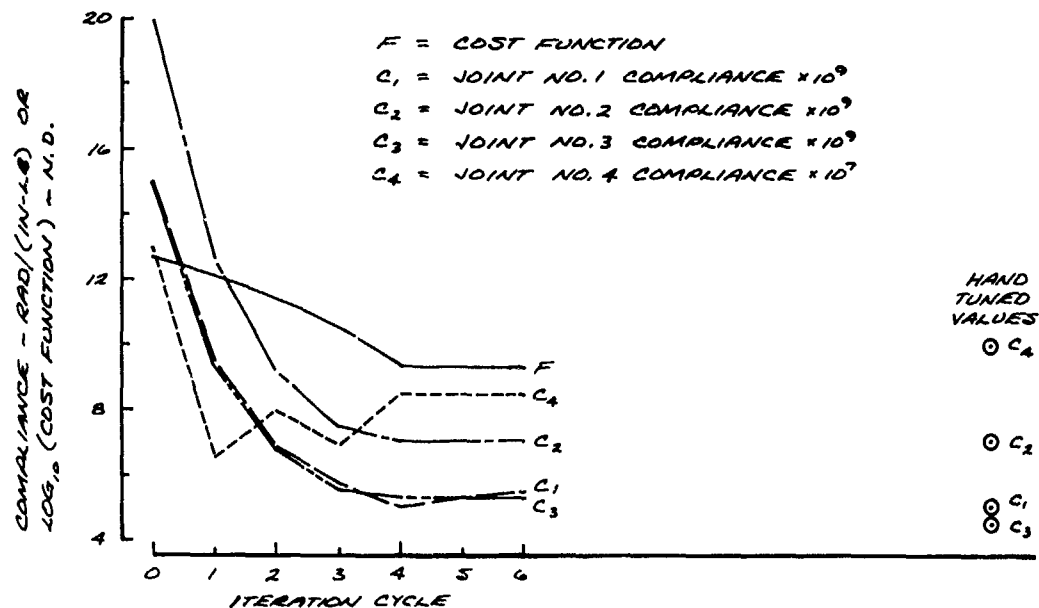


FIGURE 11
TACTICAL MISSILE APPLICATION SOLUTION NO. 2
UNEQUAL WEIGHTING FACTORS

REFERENCES

1. Alley, Jr., V. L. and Leadbetter, S. A., "The Prediction and Measurement of Natural Vibrations on Multistage Launch Vehicles", American Rocket Society Launch Vehicles: Structures and Materials Conference Report, April 1962.
2. Maloney, J. G. and Shelton, M. T., "Structural Dynamic Properties of Tactical Missile Joints - Phase 2", General Dynamics, Pomona Division Report No. CR-6-348-945-002, September 1971.
3. Leaker, G., Maloney, J. G., Shelton, M. T., and Underhill, D. A., "Structural Dynamic Properties of Tactical Missile Joints - Phase 3", General Dynamics, Pomona Division Report No. CR-6-348-945-003, May 1974.
4. Hall, B. M., Calkin, E. D. and Sholar, M. S., "Linear Estimation of Structural Parameters from Dynamic Test Data", AIAA/ASME 11th Structures, Structural Dynamics, and Materials Conference, Denver, Colorado, April 22 - 24, 1970.
5. McIntyre, K. L., "Modified Bolzer-Myklestad Modal Analysis Final Report - CWA 245", General Dynamics/Pomona TM-348-15.1-3, July 24, 1961.
6. Fox, R. L. and Kapoor, M. P., "Rates of Change of Eigenvalues and Eigenvectors", AIAA Journal, Vol. 6, Number 12, December 1968, p. 2426.

VIBRO-ACOUSTICS

DYNAMIC STRAIN MEASUREMENT TECHNIQUES AT ELEVATED TEMPERATURES

R. C. TAYLOR

AIR FORCE FLIGHT DYNAMICS LABORATORY
WRIGHT-PATTERSON AIR FORCE BASE, OHIO

Strain gage techniques for use in a combined thermal acoustic environment were investigated. The design limits of the program were strain levels of 1000 micro-inches/inch and temperature of 1400°F. To verify the developed methods, strain gages were installed on three panels which were then tested in the AFFDL Sonic Fatigue Facility at 500°F, 1200°F, and 1400°F. Epoxy adhesive, ceramic cement, and flame-sprayed ceramic bonded gages exhibited excellent results although lead wire failures were common.

INTRODUCTION

The measurement of strain during sonic fatigue tests of aircraft structures is essential to determine structural response and estimate fatigue life. Of the many tests that have been performed at the Air Force Flight Dynamics Laboratory (AFFDL) Sonic Fatigue Facility, (Reference 1), those that presented a difficult strain measurement situation were the tests run in conjunction with elevated temperatures. It is in such an environment that high thermal stresses and the dynamic strains of acoustically induced vibration combine to reduce the life of the most carefully chosen and installed strain gage system.

In a typical high temperature acoustic test in the AFFDL, the test article is subjected to a high intensity sound field and simultaneously heated to its operational temperature. These tests are performed on aircraft structures to duplicate the noise and heat of jet engine exhaust experienced in service. In the test facility, the sound field is simulated using sound generators and heat is induced by means of quartz lamps with reflectors. Most tests of this nature are performed in the 1 by 1 foot progressive wave test section of the small test chamber illustrated in Figure 1. The test specimen is mounted on the side of the test section and is exposed to the sound pressure from within and to the heat lamps on the outside. Not only are the strain gages exposed to the heat and vibration, but also the lead wires which may extend several inches into the heated zone.

Strain gages used in these tests have been commercially available resistance type gages designed for high temperature and adhesive bond-

ing. Weldable gages have not been used because welding may cause local stress concentrations and therefore alter the fatigue characteristics of the base material. For the tests conducted at temperatures between 600°F and 1200°F, free-filament (unbacked) type wire gages were used and, depending on the maximum temperature expected, the gages were bonded with ceramic cement or flame-sprayed ceramic. To minimize the effects of a gage installation on the vibratory response of the structure, the mass of the gage, adhesive, and lead wires must be kept as low as practical. Gage lengths are usually 1/8 inch or less and lead wires are size 26 AWG or smaller. However, in the interests of long fatigue life, there is usually a compromise between low mass and strength.

The results of early high temperature sonic fatigue tests were discouraging. In the year 1969, an AFFDL test report on the F-111 Aft Center Body Panel Test contained these words: "Very little strain data were acquired because of the rapid disintegration of the gage-lead-wire or the gage-panel interface bond under the combination of high temperatures and high sound pressure levels". With panel temperatures as high as 1200°F, the gage installations did not last long enough to record the strain data. High temperature free filament gages had been installed by the flame-spray technique and the Nichrome ribbon leads were installed in glass fiber tubing and held down by straps of Nichrome ribbon spot welded to the panel. Although these methods had been used successfully in other vibration tests, they did not work in the high temperature acoustic environment.

Then in 1972, during the AFFDL test of

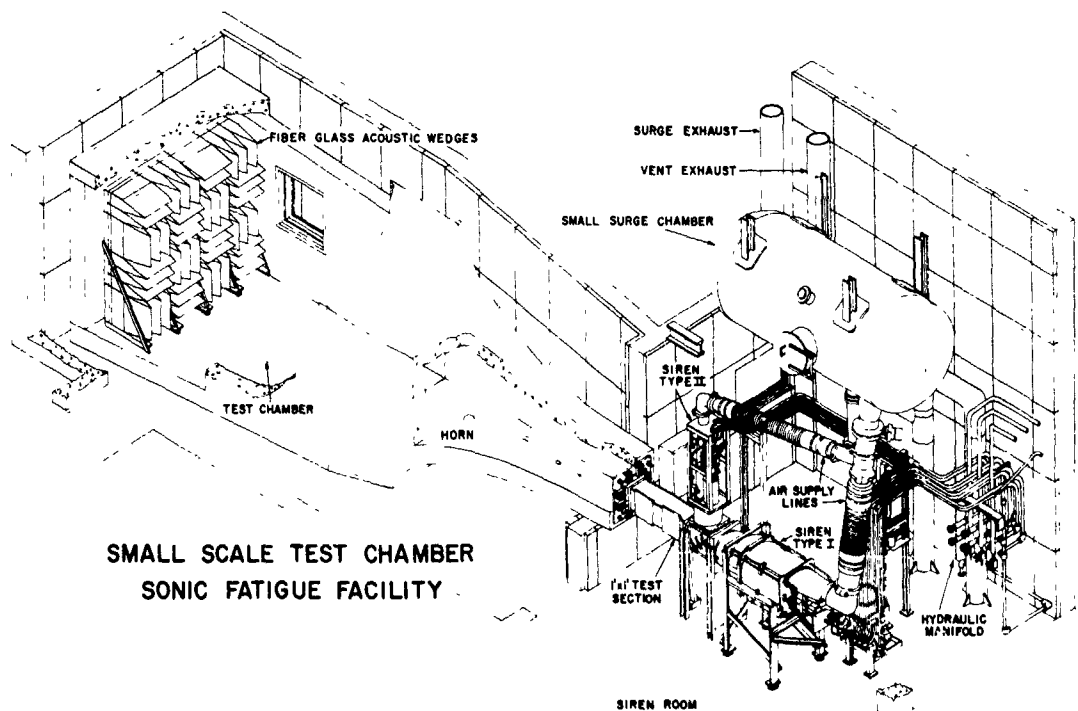


Figure 1. Small Test Chamber

brazed honeycomb panels, free-filament gages were used at temperatures to 900°F. The gages were attached using a ceramic cement. Out of 12 gages installed, data were obtained from only 2 gages at 800°F.

To meet the requirement for reliable strain data from fatigue tests in the thermal acoustic environment, an experimental program was undertaken to develop effective strain measuring methods. This development was performed under contract for the Air Force. The verification tests were conducted by Air Force personnel at the AFFDL Sonic Fatigue Facility in cooperation with the contractor. This paper summarizes the contractual developments and the results of measuring strain at high temperatures during the verification tests. A complete discussion of the contract program is available in an AFFDL report, Reference 2.

DEVELOPMENT PROGRAM

The objective of the program was to develop and demonstrate static strain, dynamic strain, and temperature measurement techniques that exhibit a high degree of accuracy and reliability under test conditions where high level structural vibration is combined with heating. The methods to be developed were to withstand

strain levels approaching 1000 micro-inches per inch, dynamic; 2000 micro-inches per inch, static; at temperatures up to 1400°F. The reliability requirement was specified as 1 hour of operational life at these limits of thermal and dynamic loading. Three temperature ranges were selected for investigation, 200°F to 500°F, 500°F to 800°F, and 800°F to 1400°F. For each range, the program consisted of selecting the strain measuring device, developing a reliable attachment method, developing a compatible lead wire system and designating complete instrumentation requirements for measurement and calibration.

A literature search was conducted to determine the most suitable device for strain measurement. Considering that the attachment of the sensor would be to thin skins and that the method should have minimum effect on the vibratory characteristics of the structure, the bonded resistance strain gage was selected. For the temperature range, 200°F to 500°F, standard resistance gages were investigated. For higher temperatures, up to 1400°F, many special alloyed gages were fabricated primarily to meet the static strain requirements of the program.

The most difficult and time consuming portion of the program was the development of a temperature compensation technique for static

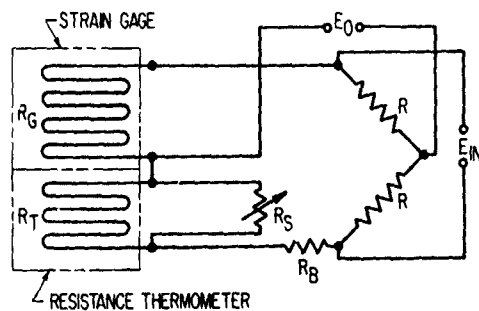


Figure 2. Resistance Thermometer Compensated Gage

strain measurement at high temperature. A number of compensation techniques were investigated and the resistance thermometer compensation method was selected for further development. For this method, a resistance thermometer element is bonded adjacent to the active gage and connected to the compensating arm of the strain gage bridge as shown in Figure 2. Four alloys were investigated for the compensating element in conjunction with Platinum 8% Tungsten active elements and bonded to Inconel X test specimens. Excellent temperature compensation was achieved with platinum rhodium and platinum rhodium ruthenium compensating elements, however their application is limited to approximately 1250°F and 1050°F, respectively. Figure 3 shows the low apparent strain exhibited by these compensated gages.

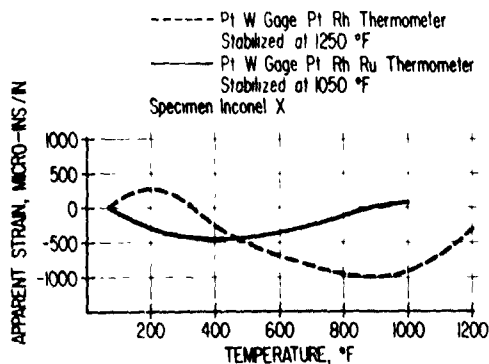


Figure 3. Apparent Strain, PT RH and PT RH RU Thermometers

Gage attachment methods selected for application to sonic fatigue testing included an organic cement for the lower temperatures, and ceramic cements and flame-sprayed ceramic for the higher temperatures. In general, the selection of a lead wire material for high temperature testing is based primarily on the temperature

properties of the material. The size and type to be used is a function of availability and the experimental results of thermal acoustic testing. Therefore, several lead wire sizes were selected to investigate the effects of wire size. Wire sizes included .003 inch and .005 inch diameter wire and .003 x .015 inch and .005 x .031 inch ribbon. Materials considered were Nichrome V, Constantan, nickel clad copper, and stainless steel clad copper.

An assumption was made that strain gage and thermocouple installation techniques used in testing gas turbine engines might also work in a high temperature, high intensity acoustic environment. To verify this assumption, the following test was conducted in the AFFDL Sonic Fatigue Facility. Chromel-Alumel thermocouples were bonded to a 14 x 20 inch panel of AISI 321 stainless steel using four attachment methods. For operation between 300°F and 500°F, two thermocouples were attached with an epoxy cement. For the range, 500°F to 800°F, two thermocouples were bonded with an epoxy using a method developed by NASA Flight Research Center, Edwards AFB. Four thermocouples were installed for operating in the 800°F to 1400°F range; two were bonded with a ceramic cement and two were installed by the flame spray method. The flame spray application consisted of nickel aluminide over the thermocouple junction and high purity aluminum oxide over the lead wires. An important factor was that each thermocouple wire was continuous from the junction, located near the center of the panel, to the edge of the panel and was bonded to the panel for the entire length. Near the edge of the panel, the thermocouple wire was spot welded to insulated extension wire.

The panel was mounted on the side of the test section of the small test chamber. A stainless steel mounting frame was placed over the panel which left a rectangular area of the panel, 7.8 x 17.5 inches, exposed to the heat generated by the lamps. A layer of asbestos cloth was inserted between the panel and frame to reduce the heat conduction into the frame. The asbestos layer also enabled the lead wires coming off the panel to be brought out between the panel and frame. Finally, a large sheet of Marinite insulating material was installed to mask the frame and to protect the test section. During the test, the panel was subjected to a random noise spectrum, 150 dB (re: $2 \times 10^{-5} \text{ N/m}^2$) overall sound pressure level (SPL), and to the heat from the quartz lamps. The panel temperature was held at 500°F for the first 30 minutes, 800°F for 30 more minutes, and then increased to 1400°F for the remainder of the test. Total test time was 1 hour 30 minutes. None of the thermocouple installations failed during operation within their design temperature range. The results of this test indicated that these methods that had been known to give good performance in turbine blade tests were promising for sonic fatigue testing.

VERIFICATION TESTS

How well strain gages would perform using these methods under actual conditions of heat and high intensity sound was determined next. These verification tests (similar to the previous test of thermocouples) were also performed in the AFFDL Sonic Fatigue Facility utilizing the small test chamber. Three panels were prepared for testing at 500°F, 1200°F, and 1400°F respectively. The 1200°F panel was made from a .023 sheet of Inconel X alloy. The temperature was chosen to test static strain gages compensated to 1200°F. The panel was instrumented with nine strain gages of Platinum 8% Tungsten and Nichrome V alloys, and five Chromel-Alumel thermocouples. All gages and lead wires were attached using ceramic cement. Lead wires consisted of .005 x .031 inch Nichrome V, .005 inch diameter Nichrome V, and .003 inch diameter Platinum 8% Tungsten. The lead wires were welded to glass-fiber sleeved extension leads in the area of the panel to be covered by the frame. The panel with gages installed is shown in Figure 4.



Figure 4. 1200°F Test Panel

In preparation for testing, the panel was mounted on the side of the facility test section as previously described and shown in Figure 5. The strain gages were connected to the facility instrumentation system used to condition and record the signals on magnetic tape. The thermocouple outputs were connected to strip chart recorders located with the specimen heating equipment and were used to control the quartz lamp heaters. The temperature history of the panel measured during the test is shown in Figure 6. For the test of this panel, the sound was generated by a low-frequency pure tone siren. A view of the siren, quartz lamps, and test section with panel installed is shown in Figure 7. A random noise was generated over a narrow band, 125 to 225 Hz. A microphone located inside the test section was used to establish a SPL of 160 dB. The test was terminated after 33 minutes when all channels of strain data were lost.



Figure 5. Test Section, With 1200°F Panel Installed

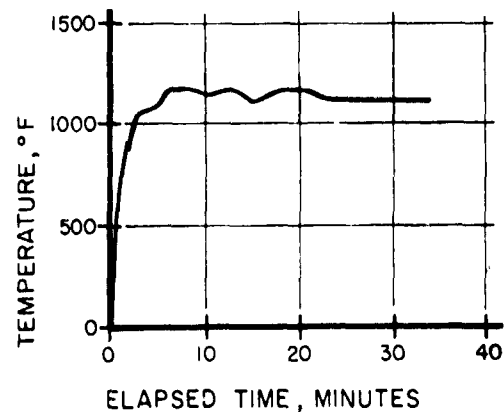


Figure 6. Temperature History, 1200°F Panel Test



Figure 7. Small Chamber Test Section, Siren, And Quartz Lamps

Following the test, the panel was inspected to determine the nature and cause of the failures. Two gages had failed completely. Seven gages survived the test but had lead wire failures. Because of high stresses in the clamped area some leads broke and others shorted to the panel. Gages and sections of lead wire near the center of the panel, where the stresses were lower, survived. Noting the fact that the panel had buckled, it was concluded the failures were caused by the inability of the ceramic cement to withstand the high strains caused by the buckling.

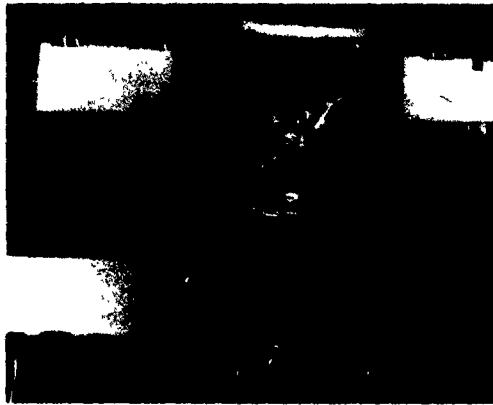


Figure 8. 1400°F Test Panel

The 1400°F panel tested next was fabricated from a sheet of .025 Rene' 41. Nine strain gages of Platinum 8% Tungsten, Nichrome V, and Karma and three Chromel-Alumel thermocouples were installed using the Rokide flame spray technique. A photograph of the panel is shown in Figure 8. Gage lead wires of .005 inch diameter Platinum 8% Tungsten wire, .005 inch Nichrome V wire, and .003 x .015 inch Nichrome V ribbon were welded to glass-fiber sleeved extension leads. To prevent shorting problems that occurred during the test of the first panel, glass-fiber tape was placed between the panel and the external leads. To avoid buckling the panel, the sound source was changed from the pure tone siren to an air modulator capable of producing a wideband spectrum. The spectrum was shaped as near as possible in accordance with MIL-STD-810 which defines the sound field characteristics associated with aircraft and missile systems. The instrumentation was connected as before. With the acoustic level at 160 dB overall SPL the panel was heated to 800°F, cooled below 200°F, then heated to 1400°F. This took approximately 49 minutes. Having reached 1400°F, the test continued one hour longer. Figure 9 shows panel temperature versus elapsed test time. Dynamic strain levels averaged about 100 micro-inches per inch. These strain levels are typical of many sonic fatigue tests.

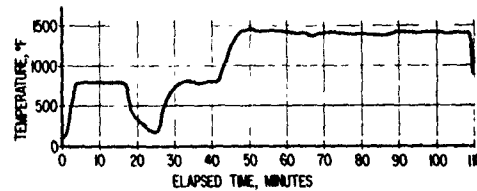


Figure 9. Temperature History, 1400°F Panel Test

An inspection of the panel after testing revealed that, again, lead damage in the area under the frame was the principal cause of data loss. In most cases, the cause was failure of the splice between lead wires and extension leads. However, a checkout of the gages indicated that all but one were functional.

The methods developed for the 200°F to 500°F temperature range were tested last. For this test a .020 sheet of AISI 321 stainless steel was used. Seventeen glass-fiber reinforced epoxy and phenolic backed gages were installed using an epoxy-phenolic adhesive. To compare the life of backed and unbacked gages, seven unbacked gages were also installed with flame-sprayed ceramic and ceramic cement. Lead wire types for the epoxy installed gages included .005 inch diameter Constantan wire, .005 inch diameter bare nickel clad copper wire, and .005 inch diameter polyimide copper wire. The lead wires were connected to the gages using 580°F solder and attached to the panel using an epoxy adhesive. Lead wires for the ceramic cemented and flame-sprayed gages included .005 inch diameter nickel clad copper wire, .005 inch diameter Nichrome V wire, .003 x .015 inch Platinum 8% Tungsten ribbon, and .004 x .031 inch Nichrome V ribbon. These lead connections were welded. The organic backed gage installations were coated with an aluminum filled silicone to provide a reflectivity similar to the bare test panel. This prevented the temperature of the gage installations from rising excessively above the test temperature (due to the dark color of the adhesive). Figure 10 shows the panel before testing. Heat and sound were applied as in the previous tests. With the SPL reduced to 150 dB, the panel was heated in 100 degree increments to 500°F. Although Figure 11 shows that one area of the panel remained below 500°F throughout the test, other thermocouples which failed before test termination measured temperatures of 500°F and above. The test lasted 44 minutes.

The flame-sprayed and ceramic cement installed gages failed early in the test. Panel buckling had caused the strains to exceed the limits for these attachment methods. Analysis of the panel after testing indicated that all of the epoxy adhesive bonded gages were functional and all failures had occurred in the lead wire system.



Figure 10. 500°F Test Panel

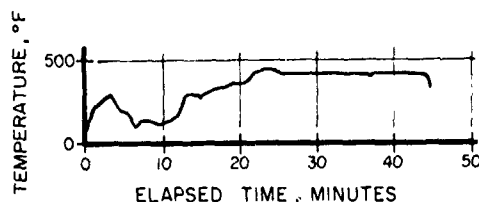


Figure 11. Temperature History, 500°F Panel Test

CONCLUSIONS AND RECOMMENDATIONS

A post-test examination of the three panels tested identified gaging techniques that should be considered for use in a high temperature and intense acoustic environment. The ceramic cement and flame-spray installed gages on the 500°F and 1200°F test panels had failed because the panels had buckled and strains exceeded the limits for these materials. Static strain channels for the 1200°F panel test, were driven over the recording limit of + 1200 micro-inches per inch indicating the actual strains were well above this value. Ceramic cements are limited to about 0.5% strain (5,000 micro-inches per inch) and flame-spray installed gages are usually limited to 1.5% strain. Ceramic cements are suitable for high temperature acoustic tests if the static strains do not approach the yield point of the material. If large thermal stresses are anticipated, flame spray attachment would be preferred over ceramic cement; however, neither method may endure.

The principal weakness in the gage installations was the relatively short life of the lead wire systems. Failures in the flame sprayed installations on the 500°F panel were partially due to the large size lead wires used. Gages with .005 x .031 inch ribbon leads which failed

were installed adjacent to gages with .003 inch diameter wire leads which did not fail. Furthermore, flame sprayed, .003 inch diameter, thermocouples on the 1400°F panel did not fail. It may be concluded that small diameter lead wires and thermocouples installed by the flame spray technique can be expected to perform satisfactorily in high temperature sonic fatigue tests that are not over 1400°F or more than 1 hour duration. Because of the poor results obtained with the .005 x .031 inch Nichrome V ribbon leads, this type wire is judged as too heavy for this application. Because of the high strains that developed in or near the clamped area of the panels, other arrangements for bringing the lead wires off the panel should be considered on future tests. Locating the lead wire splice in a lower stress area and running the leads over the frame instead of between the panel and frame are two possibilities. Also, as indicated by the earlier panel test of thermocouples, flame spraying or cementing the lead wires closer to the edge of the panel may extend the life of the lead wire installations.

In view of the high percentage of gages on each panel that remained functional after the test, it is believed that the gage types and attachment methods tested are generally satisfactory for the test conditions investigated. To summarize, the following gage and bonding combinations proved to be successful for high temperature high noise tests lasting up to one hour in length: for temperatures to 500°F, standard resistance strain gages attached with organic cements; for temperatures to 1200°F, unbacked gages attached with ceramic cement; for temperatures to 1400°F, flame-sprayed gages.

REFERENCES

1. A. W. Kolb and H. A. Magrath, "RTD Sonic Fatigue Facility, Design and Performance Characteristics," Shock and Vibration Bulletin, pp 17-41, January 1968.
2. S. P. Whuk, M. E. Low, and J. G. MacLean, "Development of Strain and Temperature Measurement Techniques for Use in Combined Thermal Acoustic Environment," AFHDL-TR-74-95.

AN ACTIVE LINEAR BRIDGE FOR STRAIN MEASUREMENT

Paul T. JaQuay

Air Force Flight Dynamics Laboratory
Wright-Patterson Air Force Base, Ohio

Constant voltage bridges operated in a quarter-bridge configuration are frequently used in strain measuring. This paper analyzes the bridge characteristics in this configuration both under balanced and unbalanced conditions. The analysis also is made of the shunt resistance method of bridge calibration and shows it to be an undesirable method for use under large offset conditions. An active linear bridge circuit is then presented that offsets the disadvantages revealed in the quarter-bridge analysis.

INTRODUCTION

The Air Force Flight Dynamics Laboratory, (AFFDL) Sonic Fatigue Facility (Reference 1) Wright-Patterson Air Force Base operates three acoustic test chambers to conduct experimental studies on aircraft and missile structures and equipment in a high intensity sound environment.

The response of the test specimens to high intensity sound is measured by transducers, which are located on or near the specimen, and are connected to the data acquisition system. The data from typical tests consists of the outputs of microphones, strain gages, accelerometers and displacement transducers. Of particular importance in most experiments and tests are the stress levels and their locations in the test specimens. As a consequence many strain measuring channels are provided in the Sonic Fatigue Facility data acquisition system. These strain measuring modules consist of typical constant voltage strain gage bridge supplies of a standard configuration as shown in Figure 1. These modules are adaptable to all bridge configurations from quarter-bridge to full bridge, but almost all strain measurements in the Sonic Fatigue Facility use the quarter-bridge configuration. Although other bridge configurations requiring gages on both sides of a specimen are more advantageous under certain conditions in regard to linearity and sensitivity, they are usually more difficult and often impossible to imple-

ment on real structures. This is due in part to non-accessibility of the reverse side of a structure often caused by a brace or support member covering the area of interest. For this and other reasons such as added cost, increased set-up time, and the difficulty of insuring equal and opposite dynamic strain on bending and flexing specimens, the quarter-bridge configuration is the only one discussed in this paper.

Often in structural sonic fatigue tests it is necessary to perform strain measurements at elevated temperatures as high as 1400°F. When strain gages are heated the static unstressed resistance increases. This increase in static, unstressed resistance results in a large static unbalance of the strain bridge. This increase in static gage resistance can be as high as 9 or 10% of the nominal gage resistance while the balance range of the bridges at the Sonic Fatigue Facility is approximately $\pm 2.5\%$ for 120 ohm gages. The inability to balance the bridge at high temperatures, the knowledge that off-null bridge measurements are non-linear, the uncertainty of bridge errors at these large offsets, and the desire to know quantitatively the bridge characteristics under offset as well as ideal conditions, were the motivating factors leading to this investigation.

Under the assumption that restoration of d-c balance would restore original operating conditions (sensitivity and calibration) the first approach

taken to solve this large static unbalance problem was to develop an automatically balanced bridge. This approach resulted in an active circuit capable of maintaining a balanced bridge under all conditions, no signal being generated by the bridge itself. The dynamic data was available at the output of the active element (see Figure 6). However, the same non-linear characteristics were still present in the automatically balanced bridge circuit. At this point it was decided to determine whether d-c balancing of the bridge would indeed restore the original operating conditions as was assumed at the outset. An analysis of the bridge characteristics was therefore undertaken.

ANALYSIS OF CONSTANT VOLTAGE BRIDGE CHARACTERISTICS

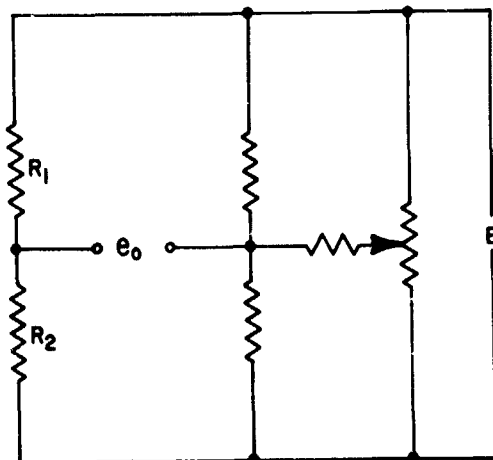


FIGURE 1, TYPICAL BRIDGE CIRCUIT

The constant voltage strain gage bridge modules in the Sonic Fatigue Facility have the circuit configuration as shown in Figure 1. This circuit is simplified in Figure 2 to facilitate analysis (quarter-bridge only discussed). The equation of the output of the bridge in Figure 2 is:

$$e_o = \left(\frac{R_2}{R_1 + R_2} - \frac{R_4}{R_3 + R_4} \right) E \quad (1)$$

where R_1 is chosen as the active element and R_3 as the balance element. If maximum sensitivity (equal arm) conditions are assumed (Reference 2) the equation for the

bridge simplifies to:

$$e_o = \left(\frac{R}{2R + \Delta R} - \frac{1}{2} \right) E \quad (2)$$

where $R_1 = R_2 = R$ and $R_3 = R_4$

or

$$e_o = \left(\frac{1}{2 + \frac{\Delta R}{R}} - \frac{1}{2} \right) E \quad (3)$$

where ΔR represents the deviation in resistance of the active element circuit from the ideal conditions assumed in Equation 2. ΔR has many contributing components; lead resistance, change in lead resistance with temperature and acoustic excitation, termination resistance, change in termination resistance with temperature and acoustic excitation, plus the following factors affecting gage resistance: nominal value error, installation apparent strain error, temperature sensitivity, voltage sensitivity, temperature expansion coefficient error, physical distortion of specimen with temperature and installation, and finally, the desired component the change in gage resistance due to strain variation. (This analysis assumes a high impedance load at the bridge output terminals so that the bridge terminals are essentially open-circuited.) The bridge output equations (1 through 3) are purposely expressed in two terms, one for each branch of the bridge, to show the contribution each makes to the output signal. The first term is the contribution of the balancing branch (a constant for a particular measurement). Examination of the first term shows it to be inversely proportional to ΔR and therefore a non-linear function of ΔR .

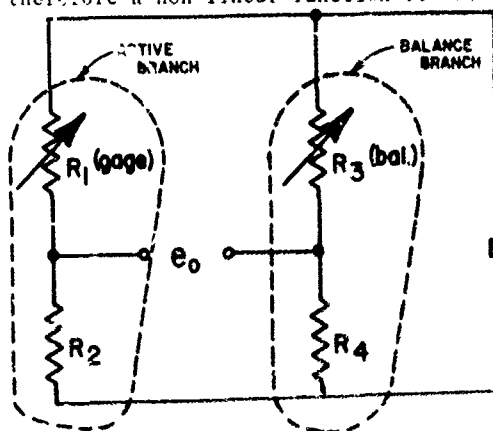


FIGURE 2, SIMPLIFIED BRIDGE CIRCUIT,

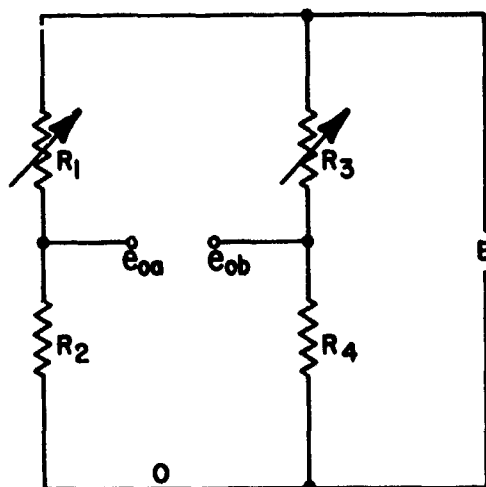


FIGURE 3, BRIDGE CIRCUIT SHOWING INDEPENDENCE OF BRANCH OUTPUTS,

Since there is no circuit element common to both branches and hence no electrical coupling between the outputs e_{oa} and e_{ob} , it is obvious from the circuit diagram given in Figure 3 that the two branch outputs are completely independent of each other. From this observation and the fact that e_{ob} is constant during a test measurement it can be concluded that the bridge output characteristics are completely determined by the active branch. Figure 4 shows a plot of each term of the bridge equation with one side of the excitation source as the zero reference. Curve A, Figure 4 shows the characteristic curve for the active branch output, designated e_{oa} , on Figure 4, as R_1 is varied and Curve B is the d-c balance term output designated e_{ob} on Figure 4 as R_3 is varied. Curve B would normally coincide with Curve A if $R_1 = R_3$, so Curve B is shown on the left for purposes of illustration. When e_{ob} is made equal to e_{oa} the bridge is said to be balanced. However, from the foregoing discussion it was shown that this balance condition has no significance in the bridge operation except to eliminate a d-c offset in the bridge output. For this reason this bridge condition is designated as "d-c balance" in this paper. The location or value of e_{oa} on Curve A, Figure 4, is the operating point and the slope of the Curve at that location on

the Curve is the sensitivity of the bridge to a change in strain.

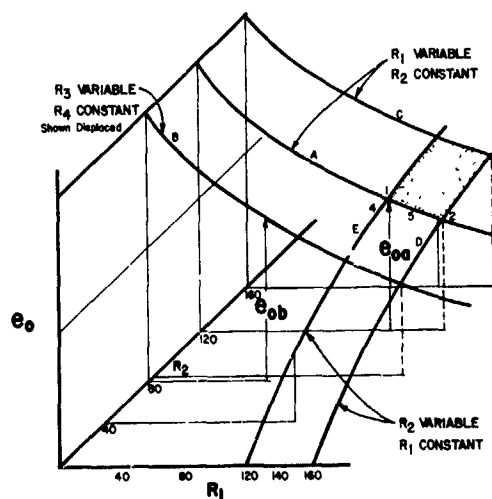


FIGURE 4, PLOTS OF e_{oa} & e_{ob} OF THE CIRCUIT OF FIG. 3.

The sensitivity can be obtained by differentiating the bridge output Equation (3) with respect to the ratio $\frac{R_1}{R_2}$ or Equation 1 with respect to $\frac{R_1}{R_2}$ so that it is independent of nominal value of gage resistance. This gives the sensitivity equation:

$$\text{Sensitivity} = \frac{d e_o}{d \left(\frac{\Delta R}{R} \right)} = \frac{-E}{\left(2 + \frac{\Delta R}{R} \right)^2} \quad (4)$$

(using Equation 3)

$$\text{or} = \frac{d e_o}{d \left(\frac{R_1}{R_2} \right)} = \frac{-E}{\left(1 + \frac{R_1}{R_2} \right)^2}$$

(using Equation 1)

Expressing the change of sensitivity between Points 1 and 2 as a percentage gives:

$$\% \text{ Sens. Change} = \left(\frac{|S_1| - |S_2|}{|S_1|} \right) 100 = \left(1 - \frac{|S_2|}{|S_1|} \right) \times 100 = \frac{\frac{\Delta R}{R} \times 100}{1 + \frac{\Delta R}{R}} \approx$$

$$\frac{\Delta R}{R} 100 = \% \Delta R$$

where S_1 = slope at Reference Point and $|S_1| = \frac{E}{4}$ (for equal arm bridge). It should be noted that the constant term, which represents the bridge balance branch contribution, drops out, which again shows that the balance branch does not influence or determine either the operating point or the sensitivity of the bridge. From Equation 4 it follows that the determining factor establishing the sensitivity is the ratio of the two elements of the active branch.

Another factor of interest in the measurement of strain using constant voltage bridges is non-linearity error. The non-linearity of the bridge manifests itself in different absolute outputs for equal positive and negative excursions of ΔR . This non-symmetry of the strain signal is present at all times and is a direct function of the magnitude of ΔR . This can be shown by calculating the % Non-Symmetry where non-symmetry is defined $|e^-_o| - |e^+_o|$. Expressing this as a percentage the expression is as follows:

$$\% \text{Non-Symmetry} = \left(\frac{|e^-_o| - |e^+_o|}{|e_o \text{ ave}|} \right) \times 100 = \% \Delta R$$

$$e^-_o = \left(\frac{R}{2R - \Delta R} - \frac{1}{2} \right) E = \frac{\Delta R E}{4R - 2\Delta R}$$

bridge output for $R_1 < R_2$

(ΔR negative)

$$e^+_o = \left(\frac{R}{2R + \Delta R} - \frac{1}{2} \right) E = \frac{-\Delta R E}{4R + 2\Delta R}$$

bridge output for $R_1 > R_2$

(ΔR positive)

$$e_o \text{ ave} = \frac{1}{2} (|e^-_o| + |e^+_o|)$$

It should be pointed out that in computing the non-symmetry the constant terms (balance terms) cancel each other and therefore the condition of balance has no effect on the non-symmetry.

SENSITIVITY CORRECTION

The foregoing discussion shows that the sensitivity is a function of the active branch elements only. From a calibration standpoint then it is advantageous to maintain the same ratio of the active branch elements throughout the complete interval of strain measurement. If an unwanted and uncompensated resist-

ance change occurs in the active circuit exclusive of the gage itself, the effect is a change in sensitivity of the bridge. It is then desirable to restore the bridge to its original sensitivity and therefore its original calibration. This can be done by changing the series element R_2 (Figure 2). This sensitivity

correction capability is not provided for in the Sonic Fatigue Facility bridges or in most other commercial bridges. However, when R_2 is changed the operating

point is not returned to the original operating point at Point 1, Curve A, Figure 4, but moves along the Curve D to another Curve C, which has approximately the same slope but is displaced along the R_2 axis to Point 3. Curve D is the operating curve for an equal arm bridge where resistance R_2 is the variable and all

bridge resistances are equal to $R + \Delta R$ at Point 3. The operating Curve for the bridge with these new values of R_1 and R_2

and where R_1 is the variable element is the Curve C. If the offset, however, is caused by an increase in the gage resistance due to heating of the gage, another factor called the gage factor must be considered before the temperature effects on the sensitivity of the bridge can be determined. The expression for strain is $\epsilon = \frac{\Delta R}{R} \times \frac{1}{GF}$ where GF is the gage factor for the strain gage being used. In this

expression the term $\frac{\Delta R}{R}$ is a constant for a given strain regardless of temperature, which means that as R increases ΔR also increases by the same percentage. Since the bridge output is proportional to ΔR

and not to the ratio $\frac{\Delta R}{R}$, the decrease in slope of the operating curve would be largely offset by the increase in ΔR and the bridge sensitivity would remain essentially constant. However, the GF term is temperature sensitive, decreasing with increasing temperature and acts to hold ΔR constant. The net result is that the overall bridge sensitivity follows essentially the slope of the operating Curve A, Figures 4 and 5.

It would seem from looking at Curve C, Figure 5, that the sensitivity could be restored by increasing R_2 and changing the operating point from Point 2 Curve A to Point 3 on Curve C (as for the offset due to lead resistance) where the slope is the same as the original slope at Point 1. However, the slope of these curves is proportional to the ratio of ΔR to the gage resistance which is not

changed by changing R_2 so the sensitivity stays essentially the same.

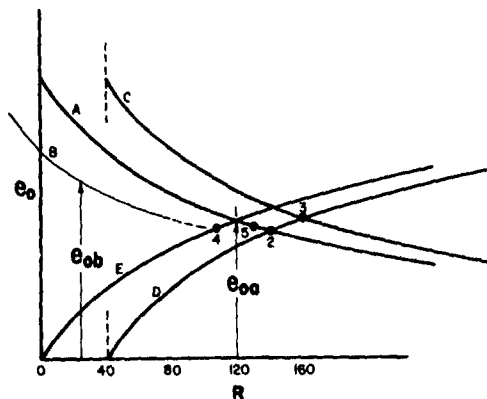


FIGURE 5, TWO DIMENSIONAL PLOT OF FIGURE 4.

CALIBRATION

Calibration of the strain channels at the AFFDL Sonic Fatigue Facility uses the common shunt resistor method in which a precision resistance is shunted across R_2 of Figure 2 or 3 causing an

apparent strain $\epsilon_a = \frac{\Delta R_2}{R_2} \times \frac{1}{GF}$. This

temporarily moves the operating point from Point 1 along Curve E to Point 4 in Figure 4. Curve E is the operating curve for the original equal arm bridge but where R_2 is the variable element.

The voltage difference between Points 1 and 4 is the output due to ϵ_a and from which e_o is calculated using the Equation

$$e_o = \frac{EGF\epsilon_a}{4}. \text{ This is then taken as the}$$

calibration for this apparent strain at the operating Point 1, Figure 4. E is the bridge excitation voltage. This calculation assumes an equal arm bridge configuration. It also assumes that the reduction of R_2 by an amount ΔR_2 causes the same bridge output as an equal increase of R_1 . However, this is not

exactly the case because the Curves for R_1 and R_2 are not exactly symmetrical to each other about their common point for positive and negative deviations respectively of the two elements. It is dif-

ficult to see the relative shapes of Curves A and E, Figure 4, due to the three dimensional nature of the figure. Figure 5 is the same set of curves as Figure 4, but with Curves D and E rotated into the same plane as Curve A and with Curves B, C, and D displaced so as to show the relative shapes of the curves and the output voltages. This displacement is necessary because Curves A, B, and C would be superimposed as would be Curves D and E. It can be seen that the shapes of Curves A and E are such that the output for a negative deviation of R_2 , $(-\Delta R_2)$, is not precisely equal to the output for a positive deviation of R_1 , $(+\Delta R_1)$. There are several ways to show

this and at the same time determine the approximate magnitude of the error. One method is to calculate the output of the bridge using a negative change $(-\Delta R_2)$ of R_2 and for this same output calculate the equivalent change $(+\Delta R_1)$ of R_1 . From these values of ΔR a percentage error can be calculated. Putting these ΔR terms in the bridge Equation (1) yields the following equations:

$$e_{o1} = \left(\frac{R_2}{R_1 + R_2 + \Delta R_{1e}} - \frac{R_2}{R_1 + R_2} \right) E$$

$$e_{o2} = \left(\frac{R_2 - \Delta R_2}{R_1 + R_2 + \Delta R_2} - \frac{R_2}{R_1 + R_2} \right) E$$

Setting $e_{o1} = e_{o2}$ gives:

$$\frac{R_2}{R_1 + R_2 + \Delta R_{1e}} = \frac{R_2 - \Delta R_2}{R_1 + R_2 + \Delta R_2}$$

$$\Delta R_{1e} = \frac{R_1 \Delta R_2}{R_2 - \Delta R_2}$$

where: $\Delta R_{1e} = \Delta R_1$ equivalent of ΔR_2

% Error = % difference between ΔR_{1e} and ΔR_2

$$= \left(\frac{\Delta R_{1e} - \Delta R_2}{\Delta R_2} \right) 100 = \left(\frac{R_1 - R_2 + \Delta R_2}{R_2 - \Delta R_2} \right) 100 \quad (5)$$

For the equal arm bridge case $R_1 = R_2$ and Equation (5) reduces to:

$$\% \text{ Error} = \left(\frac{\Delta R_2}{R_2 - \Delta R_2} \right) 100$$

A very good approximation to this exact expression is given by the series:

$$\% \text{ Error} \approx \left[\frac{\Delta R_2}{R_2} + \left(\frac{\Delta R_2}{R_2} \right)^2 + \left(\frac{\Delta R_2}{R_2} \right)^3 + \dots \right] 100$$

This gives the approximate error for an ideal bridge configuration (equal arm). Suppose the bridge is offset due to some lead resistance in the gage circuit (2 wire system). In this case, the value of R_1 is no longer equal to R_2 and the complete error Equation (5) must be used. As before the exact expression can be approximated very closely by the following:

$$\% \text{ Error} \approx \left[\frac{R_0}{R_2} + \frac{\Delta R_2}{R_2} + \left(\frac{\Delta R_2}{R_2} \right)^2 + \dots \right] 100$$

where $R_0 = R_1 - R_2$ = the offset resistance

The first order approximation then is:

$$\% \text{ Error} \approx \% R_0 + \% \Delta R_2$$

This is quite good for values of ΔR in the range of zero to ten percent. Of course, it is obvious that as the $\% R_0$ term gets larger relative to the $\% \Delta R$ term, which is usually limited to small percentages, that it will become the dominate factor in the error calculation. This shows that the calibration error is increased by approximately the same percentage as the offset resistance causing the offset. This calibration error applies to a gage resistance offset also since the bridge output is not due to a ΔR of the gage itself. It must be pointed out that an optimum calibration procedure would provide calibration at the expected operating point on Curve A without introducing additional errors due to a bridge offset. This would be especially desirable if accurate results are desired when large offsets are anticipated.

The shunt resistance method of calibration, of course, is an indirect calibration method because the source of the calibration signal is not due to the input of a standard quantity of the measurand. This method is based on the calculated value of the bridge offset using known values of some components and assuming the remainder to be ideal. The known component values are the resistances of R_2 and the shunting resistor. The

assumed relationship is that the strain gage circuit resistance and series resistance R_2 are equal. Since calculations are part of the calibration procedure it would seem that a better approach to calibration would be to calculate directly the output of the bridge using some assumed standard value of strain signal. For a known amplifier gain, the output for this standard strain is readily obtained without the added inaccuracies of balance resolution, component, and measurement tolerances. This new method would also eliminate the requirement for balancing the bridge if a-c coupling is used. If the offset change is known, can be approximated, or can be measured the output could be calculated at or near the actual operating point and thus improve the calibration accuracy even more.

ACTIVE LINEAR BRIDGE

The foregoing analysis revealed the fact that maintaining d-c balance is not the solution to eliminating bridge measurement errors, as was originally assumed. The only solution that would eliminate the errors would be a circuit that either eliminated the bridge non-linearity or compensated for it. The auto-balancing bridge circuit, Figures 6 and 7, mentioned earlier, still exhibited the same non-linear bridge characteristics and therefore, was not considered to be a solution to the problem. However, if the circuit of Figure 7 is carefully studied a promising and potentially useful characteristic is noted. To those familiar with operational amplifiers and circuits, it is obvious that the voltage at e_2 must be essentially equal to the voltage at e_1 . If e_1 is constant and if R_2 is a fixed resistance then the current i is also constant. Since the supply voltage E is constant the amplifier current i_a through R_a is also constant and any change of R_a will be exhibited as a linearly proportional change in the voltage at e_o . However, in this circuit the amplifier is required to supply the entire gage current. This undesirable condition can be corrected by reconnecting R_1 as shown in Figure 8.

This, then, is the final circuit arrangement of the active linear bridge. Calculations and measurements confirm the linearity of the circuit for large variation of ΔR . Since the circuit is completely linear, the bridge sensitivity does not change with static offset, and the calibration is a constant regardless of operating point. Thus for dynamic measurements it is not sensitive to static variations of any of the contributing components of ΔR mentioned pre-

viously. In addition, the active nature of the circuit allows the inclusion of compensation for changes in specimen characteristics with temperature. If an appropriate temperature-proportional voltage is inserted in series with e_1 of Figure 8, the static excitation current can be varied to cause a change in sensitivity with temperature.

Another desirable benefit can be obtained from this circuit. If the voltage and resistive parameters are chosen properly, the output voltage e_o can be made zero for zero strain. This permits measurement of static as well as dynamic strain. In the breadboard model of this circuit the excitation voltage E is a ± 15 V dual IC regulator which is also used to supply the amplifier power. This eliminates the requirement for separate supplies for the bridge and amplifier circuits. In this circuit the values of resistors R_1 and R_2 are chosen to give the approximate strain gage current required with the amplifier inoperative. The amplifier is then made operative and the voltage e_1 adjusted to bring the output to zero. In so doing the amplifier drive current is minimized.

SUMMARY AND CONCLUSIONS

The analysis of the constant voltage bridge circuit characteristics has revealed several interesting as well as useful facts which are summarized here.

1. Bridge d c balance does not affect linearity.
2. Bridge d-c balance does not affect sensitivity.
3. Sensitivity of bridge is determined by active branch component values only.
4. Static change in gage circuit resistance causes change in bridge sensitivity (and therefore calibration).
5. % sensitivity change determined to be approximately equal to % ΔR .
6. % non-symmetry determined to be approximately equal to % ΔR .
7. d-c balance unnecessary for dynamic measurements only.
8. Calibration error for shunt resistance method approximately equal to % ΔR + % offset.

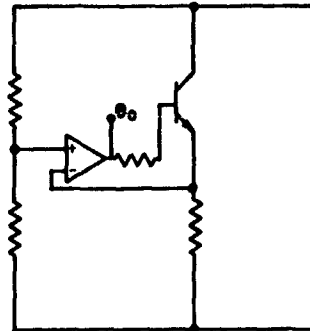


FIGURE 6, ORIGINAL AUTO-BALANCE BRIDGE CIRCUIT

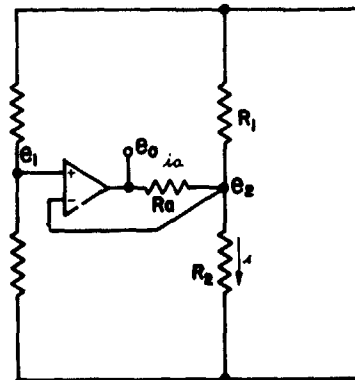


FIGURE 7, SIMPLIFIED AUTO-BALANCE CIRCUIT

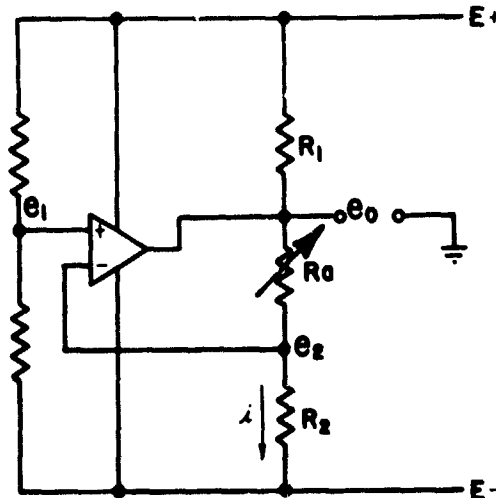


FIGURE 8, ACTIVE LINEAR BRIDGE

The equations developed for % non-symmetry, % sensitivity change, and calibration error, although applicable over the complete useful range of strain gage linearity, are not meant to be exact expressions but only to show roughly the bridge characteristics.

Finally it should be reemphasized the active linear bridge alleviates the problems of calibration and sensitivity change with a change in static operating point.

In the interest of completeness all known factors influencing strain measurement using constant voltage bridges in quarter-bridge configurations have been included without comment as to their relative significance. What may be insignificant today may be most significant in the future, and what may be significant to one may be insignificant to others.

REFERENCES

1. A. W. Kolb and H. A. Magrath, "RTD Sonic Fatigue Facility, Design and Performance Characteristics", Shock and Vibration Bulletin, pp 17-41, January 1968.
2. W. L. Everitt, "Communication Engineering", p 306, McGraw Hill, New York, NY, 1937.

VIKING DYNAMIC SIMULATOR VIBRATION TESTING AND ANALYSIS MODELING

A. F. Leondis
General Dynamics Convair Division
San Diego, California

Ground vibration surveys were performed on the Viking Dynamic Simulator to verify its accuracy in providing in-flight responses equivalent to the actual Viking spacecraft. Modal properties measured included mode shapes, modal damping, frequencies and internal forces in the principal adapter trusses. Damping was measured by means of the free decay and also by means of responses measured during constant-force excitation at various frequencies near resonance.

The ground vibration data were used to modify an analytical model to cause it to more closely simulate the test data. The criteria used to select the best agreement are discussed.

INTRODUCTION

In order to provide increased confidence in the analysis and testing of the Viking Spacecraft and related flight components, the decision was made to fabricate and flight-test a Viking Dynamic Simulator (VDS) on the first Titan Centaur, early in 1974, approximately a year and a half prior to the planned Viking launches.

The Convair Aerospace Division of General Dynamics Corporation provided the services and material necessary to design, fabricate and test the Viking Lander Dynamic Simulator (VLDS) and the Viking Orbiter Dynamic Simulator (VODS). These simulators with the Proof Flight Lander Adapter (PFLA) supplied by the Langley Research Center and the Viking Spacecraft Adapter (V-S/C-A) supplied by the Jet Propulsion Laboratory comprise the VDS. (See Figure 1).

Also shown in Figure 1 is a sketch of the Sphinx spacecraft which was supplied by the Lewis Research Center and was an operational spacecraft. The Sphinx was not part of the primary mission of the VDS.

The basic design requirements for the VDS provided that all important modal characteristics were similar to those of the Viking and that these modes were uncoupled. These requirements also provided for two ground vibration surveys (GVS) to be conducted.

The first GVS was performed on the VODS [1]. The second GVS was performed on the entire VDS and is the subject of this paper as well as Reference [2].

The latter part of this paper also considers the problems encountered in developing the mathematical or analysis model of the VDS [3].

The VDS was cantilevered for the GVS at the base of the Centaur Truss Adapter (CTA). This was particularly desirable because that location was used in analysis as the junction of modal properties of the VDS and the Titan Centaur for modal synthesis using the method of Hurty [4].

It may be noted that the VDS was intentionally designed to have some specific modal characteristics which were considered important in simulation of the Viking and to have no other unrelated modes in the range up to 50 Hz. The result was an ideal dynamic test structure that in the noted frequency range behaved essentially like 3 rigid bodies connected by elastic framework. It is believed that the quality of the results obtained are to some extent due to the VDS being such an ideal structure.

Test objectives included the measurement of modal damping, measurement of

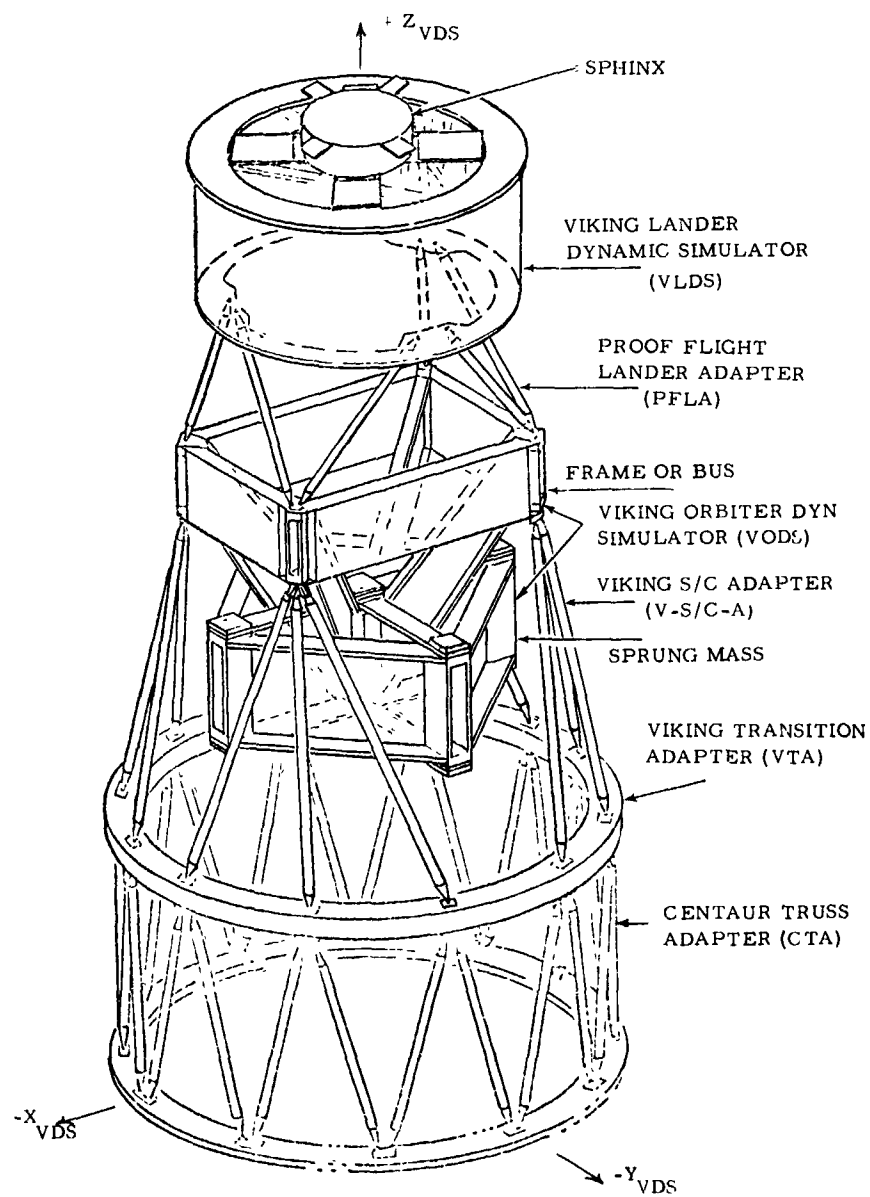


FIGURE 1 - SKETCH OF VIKING DYNAMIC SIMULATOR

forces in both the PFLA and in the V-S/C-A together with frequencies and mode shapes with an accuracy sufficient to show .05 or less modal coupling. Modal coupling was defined as the ratio of the off-diagonal generalized mass term to the square-root of the product of the corresponding diagonal terms.

TEST EQUIPMENT

The foundation for the test specimen was particularly important. Considerable effort was invested to assure that the aft attach points of the specimen would not move. The success of the test depended upon the specimen being cantilevered at the aft end. The foundation was a 12' x 12' x 6" mild steel plate that was carefully leveled, grouted, and anchored to the existing ground level reinforced concrete slab. The selection of this 35 thousand lb. steel plate was partly justified by consideration of the lateral inertia load factors used to design the VDS. The lateral load factor was 2.9 gravities (g's), the VDS weight was 7850 lbs., and the center of gravity was 143 inches above the base. As a result, the combination of such loads would be sufficient to overturn even such a massive base. Of course, it was recognized that such loads would not be used in the course of the test but they helped to justify the base plate. In the course of testing it was found that the base sometimes moved as much as one percent of the motion of the maximum antinode of the test specimen.

Three 50 lb. electro-dynamic exciters were positioned and connected to the specimen through adjustable length drive rods and impedance heads so as to apply oscillatory forces at pre-selected locations. These shakers were adequate for the originally planned test program but could usefully have been larger to provide more force for measurement of modal damping at higher amplitudes. Crystal accelerometers were used to record mode shapes at 33 pre-selected locations.

An exceptional component in the monitoring and data acquisition system was the "CO/Quad Analyzer" [5]. This electronic device provides direct current (DC) voltages that are proportional to selectable amplitude and phase relationships between two applied signals. The reference signal to the CO/Quad Analyzer was a continuous analog voltage from the force section of the impedance head near an exciter. Signals such as acceleration or strain gage outputs from the struts were selected by a matrix switch and resolved with respect to the

force signal. The CO/Quad Analyzer used in combination with tracking filter analyzer was an extremely sensitive frequency and phase monitor of modal excitation.

A digital computer was used extensively for data acquisition, data manipulations, and result formatting.

TEST PROCEDURE

A major factor in planning the sequence of tests was the time required to relocate shakers from one position to another. Depending upon the amount of equipment necessary to move to a different position, it could require as much as a days working time. This, therefore, determined the sequence of tests in many cases.

To search for modes, a number of frequency sweeps were made in which excitation was applied to each of the 6 translation and rotation degrees-of-freedom of the overall test specimen. These sweeps were made from 3 Hz to above 50 Hz. Small force levels were used in conducting these sweeps because it was necessary to insure that the structural integrity of the test specimen was protected against any damage including excessive vibration fatigue. As a result, these tests were conducted at levels not larger than half the limit load conditions used for design or, if ample margins existed, not larger than half the limit load increased by the margin.

The originally planned number of shaker configurations was sufficient to adequately excite all modes predicted by analytical methods prior to testing. In general, the various modes of the structure responded as expected and were similar to the predicted modes.

The existence of the modes was determined by an increase in response at the resonant frequency during the sweep. After completion of a sweep, if the shaker configuration was judged acceptable, one or more mode shapes could be measured while holding the frequency and amplitude constant during a "dwell". The process of tuning the modes of the VDS was, in general, not difficult because of light damping and usually well spaced modes.

The use of a digital computer with an analog to digital converter was particularly valuable in rapidly evaluating the orthogonality or modal coupling between the various measured modes.

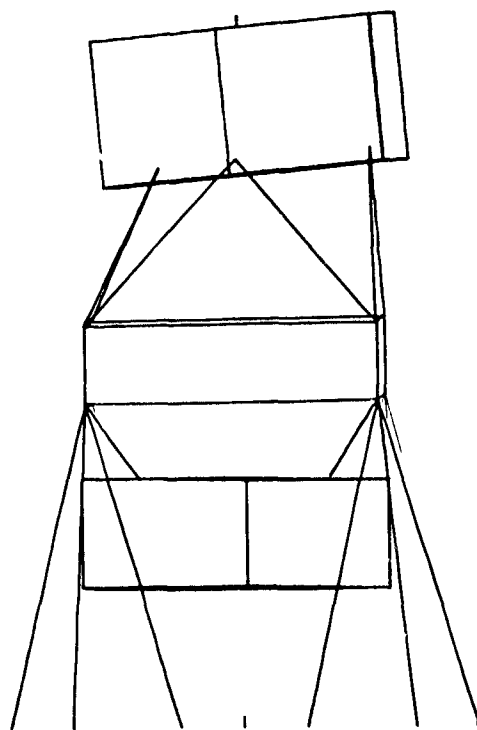
The first mode at 4.48 Hz and the second at 4.66 Hz were first observed to have rather strong coupling of .11. Both of these

modes were similar in that they were essentially rigid body translations normal to the vehicle centerline and roughly normal to each other. The peculiar thing about both of them was that the direction of translation changed counter-clockwise (seen from above) as the amplitude of either mode was increased. This is believed to be due to non-linearities in the various adapters. This effect of rotation of the plane of vibration was stronger than the effect of the direction of the applied force since efforts to use different shaker configurations did not significantly alter the rotation vs. amplitude. The first mode was observed to rotate its plane of vibration 17 degrees while increasing the amplitude from .1 g to .22 g (amplitude of the largest amplitude accelerometer).

Modes 1 and 2 were made orthogonal by selection of modal data taken at amplitudes where their planes of vibration were at right angles. The final coupling value was .0042 and could have been smaller, if desired.

The more standard concept of canceling an unwanted mode while exciting the desired one was used with good results in several cases. If we limit consideration to only those modes below 50 Hz, there are 66 independent coupling terms. Of these, only two remained above the .05 goal at the conclusion of testing. Both of these terms, 1,4 and 11,12 were felt to be due to non-linear action of the PFLA. In Mode 4, the VLDS showed a large amount of torsion and pitch rotation. See Figure 2. (Pitch rotation is about an axis normal to the paper.) This figure and the next two, are idealizations showing the deformations of the structure in three modes of special interest. These figures are orthogonal projections upon the X-Z plane as defined in Figure 1. Each figure shows the measured or test mode at the left and the corresponding mode determined by the NASTRAN computer program at the right for comparison.

Figure 3 shows the mode shape of Mode 11 which had 40 percent coupling with Mode 12,



TEST MODE 4
9.44 Hz

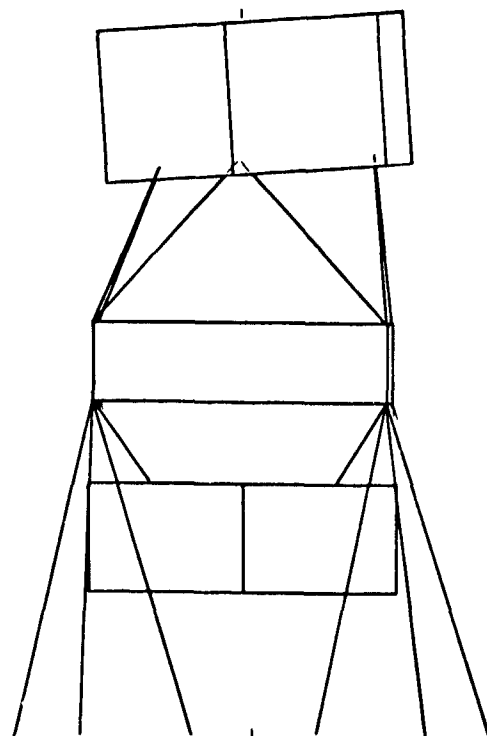
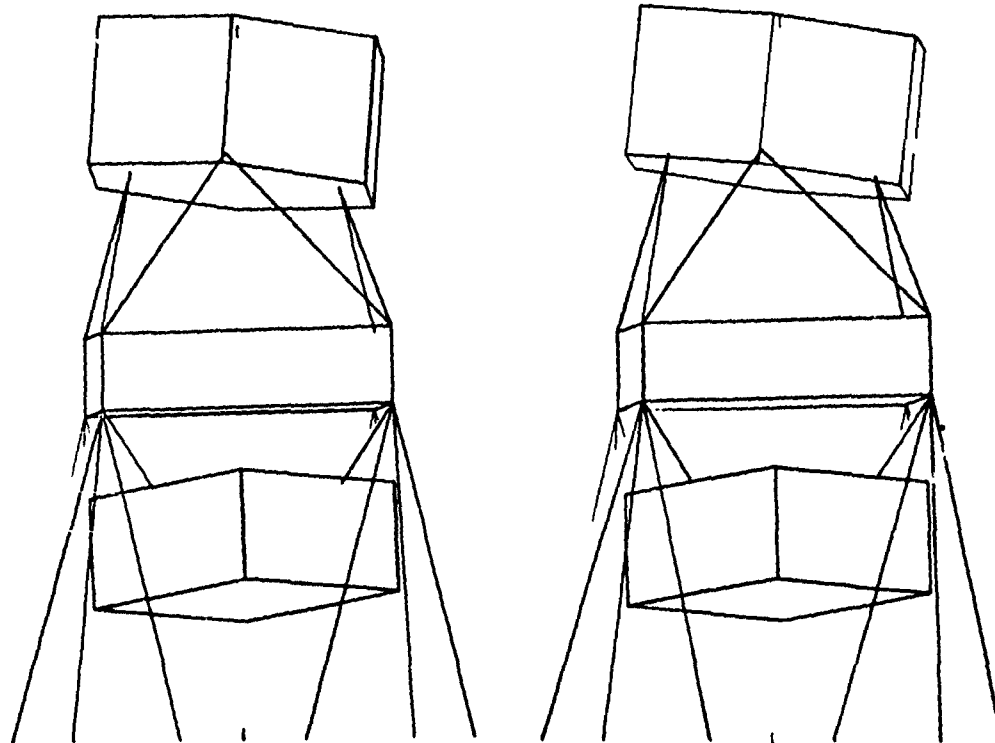


FIGURE 2
ANALYSIS MODE 4
9.45 Hz



TEST MODE 11
42.15 Hz

FIGURE 3

ANALYSIS MODE 11
38.65 Hz

as measured in the test. Mode 12 is shown in Figure 4 (solid line) and may be seen to contain a large amount of pitch rotation. The amount of Mode 11 that was present in (coupled with) Mode 12 was removed and the result plotted as the dotted image in Figure 4. It is considered of interest that the difference between the solid and dotted images in Figure 4 is as large as 40 percent coupling. The final generalized mass matrix is shown in Table 1.

EXPERIMENTAL DAMPING

Experimental damping was determined for the free-decay of the modes by making logarithmic-decrement plots in all cases at high amplitude and sometimes only by the method of number of cycles to half amplitude (n) at smaller amplitudes. The fraction of critical damping was taken as $\ln 2 / 2\pi n$ or $.11/n$. The resulting values of damping are shown in Figure 5 as a percentage of critical damping.

Another method also used to evaluate

damping is based upon the work of Kennedy and Pancu [6]. In this method the vector response of a given measurement may be plotted while a constant excitation force is swept through the frequency range near resonance. The fraction of critical damping,

$$\text{Zeta} = (\Delta F / \Delta \theta) (1/F_n)$$

where ΔF is a difference in excitation frequency between two points of the response.

$\Delta \theta$ is the change of phase angle associated with ΔF (radians) and

F_n is the natural frequency of the mode.

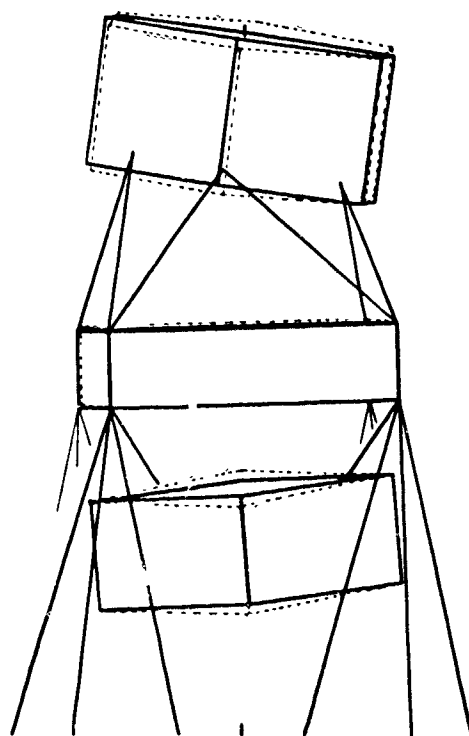
One mode which was examined using this method yielded the following data:

Mode 6 - Freq of Excitation - Response Phase

13.4223 Hz.	77.7 Deg.
13.4234	81.1
13.4244	84.0
13.4257	87.1
13.4268	90.0
13.4279	94.0
13.4291	96.7
13.4302	98.8
13.4315	101.3

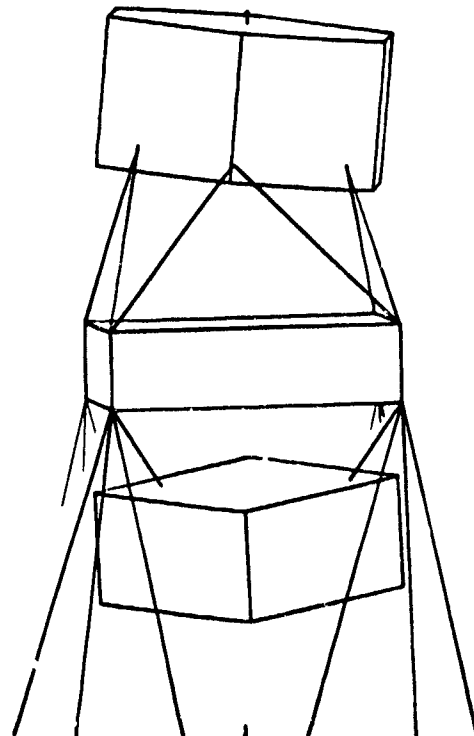
TABLE 1 - GENERALIZED MASS MATRIX (TEST MODES)

Mode	1	2	3	4	5	6	7	8	9	10	11	12
1	1.000											
2	.004	1.000										
3	-.040	-.014	1.000									
4	.089	.006	.007	1.000								
5	-.005	.026	-.010	.030	1.000							
6	-.013	-.019	.044	.006	-.019	1.000						
7	-.016	.027	-.017	.045	+.012	-.032	1.000					
8	.017	-.028	-.033	.026	.005	-.022	.027	1.000				
9	-.018	.017	.019	-.043	.006	-.027	-.003	-.027	1.000			
10	-.002	-.027	.008	-.047	-.041	.007	.034	.006	-.018	1.000		
11	.007	.040	.021	.007	.011	-.011	-.020	.017	-.018	.017	1.000	
12	-.026	-.015	.013	.027	.007	-.000	.001	.019	-.003	-.022	.403	1.000



TEST MODE 12
43.80 Hz

(Dotted image shows change to make this mode normal to Test Mode 11.)



ANALYSIS MODE 12
40.13 Hz

FIGURE 4

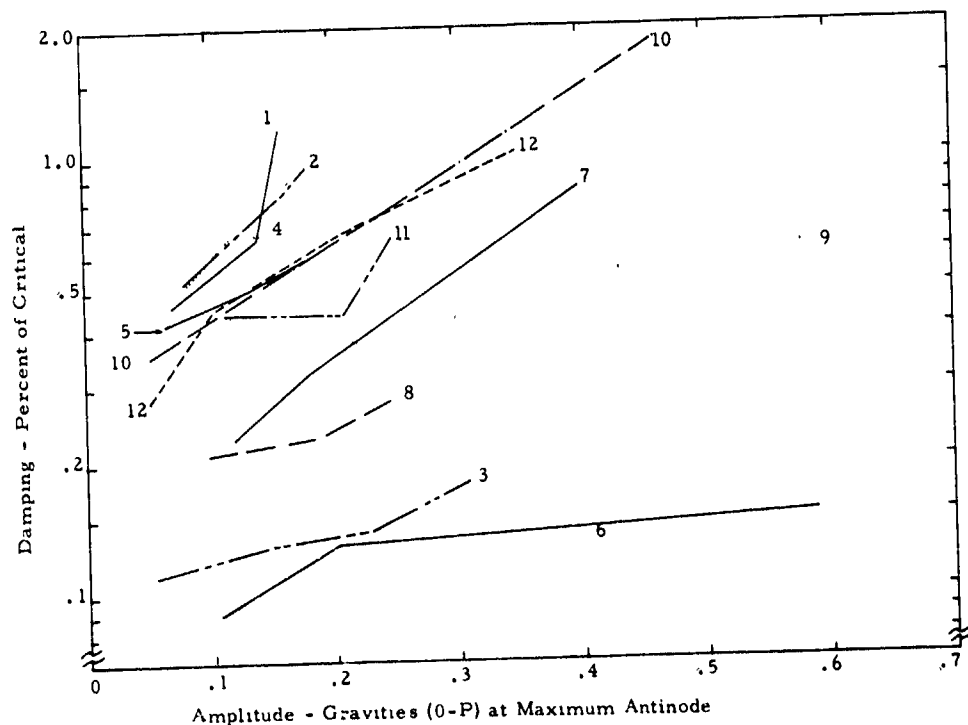


FIGURE 5 - Experimental Damping vs. Amplitude Damping was Determined by Free Decay. Numbers in the Figure Identify the Modes in Order of Increasing Frequency.

In the analysis of such data, it becomes apparent that many combinations of data points may be used and that due to some unavoidable errors, some scatter of the determined damping is to be expected. It is felt that use of adjacent points (such as the 90 deg. pt. and the 94.9 deg. pt.) or points close together will tend to increase the risk of errors while points farther apart tend to minimize these risks. The average of several combinations of far-apart points in the above data provided Zeta = .158% to .166% (measured at a response amplitude of .16 g's). These values may be compared with the damping obtained by free decay, shown below and in Figure 5.

Mode 6 Damping by Free Decay [2]	
Response Amplitude (Max. Antinode)	Damping - Zeta (% C/Cc)
.107 g's	.09
.202 g's	.13
.59 g's	.15

ANALYSIS MODELING PROGRAM

The data obtained in the Ground Vibration Survey have been used directly in some

phases of analysis. It was decided that a mathematical or analysis model should also be available to avoid the inconsistencies associated with non-linearities and experimental error. The logical starting point for such a task was the math model available from the design phase which was written in the NASTRAN program format. This model had been updated several times due to minor changes in the VDS during fabrication and had been used to predict the modes for the GVS. It may be noted that two versions of the math model were developed to account for the differences between the test and the flight article.

One difference was the weight of the Sphinx Spacecraft. The Sphinx model used in the GVS was somewhat lighter than the final flight version. The other difference was in the attachment flexibility of the Centaur Truss Adapter (CTA).

ATTACHMENT FLEXIBILITY

The base of the test specimen used in the GVS was, of course, constrained to a flat and round configuration since it was cantilevered

at that point. The concern for the attachment flexibility centers on the fact that the twelve points which are the base of the test specimen (and also the base of the CTA) are not constrained to remain in a flat and round pattern when attached to the Titan Centaur launch vehicle. This is equivalent to the introduction of additional flexibility, which was not measured in the test.

The method used to account for this effect was to use a "hard" influence coefficient matrix to represent the test configuration and a different "soft" matrix for the flight version. The hard matrix was developed from a theoretical solution with a hard boundary condition which was corrected to agree with the results of a separate test of the CTA structure.

The method of determining the soft matrix was first to evaluate a matrix for an entire elastic model of the CTA and all items down into the region of the Centaur liquid hydrogen tank. Then this model was changed to substitute a rigid structure in place of the CTA and the matrix was reevaluated. The difference between these last two matrices was the theoretical soft matrix including attachment flexibility. This last soft matrix was also corrected by the same ratios used to reflect the CTA test results noted above.

In summary, the "Test Math Model" used the light weight Sphinx and the hard influence coefficient matrix. This model was compared with test data. The "Flight Math Model" used the heavy Sphinx and the soft influence coefficient matrix and was used for analysis to predict flight responses.

OPTIMIZATION OF ANALYSIS MODEL

The method used to optimize the analysis model was one of trial and error with consideration of 5 criteria to indicate the degree of closeness of agreement. Judgement was used to decide which math model parameters might be altered to improve agreement with the test data. The use of the NASTRAN computer program was quite effective and convenient to use for this work and is a credit to those persons in NASA and elsewhere who conceived and developed it.

The criteria used to optimize the test math model were (1) frequency, (2) mode shape plots, (3) effective mass per mode, (4) generalized mass terms and (5) force coefficient data. Frequencies and mode shape plots require little discussion here except to note that Figures 2, 3 and 4 represent a comparison of three test modes shown at the left of the figure and the

corresponding analysis modes. A complete set of these figures is shown in Reference [3].

The "effective mass" of the i th mode of a cantilevered structure in the j th coordinate may be defined as:

$$EM_{ij} = \frac{F_{ij}^2}{\omega_i^4 M_i}$$

where F_{ij} = base reaction force in the j th coordinate per unit generalized amplitude of the i th mode (lb/in or in-lb/in)

ω_i = circular natural frequency of the i th mode (rad/sec)

M_i = generalized mass of the i th mode (lb-sec²/in)

The effective mass is a true property of a cantilevered mode and the sum of the effective masses for all modes equals the total mass property for that coordinate. Most modes are primarily active in one or two coordinates so that their effective masses in other coordinates are small and usually unimportant. In the case at hand, the differences between test and analysis effective masses were divided by the total rigid body mass in each coordinate to better indicate the effect on the whole system. The higher modes contribute only a small effective mass so that this criterion is not critical of errors for higher modes. Modes above the 10th mode were not considered for optimization of the math model but are shown in Table 2. A more complete discussion of effective mass is available in Reference [7].

The generalized mass matrix used for comparison included a full set of analytical modes followed by a full set of experimental modes and the rigid body modes. While such a matrix contains a great wealth of information, the terms used for this criterion were the off-diagonals related to similar modes (e.g. the 1st analytical mode and the 1st experimental mode, etc.). A summary of these terms is shown in Table 3. The reason for Mode 3 having a value greater than one is that the analytical modes were normalized to unit generalized mass in the original NASTRAN solution and were subsequently transformed to 18 degree-of-freedom modes for comparison with the test data. The analytical modes, however, were not renormalized after this transformation so that their generalized masses in some cases (as in the case of Mode 3) were greater than unity.

It may be seen in Table 3 that Mode 12

TABLE 2

PERCENT ERROR OF EFFECTIVE MASS

Defined as $(EM_t - EM_a) 100 / M_{rb}$		
EM_t	=	Effective Mass of Test Mode
EM_a	=	Effective Mass of Analysis Mode
M_{rb}	=	Total Rigid Body Mass
(In the above equation, it is understood that all mass terms must relate to the mass coordinate)		
MODE	COORDINATES (VDS)	TEST MATH MODEL
1	1	-.04
1	5	-.55
2	2	-.98
2	4	-1.04
3	6	-4.8
4	6	-1.87
5	2	-.73
5	4	-1.60
6	3	.33
7	5	-1.65
8	5	1.36
8	6	.60
9	3	.50
10	4	.24
11	6	-.36
12	5	.02

is noticeably worse than the other modes.

The force coefficient data was considered more important than many other responses of the math model because the margins of safety were expected to be somewhat lower on these strut elements. As a result, a somewhat heavier weight was assigned to the importance of having good agreement between the force coefficients for the math model and the test data. To facilitate comparisons, the following relation was devised to represent the composite error (C. E.):

$$C. E. = \left[\frac{\sum_i \left\{ |F_{ti}| \left[\frac{100 (F_{ti} - F_{ai})^2}{F_{ti}} \right] \right\}}{\sum_i |F_{ti}|} \right]^{1/2}$$

TABLE 3

GENERALIZED MASS TERMS BETWEEN
SIMILAR TEST AND ANALYSIS MODES

MODES	TEST MATH MODEL
1	.996
2	.996
3	1.008
4	.991
5	.998
6	.999
7	.998
8	.997
9	.988
10	.947
11	.936
12	.779

where F_{ti} = the force in the i th strut for unit generalized amplitude of a given test mode

F_{ai} = the force in the i th strut for unit generalized amplitude of the corresponding analytical mode

i = an index denoting the various struts (6 for the PFLA and 12 for the V-S/C-A).

In the above relation it may be seen that if all test coefficients in a set are equal in size, the resulting C.E. is the root-mean-square. When the test coefficients are unequal, the errors associated with the small coefficients are reduced while the errors associated with the large coefficients are given greater importance. Table 4 presents the C.E. for the test math model force coefficients.

TABLE 4
COMPARISON OF COMPOSITE
PERCENT ERRORS FOR MODAL
FORCE COEFFICIENTS

TEST MATH MODEL		
MODE	PFLA	V-S/C-A
1	9.62	11.50
2	12.83	7.83
3	10.22	11.01
4	5.49	278.72*
5	6.64	8.38
6	66.33*	13.77
7	14.13	15.18
8	121.51	31.68†
9	6.90	5.78
10	27.96	86.17
11	73.29	156.65
12	60.67	105.20
13	39.47	43.21

* These large errors occur in the adapter which carries the smaller load and the error is caused almost entirely by one test measurement which is much smaller than the corresponding analysis value.

† These large errors are unexplained but Mode 8 involves large motions of the VLDS and the errors may be associated with nonlinearities (clearance) at the ends of the PFLA.

These higher frequency modes are expected to be less accurate than the lower frequency modes.

FINAL ANALYSIS MODEL DATA

The final product intended for pre-flight as well as post-flight analysis included complete mode shape data with generalized mass and stiffness data. The modal data included rigid body modes (for unit deflections of the 6 rigid body degrees of freedom of the base) as well as static elastic modes (for unit accelerations of the same degrees of freedom of the base). The static elastic modes were intended for use in modal acceleration methods such as recommended by Hintz [8].

Force coefficients were provided for the '8 Viking struts and many other members which were detailed in the NASTRAN model but were not measured by test.

Modal damping values recommended for use in analysis were the same as observed in test at the maximum amplitudes tested. This practice is considered conservative in that no mode was observed to decrease its damping at or near these maxima.

REFERENCES

1. J. S. Gacho and A. F. Leondis, "Viking Orbiter Dynamic Simulator Vibration Test Report", General Dynamics/Convair Aerospace Report SD-73-095 (Aug. 1973)
2. A. F. Leondis, "Viking Dynamic Simulator Modal Test Report", General Dynamics/Convair Aerospace Report SD-73-096 (Aug. 1973)
3. A. F. Leondis, "Viking Dynamic Simulator Mathematical Model Report", General Dynamics/Convair Aerospace Report SD-73-097, (July 1973)
4. W. C. Hurty, "Dynamic Analysis of Structural Systems using Component Modes", AIAA Journal Vol. 3 No. 4, (April 1965)
5. Spectral Dynamic Data Sheet SD109B 3/70 "Co/Quad Analyzer", available from Spectral Dynamics Corp. of San Diego, P. O. Box 671, San Diego, Cal. 92112
6. C. C. Kennedy and C. D. P. Panou, "Use of Vectors in Vibration Measurement and Analysis" Journal of the Aeronautical Sciences, Vol. 14, No. 11, pp. 603-625 (Nov. 1947)
7. R. M. Bamford, B. X. Wada and W. H. Gayman, "Equivalent Spring-Mass System for Normal Modes", Technical Memorandum 33-380, Jet Propulsion Laboratory, Pasadena, Cal. (Feb. 1971)

8. R. M. Hintz, "Analytical Methods in Structural Mechanics", General Dynamics/Convair Aerospace Memorandum SD-73-122 (Aug. 1973)

DISCUSSION

Mr. Bockemuhle (Northrop Corporation) You showed a comparison of the analytical mode shapes with the vibration test mode shapes. How did you determine the mode shapes from the vibration test?

Mr. Leonidis. The particular mode shape that you saw was determined by consideration of 18 degrees of freedom relating to the 3 masses and the 6 degrees freedom of each of those masses. Each of the masses were instrumented at several locations and their resonant frequencies were relatively well above the frequency range of the vibration test; as a result the test measurements identified the 6 rigid body coordinates of motion for each of these masses. This constitutes an 18 degree of freedom vector for each mode and the plot is constructed by simply perturbing the undeflected structural picture of the model in the way you would expect it to move in accordance with that mode shape.

ANALYSIS AND FLIGHT TEST CORRELATION
OF VIBROACOUSTIC ENVIRONMENTS ON A
REMOTELY PILOTED VEHICLE

Stephen Zurnaciyan
and

Paul Bockemohle

Northrop Corporation Electronics Division
Hawthorne, California

The specification of dynamic service environments for airborne electronic equipment on a remotely piloted aircraft requires both analysis and flight test data. This paper presents the results of a comprehensive analytical prediction and instrumented flight test program conducted for the evaluation of environmental vibration and acoustic levels on the AQM-34L model remotely piloted vehicle (RPV). Both empirical and analytical techniques were used to arrive at the predicted levels; satisfactory correlation was achieved between these levels and the flight test data. The reported activity was performed by Northrop Corporation Electronics Division under contract to USAF Aeronautical Systems Division with the objective to establish equipment environmental specifications for current as well as future RPVs.

INTRODUCTION

The requirement to specify environmental vibration criteria for the design and testing of airborne electronic equipment has provided considerable challenge to environmental engineers. To satisfy this requirement in terms of a realistic set of specifications calls for extensive flight test data encompassing the full range of operational environments encountered by the equipment. Whenever such data are not readily available, as in the case of a new vehicle design, environmental flight data from a similar vehicle are often used for extrapolation to the new design. A concurrent effort directed at the analytical prediction of the principal sources of vibro-acoustic excitation and the attendant vibratory responses of the vehicle structure and the equipment payloads is essential to the proper establishment of the objective specifications.

This paper presents the results of a comprehensive analytical prediction and instrumented flight test program conducted for the evaluation of environmental vibration and acoustic levels experienced on a representative class of jet-powered remotely piloted vehicles. The reported activity was performed by Northrop Corporation Electronics Division, under contract to the USAF Aeronautical System Division, as part of an overall program for the specification

of vibration, thermal, and climatic environments for airborne equipment installed in future RPV's.

The vehicle class and the equipment complement considered in this investigation belonged to the AQM-34L category of special purpose, air-launched, remotely piloted aircraft shown in Figure 1. It is powered by a single, fuselage-mounted turbojet engine and is launched from the wing of a C-130 carrier airplane. A typical mission consists of the ground test run-up of the RPV turbojet engine, followed by a take-off and carry phase during which the RPV is held under the C-130 wing as shown in Figure 2. Just prior to launch, the vehicle turbojet engine is started. Subsequent to launching, and during the powered free-flight mode, the turbojet engine is the sole source of vehicle propulsion. This portion of the mission is carried out at various speeds and at various altitudes. Upon completion of the mission, the vehicle is brought to a recovery altitude and the engine power is reduced. The deployment of a drogue chute followed by the main chute allows the mid-air recovery of the RPV by a helicopter.

The external configuration of the RPV and the various equipment bays inside the fuselage are also shown in Figure 1. Of particular interest in the present investigation were those equipment payloads stored in the aft bay or the naviga-

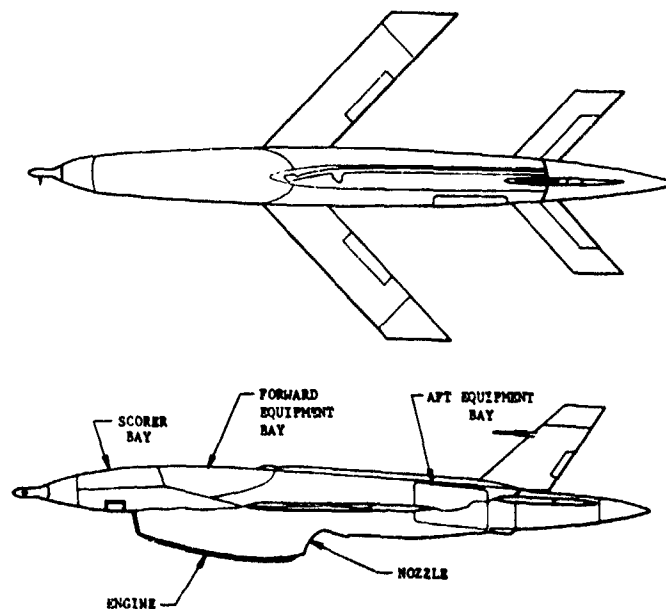


Figure 1 External Configuration of Model AQM-34L Remotely Piloted Vehicle

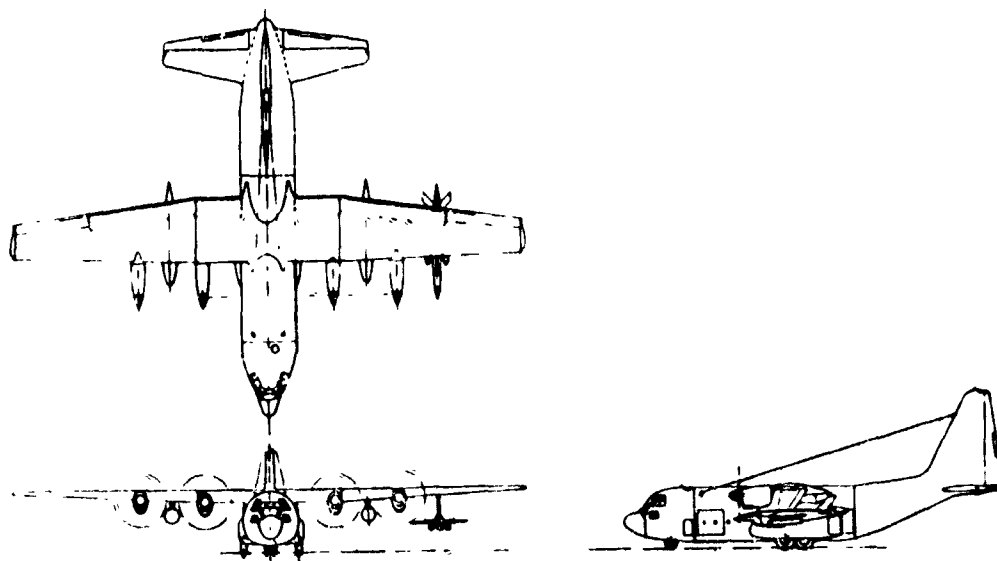


Figure 2 C-130 Launch Aircraft and RPV in Captive Takeoff Mode

tion compartment, the forward equipment bay, and the nose cone or the scorer bay. Operational environments in these equipment locations differed significantly during the various phases of ground run-up, C-130 carry, and powered flight.

Analysis was performed to predict several trends in terms of the worst case vibration response vs. flight condition and external acoustic environment. An empirical correlation technique was used to establish these trends. The analysis was further extended to predict the peak response levels of individual equipment items by using a finite-element dynamic modelling technique based on the detailed mass and stiffness properties of the mounting structure.

The environmental flight test program utilized an AQM-34L model test vehicle and consisted of several ground and flight tests. The dynamics data instrumentation consisted of 29 accelerometers with two flush-mounted microphones. The scope of the flight test program was planned to reflect both normal as well as extreme service environments encountered by the equipment payloads. The resulting data provided both qualitative and quantitative comparisons with the predicted levels and also served to substantiate the underlying assumptions of the analysis. It was concluded that the analytical methods provided realistic predictions of the actual vibroacoustic environments experienced on the subject vehicle. Further refinements of the predictive methods coupled with the expanded usage of digital computers will further enhance their applications on new flight vehicles.

SUMMARY OF PREDICTED VIBROACOUSTIC ENVIRONMENTS

The analytical prediction of vibroacoustic environments on a jet-powered flight vehicle may be achieved in several different ways. A straight-forward analytical approach may consist of predicting a composite acoustic sound pressure field as the loading function to be used in conjunction with an interconnected, finite-element structural model of the total vehicle and its equipment payloads. This approach would represent a costly and time-consuming task. The chosen approach consisted of developing the primary structure response, using an empirical prediction technique, based on the worst case acoustic noise field, and analytically modelling various selected equipment/structure subassemblies to establish the peak vibration responses (1).

The acoustic noise spectra associated with the various external acoustic environments were first established using the pertinent C-130 aircraft and AQM-34L model vehicle data (3). These included the C-130 turbo-prop engine and the turbojet engine acoustic sound pressure levels during ground run-up at maximum power settings. The aerodynamic boundary layer noise levels were established to correspond to the

RPV free-flight mode at low altitude and maximum velocity. These spectra are shown in Figures 3, 4, and 5.

As evidenced by these levels, the vehicle primary structure received the maximum discrete frequency acoustic input from the C-130 prop blade rotations. The fuselage stations aft of the turbojet engine nozzle were subjected to a broadband acoustic field generated by the engine exhaust whereas the forward sections experienced the highest acoustic input from the aerodynamic boundary layer turbulence. During a typical flight, the different input levels from each of the above sources interact over the vehicle surfaces to form a composite acoustic spectrum. No effort was made in the analysis to develop such a spectrum for each flight condition. This was based on the assumption that the various equipment bays treated here reflected zones of maximum acoustic input from each of the aforementioned sources, and that any change in the given sound pressure levels due to superposition would be negligible.

The prediction of the vehicle primary structure response to the external acoustic environment was accomplished through an empirical approach devised by P. T. Mahaffey and K. W. Smith of Convair/Fort Worth. This approach consists of equating previously measured structural vibration data on a B-58 aircraft to the external acoustic sound pressure levels on an octave band basis (2).

In a typical application, the vehicle fuselage stations are partitioned into representative equipment zones where the predicted sound pressure levels remain essentially constant and the corresponding vibration levels are given in terms of wideband acceleration response envelopes.

Despite many obvious differences between the present RPV and the B-58 aircraft, this technique predicts the expected vibration environments with surprising accuracy provided that the excitation is of acoustic origin and broadband in frequency content and the vehicle propulsion is by a jet engine (4). In these areas there is a commonality between the two vehicles. As might be expected, however, the predictions for a smaller vehicle result in vibration levels which are too high in the low frequency region and too low in the high frequency region, as will be shown to be the case here.

The Mahaffey-Smith correlations are established on the basis of various risk levels or upper confidence lines, reflecting the statistical trend associated with the predictions. These levels were selected to be the upper 60% and 95% confidence lines for purposes of comparison. Figures 6, 7, 8, and 9 show the corresponding primary structure vibration levels at selected fuselage locations on the basis of both confidence lines.

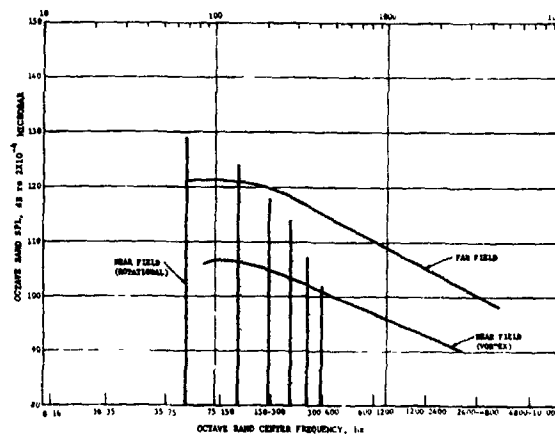


Figure 3 Predicted C-130 Launch Aircraft Turboprop Engine Acoustic Spectra

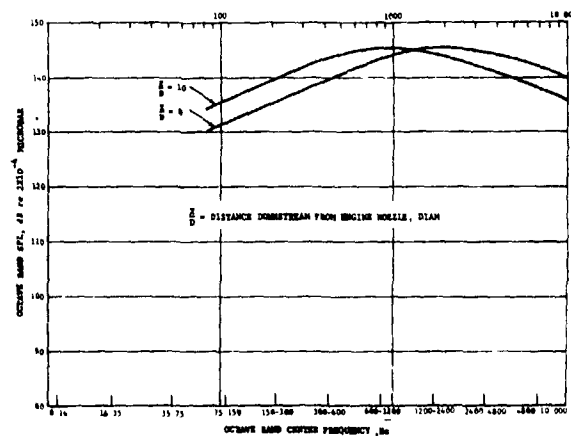


Figure 4 Predicted RPV Turbojet Engine Near Field Acoustic Spectra

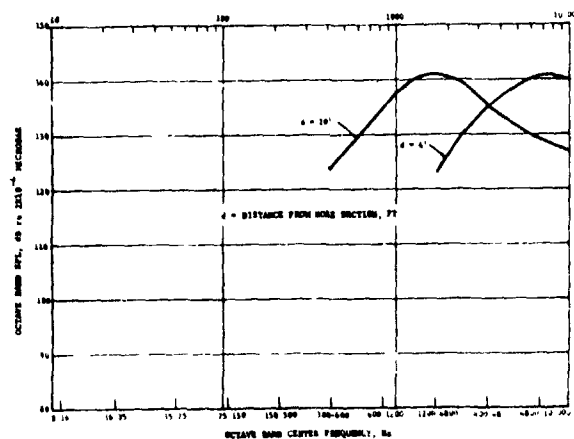


Figure 5 Predicted Acoustic Spectra Due to Aerodynamic Boundary Layer Turbulence

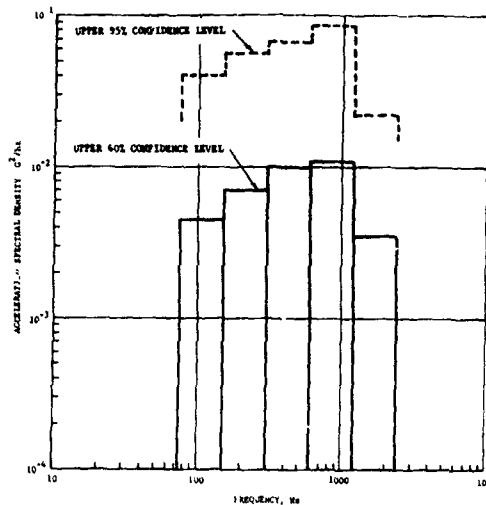


Figure 6 Predicted Acceleration Power Density Spectra at Navigation Equipment Bay of RPV (Turbojet Engine Noise)

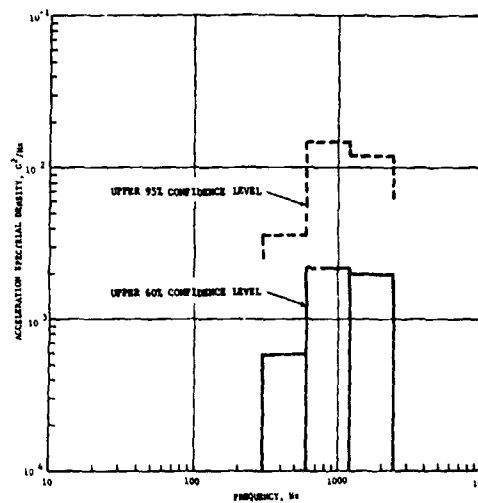


Figure 8 Predicted Acceleration Power Density Spectra at Forward Fuselage Stations of RPV (Aerodynamic Boundary Layer Turbulence)

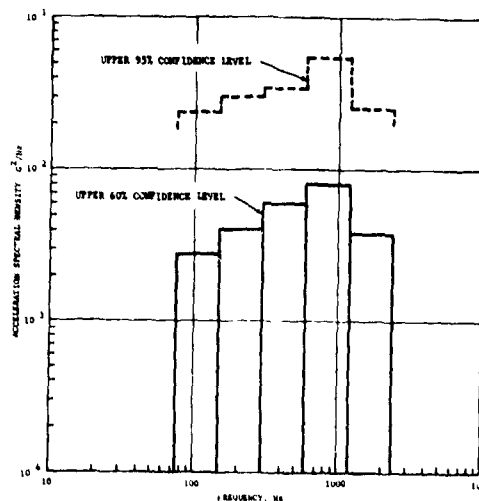


Figure 7 Predicted Acceleration Power Density Spectra at Mid-Fuselage Stations of RPV (Turbojet Engine Noise)

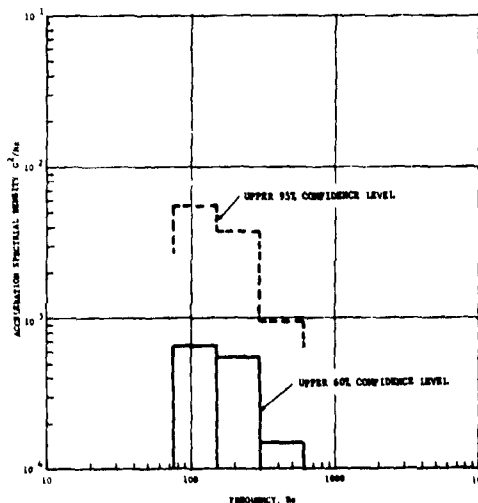


Figure 9 Predicted Acceleration Power Density Spectra at Forward Fuselage Stations (C-130 Propeller Far Field Noise)

PREDICTION OF EQUIPMENT VIBRATION LEVELS

In order to assess the maximum vibratory response of equipment payloads installed in a typical RPV, certain equipment items in the AQM-34L vehicle were selected for detailed analysis. The primary selection criteria were that the particular equipment had to be functionally critical and also be typically mounted by the use of a built-up, secondary structure. Furthermore, at least one equipment item with its inde-

pendent mounting assembly was to be included from each of the principal fuselage compartments. This resulted in the selection of the following equipment/structure assemblies:

1. The Scorer equipment and mounting frame;
2. Forward equipment and shelf assembly;
3. Flight Control, Heading/Turn-Rate, Interconnecting equipment assembly;

4. Computer/Converter and tray assembly.

The procedure that was followed in the vibration response analysis centered on the accurate prediction of the equipment vibration transmissibilities along the three reference axes. This was accomplished by constructing the appropriate finite-element structural models corresponding to each of the foregoing equipment/structure assemblies. For simplicity, it was assumed that each equipment item behaved as a rigid body without regard to its packaging or internal vibration characteristics and that the spring/dashpot properties were derived solely from the stiffness and construction of the secondary mounting structure, i.e., tray, frame, rails, etc. Figures 10 a, b and 11 a, b illustrate the actual configuration and the finite-element structural model, respectively, of the Scorer equipment and its mounting frame. Similar analysis techniques were used in generating the dynamic models for the other equipment, as

shown in Figures 12, 13, and 14. A digital computer program was used to calculate the mode shapes and the modal frequencies of each equipment/structure assembly. Figures 15 a, b, c, and d are typical geometry view plots of the four assemblies. Typical vibration mode shapes and frequencies are shown in Figure 16 corresponding to the first six modes of the Scorer equipment and the mounting frame. The computer generated modal data were subsequently used by the same program to compute the desired base motion transmissibility functions for each equipment item considered in the analysis. Representative transmissibility curves from each of the four equipment assemblies are shown in Figures 17, 18, 19, and 20. The viscous damping constant associated with each curve is also given as a percent of the critical.

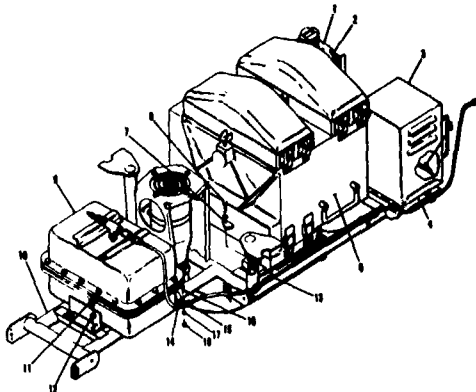


Figure 10(a) Pictorial View of Scorer Equipment Assembly

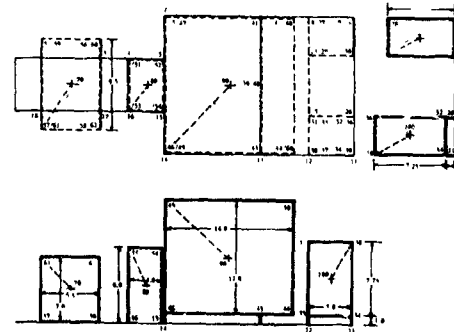


Figure 11(a) Finite-Element Vibration Model of Scorer Equipment Assembly

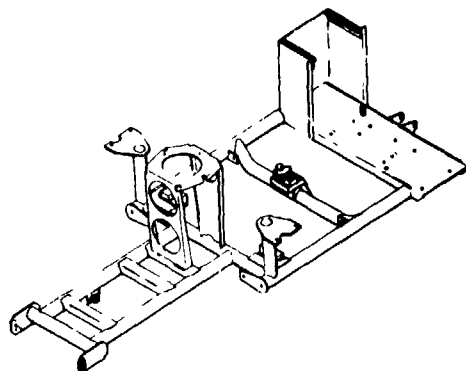


Figure 10(b) Pictorial View of Scorer Mount Frame

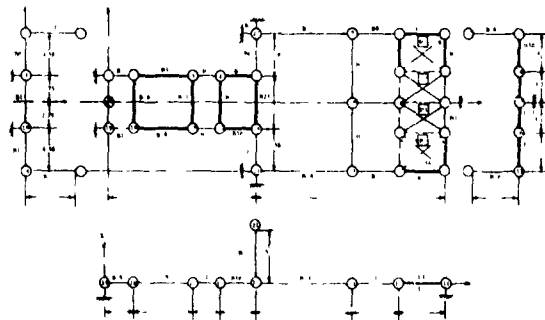


Figure 11(b) Finite-Element Vibration Model of Scorer Mount Frame

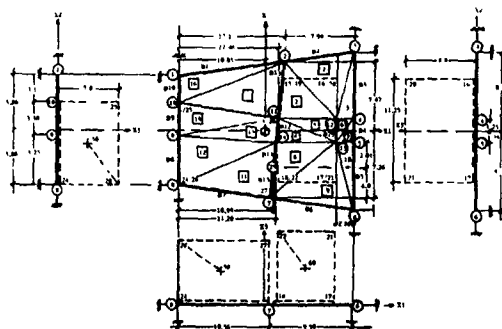


Figure 12 Finite-Element Vibration Model of Forward Equipment Shelf Assembly

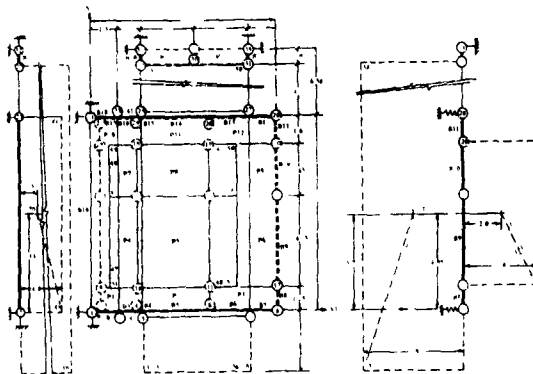


Figure 13 Finite-Element Vibration Model of Flight Control Equipment Assembly

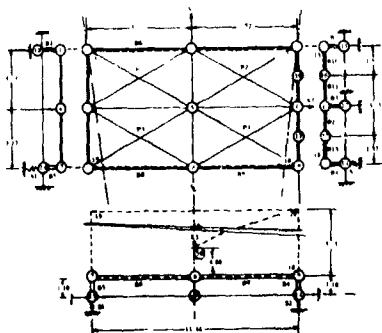


Figure 14 Finite-Element Vibration Model of Converter/Computer Equipment Assembly

The analysis of the equipment vibration response was performed as if each equipment and its mounting structure were driven by the vehicle primary structure at a set of fixed boundary points. The resulting prediction is analogous to the solution of a linear, multi-degree freedom system subjected to a prescribed base motion (5, 6, 7). The equipment acceleration levels were computed by multiplying the primary structure vibration levels by the square of the transmissibility along each axis and enveloping the resulting curves in the form of straight line vibration envelopes. Figures 21 a, b, and c illustrate the resulting response envelopes for a typical equipment mounted inside the aft fuselage compartment.

SUMMARY OF MEASURED VIBROACOUSTIC ENVIRONMENTS

The field measurement of the vibroacoustic environments on the AQM-34L model RPV was conducted during several flight events and ground tests. These conditions reflected both normal as well as extreme operational environments of the vehicle and its equipment payloads. For data collection purposes, these operational environments were grouped into three distinct modes. These were the ground test stand engine run-up, the C-130 captive flight, and the free flight.

Acoustic sound pressure levels were recorded during each of these modes by means of two flush mounted microphones as shown in Figure 22. The choice of the microphone placement locations was based on the expected severity of the acoustic sound pressure levels at the respective fuselage stations.

The maximum octave band sound pressure levels were recorded by the aft microphone during the ground engine run-up mode at maximum power settings and also during the low altitude free flight mode. These levels are shown in Figure 23.

The acoustic environment resulting from the aerodynamic boundary layer turbulence was recorded by the forward microphone during the free flight mode at low altitudes and maximum speed. The octave band sound pressure levels corresponding to this environment are shown in Figure 24. Also shown in Figure 24 are the sound pressure levels experienced at the forward fuselage stations due to the ground engine run-up which were included to characterize the worst case acoustic environments generated by the turbojet engine at these locations.

The C-130 captive flight measured acoustic sound pressure levels are shown in Figure 25 which were recorded by the forward microphone under take-off conditions. The high and low levels represented the right and left pylon mounting configurations, respectively, under the

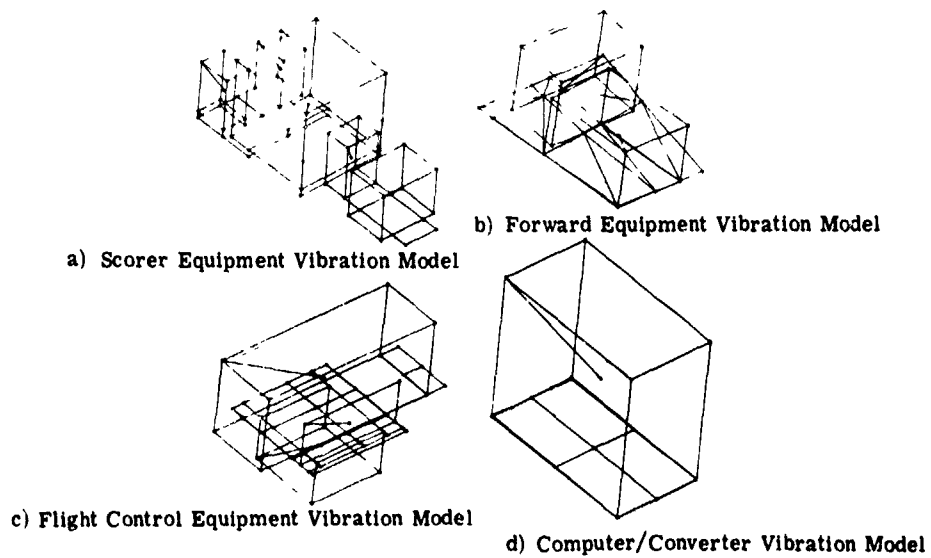


Figure 15 Geometry View Plots of Various Equipment Assembly Vibration Models

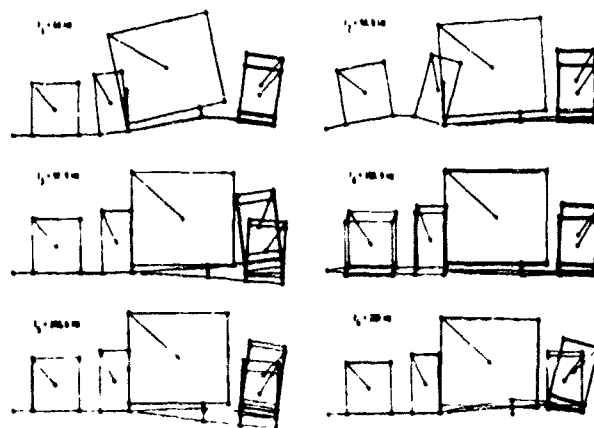


Figure 16 First Six Vibration Mode Shapes and Corresponding Frequencies of Scorer Equipment Assembly

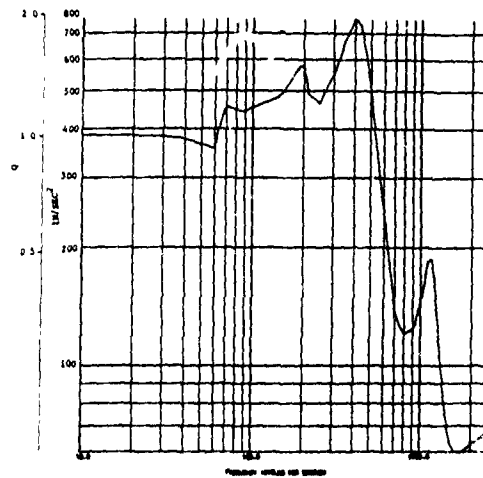


Figure 17(a) Transmissibility Along Fore-Aft Axis of Typical Scorer Equipment ($C/C_{cr} = 10\%$)

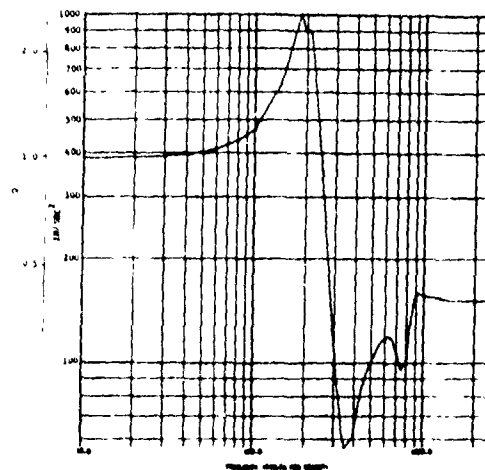


Figure 17(b) Transmissibility Along Lateral Axis of Typical Scorer Equipment

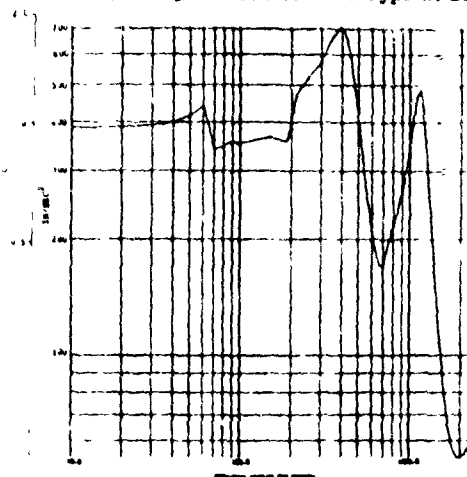


Figure 17(c) Transmissibility Along Vertical Axis of Typical Scorer Equipment

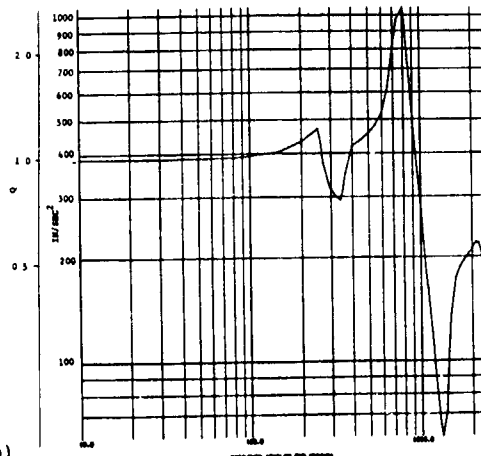


Figure 18(a)
Transmissibility Along Fore-Aft Axis of Typical Forward Bay Equipment ($C/C_{cr} = 10\%$)

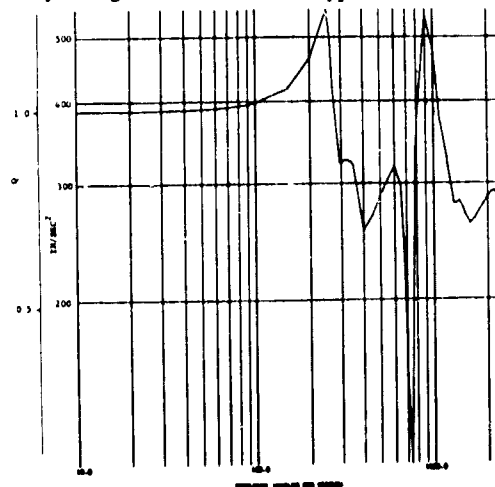


Figure 18(b) Transmissibility Along Lateral Axis of Typical Forward Bay Equipment

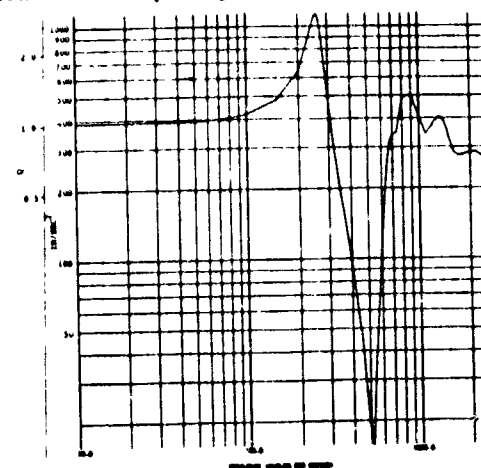


Figure 18(c) Transmissibility Along Vertical Axis of Typical Forward Bay Equipment

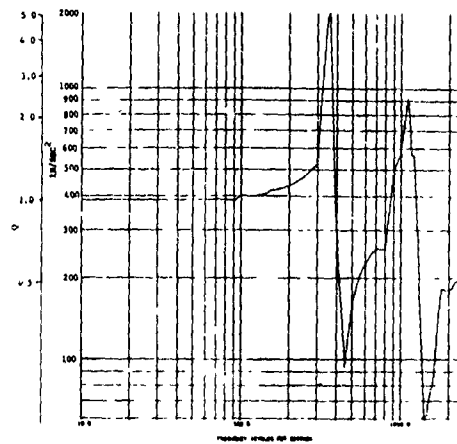


Figure 19(a)
Transmissibility Along Fore-Aft Axis of Typical Flight Control Equipment ($C/C_{cr} = 4\%$)

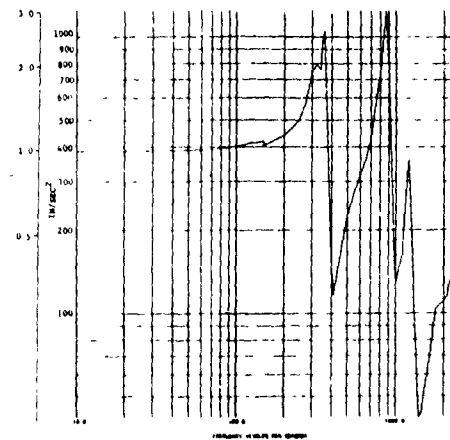


Figure 19(b) Transmissibility Along Lateral Axis of Typical Flight Control Equipment

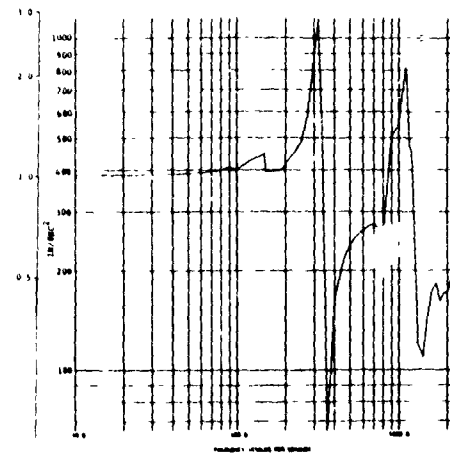


Figure 19(c) Transmissibility Along Vertical Axis of Typical Flight Control Equipment

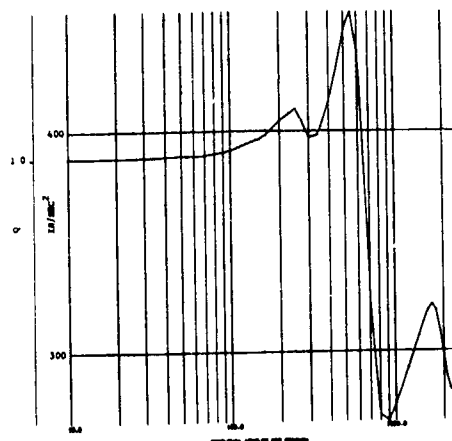


Figure 20(a)

Transmissibility Along Fore-Aft Axis of Computer/Converter Equipment ($C/C_{cr} = 10\%$)

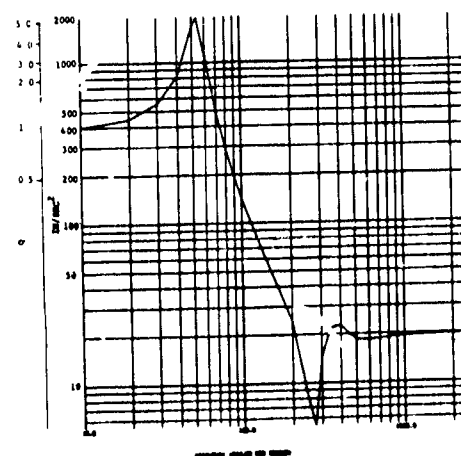


Figure 20(b) Transmissibility Along Lateral Axis of Computer/Converter Equipment

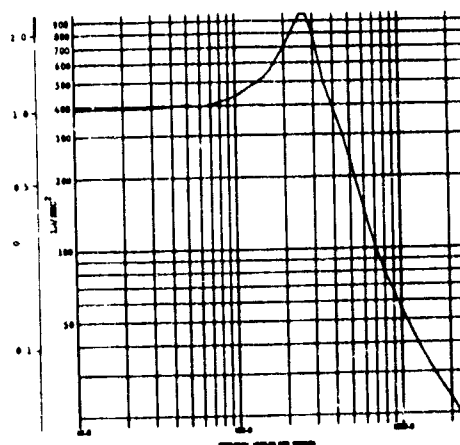


Figure 20(c) Transmissibility Along Vertical Axis of Computer/Converter Equipment

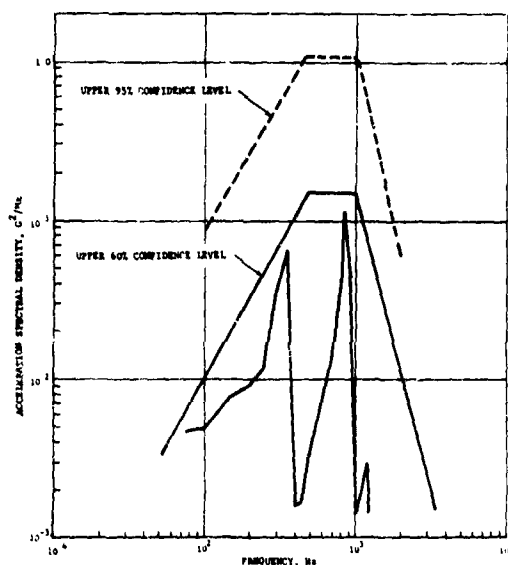


Figure 21(a) Predicted Acceleration Power Density Spectra Along Lateral Axis of Typical Equipment in Aft Fuselage Section

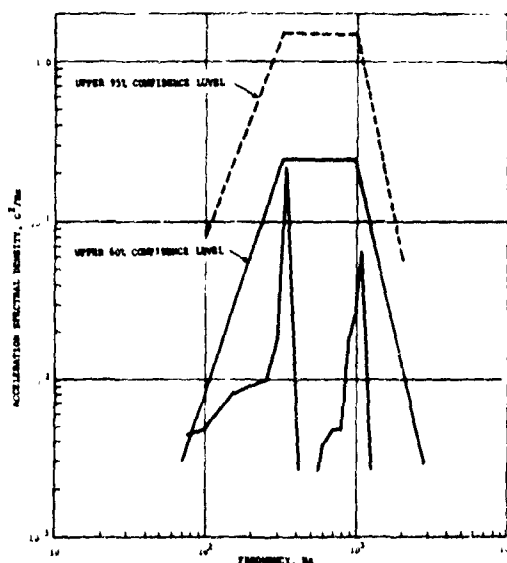


Figure 21(b) Predicted Acceleration Power Density Spectra Along Fore Aft Axis of Typical Equipment in Aft Fuselage Section

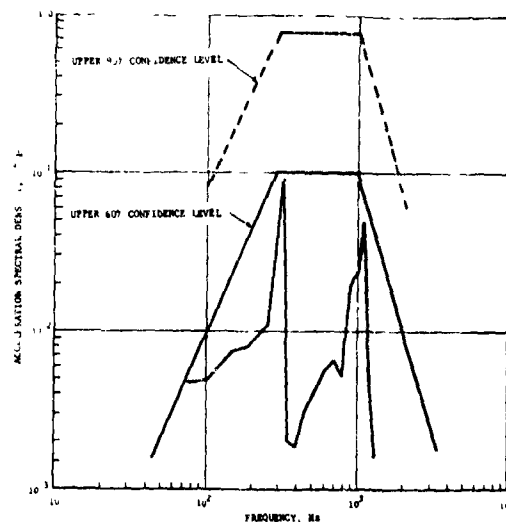


Figure 21(c) Predicted Acceleration Power Density Spectra Along Vertical Axis of Typical Equipment in Aft Fuselage Section

C-130 wing. The first few frequency peaks noted in Figure 25 represented the propeller rotational frequencies of the C-130 turboprop engines.

The vehicle primary structure vibration levels resulting from the foregoing acoustic environments were measured by means of accelerometers installed at critical location on the airframe as shown in Figure 22. The sensing axis of each accelerometer is also shown with respect to the vehicle reference axes. Time intervals of recorded vibration data during the various ground test and flight events were selected which were sufficiently stationary to allow acceleration spectral density analyses using a "real time" spectrum analyzer and an ensemble averager. An effective filter bandwidth of 6.4 Hz over the frequency range of 10 to 2000 Hz was also used. The results were given in the form of composite straight line envelopes established by the acceleration spectral density graphs corresponding to each measurement axis.

The highest overall vibration levels of the primary structure were noted in the mid- and aft-fuselage stations of the vehicle corresponding approximately to the location of the navigation equipment bay. These levels are shown in Figures 26 and 27. The severity of the vibration levels at these locations were attributed to the turbojet engine acoustic noise levels formed at the exhaust nozzle and its vicinity at maximum power settings of the engine during powered flight and ground test run-up modes.

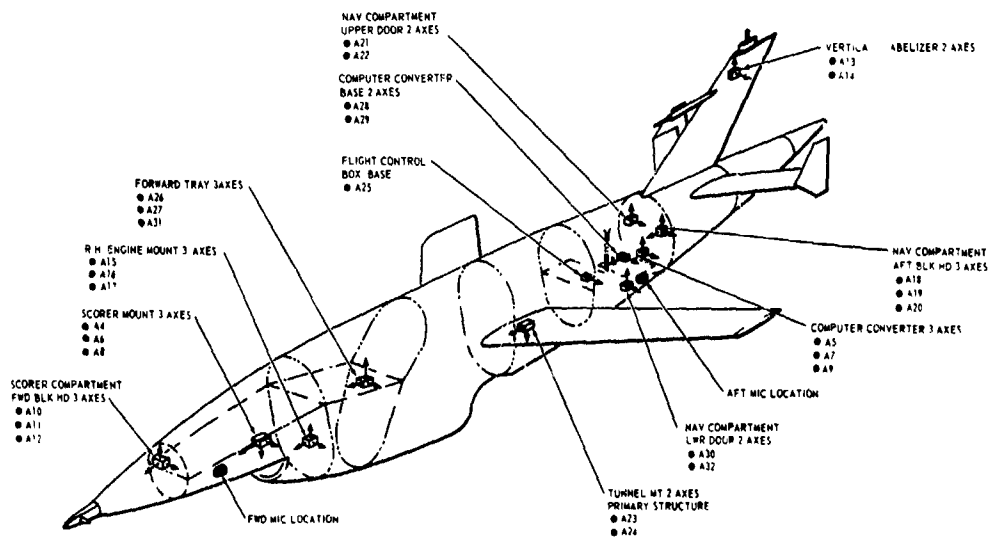


Figure 22 Accelerometer and Microphone Instrumentation Placement on Vehicle Airframe

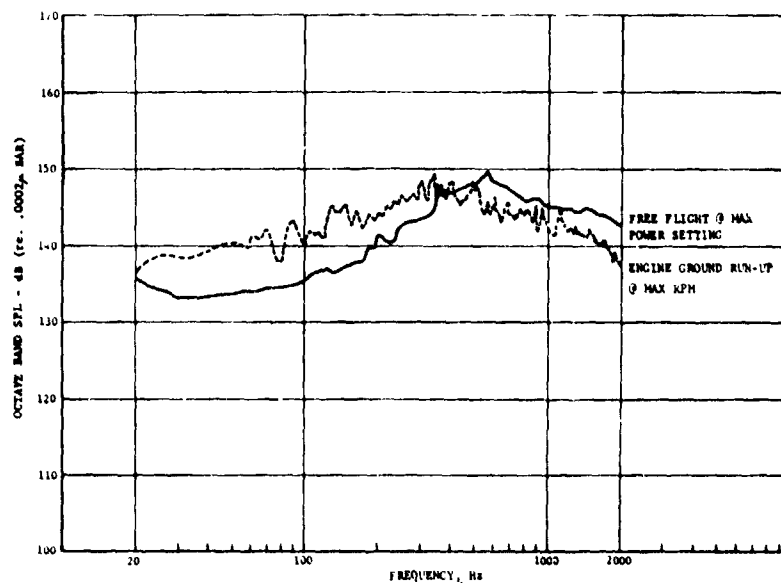


Figure 23 RPV Turbojet Engine Acoustic Spectra Measured at Aft Microphone Location

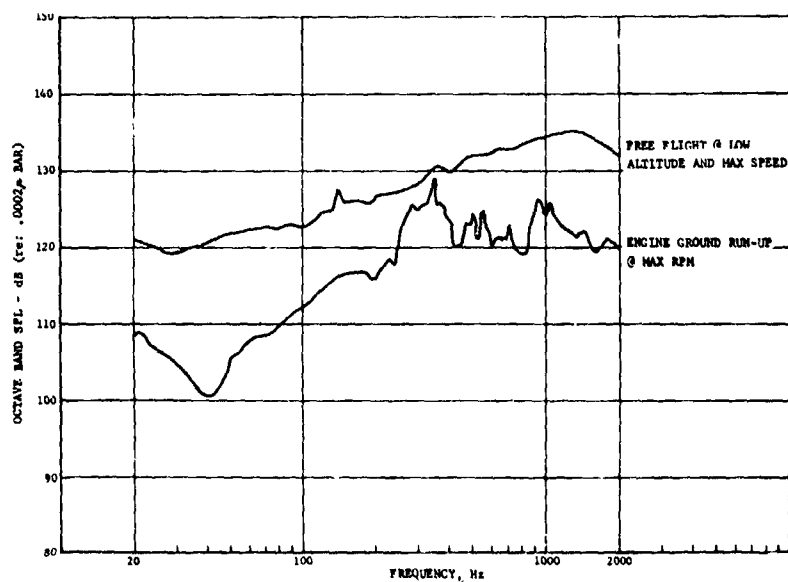


Figure 24 Acoustic Spectra Measured at Forward Microphone Location Due to Boundary Layer Turbulence and Engine Ground Run-up

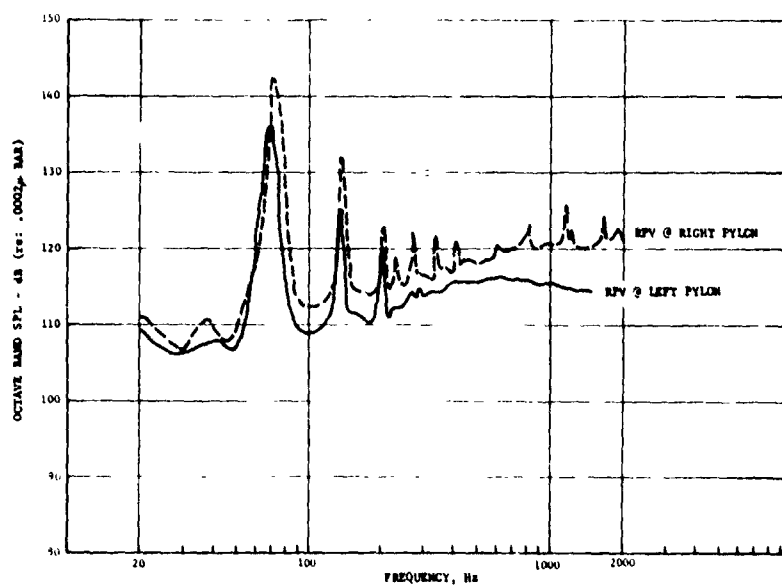


Figure 25 C-130 Acoustic Spectra Measured at Forward Microphone Location During Captive Take-off

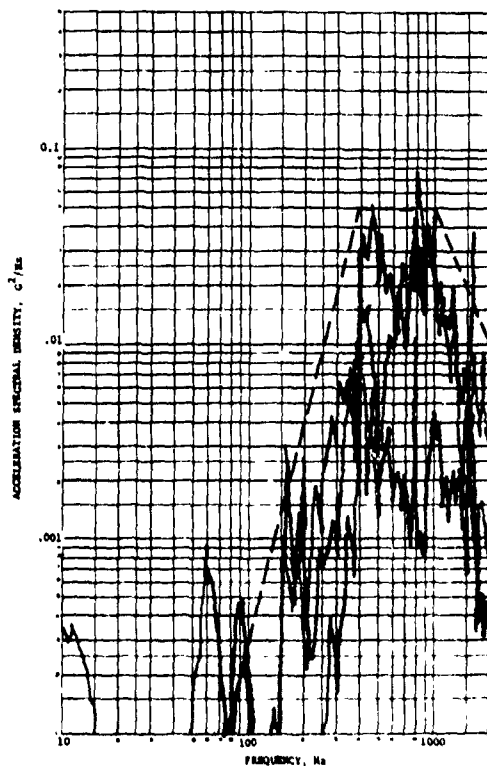


Figure 26 Measured Acceleration Power Density Spectrum at Mid-Fuselage Stations

The vibration levels experienced at the forward fuselage stations were attributed primarily to the aerodynamic boundary layer turbulence during low altitude, high speed powered flight of the RPV. These levels were considerably lower than the aft fuselage structural vibrations noted earlier with a distinct shift towards higher frequencies. Figures 28 and 29 depict the aerodynamically induced vibration levels at the Forward equipment bay and the Scorer bay in the forward fuselage sections of the RPV, respectively.

The vibration measurements at these stations also showed the presence of discrete frequency response peaks corresponding to the C-130 propeller blade passage harmonics during captive take-off. These levels were noted not to exceed $0.5 G_{pk}$ along any axis.

CORRELATION BETWEEN PREDICTED VS. MEASURED VIBROACOUSTIC ENVIRONMENTS

The analytical prediction of the vibration environments on the AQM-34L model RPV was predicted on the major assumption that the primary excitation was random and essentially

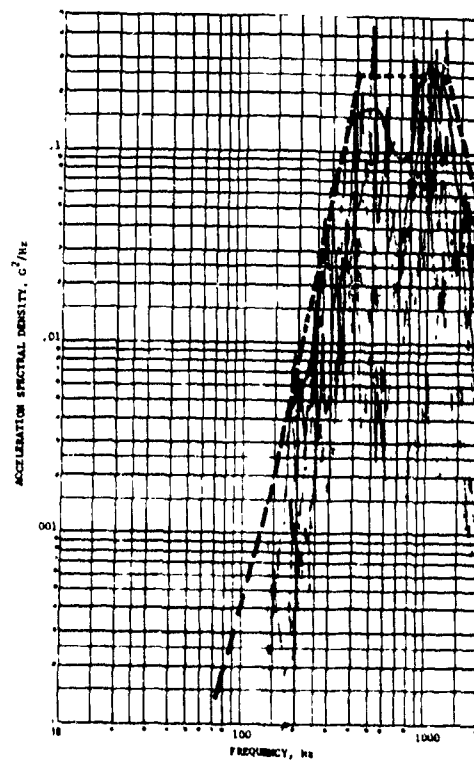


Figure 27 Measured Acceleration Power Density Spectrum at Navigation Equipment Bay

acoustic in origin. It was further assumed that the vibration levels experienced by the vehicle primary structure in turn resulted in the random response of the secondary structure and the equipment payloads. A careful review of the flight and ground test data substantiated these assumptions.

The analysis indicated that the maximum vibration response levels in the aft fuselage stations downstream from the engine exhaust nozzle would result from the ground engine run-up at high rpm settings. Similarly, the maximum vibration response levels in the forward fuselage stations would result from the aerodynamic boundary layer turbulence produced during low altitude, high speed, powered flight. It was also predicted that the C-130 launch aircraft captive environment did not contribute to any significant vibrations of the vehicle structure in comparison to the foregoing levels. The presence of certain discrete frequency sinusoids due to the turbo-prop engine rotational effects were below these levels on an overall basis. The measured vibroacoustic levels on the test vehicle were in general agreement with these trends.

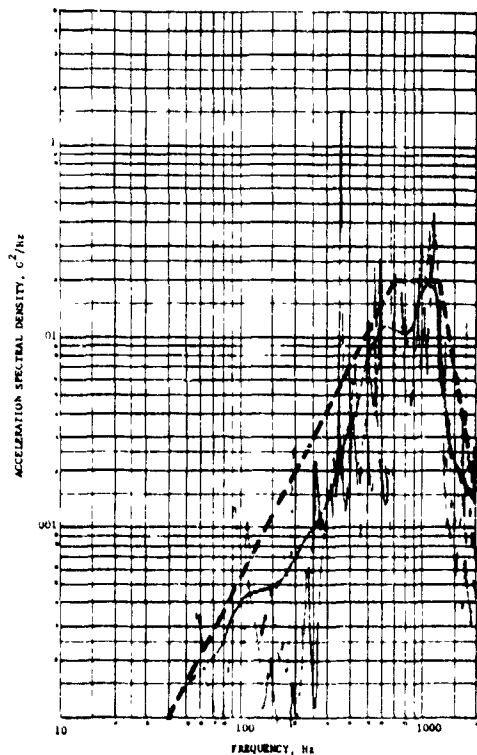


Figure 28 Measured Acceleration Power Density Spectrum at Forward Equipment Bay

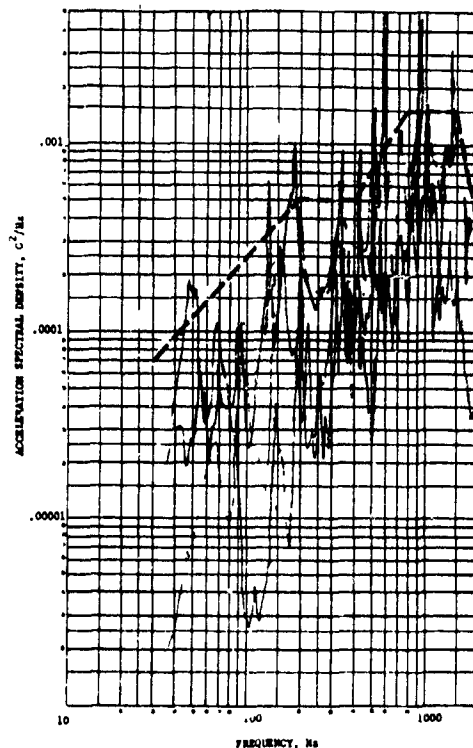


Figure 29 Measured Acceleration Power Density Spectrum at Scorer Equipment Bay

In assessing the magnitudes of the vibration levels predicted by the Mahaffey-Smith technique and their correlation with the measured levels, it is useful to start first with the external acoustic sound pressure levels. Figure 30 illustrates the correlation between the predicted vs. measured acoustic environments at aft fuselage stations. The $X/D = 0$ curve represents the predicted levels at the nozzle location and $X/D = 10$ at the position of the aft microphone, which is roughly the center of the Navigation equipment bay. The latter curve gives levels that are within 5 dB of the measured levels and is considered acceptable. The predicted acoustic levels at $X/D = 10$ were utilized in the Mahaffey-Smith prediction of the primary structure vibration levels at the Navigation equipment bay. Both 60% and 95% confidence levels were used in these predictions as shown in Figure 6.

Figure 31 illustrates the correlation between the predicted levels vs. the narrowband primary structure response measurement at the same location. As evidenced by these levels, the 60% curve predicts too low of a vibration level, however, the 95% curve yields an acceptable prediction. Even this curve does not completely equal the straight line envelope of the measured levels. A comparison of the predicted

vs. measured levels shows that the predictions are approximately 10 dB higher in the low frequency region and about 5 dB lower in the high frequency region than the measured levels. This result agrees well with the long-held notion that the Mahaffey-Smith technique, which was based on the large B-58 aircraft data, predicts too high a level in the low frequencies and too low a level in the higher frequencies for a smaller vehicle.

Figure 32 illustrates the predicted vs. measured acoustic environments at the forward fuselage stations. The forward microphone is located approximately 4 ft. aft of the vehicle nose section. The acoustic prediction for $X = 4$ ft. does not agree well with the measured levels; in fact, the predicted levels for $X = 20$ ft. come closer to the measured data. This indicated that the actual turbulence was greater than predicted at fuselage stations aft of the nose section. This was further reinforced by the presence of the attitude reference indicator at 3.5 ft. upstream from the microphone location which resulted in the higher boundary layer turbulence due to its protuberance into the airflow.

The resulting Mahaffey-Smith prediction of the primary structure vibration levels at the Scorer equipment bay was based on the latter

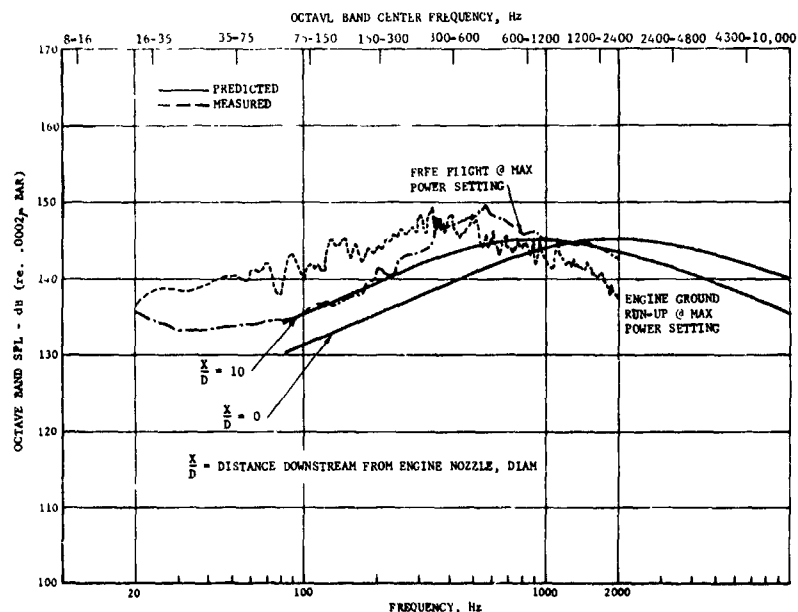


Figure 30 Predicted vs Measured Turbojet Engine Acoustic Spectra at Aft Microphone Location

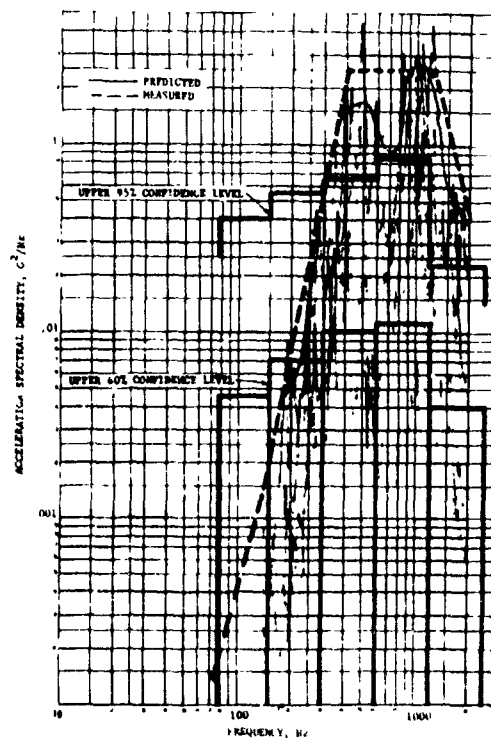


Figure 31 Predicted vs Measured Acceleration Power Density Spectra at Navigation Bay

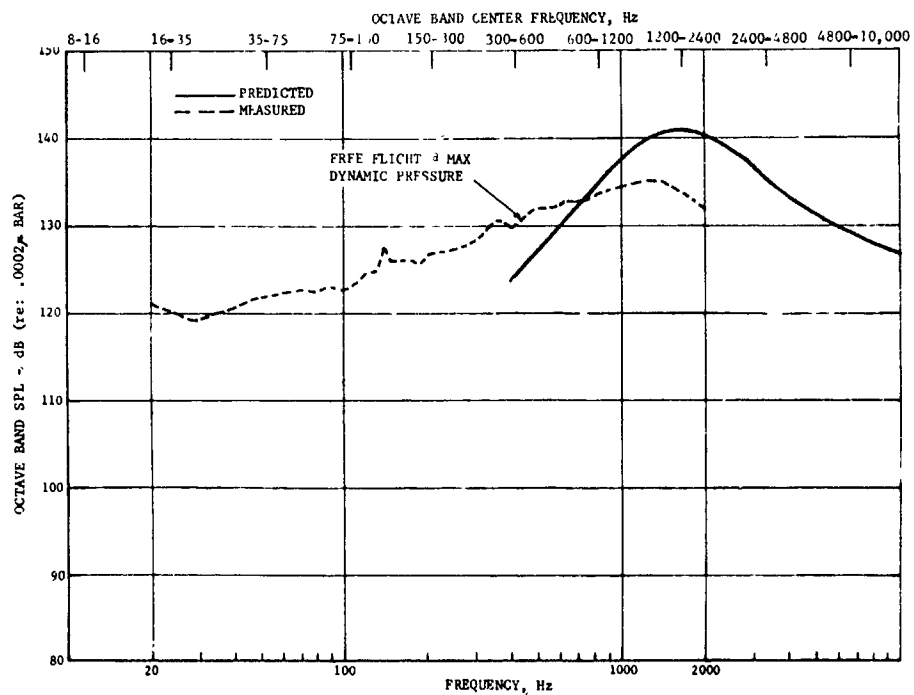


Figure 32 Predicted vs Measured Acoustic Spectra at Forward Microphone Location Due to Aerodynamic Boundary

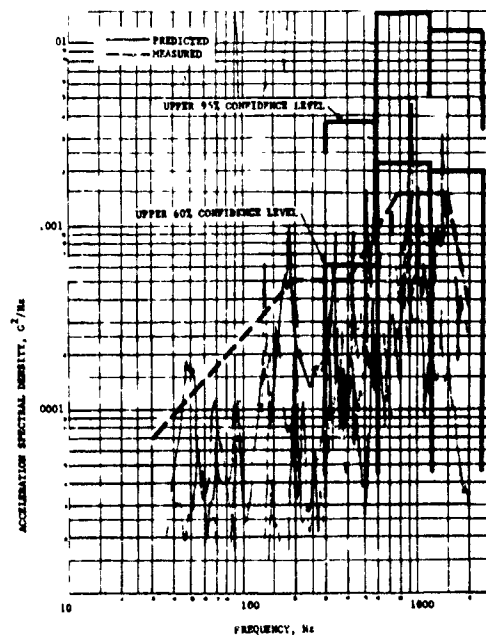


Figure 33 Predicted vs Measured Acceleration Power Density Spectra at Scorer Equipment Bay

curve. Both 60% and 95% confidence levels were used in these predictions as shown in Figure 8. Figure 33 illustrates the correlation between the predicted levels vs. the narrowband primary structure response measurement at the Scorer equipment bay. These levels show that the actual vibration response of the forward fuselage is satisfactorily enveloped by the 95% confidence level Mahaffey-Smith predictions, while the 60% confidence level predictions are in closer agreement with the measured levels. The magnitudes involved are also considerably lower than those noted in the aft fuselage stations. This reflects the characteristic difference between boundary layer noise vs. engine noise excitation and the attendant primary structure response levels on the present vehicle.

CORRELATION BETWEEN PREDICTED VS. MEASURED EQUIPMENT VIBRATION LEVELS

The analytical prediction of the equipment vibration levels was based on the assumption that the dynamic coupling between the equipment payloads and vehicle structure could be approximated by a base driven, mass-spring-dashpot type of analytical model. Such an idealization also assumed that the mass loading of the vehicle structure by the equipment weights would not appreciably alter the response of the primary structure and hence, allow the Mahaffey-Smith predictions to be used in lieu of a properly developed forcing function.

In order to assess the consequences of these assumptions as well as to ascertain the peak response levels of selected equipment items, a limited amount of equipment vibration data was compiled and processed at the end of the flight test program. Comparisons of the resulting data with the analytically predicted levels, however, was not carried out on a one-to-one basis; rather, the vibration levels measured on the primary structure and the equipment items were ratioed to establish the corresponding equipment transmissibilities, which were subsequently used for correlation purposes.

The reason for this procedure was the difficulty of matching the accelerometer locations with the nodal network corresponding to each equipment/structure subassembly, and the poor correlations observed between the peak response levels at the various equipment nodes and the measured levels. Thus, a more plausible approach for purposes of equipment response correlations was to envelope the predicted nodal transmissibility curves into a single omnidirectional curve and compare this curve with its counterpart obtained from the flight test data.

This was carried out at two separate locations on the test vehicle, each corresponding to a representative equipment zone in the forward and aft sections of the fuselage.

Figure 34 illustrates the transmissibility envelopes of the Forward equipment shelf struc-

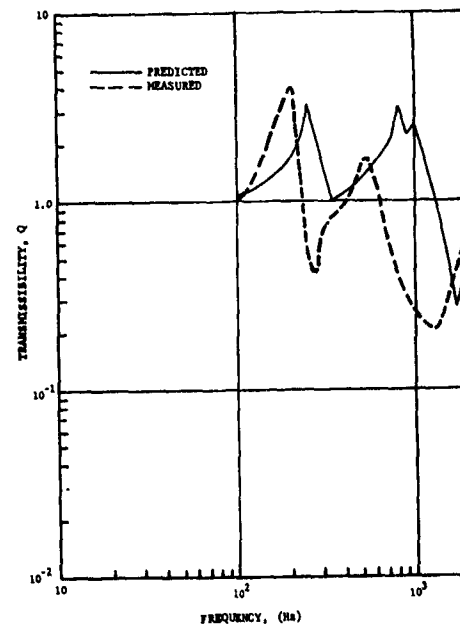


Figure 34 Predicted vs Measured Transmissibility Envelopes at Forward Equipment Shelf ($C/C_{cr} = 10\%$)

ture obtained by combining the individual transmissibilities along each equipment axis. The trends exhibited by both curves are similar in terms of the peaks and notches shown. The maximum measured Q of 4 at 200 Hz compares favorably with the maximum predicted Q of 3.5 at 250 Hz. Thus the correlation between the two transmissibility envelopes for this structure was considered satisfactory.

Similarly, Figure 35 illustrates the measured and predicted envelope transmissibility curves for the Computer/Converter located in the aft fuselage section. The maximum Q of 3.5 at 50 Hz also compares favorably with the maximum predicted Q of 5 at approximately the same frequency as reflected by the first set of peaks on both curves. The remainder of both curves, however, differ considerably from each other. A possible explanation of this difference may lie in the analytical treatment of the Computer/Converter as a six-degree-of-freedom rigid body mounted on a flexible tray structure. This type of an analytical model does not account for the local mass and stiffness characteristics of the equipment box structure on which the accelerometers were mounted. Neither are the internal packaging and other vibration characteristics accounted for in the equipment structure model. Thus, the likelihood of minor discrepancies at higher frequencies between the measured and predicted levels could increase, especially for large equipment items,

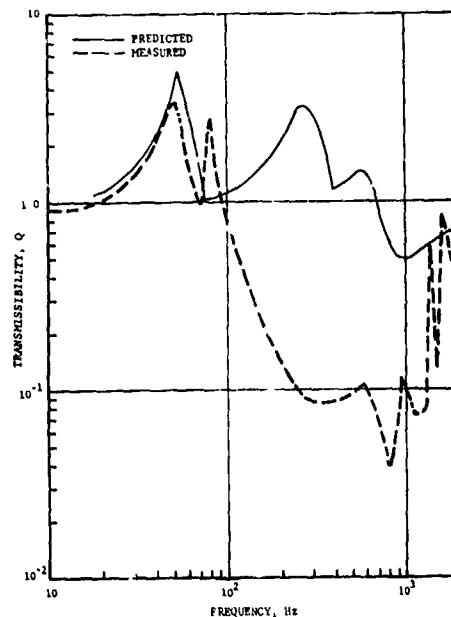


Figure 35 Predicted vs Measured Transmissibility Envelopes at Computer/Converter Equipment ($C/C_{cr} = 10\%$)

based on the coarseness of the analytical model.

In summary, it is reasonable to conclude that the analytical prediction of vehicle vibro-acoustic environments using the techniques outlined and demonstrated here results in the realistic estimates of equipment vibration levels experienced in a general class of jet-powered, air-launched RPV. The opportunity to verify these environments as well as the equipment responses on the AQM-34L vehicle through a successful flight test program justifies this conclusion.

REFERENCES:

1. J.M. Brust and H. Himelblau, "Comparison of Predicted and Measured Environments for Skybolt Guidance Equipment," Shock and Vibration Bulletin 33 (Part III): 231-280, (1964).
2. P.T. Mahaffey and K.W. Smith, "Method for Predicting Environmental Vibration Levels in Jet Powered Vehicles," Journal of Noise Control, Vol. 6, p. 20-26, July 1960.
3. P.A. Franken and E.M. Kerwin, Jr., "Methods of Flight Vehicle Noise Prediction," WADC TR 58-343, November 1958.
4. R.B. Bost, "Prediction of Flight Vibration Levels for the Scout Launch Vehicle," Shock and Vibration Bulletin 36 (Part V): 85-95, (1967).
5. A.J. Curtis and T.R. Boykin, Jr., "Response of Two-Degree-of-Freedom Systems to White Noise Base Excitation," Journal of the Acoustical Society of America, Vol. 33, No. 5, p. 655-663, May 1961.
6. S.H. Crandall, Random Vibrations, Technology Press, Cambridge, Mass., 1958.
7. W.C. Hurty and M.F. Rubinstein, Dynamics of Structures, Prentice-Hall, Inc., Englewood Cliffs, N.J., 1964.

ACKNOWLEDGEMENTS

The authors gratefully acknowledge the guidance and encouragement of Messrs. J.M. Brust, L.R. Beuder, and C.L. Jones towards the successful completion of this program and the writing of this paper. Thanks are also due to Mrs. Verna Hoff for typing the entire manuscript and to Mr. Bob Horton for his assistance with the artwork.

AERO-ACOUSTIC ENVIRONMENT OF RECTANGULAR CAVITIES
WITH LENGTH TO DEPTH RATIOS IN THE RANGE OF FOUR TO SEVEN

L. L. Shaw and D. L. Smith
AIR FORCE FLIGHT DYNAMICS LABORATORY
WRIGHT-PATTERSON AIR FORCE BASE, OHIO

This paper presents the results from a flight test where the aero-acoustic pressure environment was measured in three open rectangular cavities and one cavity with an ogive cylinder mounted in it. The cavities tested were 9 inches wide, 40 inches long, and either 10 inches, 8 inches, or 5.7 inches deep resulting in length to depth (L/D) ratios of 4, 5 and 7 respectively. They were instrumented with both static and dynamic pressure transducers as well as an accelerometer and a thermocouple. The resulting data were correlated with empirical wind tunnel aero-acoustic predictions and formed the basis for a modified prediction method. This prediction scheme enables aircraft designers to predict the fluctuating pressure amplitudes for the broadband and three resonant frequencies. The predictions apply to rectangular cavities with a L/D ratio in the range of 4 to 7 for the Mach number range of 0.6 to 1.3 which were the ranges of the flight test. The prediction scheme considers the longitudinal variation of the amplitude due to the standing waves that were observed to occur for each resonant frequency. An example is included and compared to results obtained from a prediction scheme presented in the literature.

INTRODUCTION

The aero-acoustic phenomenon associated with pressure oscillations excited by flow over open cavities has been studied during the past twenty years by several investigators (References 1-7). Some knowledge has been gained about the phenomenon but due to the complex nature of the problem, it is not completely understood. Methods to predict the pressure oscillations occurring in cavities, as determined from wind tunnel tests, have been reported in Reference 2. The objective of this test program was to verify and/or modify these prediction methods with flight data. This paper briefly presents the flight test results for three rectangular cavities with length to depth (L/D) ratios of 4, 5 and 7 for Mach numbers from 0.6 to 1.3. Also included is a brief discussion of the results from the L/D = 7 cavity with a store mounted in it. A prediction technique for determining the amplitude and frequency content of the oscillating pressure is presented and compared to results obtained in Reference 2.

The complete results from the flight test of the L/D = 4 cavity are reported in Reference 8 and the results for the L/D = 5 and 7 are reported in Reference 9.

DESCRIPTION OF TEST ARTICLE

Each cavity was 40 inches long, 9 inches wide, and either 10 inches, 8 inches or 5.7 inches deep. They were constructed of 0.250 inch thick aluminum (6061-T6) and were mounted in a modified SUU-41 munitions dispenser pod. The modified pod with a cavity mounted in it is shown in Figure 1. The pod was carried on the triple ejection rack (TER) of the left pylon of a RF-4C aircraft. The mounting is schematically illustrated in Figure 2.

INSTRUMENTATION AND DATA REDUCTION PROCEDURES

The cavities were instrumented with nine microphones, one accelerometer, one thermocouple and three static pressure ports. The location of the instrumentation is shown in Figure 3. A complete description of the

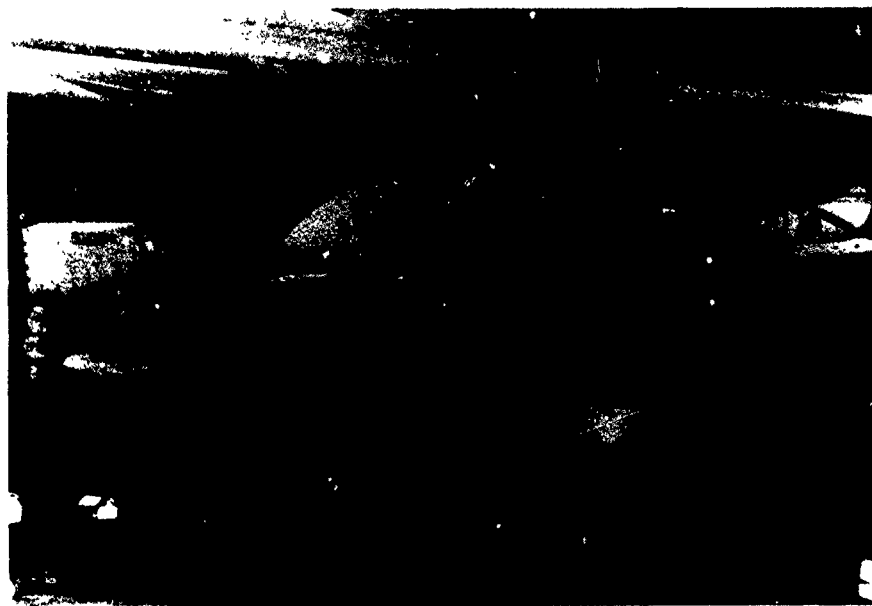


Fig. 1 - Ten Inch Cavity Mounted in Modified Pod

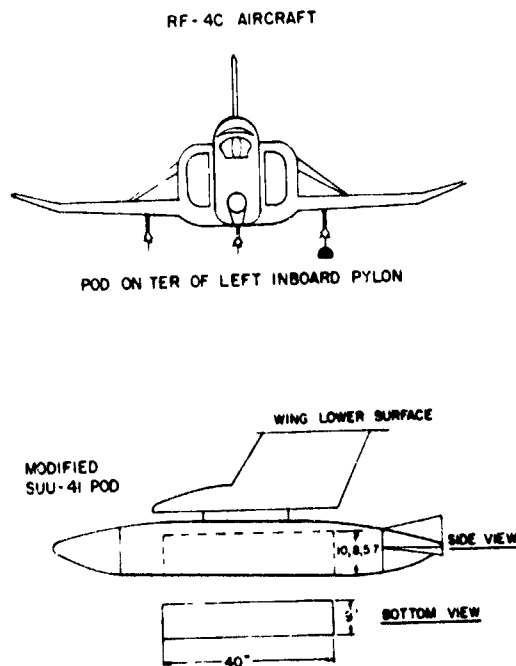


Fig. 2 - Modified SUU-41 Pod Mounted on RF-4C Test Aircraft

data acquisition instrumentation is given in References 8 and 9. All data were continuously recorded on two fourteen channel tape recorders. The magnetic tapes recorded in flight were analyzed on a Hewlett Packard (5450) Fourier Analyzer. Overall fluctuating pressure level, one-third octave band, and narrowband (2 Hz) analyses were performed for selected microphones and flight conditions. Sample lengths for all analyses were eight (8) seconds or less which insured that non-stationary effects were negligible. Further details of the calibration and data reduction procedures are given in References 8 and 9.

TEST PROCEDURES

Data were obtained at altitudes of 3,000, 20,000, and 30,000 ft. The aircraft, while maintaining a constant altitude, was slowly accelerated (for a period of approximately 2 to 3 minutes) over a Mach number range with data being recorded continuously. The Mach number ranges covered were 0.61 to 0.93 for 3,000 ft and 0.61 to 1.30 for 20,000 ft, and 30,000 ft. The angle of attack of the SUU-41 pod and the aircraft were investigated. It was found that the angle of attack of the SUU-41 pod was small for all test conditions and consequently was not considered during the analysis of the data. Flights requiring speeds in excess of $M = 0.9$ below 30,000 ft altitude were flown over Lake Huron with the remaining flights being flown over Washington Courthouse, Ohio.

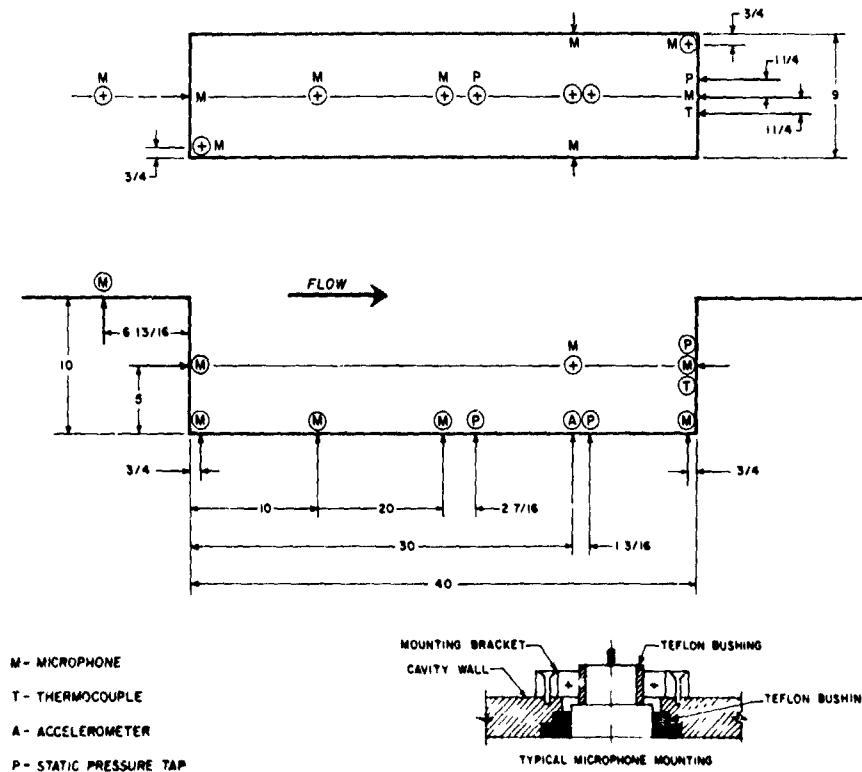


Fig. 3 - Open Cavity Instrumentation Location

TEST RESULTS

a. Static Pressures

The longitudinal variation of the static pressure along the floor of the $L/D = 4$ cavity is shown in Figure 4 for an altitude of 30,000 ft. The data are presented as the difference between the cavity static pressure P_c and the free-stream static pressure P_∞ normalized with the free-stream static pressure. The static pressure increased towards the rear of the cavity as was observed in wind tunnel investigations (References 2, 5 and 7). The static pressure at each location also showed a tendency to increase with Mach number. This Mach number effect was also observed in References 2 and 7, however, this trend did not continue above Mach 2 in the references.

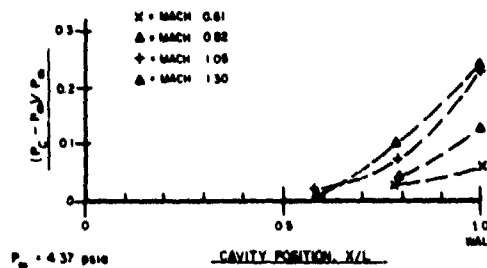


Fig. 4 - Longitudinal Variation of Static Pressure Along Cavity Floor for an Altitude of 30,000 Feet for $L/D = 4$

The flight test results from the cavities with L/D ratios of 5 and 7 displayed similar trends. Static pressures for all L/D ratios were compared but no apparent trend with L/D was observed. The total spread of all the static pressure data recorded (all Mach numbers, all L/D ratios and all altitudes) at each position is shown in Figure 5. The maximum pressure measured at each location increased towards the rear of the cavity. The total spread in the data at each location also increased towards the rear with the data spread at the rear being a factor of 3 greater than at the center. Also included in Figure 5 are the results from the L/D = 7 cavity with a store. The observed cavity static pressures with the ogive store were generally within the range of those obtained in the empty configuration.

b. Cavity Temperature

Cavity temperatures were measured with a thermocouple mounted near the center of the aft wall. The results for the L/D = 7 cavity with a store are shown in Figure 6, along with wind tunnel results from Reference 2 where the recovery factor is presented versus the free-stream Mach number. The wind tunnel data show a trend for the cavity temperature to approach the stagnation temperature with increasing Mach number. At the lower Mach numbers the flight test data fell well above the wind tunnel results but at supersonic speeds the data agreed quite well.

c. Vibration

An accelerometer was installed in the cavities to insure that the vibration input did not significantly affect the microphone output. The vibration sensitivity of the Gulton microphones was reported to be 90 dB/1g, i.e. 1g acceleration of the microphone would not produce more than a 90 dB sound pressure level reading. The maximum one-third octave band acceleration measured at any flight condition was 30 g's rms. In all cases the measured fluctuating pressure level was at least 30 dB greater than the vibration induced level, thus it was assumed that the vibration of the cavity walls had no significant effect on the microphone outputs.

d. Fluctuating Pressures

The fluctuating pressure levels were obtained from the nine microphones for each cavity configuration (L/D = 4, 5, 7). The overall pressure levels from the forward end of the cavity for 3,000 and 20,000 ft altitudes are shown in Figure 7. The overall fluctuating pressure level is seen to increase with Mach number and at any Mach number the highest level occurs at the lowest altitude. This figure is typical of all test results. However, the results from other longitudinal locations showed greater differences between

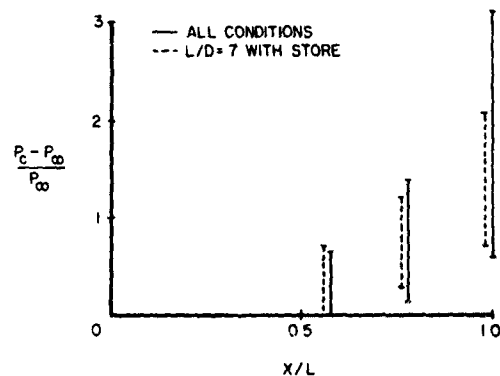


Fig. 5 - Total Spread of All the Normalized Static Pressure Data

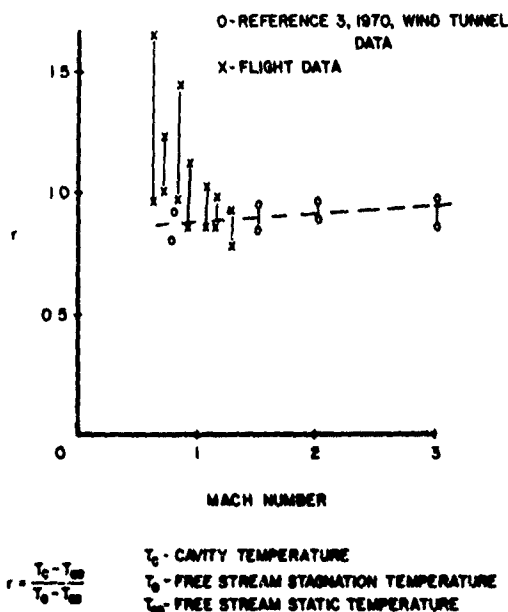


Fig. 6 - Comparison of Flight Test Recovery Factors for L/D = 7 Cavity with Ogive Store to Wind Tunnel Results from Reference 2

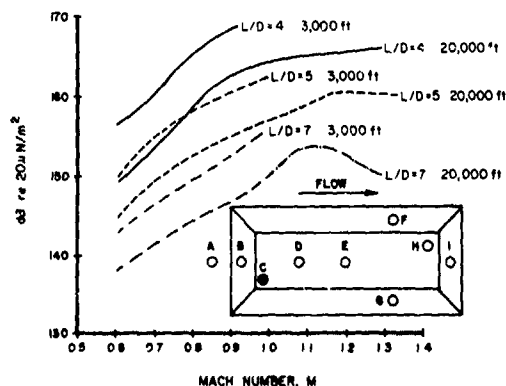


Fig. 7 - Overall Fluctuating Pressure Levels from the Front of the Cavities

the levels measured at different altitudes resulting in a lack of free-stream dynamic pressure (q) scaling. In Reference 2 it was assumed that the flow induced cavity oscillations scaled with free-stream dynamic pressure, however, the flight test data show that the fluctuating pressure levels do not scale at certain longitudinal locations as is illustrated in Figure 13.

Typical narrowband spectra from the front of the cavity for the 20,000 ft altitude and a Mach number of 1.30 for each L/D ratio are shown in Figures 8, 9 and 10. The resonant frequencies are evident and agree well with the frequencies determined from the modified Rossiter equation (Reference 2):

$$S = \frac{fL}{V} = \frac{m - 0.25}{\left(1 + \frac{K-1}{2} M^2\right)^{1/2}} + 1.75 \quad (1)$$

$$m = 1, 2, 3$$

K = ratio of specific heats

where the $m = 1$ frequency is referred to as the mode one frequency, etc. The nondimensional resonant frequencies calculated for all observed resonances are shown in Figure 11 along with data from Reference 2 and compared to the modified Rossiter equation. The agreement is quite good.

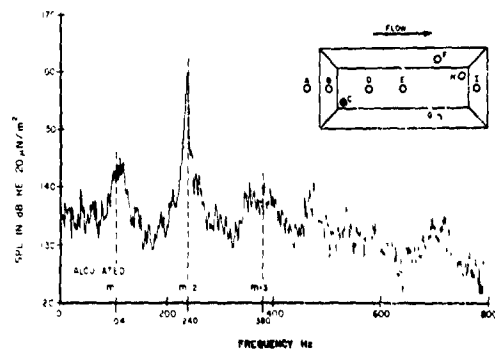


Fig. 8 - Narrowband (2 Hz) Spectrum from the Front of the L/D = 4 Cavity for an Altitude of 20,000 Feet at Mach Number 1.30

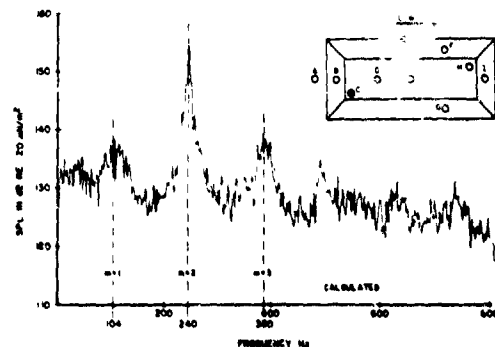


Fig. 9 - Narrowband (2 Hz) Spectrum from the Front of the L/D = 5 Cavity for an Altitude of 20,000 Feet at Mach Number 1.30

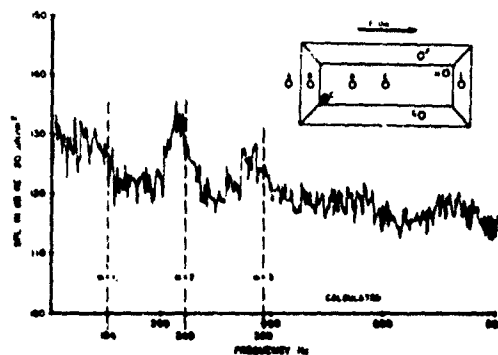


Fig. 10 - Narrowband (2 Hz) Spectrum from the Front of the L/D = 7 Cavity for an Altitude of 20,000 Feet at Mach Number 1.30

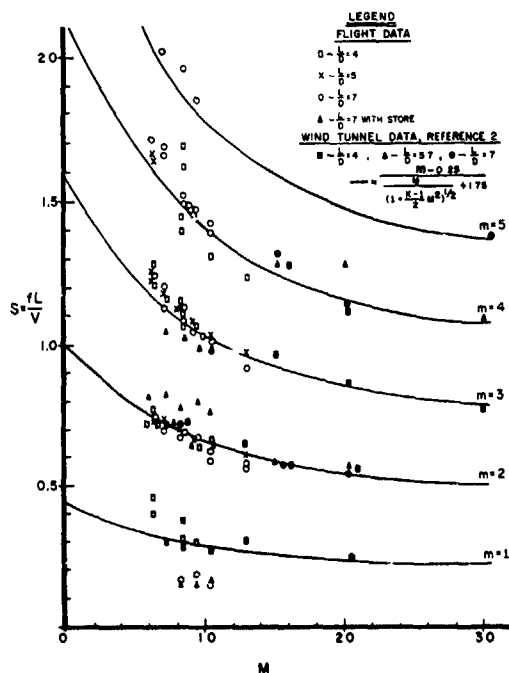


Fig. 11 - Nondimensional Resonant Frequencies as a Function of Mach Number

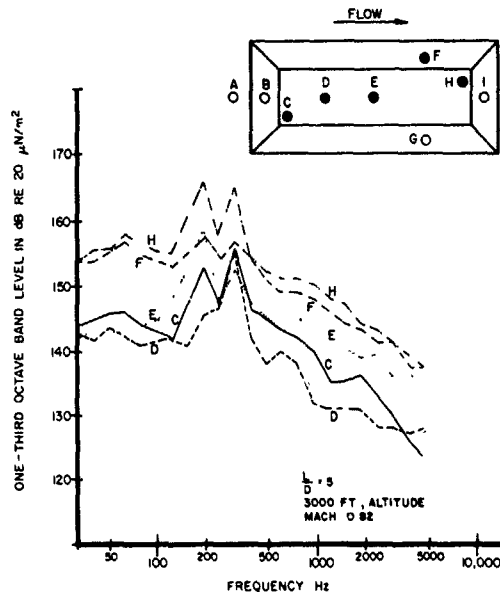


Fig. 12 - One-Third Octave Band Spectra from the L/D = 5 Configuration Depicting Longitudinal Variation

Typical longitudinal variation of the one-third octave band spectra from the L/D = 5 configuration are shown in Figure 12 for an altitude of 3,000 ft and a Mach number of 0.82. It is evident that fluctuating pressure levels increase by approximately 10 dB from the front to the rear of the cavity. The longitudinal variation is shown in Figure 13 for the mode two frequency at Mach 0.82 for all altitudes. The measured one-third octave band level containing this frequency is normalized with the free-stream dynamic pressure and plotted against the non-dimensional cavity location. The lack of dynamic pressure scaling is evident at a number of cavity locations and only scales at $X/L = 0$ and $X/L = 0.5$. The results from the L/D = 4 and 7 configurations displayed similar trends.

In Reference 2, mode shapes were presented for the first three modal frequencies and are shown in Figure 14. These mode shapes were obtained in a wind tunnel from microphone outputs on an axis along the longitudinal center line of the cavity. It was assumed that the flight test data followed similar variations and ramped sinusoidal equations were derived to fit the data. The resulting equations describing the variation in the normalized sound pressure level

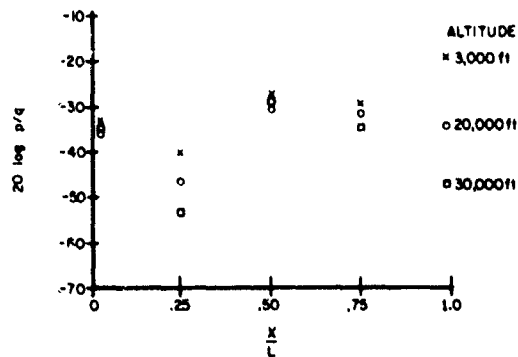


Fig. 13 - Longitudinal Variation of the Mode 2 Resonant Frequency One-Third Octave Band Peak for L/D = 5

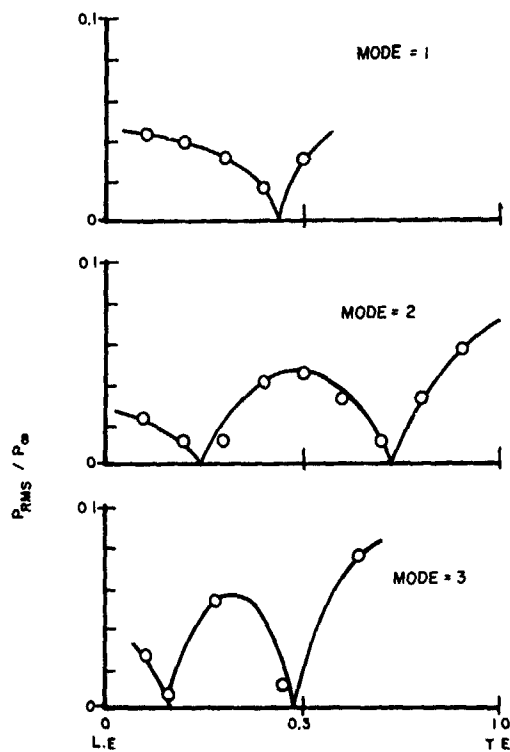


Fig. 14 - Suggested Shape for First, Second and Third Order Modes from Reference 2

$20 \log (P_m/q)_{X/L}$ with normalized longitudinal distance X/L as determined from the 3,000 ft altitude data are:

$$20 \log (P_m/q)_{X/L} = 20 \log (P_m/q)_{\max} \quad (2)$$

$$-10 [1 - \cos(a_m X/L)]$$

$$+ (0.33L/D - 0.6)(1 - X/L)]$$

where: $20 \log (P_m/q)_{\max}$ = the Sound Pressure level at $X/L = 1$

$$a_1 = 3.5$$

$$a_2 = 6.3$$

$$a_3 = 10.0$$

It should be noted that these equations account for the changes in level with the L/D ratio. The flight test data indicated that the increase in the SPL toward the rear of the cavity is greater for shallow cavities and must be accounted for in the equations. Figure 15 illustrates this variation by presenting the mode 2 one-third octave band normalized fluctuating pressure level at the fore and aft end of the cavity for each of the three L/D ratios. There is about an 8 dB increase for the $L/D = 4$ cavity but a 17 dB increase for the $L/D = 7$ cavity. The above equation predicts a 7 dB increase for the $L/D = 4$ cavity and a 17 dB increase for the $L/D = 7$ cavity. The results from these equations are plotted in Figure 16 for an altitude of 3,000 feet and a Mach number 0.82 for $L/D = 5$ cavity where the fluctuating pressure has been normalized with the free-stream dynamic pressure. The flight test data are also shown in the figure. The agreement is seen to be quite good. Comparisons to the results from the other L/D ratios were just as good, except at $X/L = 0.75$ where the microphone was located on the center of the side wall rather than the floor, thus indicating variation in the depth direction.

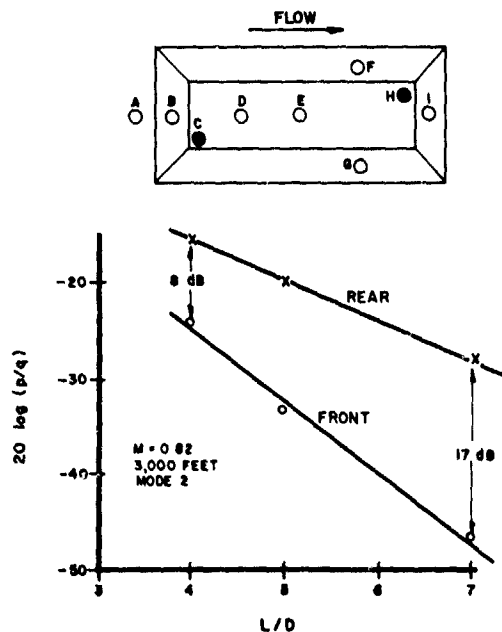


Fig. 15 - One-Third Octave Band Mode 2 Levels from the Front and Rear of the Cavities for 3,000 Feet Altitude and Mach Number 0.82

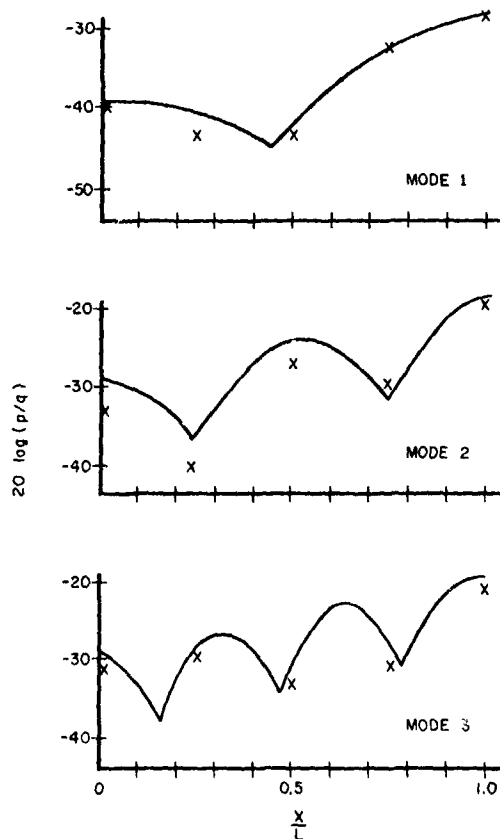


Fig. 16 - Comparison of the Prediction Scheme with Data for $L/D = 5$ from 3,000 Foot Altitude and Mach Number 0.82

The solution of these equations requires the determination of

$$20 \log (P_m/q)_{\max}$$

for each mode frequency. The normalized expression for the mode 2 maximum level was determined from a second order least square curve which encompassed all measured data points. This curve is shown in Figure 17 and is given by:

$$20 \log (P_2 \max/q) = 9 - 3.3L/D + 20 \log (-M^2 + 2M - 0.7) \quad (3)$$

Where: $P_2 \max$ = mode 2 rms pressure

q = free-stream dynamic pressure

M = Mach number

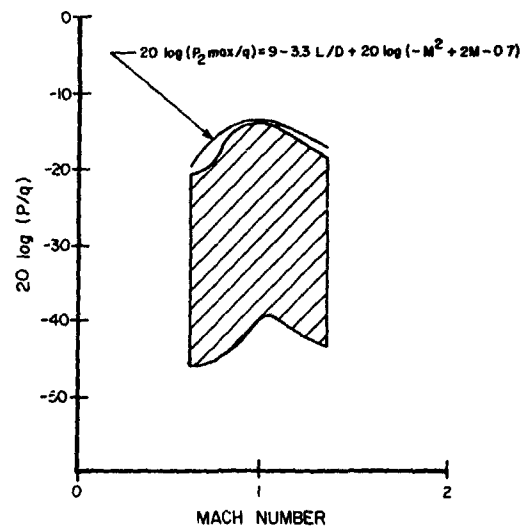


Fig. 17 - Prediction Curve for Peak One-Third Octave Band Level at the Aft End of the Cavity

The expressions for the normalized fluctuating pressures corresponding to the other mode frequencies were determined to be

$$20 \log (P_1 \max/q) = 20 \log (P_2 \max/q) - 2(L/D)^2 + 26(L/D) - 86 \quad (4)$$

$$20 \log (P_3 \max/q) = \begin{cases} 20 \log (P_2 \max/q) - 11 & \text{for } L/D < 4.5 \\ 20 \log (P_2 \max/q) & \text{for } L/D > 4.5 \end{cases} \quad (5)$$

Equations 1 through 5 enable the estimation of the amplitude, frequency, and longitudinal distribution of the fluctuating pressures associated with cavity resonance for cavities with L/D ratios in the range of 4 to 7. In order to predict the complete one-third octave band spectrum broadband levels are also required.

The broadband levels are seen in Figure 12, for $L/D = 5$, to increase towards the aft end of the cavity. This was also observed in wind tunnel tests (References 2, 5 and 7). In general, this increase was approx-

imately 10 dB from the front to the rear of the cavity for $L/D = 4$, 13 dB for $L/D = 5$ and 17 dB for $L/D = 7$. For prediction purposes linear variations were assumed. Figure 18 presents one-third octave band spectra from the front of the $L/D = 4$ cavity for an altitude of 30,000 ft and for various Mach numbers with the data referenced to the free-stream dynamic pressure. The normalized broadband levels are seen to increase with increasing Mach number. Figure 19 presents one-third octave band spectra from the rear of each cavity showing the L/D effect on the spectra. It is evident that at the higher frequencies the level of the normalized broadband spectra are fairly constant with variations in L/D ratio at the rear of the cavities and the level of the mode 2 frequency decreases with increasing L/D ratios. For prediction purposes the shape of the broadband spectrum was assumed to follow the curve given in Figure 20 where the frequency is normalized by the Strouhal relationship. The maximum level is established by the mode 2 resonant frequency peak, the longitudinal position and the L/D ratio of the cavity. The equation to predict the maximum broadband level, as determined from the flight test data, is:

$$20 \log (P_b \max / q) = 20 \log (P_2 \max / q) \quad (6)$$

$$+ 3.3 L/D - 28$$

$$+ 3(1-L/D)(1-X/L)$$

where P_b is the rms pressure in the peak one-third octave band of the broadband spectrum.

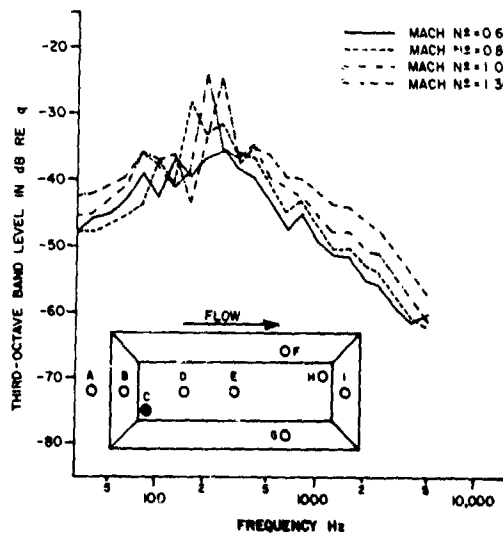


Fig. 18 - One-Third Octave Band Spectra from the Front of the $L/D = 4$ Cavity at 30,000 Foot Altitude

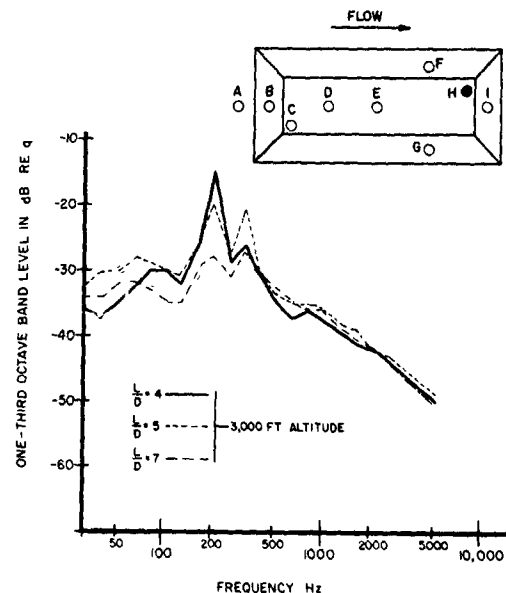


Fig. 19 - One-Third Octave Band Spectra from the Rear of the Cavity for Mach Number 0.82 for All L/D Ratios

$$20 \log (P_b \max / q) = 20 \log (P_2 \max / q) + 3.3 L/D - 28 + 3(1-L/D)(1-X/L)$$

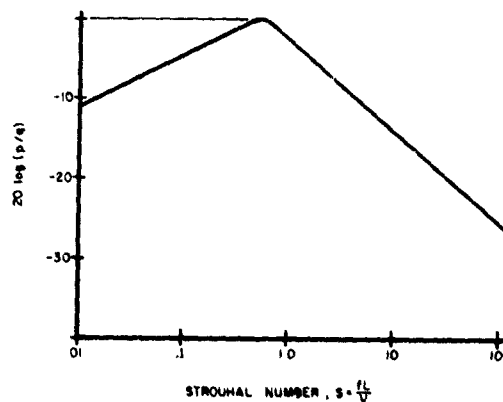


Fig. 20 - Broadband Level Versus Strouhal Number

Equations 1 through 6 and Figure 20 can now be used to predict the complete one-third octave band spectrum and distribution of the fluctuating pressures in open rectangular cavities with L/D ratios from 4 to 7 for a Mach number range of 0.6 to 1.3. For clarity an example of the application of this scheme is presented and the results are compared to those obtained using the method presented in Reference 2.

f. Example

Consider the case of an aircraft flying at Mach 0.9 near sea level with an open nearly rectangular cavity 20 ft long and L/D ratio of either 5 or 7. It is desired to predict the aero-acoustic environment at the rear of the cavity for $L/D = 5$ and at the front, center and rear for $L/D = 7$. The solution is obtained by entering equations 1 through 6 and Figure 20 with the appropriate parameters.

Equation 1 yields the first 3 modal frequencies for both cases considered. Equations 3, 4 and 5 are used to determine the maximum normalized amplitude for each mode frequency. Equation 2 is then used to obtain the amplitude of each mode frequency at the desired longitudinal location in the cavity. The maximum one-third octave broadband levels are determined from equation 6. Finally, Figure 20 is used to predict the complete broadband spectra.

The spectra obtained for the example cases are shown in Figure 21 along with the spectrum that would result using the scheme offered in Reference 2. It is seen that the scheme from Reference 2 is conservative for all cases presented with conservatism being the greatest at the fore end of the cavity. The current prediction equations account for the variation of the resonant frequency amplitudes and their longitudinal distribution as well as the variation in broadband levels. The effects of the cavity L/D ratio are also included in the equations which were not included in the Reference 2 prediction scheme. The spectrum for the center of the cavity does not show modes 1 and 3 due to the predicted longitudinal distribution of the resonant amplitudes. Figure 16 shows that modes 1 and 3 have nodes near the center of the cavity and thus the prediction scheme takes this into account, and results in the spectra given in Figure 21 for this particular location.

g. Effect of Store in Cavity

In order to determine the effect a store has on the fluctuating pressure environment in the cavity an ogive cylinder was mounted in the $L/D = 7$ cavity. This configuration was tested for the same flight conditions as the empty cavities. Figure 22 presents a com-

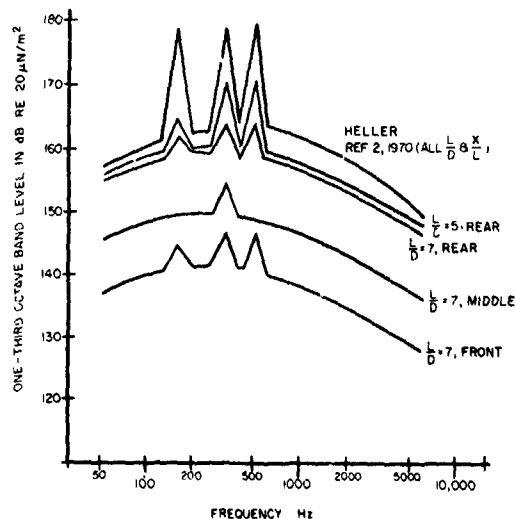


Fig. 21 - Comparison of Spectra from the Working Example and the Prediction Scheme from Reference 2

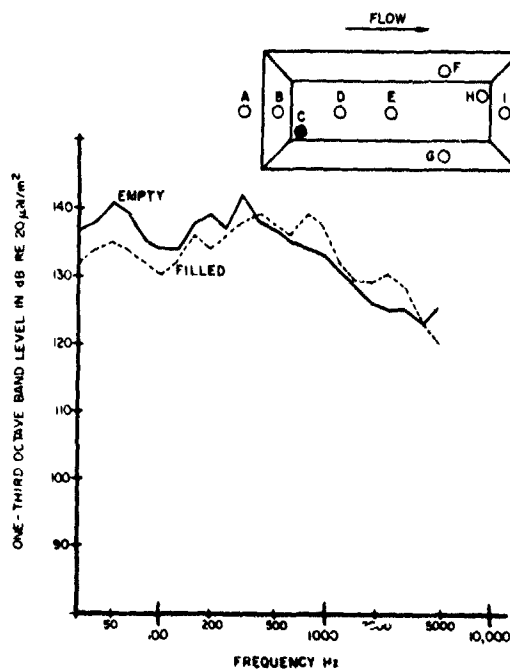


Fig. 22 - Comparison of One-Third Octave Band Spectra from the $L/D = 7$ Cavity Empty and with Store for Mach Number 0.82 and Altitude of 3,000 Feet

parison of the one-third octave band spectra from the $L/D = 7$ cavity with and without the ogive store mounted in it for a Mach number of 0.82 and an altitude of 3000 feet. The effects displayed in this figure are typical of results obtained for all other test conditions. A major effect of the store is seen to be a reduction in the amplitude of the low frequencies. This reduction was observed from the other test data to increase with altitude for any given Mach number. The effect of the store on the resonant peaks was difficult to distinguish since the peaks for the empty $L/D = 7$ cavity were only of the order of 5 to 6 dB. Reductions of 3 or 4 dB were sometimes noted. However, for prediction purposes it is recommended to predict the fluctuating pressure environment of cavities with stores in them with the equations offered in this paper. Since the flight data reviewed in this paper indicate that stores almost always reduce or have little effect on the fluctuating pressure in the cavity, utilizing these equations will result in conservative estimates.

CONCLUDING REMARKS

The experimental investigation reported herein indicates the following conclusions:

1. The cavity resonant frequencies can be accurately predicted by the modified Rossiter formula.
2. The amplitude prediction methods in Reference 2 were conservative in predicting both the resonant and broadband SPL observed in actual flight tests.
3. The equations presented are recommended for predicting more realistic SPLs for cavity L/D ratios in the range of 4 to 7 and a Mach number in the range of 0.6 to 1.3.
4. The longitudinal variation of the rms amplitude associated with each resonant frequency can be described as ordered modes.
5. At the rear of the cavity the broadband spectrum for constant flight conditions is nearly the same for all cavity L/D ratios.
6. The maximum broadband levels increased towards the aft end of the cavity by approximately 10 dB for $L/D = 4$, 13 dB for $L/D = 5$ and 17 for $L/D = 7$ cavity.
7. Increasing the cavity L/D ratio reduces the amplitude of the resonant frequencies.

REFERENCES

1. East, L. F., "Aerodynamical Induced Resonance in Rectangular Cavities," Journal of Vibration and Sound, May 1966.
2. Heller, H. H., Holmes, G. Covert, E. E., "Flow-Induced Pressure Oscillations in Shallow Cavities," AFFDL-TR-70-104, Dec 1970.
3. Krishnamurty, K., "Acoustic Radiation from Two-Dimensional Rectangular Cutouts in Aerodynamic Surfaces," NACA Tech Note 3487, August 1955.
4. Maull, D. J. and East, L. F., "Three-Dimensional Flow in Cavities," Journal of Fluid Mech 16, 620, 1963.
5. Plumblee, H. D., Gibson, J. S., and Lassiter, L. W., "A Theoretical and Experimental Investigation of the Acoustic Response of Cavities in Aerodynamic Flow," WADD-TR-61-75, 1962.
6. Roshko, A., "Some Measurements of Flow in a Rectangular Cutout," NACA Tech Note 3488, 1955.
7. Rossiter, J. E., "Wind Tunnel Experiments on the Flow Over Rectangular Cavities at Subsonic and Transonic Speeds," RAE Rep Nr 64037, R&M Nr 3438, 1966.
8. Shaw, L. L., et al, "Aero-Acoustic Environment of a Rectangular Cavity with a Length to Depth Ratio of Four," AFFDL-TR-74-19-FYA, January 1974.
9. Smith, D. L. et al, "Aero-Acoustic Environment of Rectangular Cavities with Length to Depth Ratios of Five and Seven," AFFDL-TM-74-79-FYA, April 1974.

DISCUSSION

Voice: Why did the second mode have a higher level than the first mode? Also was the cavity wall a thick panel or a thin panel?

Mr. Shaw: To answer your first question, there is still a question throughout the community who are investigating this cavity oscillation phenomena as to why it prefers one particular mode over another. Wind tunnel data has shown possibly that a scale effect controls this because one wind tunnel result showed that it preferred the first mode instead of the second mode. However most wind tunnel data has shown that the second mode is the peak in most cases but no explanation has been offered. To answer your second question, the wall of the cavity, the side walls and the floor, were constructed from $\frac{1}{2}$ " thick aluminum and the bottom plate was reinforced with angle iron. The flight vibration data indicated that it did not significantly affect the vibration measurements.

Mr. Reed: (Naval Surface Weapons Center) Did you mount your pod on a triple ejection rack? That doesn't seem like an ideal platform for studying vibration of cavities. It would seem that the vibrations of the externally mounted store alone would have a large influence on your data. How did you convince yourself that your data were not heavily influenced by mounting the pod on a triple ejection rack?

Mr. Shaw: Yes, we were well aware of that and this was the primary reason why we found in most cases that lower values were obtained from the flight test than from wind tunnel results. We realized this, but to correlate the data with actual cavity data, I agree there would be some variation. However there are similar vibrations in actual aircraft weapons bays and we feel that pod data would agree with actual flight data better than wind tunnel data which are obtained from rigid mounts. I think this is primarily the reason why we expect to see lower levels in flight tests than are seen in the wind tunnel results. We agree that there are variations, the angle of attack may not be perfectly zero as desired.

PREDICTION OF ACOUSTICALLY INDUCED VIBRATION IN TRANSPORT AIRCRAFT *

Harold W. Bartel
Lockheed-Georgia Company, Marietta, Georgia

A method is described for predicting structural vibration during preliminary design of new transport category aircraft. The method is based on broad-band random noise and vibration data measured during development tests and evaluations of two contemporary transport aircraft, and on data obtained in laboratory tests of 30 flat and curved skin-frame-stringer panels. The variation of vibration level with operating condition, direction of motion, and structural mass and rigidity is discussed, along with the formulation of vibration prediction charts and graphs.

INTRODUCTION

Estimates of vibration level are vital to the preliminary design of new aircraft. This requires consideration of all sources of vibration for representative missions and flight conditions. The success of the vibration analyst in predicting the vibration environment will, in large part, hinge on the quality of the methods, data, and information he can assemble to account for each independent source. This investigation was conducted in response to the analyst's need for additional and improved methods. The objective was to provide a method for estimating transport category aircraft structural vibration which is induced by impinging noise, in a manner that permits tailoring the estimates to a specific structural mass and rigidity. All of the work discussed herein was directed toward that end.

During the recent development of two large contemporary military cargo aircraft, a number of magnetic tape recordings of noise and vibration level were made for design, development, and structure/equipment substantiation purposes. These recordings were reassembled for use in this investigation. Additionally, a total of 30 flat and curved structural panels were laboratory tested to obtain recordings of noise and vibration data. The measured data were available in sufficient quantity and quality to allow correlation of noise and vibration levels in third-octave frequency bands, with confidence lines

statistically fitted to the data. These correlations were established with computerized sorting and plotting techniques for numerous ensembles of data, each having some common trait. The data in these correlations could then be operated upon to account for various factors and rerelated, to reveal the effects of the operations on data scatter.

The aircraft noise and vibration data were used to describe the relation between vibration level and sound pressure level, and to derive the relative difference in vibration intensity between operation on the ground and cruise with maximum pressure differential, and between different vibratory directions. The test panel noise and vibration data were used primarily to study the effects of mass and rigidity on structural response.

Aircraft Data - Airplane No. 1 had a fuselage diameter of about 14 feet and a maximum takeoff gross weight in the range of 300,000 pounds. The No. 2 airplane lower fuselage diameter was about 24 feet, with MTGW in the range of 700,000 pounds. The surface structures of both airplanes were generally similar. The fuselage wall structure is a conventional skin-frame-stringer arrangement, with circumferential frames spaced at approximately 20" and longitudinal stringers spaced at from 5" to 10" depending on location. Skin gage and the height, width, and thickness of frames and stringers are tailored to match local load conditions, and vary considerably. The wing, horizontal stabilizer, and vertical stabilizer box structures are conventional skin-rib-spar arrangements, with widely spaced chord-

* This paper is based on Lockheed research and development work funded by the U.S. Air Force Flight Dynamics Laboratory.

wise ribs, full depth spars, and integrally stiffened upper and lower skins.

Noise levels were recorded during engine runup with the airplane parked on an open runway, and during flight at 3 to 5 different speeds and altitudes. Microphones were attached to the external surface of the structure at locations typified by Figure 1 for the No. 1 airplane. Vibration levels were recorded for

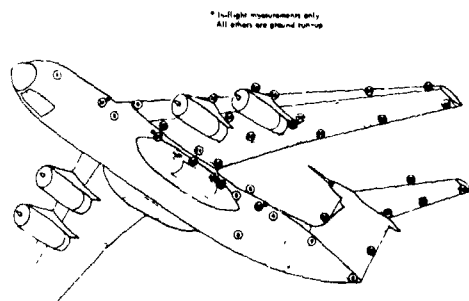


Figure 1. No. 1 Aircraft Noise Measurement Locations

the same ground and flight operating conditions as were the noise levels. Miniature crystal accelerometers were bonded to the aircraft structures at locations typical of those shown in Figure 2 for the No. 1 airplane. The accelerometers always measured vibration on frames, stringers, beams, or similar structure; never on skin plates.

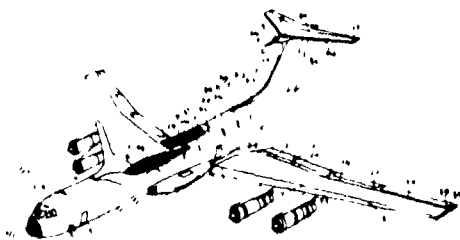


Figure 2. No. 1 Aircraft Vibration Measurement Locations

In order to correlate vibration level with noise level, the noise levels measured at the fixed microphone positions were corrected by interpolation or extrapolation to obtain noise levels on the exterior surface at each accelerometer location. All accelerometers were positioned in one of the three directions of normal, lateral, or tangential. These directions are defined relative to the structural component involved,

and have no consistent relation to the major airplane axes or to the earth. "Normal" means perpendicular to the exterior surface of the structure, while "lateral" means perpendicular to the normal and also perpendicular to the lengthwise axis of the structural element. "Tangential" means perpendicular to the other two directions, or the lengthwise direction of the frame or stringer. These vibratory directions are depicted on the flat panel structure of Figure 3.

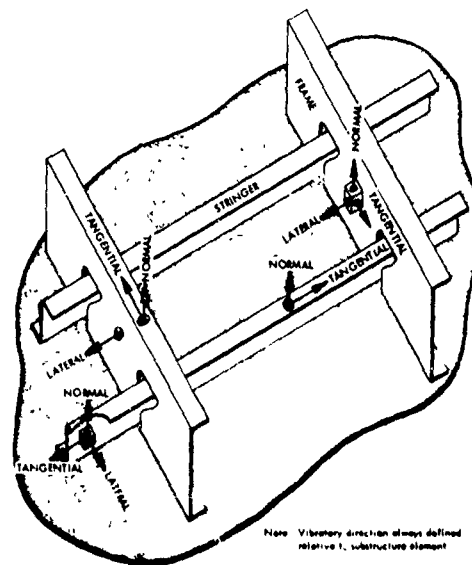
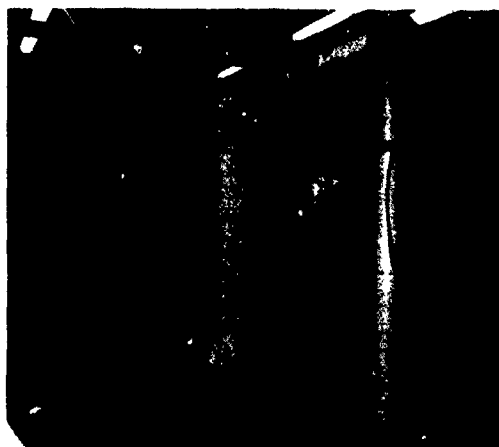
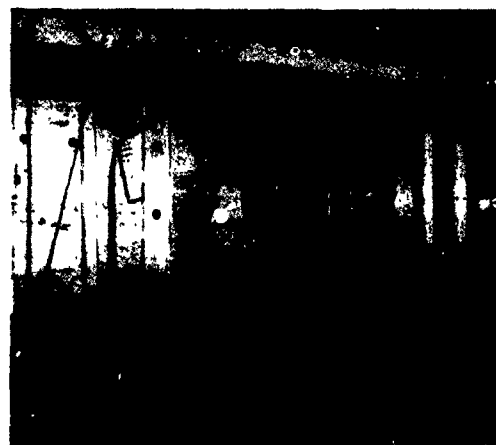


Figure 3. Definition of Vibratory Direction

Panel Data - A total of 23 flat, 20" x 30" skin-frame-stringer panels were tested in pairs in a progressive wave facility as shown in Figure 4, to determine vibratory response to acoustic excitation. The varying panel material, skin thickness, rib thickness, and rib spacing were typical of aircraft structure, and provided a range of mass and rigidity. Noise levels were measured at the center of the panel. Acceleration levels were measured at 6 locations on the frames and 6 locations on the stringers, making a total of 12 acceleration measurements on each panel. The accelerometer locations on the panel structure were approximately the same in every case; 8 being in the normal direction and 4 in the lateral. The noise and vibration data at each measurement location were recorded at each of six different sound pressure levels (SPL's). The broad-band random noise (150 to 2500 Hz) used to excite the panels typically ranged from a low of 128 dB overall to a high of 153 dB overall, with 4 intermediate levels.



(a) Left Side of Progressive Wave Chamber



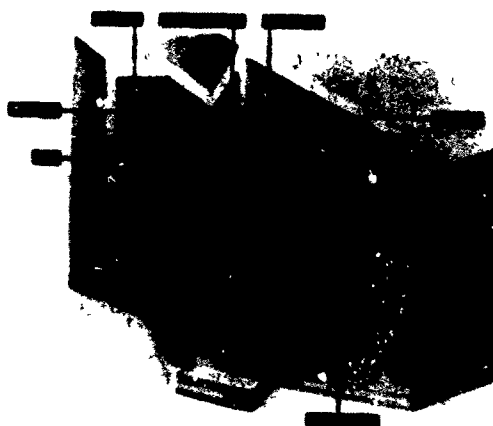
(b) Right Side - Test Panels in Place

Figure 4. Small Panel Test Facility

A group of 6 curved 48" x 72" fuselage wall panels were also tested to determine vibratory response to acoustic excitation. The test facility, shown in the conceptual rendition of Figure 5, consists of a reverberation room and an anechoic room with provisions for installing curved structural panels in the wall dividing the two rooms. Five of the panels had a curvature radius of 7 feet; the sixth panel radius was 12 feet.

The broad-band (150 to 2500 Hz) random acoustic excitation level ranged from 107 dB to 132 dB overall.

Vibration levels were measured at six points on the frames and six points on the stringers for a total of 12 locations; 8 being in the normal direction and 4 in the lateral. The noise and acceleration data were recorded on magnetic tape at the maximum and minimum SPL's as well as three intermediate levels.



(a) Noise Transmission Loss Test Facility



(b) Test Panel Installed

Figure 5. Large Panel Test Facility

DATA CORRELATION

ENSEMBLE PROPERTIES

MEAN SPL $= \bar{X} = 2.5 \times 10^3$

DATA CENTROID $= (\bar{X}, \bar{Y})$

REGRESSION LINE LOCATED THRU (\bar{X}, \bar{Y}) WITH SLOPE \bar{m} , \bar{m} DEFINED BY METHOD OF LEAST SQUARES

STANDARD DEVIATION $= \sigma = \sqrt{\frac{\sum (Y - \bar{Y})^2}{N}}$

SCATTER FACTOR $= \frac{\sigma}{\bar{Y}}$

Y (ON LINEAR SCALE)

1280

840

316

840

1280

UPPER LIMIT

60%

40%

CONFIDENCE INTERVAL

REGRESSION LINE

LOWER LIMIT

X (SPL) $= 2.5 \times 10^3$

σ STANDARD DEVIATION

Figure 6. Definition of Statistical Properties

of the standard deviation corresponding to the normal distribution percentiles for the various confidence intervals. The confidence interval lines were located through these coordinates, parallel to the regression line. The scatter factor was defined as the ratio of the vibration level at one standard deviation to the mean level, i.e. $(Y + \sigma) / \bar{Y}$. It is also the ratio of the level at the 68.27% confidence interval to the level at the regression line, at any SPL.

The aforementioned parameters were always derived for a group of data points on a linear-linear plot of the form SPL-dB versus $\log_{10} G_{rms}$. For convenience, however, such ensembles were always displayed on a log-linear plot, so that vibration level, and the various parameters involving level, could be shown and stated in terms of G_{rms} . Illustrative examples of actual data are shown in Figure 7. All measured aircraft data are included in this correlation, for all directions, all flight conditions, and all structure and equipment locations. Figure 8 shows a similar correlation for the panel data. This correlation plot contains the data from all panels (flat and curved) for both the normal and lateral directions. Being all inclusive, these data ensembles are too general for prediction purposes, and are presented primarily to show the overall range, quantity, quality and trends of the data.

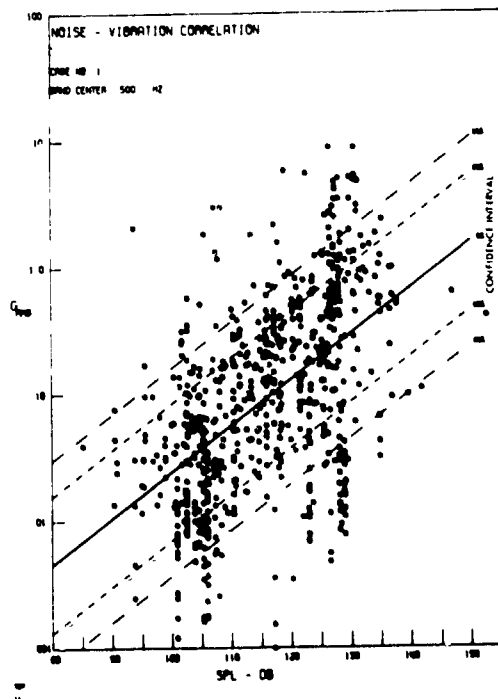


Figure 7. Noise-Vibration Correlations - All Directions and Flight Conditions for Aircraft Shell and Box Structure

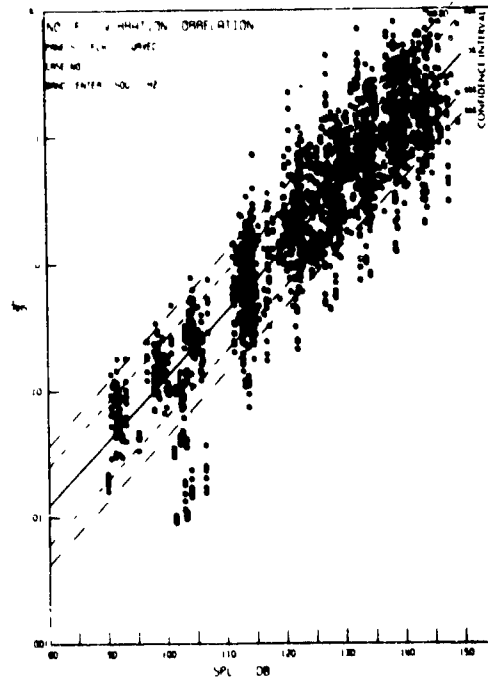


Figure 8. Noise-Vibration Correlations - Normal and Lateral Vibration - All Flat and Curved Test Panels

A comparison of the vibration levels in Figures 7 and 8 for like frequency bands and confidence levels shows the panel data to be consistently higher. This should not be construed as discrediting either of the data ensembles. Some of the aircraft data in Figure 7 include measurements near equipment items, measurements in the tangential or longitudinal direction, and measurements in pressurized cruise flight. All of these factors contribute to lower levels. Conversely, the panel data were measured under ideal conditions of sound pressure incidence, in normal and lateral directions only, and with no other load or strain applied. Lastly, two factors which are suspected to be significant in the aircraft data have not been dealt with in this study: one is the mass and damping effect of the fuel in the wing box; the other is the mass/damping/decoupling effect of the soundproofing, wiring, and plumbing attached to the fuselage shell structure. The net result of all of the aforementioned factors is for the aircraft vibration levels in Figure 7 to be lower than panel levels in Figure 8,

for the same sound pressure level. In investigations to reveal the effects of pressurized cruise flight, vibratory direction, and mass and rigidity, the influence of the aforementioned factors was minimized or eliminated by exercising selectivity in compiling the data ensembles.

FLIGHT AND PRESSURIZATION EFFECTS

Vibration in the fuselage structure changes when the airplane becomes airborne at cruise speed, and pressurized. To determine this change in vibration level, noise-vibration correlations were prepared for ensembles of measured aircraft data for ground and flight operation. Vibration measurements from 52 locations were obtained, for 3 ground operating conditions and 4 flight operating conditions, on aircraft fuselage shell structure or on components attached to it. These vibration data were collected into two separate ensembles; one for on-ground engine run-up; the other for pressurized cruise

flight. For each ensemble the mean vibration level and the levels at higher confidence intervals were defined at a common sound pressure level in each third-octave frequency band, as exemplified by Figure 9 for the 50% confidence level. The chart of Figure 10 was then derived by plotting the ratio of flight-to-ground vibration level for various confidence levels.

It would be risky to generalize that the difference in vibration response between the two operating regimes is due solely to pressurization of the fuselage; other factors could have similar effects. For example, the fuselage structure is loaded and stressed differently for each condition, being supported by the landing gear in the one case, and primarily by the wings in the other case. Also, the character of the noise excitation is different; the principal source in some frequency bands changing from engine noise to boundary layer turbulence with attendant differences in incidence angle, and space-time correlation. However, for preliminary estimation of vibration response in other transport category aircraft of similar configuration and mission, these data are considered to be a useful indicator of the relative difference between vibration on the ground and in pressurized flight. Obviously the chart in Figure 10 is not applicable to structure in the wings, empennage, wheel wells, or similar areas where there is no pressurization, and where the environmental factors do not exist in the same combination.

VIBRATORY DIRECTION EFFECTS

In both of the aircraft and all of the test panels, vibration data were measured and identified in two or three directions of motion. These directions were consistently defined as either normal, lateral, or tangential, relative to the particular structural component involved, as shown previously in Figure 3. It is clearly preferable to have a vibration prediction method for each direction, if the level is known to vary with direction. If vibration data from all directions are combined into a common noise-vibration correlation, the data from the direction of lowest level will tend to suppress the mean value. In some vibration prediction instances, (particularly for equipment where the installed orientation is not known) it is advantageous to predict vibration levels separately for each direction and envelope the results to obtain the worst case for any direction. Therefore, a means was derived to relate lateral and tangential vibration level to the level in the normal direction.

Measured aircraft vibration data (and corresponding noise levels) were assembled into separate ensembles for each coordinate direction. Only data from ground

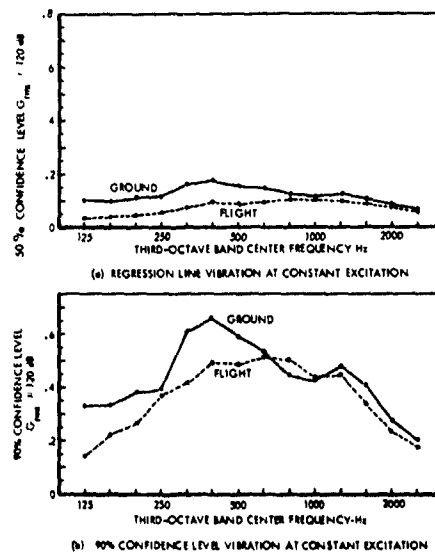


Figure 9. Comparison of Ground and Flight Vibration Levels - Aircraft Shell and Box Structure - Normal Direction

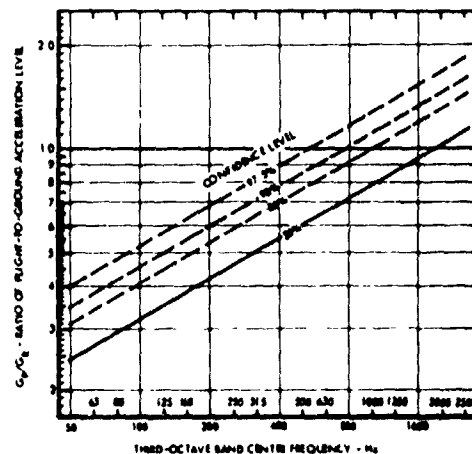


Figure 10. Flight Vibration Prediction Chart

run-ups were used in order to eliminate other extraneous environmental influences. The ensembles consisted of data from 56 aircraft structural locations in

the normal direction, 18 locations in the lateral direction and 13 locations in the tangential direction. The data in each ensemble were correlated in the usual form of G_{rms} vs. SPL-dB, and the statistical properties calculated for each third-octave band. Vibration levels at a reference noise level were compared, as shown in Figure 11 for the 50% confidence level. All directions show a tendency to maximize in the 300 to 600 Hz frequency range, indicating that the most responsive structural resonance modes are influencing vibration in all directions. Tangential vibration levels are consistently lower than normal or lateral, as expected. The test panel vibration in the normal and lateral directions was quantified in an identical manner to independently check the trends observed in the aircraft data. These panel results generally collaborated the aircraft data. Lateral and tangential vibration levels were then quantified as a proportion of normal vibration, in the form G_{lat}/G_{norm} and G_{tan}/G_{norm} , accounting for data scatter and slope of the confidence lines independently in each case. The resulting charts are shown in Figures 12 and 13. These charts were derived from aircraft data limited to the on-ground case to avoid data scatter from non-structural causes. However, the charts are believed useful for all flight conditions.

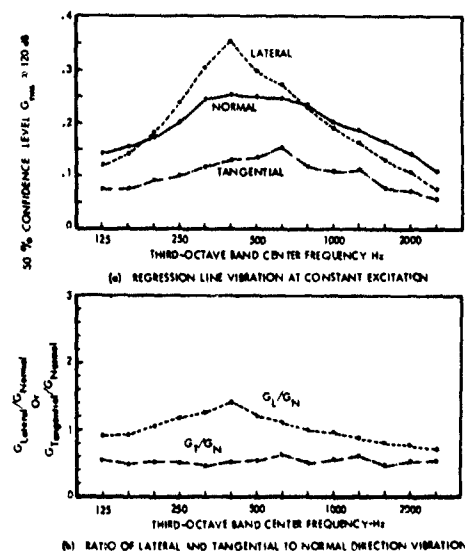


Figure 11. Comparison of Directional Vibration Levels for Aircraft Shell and Box Structure

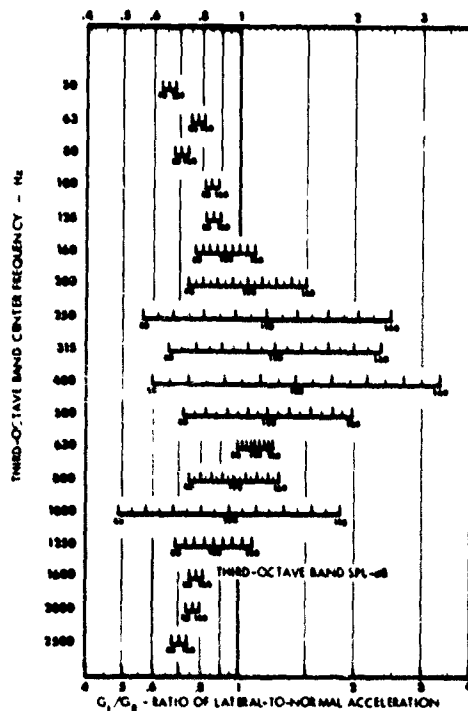


Figure 12. Lateral Vibration Prediction Chart

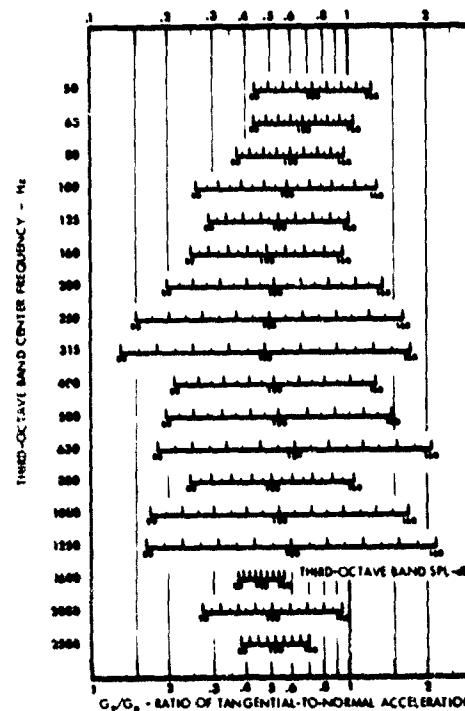


Figure 13. Tangential Vibration Prediction Chart

MASS AND RIGIDITY EFFECTS

An empirical vibration prediction method devised from measured aircraft data would suffice for predicting the vibration environment on a new airplane that is similar in size and structural configuration. However, if the new airplane structure differs significantly from these airplanes, the prediction method becomes less applicable. The applicability can be maintained, however, by incorporating a means for correcting the predicted vibration levels to account for the effects of changing structural mass and rigidity. Such was the intent herein.

Analytical Development - In transport aircraft the air-frame bending modes are well below 100 Hz. The modes in the range above 100 Hz tend to have wave lengths which are short in comparison to the diameter or thickness of the body component, and are, therefore, not readily excited by fluctuating pressures. However, the surface structure tends to be relatively thin, flexible, and free to respond at resonance to acoustic excitation at frequencies up to 2000 or 3000 Hz. This shell type of vibratory response tends to be localized, and independent of similar resonance responses which are a few wavelengths removed. Many resonance modes can be excited in the vicinity of any point on the shell surface, making the rms level in any given frequency band the summation of the contributions of all modes in that band. These resonance responses are usually linear, whereby the majority of the modes in a given band will vary with sound pressure level in similar proportions.

Thus, it may be reasoned that acoustically excited structural vibration levels are approximately proportional to the response of an arbitrary single shell mode. Space does not permit a presentation of the derivation, but it can be shown that with simplifying assumption, this proportionality is approximately given by

$$G_{rms} = \left[X^4 \left(\frac{EI_{xx}}{a} \right) + Y^4 \left(\frac{EI_{yy}}{b} \right) \right]^{.25} \frac{\phi(f_r)}{XY \left[\rho_p h + \frac{\rho_x A_x}{a} + \frac{\rho_y A_y}{b} \right]^{1.25}} \quad (1)$$

where the bracketed quantity with the exponent .25 is rigidity, and the bracketed quantity with the exponent 1.25 is mass of the structure. The nomenclature are defined in Figure 14 and in the list of symbols.

This relation can be used to investigate the effects of mass and rigidity in the measured vibration data by employing a normalizing technique. In this technique, vibration data from structural locations

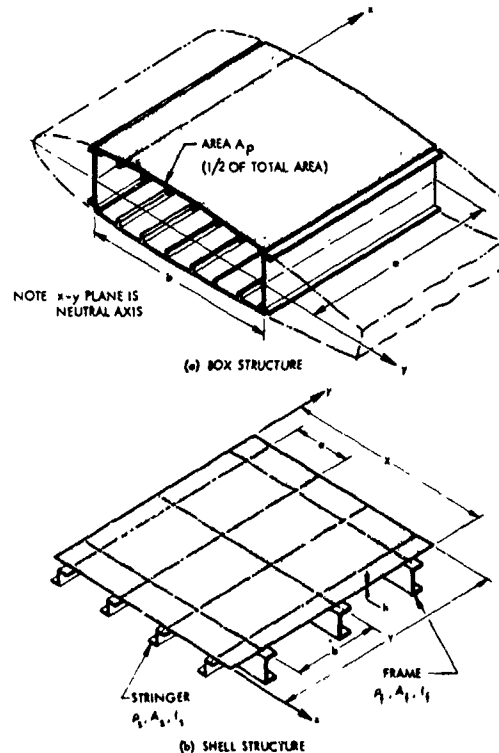


Figure 14. Coordinate System for Shell and Box Structure

of known variation in mass and rigidity are normalized to a common mass and rigidity. The reduction in scatter of the data (on a noise-vibration correlation plot) would be a measure of the ability of the relation to detect the effect of mass and rigidity.

Letting the baseline or "normal" structure be denoted by the subscript 'n', and the structure on which the data were measured be denoted by the subscript 'm',

the ratio of the baseline structure acceleration to the measured acceleration level at a given sound pressure is then given by:

$$\frac{G_n}{G_m} = \frac{\left[X \left(\frac{EI_{xx}}{a} + \frac{EI_{yy}}{b} \right) \right]_n^{.25} \left[X \left(\rho_p h + \frac{\rho_x A_x}{a} + \frac{\rho_y A_y}{b} \right) \right]_m^{1.25}}{\left[X \left(\frac{EI_{xx}}{a} + \frac{EI_{yy}}{b} \right) \right]_m^{.25} \left[X \left(\rho_p h + \frac{\rho_x A_x}{a} + \frac{\rho_y A_y}{b} \right) \right]_n^{1.25}} \quad (2)$$

For convenience, let

$$D = X \left(\frac{EI_{xx}}{a} + \frac{EI_{yy}}{b} \right) \quad \text{lb in}^2 \quad (3)$$

and

$$M = X \left(\rho_p h + \frac{\rho_x A_x}{a} + \frac{\rho_y A_y}{b} \right) \quad \text{lb/in.} \quad (4)$$

Then the normalization equation can be simplified to:

$$G_n = G_m \left(\frac{D_n}{D_m} \right)^{.25} \left(\frac{M_m}{M_n} \right)^{1.25} \quad (5)$$

The mass and rigidity of the structure of each test panel was computed, using Equations 3 and 4 with a surface area of 40" by 40", which was the minimum square area that would encompass at least two frames and two stringers in all cases. The vibration data from all of the flat and curved panels were then normalized to a common mass and rigidity using Equation 5. The data normalized were limited to vibration in the normal direction only, since the analytical development and quantifications of mass and rigidity are only valid for the normal direction of structural motion. The mass and rigidity effects on lateral and tangential vibration are not considered herein, so until such time as mass and rigidity effects on lateral and tangential vibration are investigated, predictions for these directions can be based on mass and rigidity corrected predictions for the normal direction. In essence, this assumes that mass and rigidity effects are the same in all directions.

After normalization, the noise and vibration levels were correlated in the form typified by Figure 6, and the statistical properties of the correlation were derived. A comparison of the scatter factors for the normalized and nonnormalized data correlations, is given in Figure 15. The comparison shows that this normalization increased the data scatter rather than reducing it. Indications were that the actual effects of mass and rigidity were not being correctly described by the theoretical exponents on the mass and rigidity terms. Equation 5 was subsequently altered to make the exponents

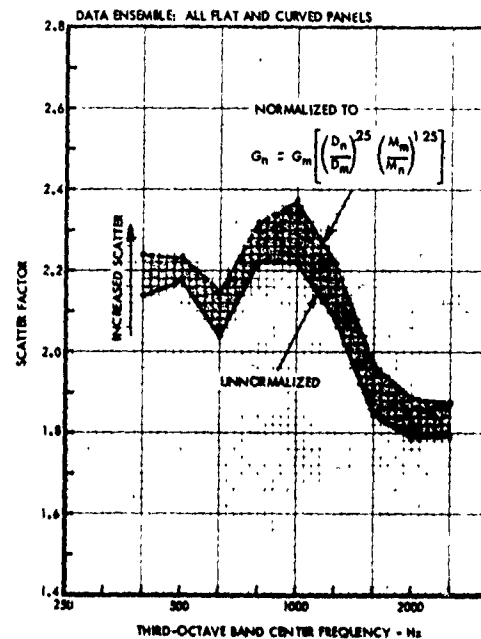


Figure 15. Effect of Normalizing Panel Data With Theoretical Equation

variable; wherein

$$G_n = G_m \left(\frac{D_n}{D_m} \right)^\alpha \left(\frac{M_m}{M_n} \right)^\beta \quad (6)$$

In this form, α and β are undetermined exponents to be empirically derived from the measured data. Subsequent correlations then revealed that α and β were interdependent; that minimum data scatter was obtained when a single optimum combination of values for α and β was used with Equation 6 to normalize the data. A three-dimensional plotting procedure was employed to derive the optimum combinations of α and β for each frequency band and each data ensemble.

Normalization Results - Optimum exponents were derived for several different ensembles of panel and aircraft data. The results of only the most significant ensembles are summarized here. Figure 16 shows the variation in the optimum exponents with frequency for an ensemble which included all flat panels and all but two of the curved panels. The

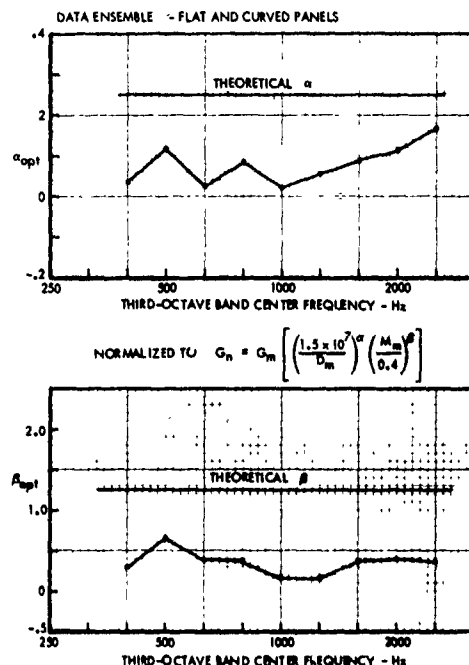


Figure 16. Variation of Optimized Mass and Rigidity Exponents with Frequency

optimum exponents are consistently lower than the theoretical values and exhibit some variation with frequency, whereas the theoretical exponents were independent of frequency. The average exponent values (for all frequency bands) are approximately one-fourth of the theoretical values. These optimum exponents provide some degree of reduction in the data scatter in every band when compared to the unnormalized case, as shown in Figure 17; whereas in Figure 15 the theoretical exponents increased the scatter factor in all frequency bands.

Similar results were obtained with the other data ensembles used. In these investigations it became evident that as the quality of the data ensemble approached the ideal, the α and β exponents approached the theoretical value. By quality is meant the lack of extraneous factors which scatter the data and are not detected in the normalizing process. However, for the best ensemble of data (a group of nine panels which had the most uni-

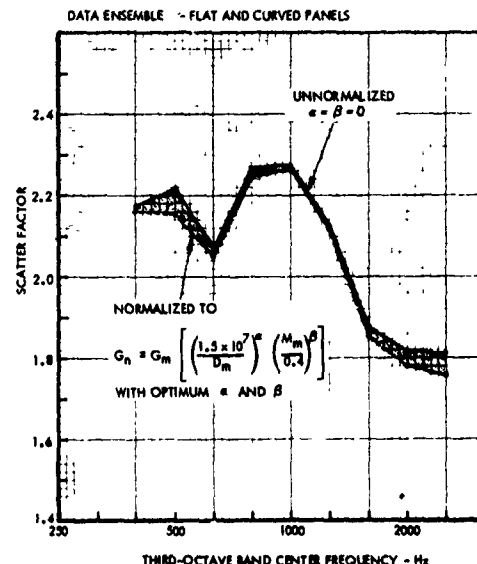


Figure 17. Effect of Normalizing with Optimum Mass and Rigidity Exponents

formity of panel aspect ratio, material, and fabrication methods, and a good range of mass and rigidity variation) the optimum α and β values were still less than the theoretical values, as can be seen in Figure 18. The optimum exponents for this

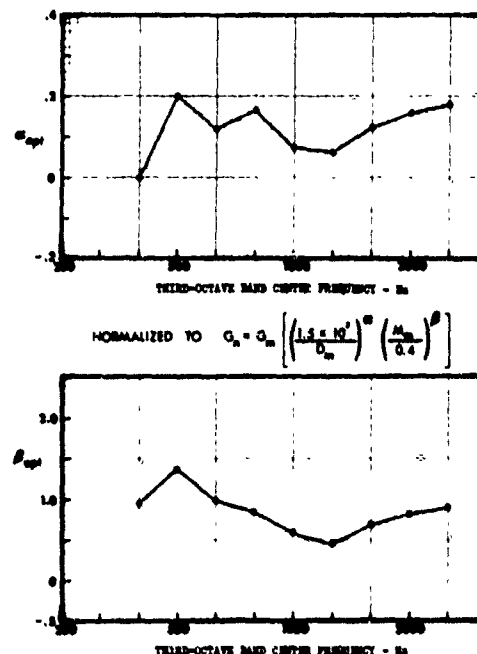


Figure 18. Variation of Optimized Mass and Rigidity Exponents for Best Ensemble

ensemble exhibit less variation with frequency than the other ensembles and also show a reasonable reduction in data scatter, as evidenced by Figure 19.

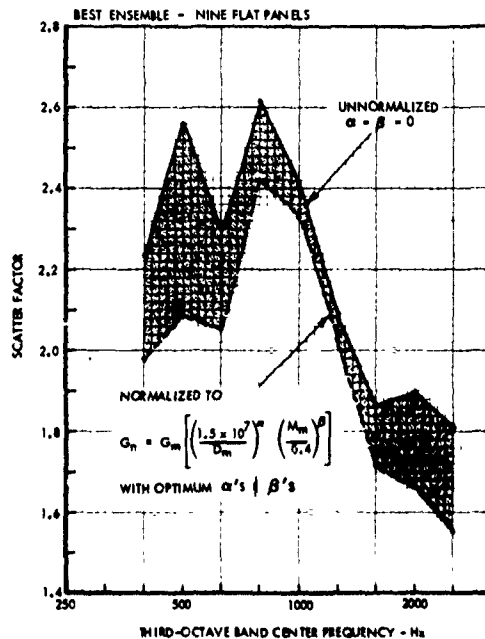


Figure 19. Effect of Normalizing Panel Data with Optimum Mass and Rigidity Exponents

Accounting for mass and rigidity effects in vibration predictions would be much simpler if the exponents α and β were not frequency dependent. Toward this end, single values were derived, and comparisons were made to determine the difference in vibration level due to normalizing with single values of α and β as opposed to using a separate α and β for each frequency band. The α and β values in the frequency bands in which reasonable quantities had been obtained were weighted according to their effectiveness in reducing data scatter, and then averaged, resulting in

$$\alpha_{\text{avg}} = 0.15; \quad \beta_{\text{avg}} = 0.86$$

These exponents were incorporated into Equation (6) to give the empirical equation

$$G_n = G_m \left(\frac{D_n}{D_m} \right)^{.15} \left(\frac{M_m}{M_n} \right)^{.86} \quad (7)$$

The aircraft shell and box structure vibration levels,

excited by a noise level of 120 dB, were then normalized to a common mass and rigidity, using:

- o Optimum exponents based on panel ensembles;
 α_{opt} ; β_{opt} variable with frequency
(Equation 6)
- o Average exponents; $\alpha = 0.15$; $\beta = 0.86$
(Equation 7)

The results of these comparisons showed that the difference in vibration level between the two normalizations was minimal, both cases giving similar levels. This is not surprising since even with the optimum exponents (minimum data scatter) the maximum reduction in scatter factor was only about 25%.

Additional investigations yielded similar results. It was concluded that the elimination of frequency dependence, by using a weighted average for α and β in the mass and rigidity relations, justified the small sacrifice of accuracy in accounting for mass and rigidity. Thus, Equation 7 became the preferred means for accounting for mass and rigidity effects in the vibration prediction method.

VIBRATION PREDICTION METHOD

In establishing the noise-vibration correlation charts to be used for vibration prediction purposes, the aircraft vibration data were subdivided into two broad structural types -- shell and box structure. The vibration data in these two sets were normalized to two reference mass and rigidity values using Equation 7. For the shell structure, the reference mass was 0.59 lb/in, and the reference rigidity was 4.38×10^7 lb/in². For the box structure, the reference mass was 2.24 lb/in, and the reference rigidity was 1.7×10^{10} lb/in². These quantities are based on a structural surface size of 40" by 40", and are approximately the mean of the values computed for all of the aircraft shell and box structure from which data are used.

The complete set of normalized noise-vibration prediction charts are included in Figures 20 and 21 for shell and box structure, respectively.

To avoid excessive clutter the data points in these correlations have been omitted. Further, the statistical scatter is described by "confidence level" lines as opposed to "confidence interval" lines. Confidence level is the likelihood that any data point will fall below the line. Thus the 50% confidence level is the mean line through the data; the 80% confidence level is the line below which 80% of the data lie; etc.

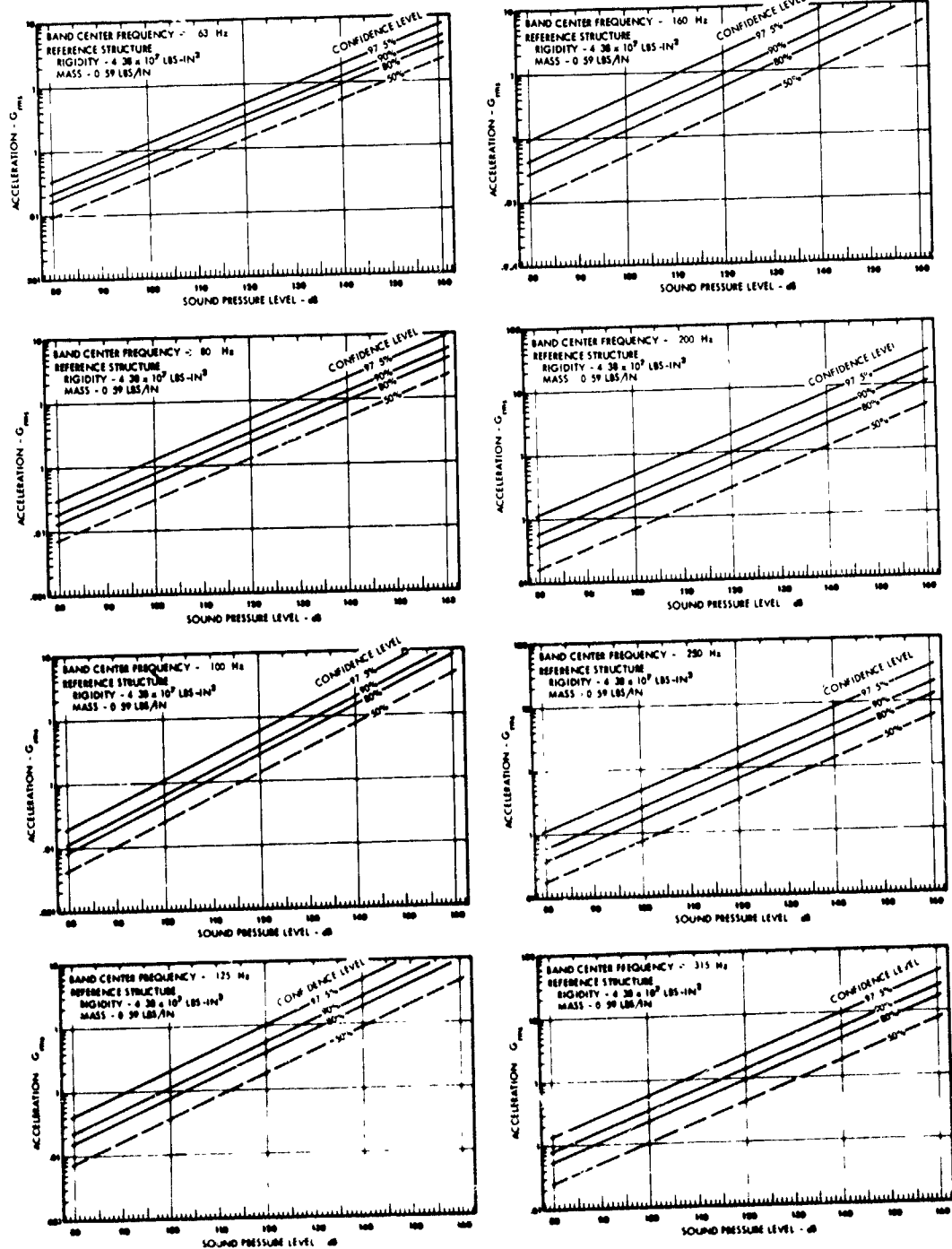


Figure 20. Third-Octave Band Vibration
Prediction Charts; Shell-Structure;
Normal Direction; Ground Operation

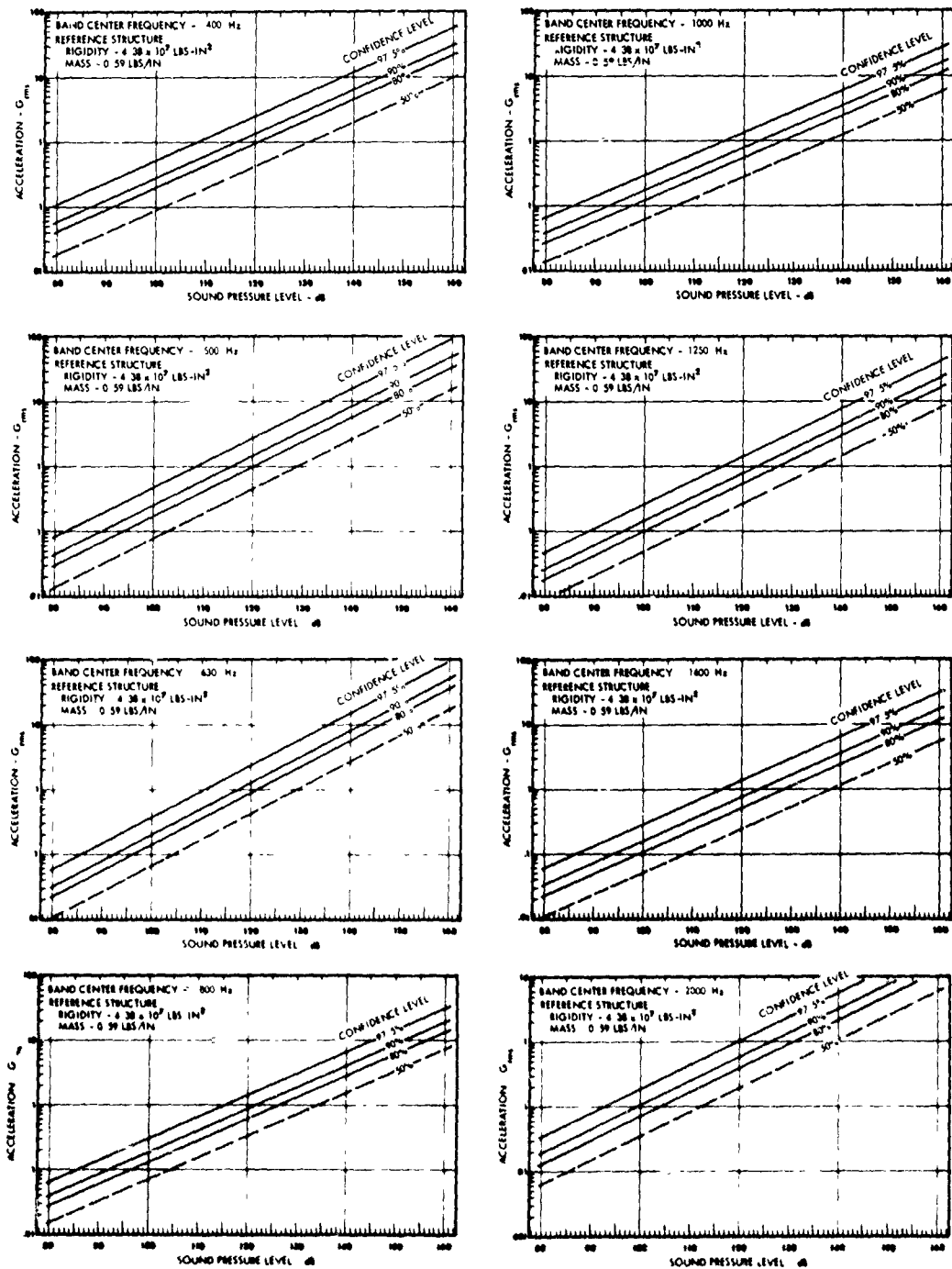


Figure 20. (Continued) Third-Octave Band
Vibration Prediction Charts. Shell
Structure; Normal Direction; Ground
Operation

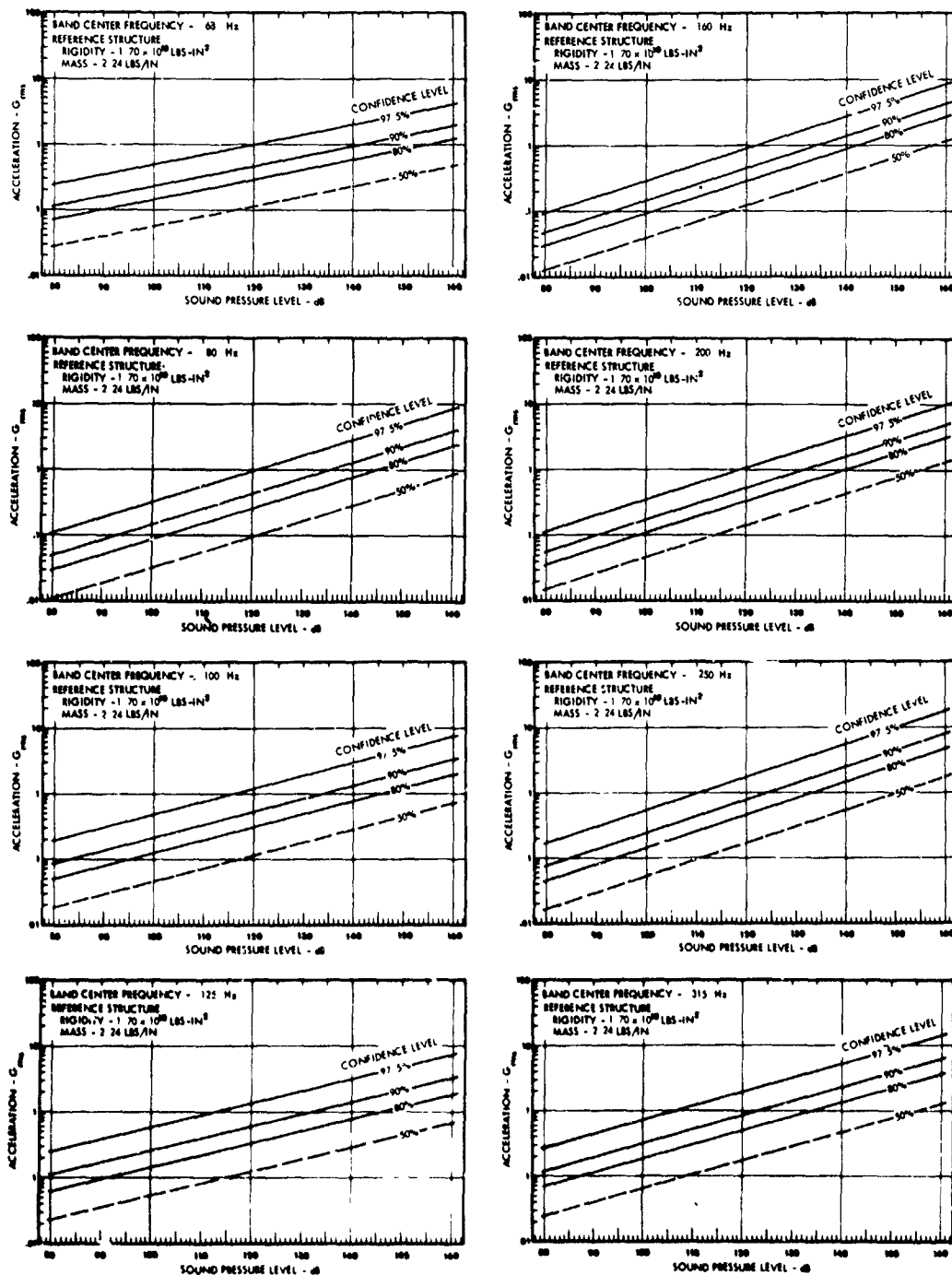


Figure 21. Third-Octave Band Vibration Prediction Charts, Box Structure; Normal Direction; Ground Operation

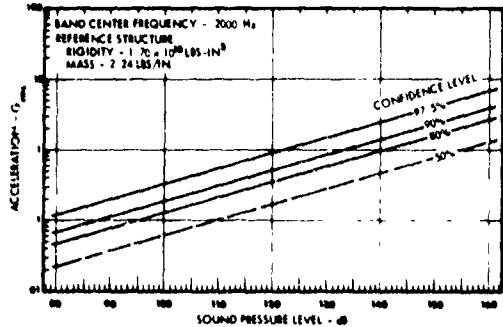
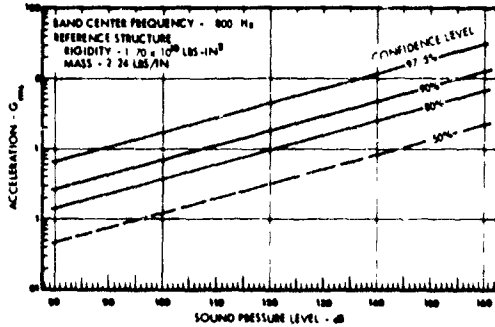
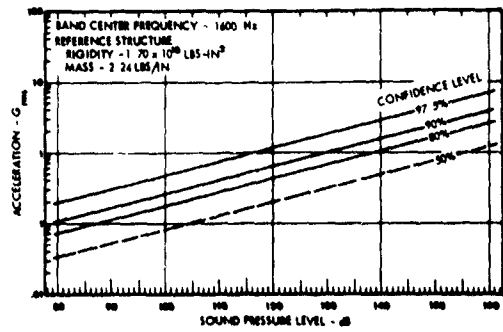
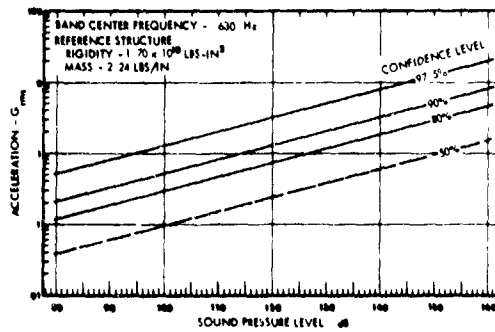
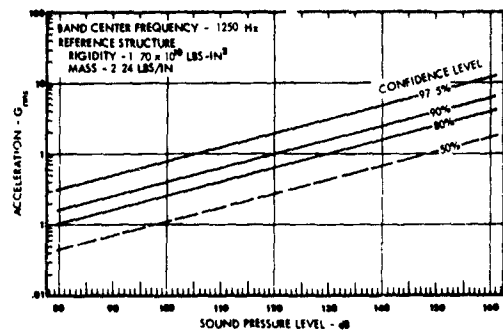
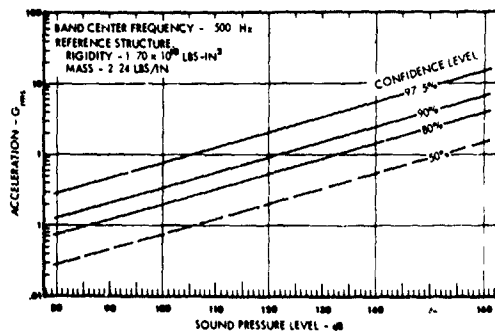
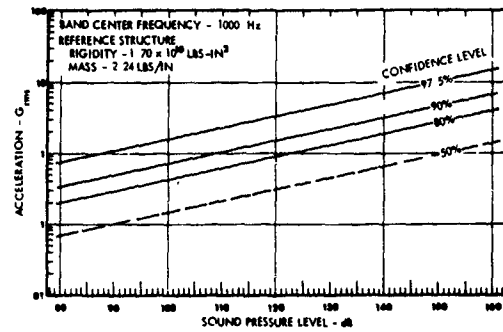
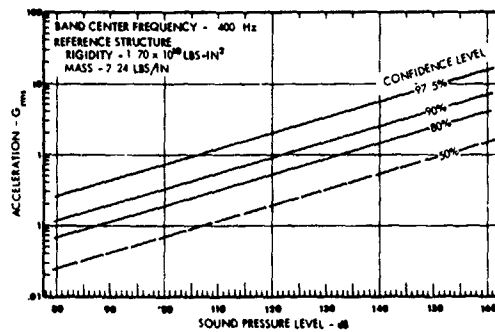


Figure 21. (Continued) Third-Octave Band
Vibration Prediction Charts. Box
Structure; Normal Direction; Ground
Operation

Vibration levels derived from Figures 20 or 21 may be corrected for values of structural mass or rigidity other than the reference value by using Equation 7, re-stated below for convenience:

$$G_P = G_R \left(\frac{D_P}{D_R} \right)^{.15} \left(\frac{M_R}{M_P} \right)^{.86} \quad (7)$$

The subscript 'P' refers to the new aircraft structure, on which the vibration levels are to be predicted, while the subscript 'R' refers to the reference structure and vibration level of the prediction charts. The values of G_R , D_R , and M_R are thus obtained from Figures 20 or 21.

For convenience, Equation 7 was formulated into a nomograph for graphical solution, and is presented as Figure 22.

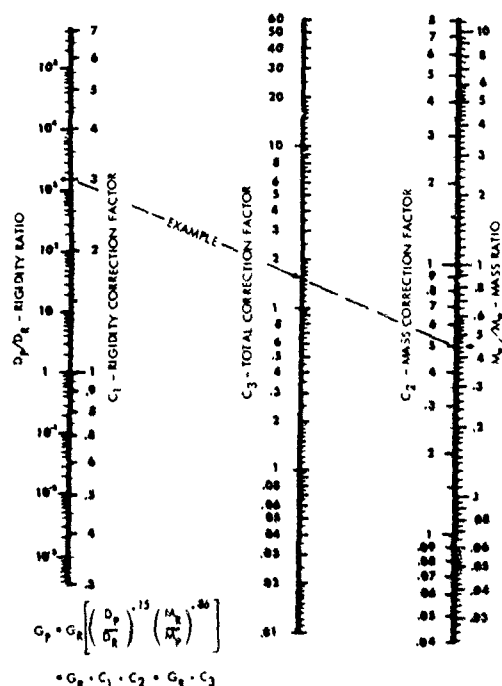


Figure 22. Mass and Rigidity Correction Nomograph

The values of rigidity, D_P , and mass, M_P , for the new aircraft structure can be estimated from the following:

$$D_P = 40 \left(\frac{EI_{xx}}{a} + \frac{EI_{yy}}{b} \right) \text{ lb-in}^2 \quad (8)$$

$$M_P = 40 \left(\rho_p h + \frac{\rho_x A_x}{a} + \frac{\rho_y A_y}{b} \right) \text{ lb/in} \quad (9)$$

In these equations, the characteristic surface area width and length X has been taken as 40 inches.

The application of the vibration prediction charts can thus be summarized in the following procedure:

1. Estimate the third-octave band noise levels for the new structure.
2. Determine which of the two sets of prediction charts (shell or box structure) is more applicable to the new structure.
3. Select a confidence level for design of the new structure.
4. Enter the selected prediction charts with the third-octave band noise levels for the appropriate frequency band, and read the third-octave band vibration level directly at the selected confidence level.
5. A vibration spectrum can then be plotted -- vibration amplitude versus frequency -- that is valid for on-ground, normal-direction vibration of the new structure, if its mass and rigidity approximate the values from the prediction charts.
6. If a mass and rigidity correction is desired, or required, compute the rigidity and mass by Equations 8 and 9. The corrected vibration level can then be computed by Equation 7. (The mass-rigidity correction can also be obtained directly from the nomograph of Figure 22.)
7. Determine vibration levels in the lateral and tangential directions by using the nomographs of Figures 12 and 13 and the above computed normal vibration levels.
8. Obtain vibration levels in pressurized cruise flight from the nomograph of Figure 10 using the above computed normal vibration levels.

OBSERVATIONS AND CONCLUSIONS

It has been found that a given noise level excites consistently higher vibration levels in laboratory test panels than it does in aircraft structure of similar mass, rigidity, and configuration.

It has been shown that in transport aircraft shell type structure, vibration levels on the frames, stringers, etc., are of similar magnitude in the normal and lateral directions. Vibration in the tangential direction is consistently lower.

Vibration on structure and equipment in the pressurized fuselage of two transport aircraft was found to be generally lower, at any given noise level, during pressurized cruise flight than during engine run-up on the ground.

It was found that there was considerable scatter in the data which the normalizing equation, being limited to mass and rigidity effects, does not detect. Variation in other factors such as damping, accelerometer positioning on the structure, unconventional vibratory response, space-time correlation, and sound incidence, could account for much of the scatter. The normalization expressions could be much improved by including a means for accounting for such other factors.

It was found that mass and rigidity effects were in opposite directions - increasing mass decreased response while increasing rigidity increased response. Thus, they tend to be offsetting. The vibration data scatter attributable to mass and rigidity were therefore relatively small. The mass and rigidity of the structure used herein is thought to be typical of most conventional transport aircraft structure, whereby the net effect of mass and rigidity on vibration would typically be small. Exceptions are not uncommon, however, and many instances are conceivable where mass and rigidity could deviate greatly from the trend found here (e.g., i.e. high strength-to-weight structure such as honeycomb and composites, and in low strength-to-weight structure such as used in high temperature environments). In such instances the effect of mass and rigidity on vibration level could be substantial.

SYMBOLS, ABBREVIATIONS, AND SUBSCRIPTS

Symbols

- c Dimension of panel bay in the x - direction; in.
- A Cross-sectional area; surface area - in²
- b Dimension of panel bay in the y-direction - in.
- C Correction factor
- D Rigidity - lb-in²
- E Modulus of elasticity - lb/in²
- f_r Resonance Frequency - Hz
- G Acceleration in multiples of gravitational acceleration; G = A/g; A is item acceleration in inches/sec²; g is 386 inches/sec².
- h Panel skin thickness - in.
- I Cross-sectional area moment of inertia - in⁴
- m Slope of least squares regression line
- M Mass - lb/in
- n Number of points in data ensemble for statistical analysis

- x Coordinate direction
- X Length of panel in x-direction - in.
- \bar{X} Mean value of abscissa
- y Coordinate direction
- Y Length of panel in y-direction - in.
- \bar{Y} Mean value of ordinate
- α Exponent of rigidity ratio
- β Exponent of mass ratio
- ρ Weight density - lb/in³
- σ Standard deviation from the mean
- ϕ Acoustic pressure density - (lb/in²)/√Hz

Abbreviations

- dB Decibel (Re: 0.0002 microbar)
- rms Root-mean-square
- SPL Sound Pressure Level - dB

Subscripts

- C Corrected quantity
- F Flight Quantity
- L Lateral direction
- m Measured quantity
- n Normalized quantity
- N Normal direction
- P Predicted value
- R Reference value
- T Tangential direction
- x, xx Value referenced to axis in x direction
- y, yy Value referenced to axis in y direction

DISCUSSION

Mr. Zurnaciyan: (Northrop Corporation) You indicated that the critical measurements were normal, lateral, and tangential, how do these relate to the vehicle axes?

Mr. Bartel: There is no relation between the direction noted and the vehicle axis. Normal, lateral, and tangential are all defined relative to the sub-structure. Normal is always perpendicular to the surface of the structure. Lateral is always lateral relative to the longitudinal frame, stringer, beam, or spar. Tangential is always tangential to the curvature of the surface of the structure.

Mr. Zurnaciyan: What was your conclusion in your test involving the panel versus the vehicle structure?

Mr. Bartel: The panel tests were conducted primarily to sort out the effects of mass and stiffness; there was no intent to establish a correlation between the panel data and aircraft data, but it came as a secondary effect and it was generally clear that panel tests, or laboratory tests of panel structures, always give higher vibration levels for a given noise level than would be obtained on aircraft structures. And there are a number of reasons for that, the correlation of the sound pressures are different, and I am sure you realize that the damping in the structure is different.

Mr. Sen Gupta: (Boeing Company) Why did the scatter factor reach a peak of 2.4 between 800 Hz or 1000 Hz?

Mr. Bartel: It is thought that the type of resonance that exists in the structure in that general frequency range is of the basic skin-body-frame bending type, or beam-bending type, which is formulated by rather simple equations. It was adapted from a single degree of freedom response beam type resonance; at the higher frequencies I think there are other resonances such as rolling, warping, and twisting of the frames and stringers; and there are coincidence type resonances at those frequencies and our expressions do not account for those.

Mr. Moskel: (Rockwell International Corporation) Have you made any comparison between other well known prediction techniques such as Mahaffey-Smith or Condos-Butler?

Mr. Bartel: No.

SIMPLIFIED TECHNIQUES FOR PREDICTING VIBRO-ACOUSTIC ENVIRONMENTS

K. Y. Chang and G. C. Kao
Wyle Laboratories
Huntsville, Alabama 35807

ABSTRACT

A simplified method has been developed to predict broad frequency range vibration criteria which account for both primary and component load impedance for structures excited by random acoustic excitations. The vibro-acoustic environments were predicted by a one-dimensional equation which utilizes four types of parameters at equipment mounting locations. These parameters consist of input impedance of support structure, acoustic mobility of structural system, input impedance of component package, and blocked pressure spectrum. A set of nomograms and design charts was developed to evaluate the force response graphically with minimum amount of manual computation. The accuracy of the equation in predicting force responses has been verified satisfactorily and the method has proved to be a practical and useful preliminary design tool for aerospace vehicles. Two example problems with different structural configurations were used to demonstrate computation procedures. Satisfactory agreements between analytical predictions and experimental measurements were observed.

INTRODUCTION

The prediction of localized vibratory criteria for space vehicle components due to acoustic excitation has been accomplished based on the empirical techniques as described in Reference 1. These techniques provide standardized approaches to predict vibro-acoustic environments with sufficient conservatism to satisfy design and test requirements for unloaded primary structures. The testing of components to such criteria is valid only when the impedance of a primary structure is sufficiently higher than that of the attached component. Otherwise, there is a strong possibility that the specimen would be overtested.

A complementary technique by which the vibratory criteria are to be specified in terms of actual forces acting on components has been considered [2]. Test specifications are given in terms of the power spectral density of a force environment which account for the

effects of component-primary structure coupling and the approach is designated as the "Force-Spectrum" method. This approach requires sophisticated measurement techniques to define the dynamic parameters required for the prediction equation. The objective of this paper is to present a simplified computation procedure to allow performance of quick estimates on force spectra. It is recognized that several analytical methods, such as the direct integration method and other numerical methods, can be used for the prediction of loads on finite cylindrical structures. Nevertheless, the resulting equations are either too sophisticated or too general and are not practical for performing quick estimates with adequate accuracies. Considering the fact that an average engineer does not have ample time to thoroughly analyze each individual problem; therefore, simplified methods are needed to solve complex problems with a minimum amount of calculations and yet provide adequate accuracy. This is accomplished by the use of charts and nomograms to reduce complex computations.

FORCE-SPECTRA EQUATIONS

The force-spectra equation is derived based on a one-dimensional structural impedance model [2]. By applying Thevenin's and Norton's theorems to this model, the equation which relates the force-spectra to external excitation forces, component impedance and dynamic properties of support structures, such as structural impedances and acoustic mobilities, is established. The final equation is obtained as follows:

$$\Phi_L(\omega) = \left| \frac{Z_L Z_S}{Z_L + Z_S} \right|^2 \cdot |\alpha(\omega)|^2 \cdot \Phi_p(\omega) \quad (1)$$

where $\Phi_L(\omega)$ = Predicted driving force spectrum

$Z_S(\omega)$ = Input impedance of primary structures

$Z_L(\omega)$ = Input impedance of component

$\alpha(\omega)$ = Acoustic mobility of primary structure

$\Phi_p(\omega)$ = Blocked sound pressure spectrum

Due to structural complexities of space vehicles, precise analytical approaches to obtain the parameters defined above are not practical. Therefore, in order to validate Equation (1), approximate equations along with measured data were used to predict the force spectra quantitatively.

An alternate approach to compute the driving force spectrum could be achieved by replacing the produce of $|\alpha(\omega)|^2 \cdot \Phi_p(\omega)$ by $\Phi_R(\omega)$, which is defined as the velocity response spectrum at the component mounting points of the unloaded primary structure. Thus, Equation (1) can be written as follows:

$$\Phi_L(\omega) = \left| \frac{Z_L Z_S}{Z_L + Z_S} \right|^2 \cdot \Phi_R(\omega) \quad (2)$$

and this spectrum may be acquired from the available experiments on the selected test specimens. A flow chart indicating the computation sequence to determine the force spectra is explained in Figure 1.

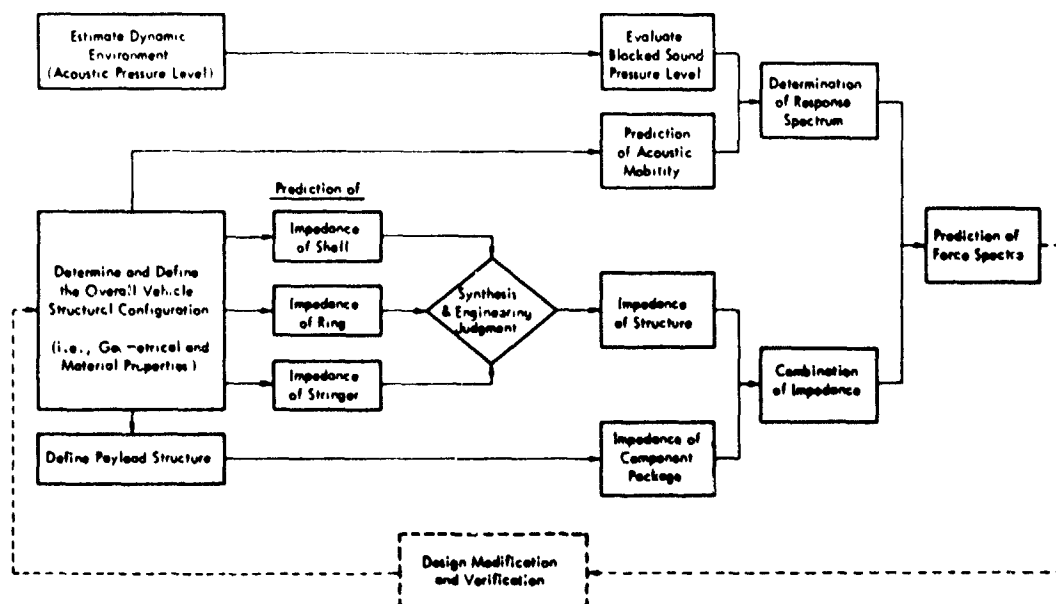


Figure 1. Flow Chart for Predicting the Force Spectra of Structures

TABLE 1. SUMMARY OF INPUT-IMPEDANCE EQUATIONS OF BEAMS, RINGS AND SHELLS

Structure Frequency	Beam	Ring	Shell	Stiffened Shell
Low Frequency Range ($f \leq f_L$)	$K_B = \frac{48 EI}{L^3}$	$K_R = \frac{EI}{0.15 R^3}$	$K_S = 2.5 Eh \left(\frac{R}{L}\right)^{1/2} \left(\frac{h}{R}\right)^{1.25}$	$K = K_S + \sum K_B$ (or $\sum K_R$) $ Z = K/\omega$
Fundamental Frequency, f_L	$\frac{1}{2\pi} \left(\frac{\pi}{L}\right)^2 \sqrt{\frac{EI}{\rho A}}$	$\frac{0.427}{R^2} \sqrt{\frac{EI}{\rho A}}$	$\frac{0.375}{L} \sqrt{\frac{Eh}{\rho R}}$	
Intermediate Frequency Range ($f_L < f \leq f_R$)	$Z_B = 2(1+i) \rho A$ $\cdot \left[\frac{EI}{\rho A}\right]^{1/4} \sqrt{\omega}$	$Z_R = i2 \sqrt{2} \rho A$ $\cdot \left[\frac{EI}{\rho A}\right]^{1/4} \sqrt{\omega}$	$Z_S = \frac{4}{\sqrt{3}} \rho h^2 \sqrt{\frac{E}{\rho R}}$ $\cdot \left(\frac{E}{\rho}\right)^{1/4} \frac{1}{\sqrt{\omega}}$	$Z = Z_S + \sum Z_B$ $+ \sum Z_R$
Ring Frequency, f_R			$\frac{1}{2\pi R} \sqrt{\frac{E}{\rho}}$	
High Frequency Range ($f > f_R$)	Same as Intermediate	Same as Intermediate	$Z_S = \frac{4}{\sqrt{3}} h^2 \sqrt{E \rho}$	$Z = Z_S$ $Z = Z_B$ $Z = Z_R$

Input impedances in the force-spectra equation are specified in terms of the "force/velocity" format. The cylindrical type structures considered herein are stiffened by stringers in the axial direction, and ring frames are attached inside the shell wall. The direction of vibratory response under consideration is referred to as that normal to the skin which is excited by impinging acoustic pressures. The approximate equations for predicting the input impedance of the above structural components are given in Table 1 in three different frequency ranges as defined below [3]:

- Low frequency range or frequencies below the fundamental frequency of the shell,
- Intermediate frequency range, and
- High frequency range or frequencies above the ring frequency of the shell.

Therefore, the evaluation of the stiffened shell impedances is obtained for these three frequency ranges as follows:

Low Frequency Impedances — The static stiffness is the predominant factor which influences the input impedance. Due to the lack of theoretical expressions for input impedances of stiffened cylindrical shells, it is assumed that at low frequencies the input

impedance at any location follows the stiffness line, this stiffness being equal to the summation of the stiffness of the individual structural elements that are present in that location. Two cases are considered in this frequency range, namely:

- If the stiffness of the ring is small in comparison to the stiffness of the stringer or the unstiffened shell, the overall stiffness can be computed by adding the stiffness of the properly modeled structural elements that are present at the input location, as follows:

$$K = K_S + \sum K_B + \sum K_R \quad (3)$$

where K_S = static stiffness of shells

K_B = static stiffness of stringers or beams

K_R = static stiffness of rings

Thus the input impedance of a stiffened cylindrical shell at low frequency follows a stiffness line whose value can be computed from the sum of stiffnesses of structural elements at that point.

- For a stiffened cylindrical shell, if rings are sufficiently stiff in comparison with the entire shell, these rings act like the boundary of structure panels. Then the characteristic impedance of the shell can be determined from the length of the spacing between two adjacent rings.

$$K = K_s + \sum K_B \quad (4)$$

The characteristic impedance represents the impedance of a structure of such a length that reflections from the boundaries are negligible. In other words, the resonance modes of a structure with any non-dissipative boundary conditions are identical to the resonance modes of a supported structure whose length is equal to the distance between the node lines.

Intermediate Frequency Impedances — Within the intermediate frequency range, which extends from the fundamental frequency to the ring frequency, the input impedances of the test specimens can be evaluated as the combination of the characteristic impedances of the primary structural components. The equation is written as:

$$Z = Z_s + \sum Z_B + \sum Z_R \quad (5)$$

where Z_s = characteristic impedance of shells

Z_B = characteristic impedance of stringers

Z_R = characteristic impedance of rings

High Frequency Impedances — The input impedance of a stiffened shell at high frequencies depends on the location of a measurement point and is evaluated by the following rules:

- Unstiffened (skin) Point — The input impedance approaches that of an infinite plate of the same thickness.
- Stiffened Point — The skin and the stiffener(s) decouple dynamically at high frequencies, therefore, the input impedance approaches that of the stiffener(s).
- Stiffened Intersection Point — The input impedance at the centers of short stiffeners segments are generally higher than those of longer stiffener segments; and the impedance at an intersection of the stiffeners is approximately equal to the sum of the

individual impedances of the two stiffeners — the ring impedance and stringer impedance.

Acoustic mobility, $\alpha(\omega)$, is defined as the ratio of the mean-square spectral density of the velocity of the mean-square spectral density of the fluctuating pressure driving the structure. This quantity is expressed by Equation (6) as follows:

$$\alpha(\omega) = \frac{S_u(\omega)}{S_p(\omega)} \quad (6)$$

where $S_u(\omega)$ has units of $(\text{in./sec})^2/\text{Hz}$, and $S_p(\omega)$ is the blocked pressure spectral density having units of $(\text{psi})^2/\text{Hz}$. The blocked pressure includes the effects of reflection and thus accounts for the pressure doubling effect when an object is immersed in a random pressure field.

Generally, the acoustic mobility for a given structure would be calculated based upon modal analysis or statistical energy analysis. However, for the purposes of presenting simplified design curves for acoustic mobility derived from acceleration data of a wide range of vibro-acoustic measurements are shown in Figure 2 for two values of damping: $Q = 20$ and $Q = 200$ [3].

Based on the empirical curves of Figure 2, the α -term is dependent on the structural damping, Q , the diameter of the cylinder, D , and the unit surface weight, m , where f is the frequency in Hz. For structural damping values other than those shown in Figure 2, the acoustic mobility term may be interpolated since an increase in Q by a factor of 10 results in an increase in the acoustic mobility term of one decade.

The blocked pressure spectrum, $\Phi_p(\omega)$, is defined as the effective acoustic pressure acting on a primary structure. The pressure is equivalent to that acting on a rigid cylinder which has the identical geometrical dimensions as the primary structure. This pressure can be determined from the far-field sound pressure measurement and is given by [4]:

$$\beta = \frac{[p_{\text{block}}^2]}{[p_{\text{far}}^2]} = 4(\pi k R)^{-2} \sum_{m=0}^{\infty} \epsilon_m \left| H_m'(kR) \right|^{-2} \quad (7)$$

where $[p_{\text{far}}]$ = measured sound pressure levels without the presence of flexible structures

k = wave number = $2\pi f/c$

- c = speed of sound in acoustic medium;
for air $c = 13,400$ in./sec
- R = radius of cylinder
- ϵ_m = Neumann factor = 1 for $m = 0$,
2 for $m \neq 0$
- $H'_m(kR)$ = derivative of Hankel function
of order, m

The foregoing equation is derived for an infinite panel and does not account for diffraction effects of structures with finite length. However, the error due to diffraction effects is considered as insignificant and will not influence the final results. In the frequency range of interest, the RMS blocked sound pressure is approximately 40 percent higher than the measured sound pressure and such a conversion factor generally leads to conservative estimates of the force spectra.

COMPUTATION CHARTS AND GUIDELINES

In order to minimize manual efforts in performing force-spectrum computations, it is necessary to reduce the derived equations into the forms of nomograms or charts so that lengthy computations can be avoided.

All equations listed in Table 1 contain a frequency dependent and a frequency independent term. Therefore, by evaluating the frequency independent terms, and later, combining with the frequency dependent term, the impedance curve can be easily constructed. The approaches, which are based on the separation of the frequency dependency to simplify the impedance prediction, are presented below.

Nomographic Charts — A nomograph, in its simplest and most common form, is a chart on which one can draw a straight line that will intersect three or more scales in values that satisfy an equation or a given set of conditions. The equations summarized in Table 1 were converted into nomographic forms, and are shown in Figures 3 through 8. Figure 3 evaluates the static stiffness of the ring frame. By knowing the values of radius, R , and the flexibility, EI , of the ring, and connecting these two values on the R scale and the EI scale with a straight line, the intersection point in the K scale represents the computational result of the given equation.

Figures 4 and 5 perform similar computations for static stiffness of beams and the frequency independent part of rings, respectively.

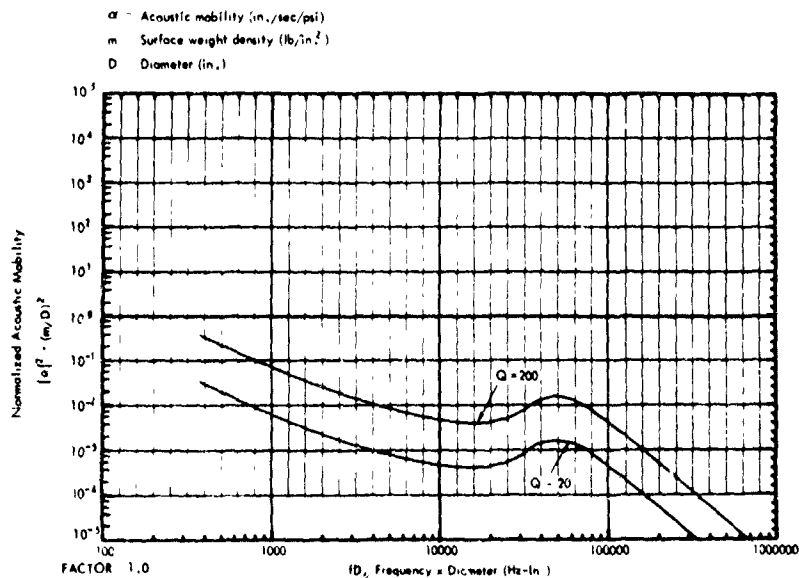


Figure 2. Velocity Acoustic Mobility Levels for Cylindrical Structures
(Based on Blocked Pressures)

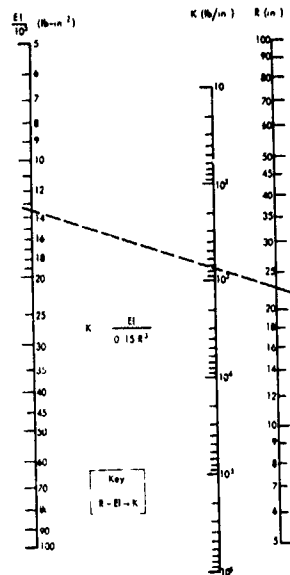


Figure 3. Nomograph for Determining Static Stiffness of Rings

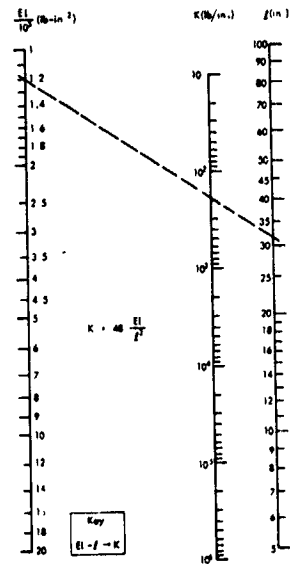


Figure 4. Nomograph for Determining Static Stiffness of Beams

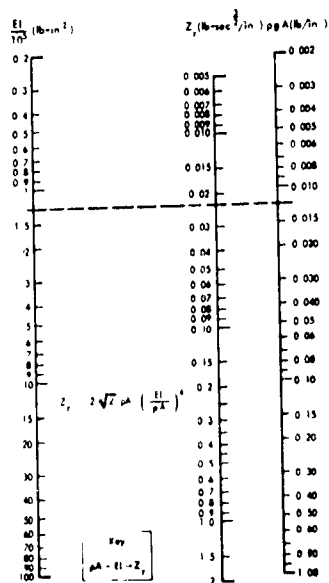


Figure 5. Nomograph for Determining Z_r of Beams and Rings

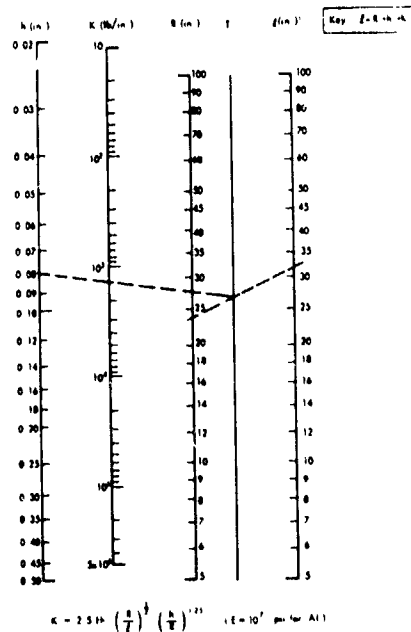


Figure 6. Nomograph for Evaluating Static Stiffness of Unstiffened Cylinders

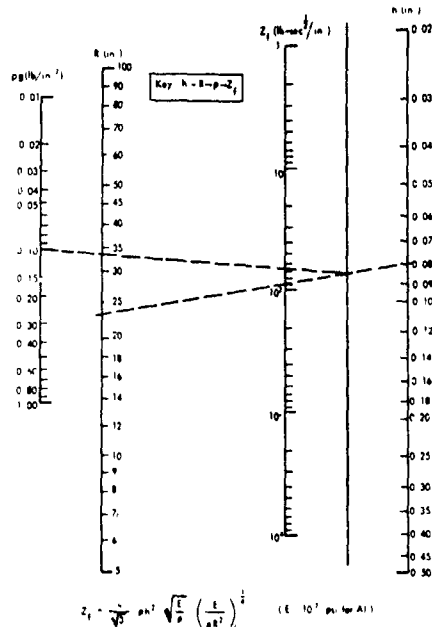


Figure 7. Nomograph for Determining Z_f of Unstiffened Cylinders

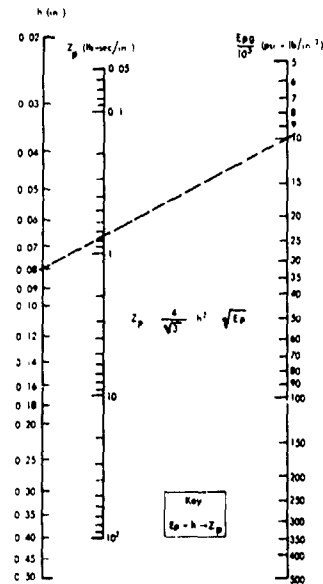


Figure 8. Nomograph for Evaluating Impedance of Infinite Plate

Figures 6, 7 and 8 are four-variable type nomograms for evaluating the frequency independent part of the remaining equations shown in Table 1. For example, in Figure 6, by using one additional axis, T, which lies between the L and R axes and need not be graduated, the four-variable equation was broken into two three-variable equations and are handled as the preceding way, i.e., connecting the L scale and the R scale with a straight line, then joining the intersection point on the T axis and the h scales with another straight line, the intersection point on the K scale is the resulting value.

Charts for Computing Structural Impedance —

The impedance of an ideal damping, spring and mass system may be represented by three intersection lines. By using this approach, the driving-point impedance for beams and rings based on the equations of Table 1 can be represented by two sets of intersection lines varying with the frequency as shown in Figure 9. In this figure, the line representing the proper stiffness value is obtained either from the result of Figures 3 or 4 for rings and beams, respectively, and the line defin-

ing the proper Z_f value of the structure is determined from Figure 5. The stiffness lines represent the impedance at low frequencies and the Z_f lines represent the impedance at high frequencies. The intersection of these two lines determines the fundamental resonant frequency of the structural system. In this figure and the following figures, a scale factor is used to obtain correct scale values for the standard diagrams.

The driving-point impedance for unstiffened cylindrical shells is shown in Figure 10, where the Z_f lines are replaced by the Z_p lines. The lines represented the proper stiffness, Z_f , and infinite-plate impedance are obtained from Figures 6, 7 and 8, respectively. At low frequencies, the impedance of cylinders follows a stiffness line and at high frequencies the impedance is equal to the impedance of an infinite plate which has a constant value. Within the intermediate frequency range, the input impedance may be represented by the Z_f line.

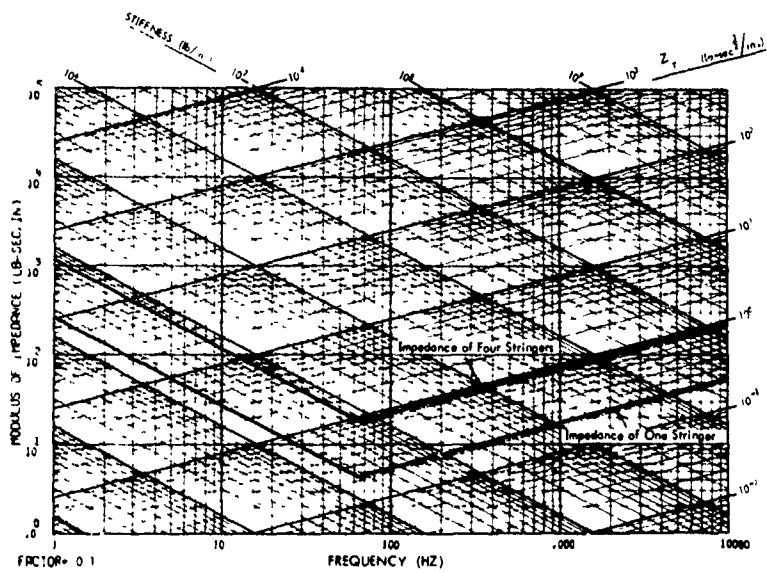


Figure 9. Impedances of Stiffeners

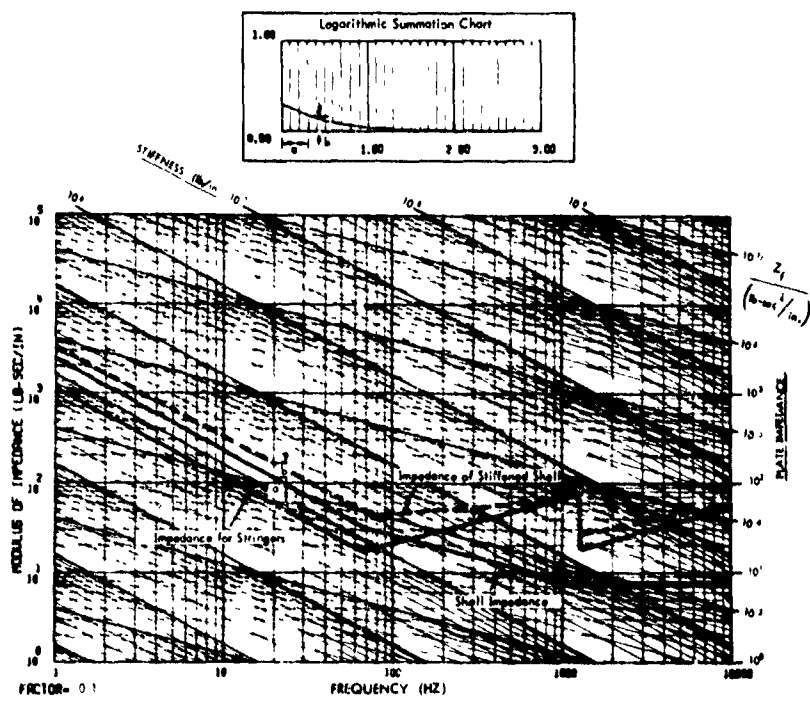


Figure 10. Impedance of Cylindrical Shell

The fundamental frequency and the ring frequency of cylinders are determined by the intersection of these three characteristic lines.

Figure 11 represents the impedance curves for the component package which are defined as an ideal damping, spring and mass system. The graph shown on the upper portion of these two charts will be used to compute the logarithmic sums of two impedance curves. The application of the logarithmic summation chart is explained in example problems.

Charts for Computing Blocked Pressure Spectrum

Spectrum — The conversion of a far-field sound pressure spectrum into a corresponding blocked pressure spectrum is achieved by multiplying the far-field spectrum by the correction coefficient, $\sqrt{3}$, as described in Equation (7). To facilitate graphical computation, Equation (7) is converted to Figure 12, in which the abscissa scale is expressed in terms of fD ; where f is the frequency in Hz, and D is the cylinder diameter in inches. To obtain the $\sqrt{3}$ - coefficient for a

particular cylinder in the frequency scale, it is accomplished by shifting the fD scale in Figure 12 to the left for the amount corresponding to the cylinder diameter, D . For example, if the diameter of a cylinder is 36 inches, the $\sqrt{3}$ - coefficient for that cylinder is obtained by shifting the fD scale by a factor of 36 to the left, as shown by the $\sqrt{3}$ - curve in

Figure 13. The blocked pressure spectrum of the far-field pressure spectrum is then obtained by adding the $\sqrt{3}$ values at each frequency point to the far-field pressure spectrum.

Charts for Computing Response Spectrum

— The velocity response spectrum is obtained by the product of the blocked pressure spectrum and the velocity acoustic mobility. The normalized acoustic mobility curves as shown in Figure 2 must be converted to

$|a|^2$ versus frequency format for use in response computation. The conversion can be accomplished graphically by shifting the abscissa scale to the left corresponding to the diameter of a cylinder, D ; and shifting the ordinate scale downward corresponding to the quantity $(m/D)^2$. For example, by applying the above procedures to an aluminum cylinder with $D = 36$ inches, $Q = 20$, and $(m/D)^2 = 10^{-6}$ lb/in.³, the velocity mobility for the cylinder curve is obtained as shown in Figure 14. The velocity response spectrum is obtained by summing up logarithmically the velocity acoustic mobility curve and the blocked pressure spectrum curve. The response spectrum is indicated by the dashed-line.

Chart for Computing Force Spectrum — The response spectra and the structural impedance obtained from Figures 14 and 11, respectively, are again plotted

on Figure 15 for final computation. The curve representing the sum of these two curves is the resulting force spectrum for the design structural system. Note that all charts developed are in same length scale and the transfer of data curves from one chart to next chart can be easily done by overlay technique.

EXAMPLE PROBLEMS

To aid in understanding the computation procedure, two examples are illustrated. The first example is used to demonstrate the procedures used to predict structural impedances of a stiffened cylinder. The predicted results were then compared with the measured data [5] to evaluate the accuracy of impedance prediction equations. The second example is used to illustrate the procedures in computing a force spectrum based on the structural configurations and the loading criteria used in Reference 2. The measured force response data was used to evaluate the accuracy and conservatism of the predicted force spectrum.

Example of Prediction of Structural Impedance

The specimen used in the prediction consists of a basic cylindrical shell, four longitudinal stringers and two ring frames. The basic cylindrical shell has overall dimensions of 96.0 in. (length) x 48.0 in. (diameter) x 0.08 in. (wall thickness). All structural elements were made of aluminum. The ring frames are built-up channel sections which are attached to the inside surface of the shell wall by means of rivets; and, the stringers are angle sections which are similarly attached to the outside surface of the shell wall. Two heavy end rings consisting of angle sections were welded to the inside surface at the two ends of the shell wall; and, thick circular plywood bulkheads were bolted to the end rings, and are used to provide radial constraint at the ends of the shell wall. Overall dimensions of the specimen are listed in Table 2.

The computations of static stiffness, Z_r , and Z_f for the primary structure components have been demonstrated previously as shown in Figures 3 through 8. The impedance computations for the configuration with two ring frames and four stringers are illustrated in Figures 9 and 10. In these two figures, the plotting scale is 10 times the true value as denoted by Factor = 0.1. In the computation, it was assumed that these two rings act like end bulkheads with high structural rigidity so that the effective length of cylinder becomes the length of the middle segment which is equal to 32 inches. In Figure 9, the impedance for one stringer and four stringers are plotted based on the values obtained from Figures 4 and 5. Similarly, the impedance curve representing the unstiffened cylindrical shell is plotted in Figure 10, in which the impedance representing the sum of four stringers is also shown, except that at high frequencies where the structural system decouples dynamically, and the impedance

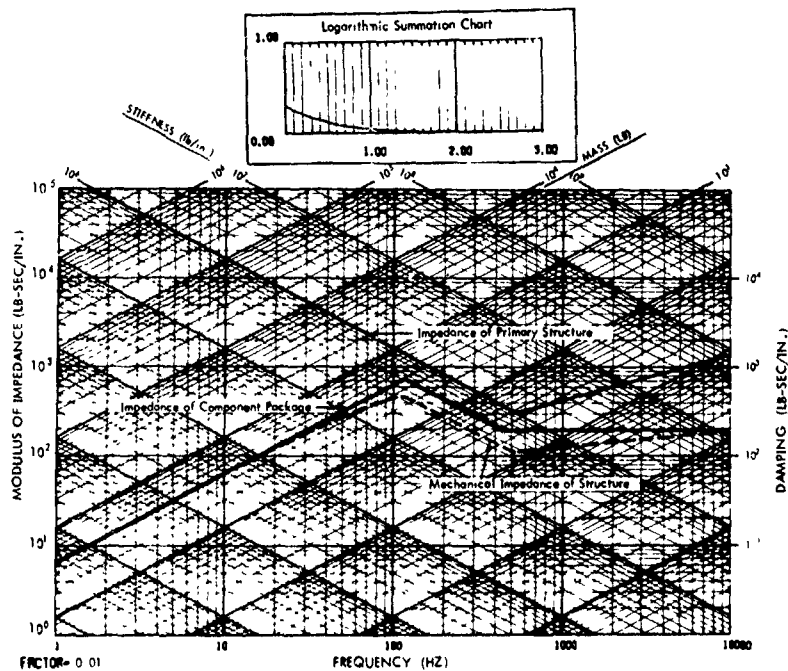


Figure 11. Determination of Structural Impedance

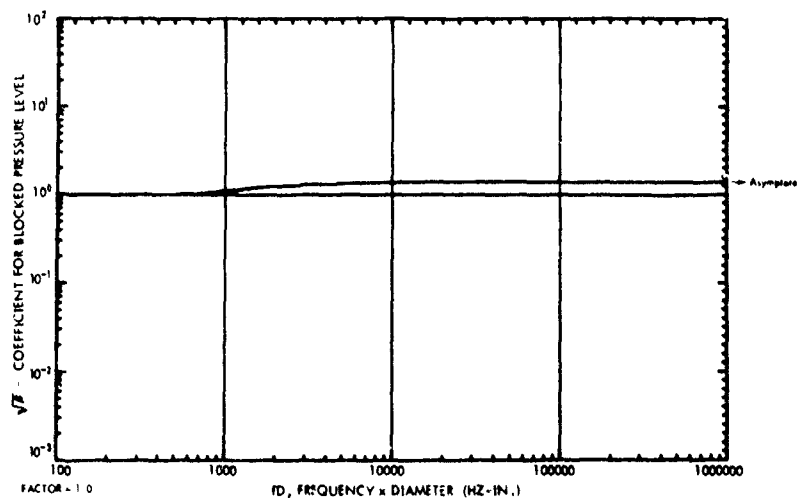


Figure 12. Theoretical \sqrt{B} -Curve for Obtaining Blocked Pressure Level of a Cylinder in a Random Sound Field

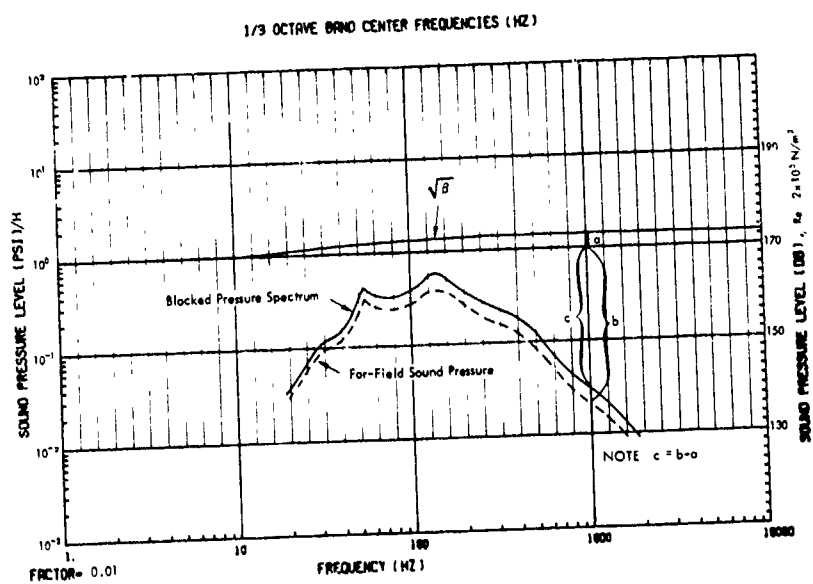


Figure 13. Determination of Blocked Pressure Spectra

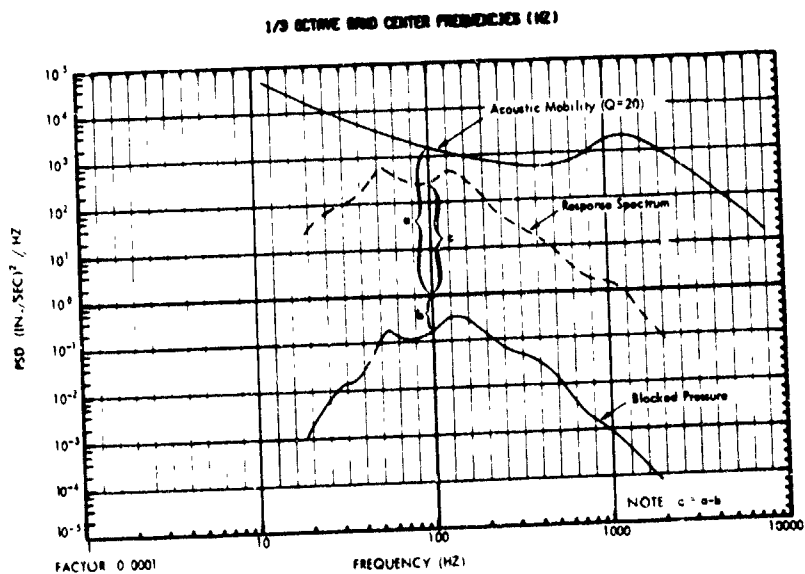


Figure 14. Determination of Structural Response Spectra

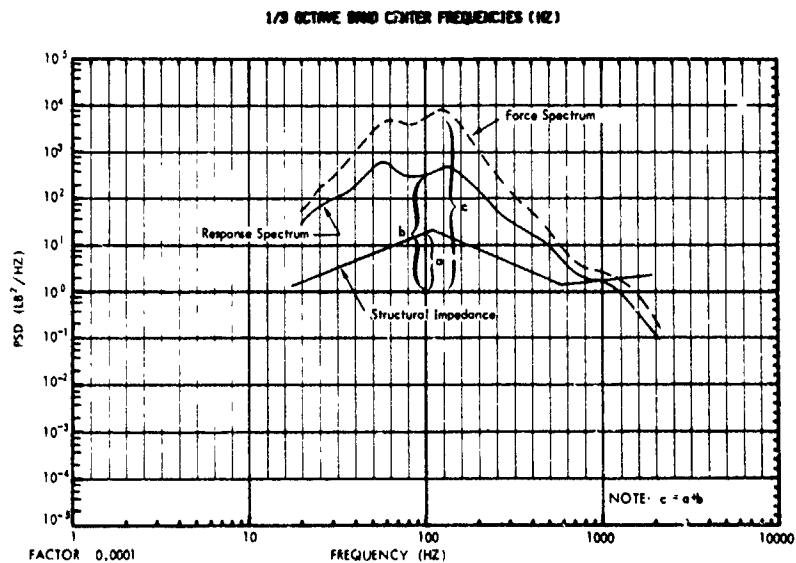


Figure 15. Computation of Force Spectra

TABLE 2. SUMMARY OF DIMENSIONS, STIFFNESS AND MASS PROPERTIES OF CYLINDER AND ITS COMPONENTS

Property	Dimension	Structural Items		
		Ring	Stringer	Shell
Mean Radius, R	(in.)	23.0	---	24.0
Overall Length, l	(in.)	144.5	96.0	96.0
Shell Skin Thickness, h	(in.)	---	---	0.08
Cross-section Area, A	(in. ²)	0.215	0.123	---
Moment of Inertia, I	(in. ⁴)	0.135	0.012	---
Weight per Unit Volume, ρg	(lb/in. ³)	0.1	0.1	0.1
Modulus of Elasticity, E	(lb/in. ²)	10^7	10^7	10^7
Weight per Stiffener *	(lb)	3.10	1.18	116.0

* Two rings spaced at 32" in the longitudinal direction and four longitudinal stringers spaced at 37.7" in the circumferential direction.

approaches that of one stiffener only. The impedance of the stiffened shell as shown in Figure 10, is equal to the linear summation of these two component impedance curves and it is obtained in the following way:

- At any frequency point, measure the difference of two impedance values and use this length as the abscissa value in the logarithmic summation chart (LSC).
- The ordinate corresponding to the abscissa in the LSC is the resulting value for these two curves in logarithmic summation.
- Add the length of the ordinate to the upper impedance curve, the resulting curve denotes the linear combination of these two impedances.

Figure 16 shows the experimental impedance data obtained from Reference 5 along with the predicted impedance for comparison. Generally speaking, the comparison is considered quite satisfactory both in low frequency and high frequency ranges. Fair agreement is also observed for frequencies just below the ring frequency. Some discrepancies are observed in the intermediate frequency region. Such discrepancies are attributed to the errors incurred in summing the impedances of the stringers. However, it may be concluded that the equation and guidelines presented are adequate for determining the structural impedances for design purposes.

Example for Prediction of Force Spectra

The structure used in the second example was a stiffened aluminum cylinder whose dimensions were 36.0 in. (diameter) \times 36.0 in. (length) \times 0.02 in. (thick). The cylinder consisted of five aluminum rings spaced at 6 inches in the longitudinal direction, and 24 longitudinal stringers spaced at 4.7 inches in the circumferential direction. All stiffeners were mounted to the cylinder wall by rivets. The dimensions of the curved panels formed by the stiffeners were 6 inches and 4.75 inches. Two steel rings of angle sections were rivetted at both ends and two circular sandwich plates were bolted to the end rings.

The simulated component package consisted of a 1/2 in. aluminum plate with lateral dimensions of 8.0 in. \times 8.0 in. The plate was supported by four sets of leaf springs at its corners. The bottom of each spring was fitted with a load washer assembly. The total weight of the component package was 3.61 pounds; the resonant frequency of the package was measured at 110 Hz.

In order to estimate the force spectra, the analytic procedures used to predict the impedance of the stiffened cylinder are essentially the same as that described in the preceding example. Hence, no analytical prediction was made and the impedance

was obtained from the experimental testing. The impedance of the component package is estimated and is shown in Figure 11. The measured impedance for the stiffened cylinder is also presented in the same figure, which is approximated by two inclined straight lines as shown. In this figure, the plotting scale is 100 times the true value as denoted by Factor = 0.01. These two impedance curves are then combined according to the logarithmic summation technique as described for the impedance of the stiffened shell except that the resultant curve is obtained by subtracting the length of the ordinate coordinate from the lower impedance curve, i.e., by summing the two individual mobility curves. The summed curve given is the impedance term in the computation of the force-spectra equation.

The measured sound pressure and the blocked pressure spectra for this example have been obtained according to the procedure as described previously and the results are shown in Figure 13. The response spectrum is then obtained by summing the acoustic mobility curve and the blocked pressure curve as shown in Figure 14. The resulting curve as shown in Figure 15 is the computed force spectrum. In Figures 14 and 15, the plotting scale is 10,000 times the correct value as denoted by Factor = 0.0001. The measured force response spectrum obtained from Reference 2 is shown in Figure 17 along with the computed force spectrum. The predicted force spectrum was slightly high, but was judged to be acceptable, since the computed results provide the more conservative estimate for design evaluation.

CONCLUSIONS

A simplified procedure has been developed to predict the interaction force between a component and its support structure (space vehicle) which is subjected to broadband random acoustic excitations. This method was derived from a one-dimensional impedance model and the computation was performed by ways of nomograms and design charts. The conclusions resulting from this study are:

- The force-spectrum equation provides satisfactory results on the predicted force environments of components mounted on space vehicles. This equation is valid for the prediction of forces in the radial direction of the support structure. However, the same concept can be expanded to include the coupling effects induced from the longitudinal and tangential directions so that the complete description of forces in all three directions is feasible.
- The simplified computation method as presented has been shown to be accurate and conservative within current acceptable tolerance limits. The computation process requires minimum manual effort and no computer assistance is required.

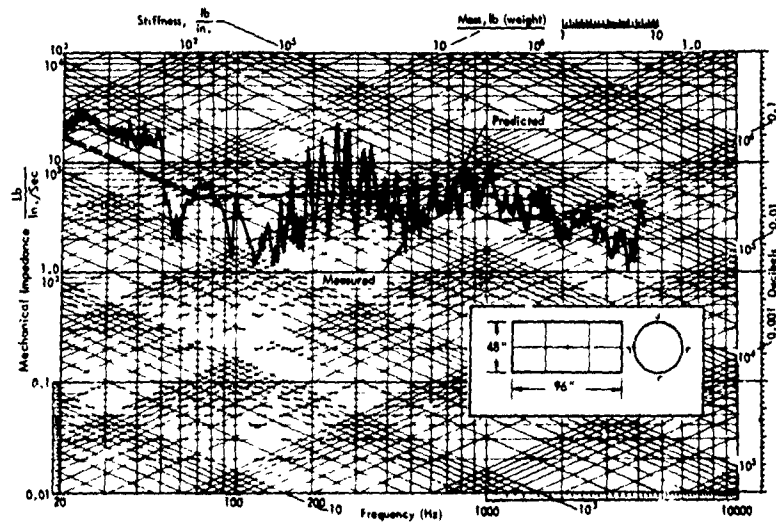


Figure 16. Measured Input Impedance: Shell with Two Rings and Four Stringers (Reference 5)

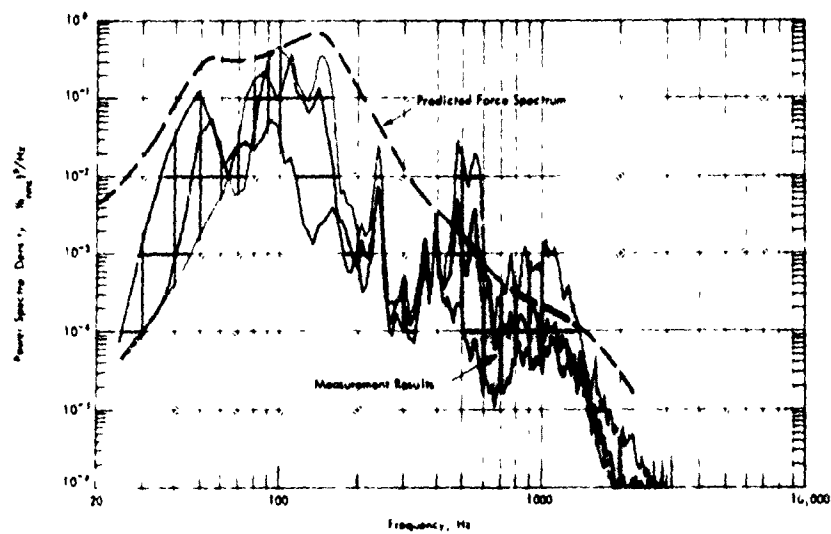


Figure 17. Measured Force Spectrum (Reference 2)

ACKNOWLEDGMENTS

This work was sponsored by National Aeronautics and Space Administration, Marshall Space Flight Center, Huntsville, Alabama, under Contract No. NAS8-25811.

REFERENCES

1. Barrett, R.E., "Techniques for Predicting Localized Vibratory Environments of Rocket Vehicles," NASA TN-D-1836, October 1963.
2. Kao, G.C., "Prediction of Force Spectra by Mechanical Impedance and Acoustic Mobility Measurement Techniques," Wyle Laboratories Research Staff Report WR 71-16, October 1971.
3. Chang, K.Y., Cockburn, J.C. and Kao, G.C., "Prediction of Vibro-Acoustic Loading Criteria for Space Vehicle Components," Wyle Laboratories Research Staff Report WR 73-9, September 1973.
4. Waterhouse, R.V., "Diffraction Effects in a Random Sound Field," JASA, Vol. 35, pp. 1610-1620, October 1963.
5. Conticelli, V.M., Kao, G.C. and White, R.W., "Experimental Evaluation of Input Impedances of Stiffened Cylindrical Shells," Wyle Laboratories Research Staff Report WR 70-12, August 1970.

USE OF A SEMI-PERIODIC STRUCTURAL CONFIGURATION
FOR IMPROVING THE SONIC FATIGUE LIFE OF STIFFENED STRUCTURES

G. SENGUPTA
Boeing Commercial Airplane Company
Seattle, Washington 98124

A light weight panel stiffened by a set of stiffeners at regular intervals is used in many structural configurations. Such panels are often subjected to various dynamic disturbances, e.g., random pressure fluctuations due to boundary layer turbulence, noise from jet engines, etc. A wave propagation method applicable to such spatially periodic structures has been developed during recent years. The purpose of this paper is to study the effect of any deviation from periodicity of stiffener locations on the panel response and sonic fatigue life. For this reason, the existing wave propagation method has been combined with the transfer matrix method to generate a solution which is applicable to semi-periodic structural configurations. Such a configuration consists of repetition of a basic unit which contains sections of unequal length and/or stiffness properties. In this study, such a method has been applied to predict the response of a semi-periodically supported beam in which the basic unit is made up of two sections of unequal lengths. The excitation considered is band-limited white noise at normal incidence. The response of the semi-periodic structure has been compared with that of a periodic structure of equal weight. The low frequency response of the semi-periodically supported beam is controlled by two modes of the basic two-span unit. When the span lengths are equal (i.e., the structure is periodic), the higher mode is symmetric and is very strongly excited by white noise at normal incidence. The lower mode is antisymmetric and is not excited. But as the span lengths are changed, the contribution of lower mode increases and that of the higher mode decreases. Because of the combination of these two opposing trends, the total response passes through a minimum for a particular semi-periodic configuration, for which one span length is about 33% shorter than the other (i.e., for a span ratio of about 2/3). For this configuration, the maximum r.m.s. stress is reduced by about 18% compared to that of a periodic structure of equal weight. The sonic fatigue life is correspondingly increased by a factor of three to five. Alternatively, the skin thickness and the panel weight may be reduced by about 14%, for the same stress level and sonic fatigue life. This work, therefore, shows that there is a possibility of increasing the sonic fatigue life and/or reducing the skin panel weight by arranging the stringers in a particular semi-periodic configuration. As a corollary to this work, one would also expect that a variation in stringer spacing, by as much as 10%, would not cause any noticeable increase in the r.m.s. stress level in the skin.

INTRODUCTION

practical structures consist of a large panel stiffened by a set of stiffeners at regular intervals. The aircraft fuselage, the upper surface blown (USB) wing or the externally blown flap (EBF), the engine nacelle, and also the submarine hull are typical examples. During takeoff, the aft fuselage is subjected to intense noise levels from the jet engine operating at maximum power. During cruise, pressure fluctuations due to boundary layer turbulence also excite the fuselage skin and supporting structure. When the convection or the trace velocity of the pressure field coincides with the natural flexural wave speed in the stiffened skin at a particular frequency,

large "coincidence" peaks appear at that frequency in the structural response and radiated noise spectra. In high speed aircraft, such a large structural stress response causes structural failure from sonic fatigue, when the structure is excited under coincidence conditions over a prolonged period. Since r.m.s. skin stress is generally maximum near the stringer locations, fatigue cracks on the skin develop near the stringers. In addition, the rivet holes cause stress concentration, aggravating the situation even further.

Many attempts have so far been made to predict the response of such structures to noise. The theories range from simple single degree of freedom approximations (1) to

more sophisticated statistical energy analysis⁽²⁾, finite element⁽³⁾ and transfer matrix⁽⁴⁾ methods and wave propagation and periodic structure theory⁽⁵⁾. Attempts have also been made to evolve simplified sonic fatigue design procedures that can be used at the preliminary design stage⁽⁶⁾. At Boeing, many carefully planned flight tests have been performed for obtaining a better understanding of the response of complex, practical structures so that the existing design methodology can be improved and the structure can be optimized from cabin noise and sonic fatigue point of view⁽⁷⁾. It is indeed hoped that all these diversified efforts will eventually give rise to a superior technology in the near future.

Returning to the analytical approaches, a significant development has taken place in utilizing the theory of wave propagation in periodic structures to predict structural response to noise and convected boundary layer fluctuations⁽⁸⁻¹²⁾. In these studies, the structure was considered to be perfectly periodic, i.e., no variation in stiffener location or spacing was allowed. In real life, of course, the structure is nominally periodic. The effect of any non-periodicity in stiffener location was first studied by Ford⁽¹³⁾ who considered the response of a two spanned beam on three simple supports. Since, in the case of fuselage structure excited by jet noise, more than two panels as well as stringers and frames participate in the response, the conclusions drawn by Ford from his simple two-span model need to be re-examined.

The free vibration of a multi-spanned structure with irregular stringer spacing was studied by Lin⁽¹⁴⁾. More recently, Lin and Yang⁽¹⁵⁾ have presented an elegant theory for predicting the free vibration characteristics of a multi-spanned structure in which the stiffnesses and spacings fluctuate in a random manner. It will be interesting to know how the panel response is affected by such irregularities.

It is difficult to fabricate an absolutely perfect periodic structure and it is also not known whether it is essential to have an exactly periodic structure from sonic fatigue point of view. The purpose of the present paper is to examine this problem by comparing the response of a periodic structure with that of a semi-periodic structure of equal weight (Fig. 1). The semi-periodic configuration consists of repetition of a basic unit which contains sections of unequal length and/or stiffness properties. The results of this study indicate that the sonic fatigue life of a stiffened structure can be prolonged, merely by arranging the stringers in a particular semi-periodic configuration.

FREE VIBRATION CHARACTERISTICS OF PERIODIC AND SEMI-PERIODIC STRUCTURES

Before looking into the problem of deter-

mining the response of semi-periodic structures it is helpful to be familiar with the free vibration characteristics of such structures. The response spectrum is easier to diagnose, once the variation in natural frequencies with various parameters is fully understood.

The free vibration characteristics and the wave propagation properties of periodic structures are well known. In an infinitely long periodic structure, free flexural waves can be propagated in certain frequency bands called "free propagation zones." The free vibration modes of an N-bay periodic structure have groups of closely spaced natural frequencies. The various modes and natural frequencies lie within various free propagation zones. As the number of panels is increased, the number of natural frequencies in each group increases and in the limit when the number of panels is infinity, the natural frequency groups are replaced by frequency bands identical with the free propagation zones of the flexural waves. A more detailed discussion on this subject can be found in Reference 16.

In the present work we are interested in the natural frequency bands and free propagation zones of a semi-periodic structure. This is done by solving the free vibration problem in absence of any external loading. The details of the theory for predicting the response are given in the Appendix. The free vibration problem is analyzed by equating the right hand side of equation (A17) to zero. A non-trivial solution exists provided

$$\det \begin{bmatrix} [S_2] [E_X(L_2)] [E_X(0)]^{-1} [S_1] \\ [E_X(0)] - e^{-i k L_1} [E_X(-L_1)] \end{bmatrix} = 0 \quad (1)$$

This equation can be solved for the wave number k which, in the context of free vibration problem, corresponds to the wave-number of the freely propagating structural waves at a particular frequency ω . Since the above determinant is of the order 4×4 , four different complex values of k can be found at a given frequency. Two of these are equal and opposite of the other two. Physically, the two unique values of k represent the wave-numbers of two orthogonal bending waves. The two negative values of k correspond to the same waves propagating in the opposite direction, along the structure. Further discussion on this aspect of the problem can be found in Reference 10.

It is much easier to visualize the wave propagation mechanism and identify the modes and the natural frequencies bounding the free propagation zones when the stringers are considered to be rigid in bending but flexible in torsion. One can then identify only one unique value of k at a particular frequency. Within the free propagation zones, the imaginary part of k is zero, and the real part varies with frequency.

At the frequencies bounding the free propagation zones, k is either $\pm \pi$ or zero. Utilizing this relationship between the bounding frequencies and the limiting values of k , the various free propagation zones or the natural frequency bands can be found from equation (1), for any combination of ℓ_1 and ℓ_2 . This was done for a semi-periodically supported beam and the results are shown in Fig. 2. The stringers were replaced by simple supports ($K_R = 0$, $K_T = \infty$) so that the mode shapes at the various bounding frequencies could be easily identified. The shaded areas represent the frequency bands within which the natural frequencies lie and free wave propagation can take place. If the structure is excited at a frequency falling outside any of the shaded areas, the structural waves decay rapidly with distance. Only the first three natural frequency bands are shown in Fig. 2 since in most sonic fatigue problems the coincidence response at low frequencies is the most severe and is of major concern. (A similar variation of the natural frequency bands with the span ratio is expected at higher frequencies.)

The frequencies in Fig. 2 have been non-dimensionalized with respect to the fundamental frequency (f_s) of a beam of length ℓ on simple supports. It is interesting to observe the variation of the natural frequency bands with the span ratio $z = \ell_1/\ell_2$. When the ratio $z = 1$, i.e., the spans are of equal length, the structure is periodic and the bounding frequencies are readily identified with the natural frequencies of a beam of length ℓ , with various boundary conditions. As z is reduced from 1.0, i.e., the intermediate support in each two-span unit is moved from the center, the width of each natural frequency band changes and ultimately as z tends to zero, the bands narrow down and converge to the natural frequencies of a beam of length 2ℓ , clamped at both ends. However, at $z = 0$, the structure becomes periodic once again, being supported on simple supports at an interval of 2ℓ . The lower boundary frequencies of the free propagation zones of this structure correspond to the natural frequencies of a beam of length 2ℓ , simply-supported at both ends, and these are marked by solid triangles along the ordinate in Fig. 2.

ANALYSIS OF RESPONSE TO NOISE

The response of a semi-periodically stiffened panel to a random pressure field convected at a given speed along the length of the structure can be calculated from equation (A18) developed in the Appendix.

Mead⁽⁵⁾ has shown that the r.m.s. stress response of a flat stiffened structure reaches a maximum for a convection speed that excites the "stringer-torsion mode" of the panel under coincidence conditions. For typical .04" thick panels stiffened at 9" intervals by stringers, this velocity corresponds to about 90 to 100 ft/sec and is much below the usual trace-

velocity of sound waves on the structures, which is about three to five times the speed of sound. Mead's work was later extended by the author and it was observed (see Fig. 3) that beyond an excitation wave-speed of about 150 ft/sec, the r.m.s. response was insensitive to variations in either the speed of convection of excitation or the rate of decay of correlation. An excitation with an infinite trace-velocity (i.e., an excitation at normal incidence) and zero decay rate is therefore generally adequate for sonic fatigue design. In this work, such an excitation was therefore used for computing the response.

In the theory, variation in stringer spacing as well as stringer stiffness are allowed within each semi-periodic unit. For the sake of simplicity, only the stringer spacing was varied and the effect on the response was observed. A structural model consisting of a beam on simple supports was used, so that the frequencies of peak response and the corresponding mode shapes could be related to the results shown in Fig. 2.

In designing structures for sonic fatigue, usually the root mean square (rms) stress is calculated first. With the help of an S-N curve applicable under random loading, the sonic fatigue life for the calculated rms stress level is then predicted⁽⁶⁾. For this reason, the r.m.s. stresses at various points on the supported beam were computed, for many different values of the span ratio z . The maximum r.m.s. skin stress was then calculated for each span ratio. The results are plotted in Fig. 4. The r.m.s. stresses are non-dimensionalized with respect to the maximum r.m.s. stress that occurs when the structure is periodic and the two spans are equal ($z = 1$).

As the span ratio $z (= \ell_1/\ell_2)$ is reduced from 1.0, the maximum r.m.s. stress drops. At $z = 2/3$, the maximum r.m.s. stress reaches the smallest value which is about 18% less than the level corresponding to $z = 1$. This, therefore, represents the most preferable semi-periodic configuration. In Fig. 4, the r.m.s. stress distribution along the beam length for this semi-periodic configuration is also compared to that of the periodic configuration.

Reduction of r.m.s. skin stress by 18% increases the sonic fatigue life by a factor of the order of three to five⁽⁶⁾. Alternatively, using this configuration one can reduce the skin thickness and therefore the panel weight, by about 14% and still have the same skin stress level. A span ratio of .67 corresponds to about 20% deviation in stringer location from the periodic structure. Therefore, this work shows that, within the limitations of the assumption used, a variation of up to 20% in support location is allowable and in fact, is likely to be beneficial, and the flatness of the curve around the minimum suggests that slight variations from the most preferable semi-periodic

configuration would not cause any major problem.

As the span ratio is reduced beyond $2/3$, the maximum r.m.s. stress increases and finally, as z tends to zero, the maximum stress reaches a value twice as high as that at $z = 1$, and this is to be expected.

Next, the computations were extended to see if the effect predicted in Fig. 4 was any different if the excitation spectrum was wider than what was originally used in the calculation. It was found that excitation with a wider band caused only a slight change in the r.m.s. stress levels and the level at $z = 2/3$ relative to that at $z = 1.0$ remained virtually unchanged.

Similarly, increasing the beam or skin loss factor also had no effect on the percentage difference between the levels at $z = 1$ and $z = 2/3$.

In order to understand the reason for the existence of the preferable semi-periodic configuration, one needs to look at the response spectra. The response spectra were plotted and analyzed for various span ratios. It was found that for all the semi-periodic configurations considered, the response spectra were dominated by two peaks. As the span ratio was varied, the relative peak levels as well as the frequency separation of the two peaks varied, as one would expect from Fig. 2. Comparison of the spectra with the natural frequency diagram of Fig. 2 showed that the frequencies of the lower modes for various semi-periodic configurations fell on the curve marked L. On the other hand, the frequencies of the higher modes fell on the curve marked H. Generally, the modes associated with these two curves are symmetric and only these modes are therefore excited by white noise at normal incidence.

When the structure is periodic and $z = 1.0$, the higher mode is strongly excited since it is symmetric. The lower mode is antisymmetric and the work done by the excitation pressure field at normal incidence, for deflecting one span, is equal and opposite to that on the adjacent span and they cancel each other. The lower mode therefore does not contribute to the total response when the structure is periodic and there is only a single peak in the spectrum for $z = 1.0$. When $z = 1/3$, the higher mode is antisymmetric and does not contribute to the response. As z tends to zero the contribution from the higher mode becomes less and less significant but the contribution from the lower mode increases steadily. To summarize, as z varies from 1.0 to 0 , the contribution from the higher mode drops from a maximum to a very small value (zero at $z = 1/3$) and that from the lower mode increases steadily from zero to a much higher value. The total response therefore passes through a minimum around $z = 2/3$ due to the combination of these two opposing trends. A

similar effect was observed by Ford⁽¹³⁾ in his work on the response of a beam pinned at three points.

CONCLUSIONS

This work shows that there is a possibility of increasing the sonic fatigue life and/or reducing the skin stress level and weight merely by arranging the stringers or the stiffeners in a particular semi-periodic configuration. This has potential application in areas where panel buckling is not the main problem. The aft section of the fuselage is a good example, since, generally, the skins remain unbuckled during takeoff when this portion of the aircraft's structure is subjected to intense noise levels. There is also application potential to wing and nacelle structure since these skins are usually buckling resistant and are also subjected to high intensity noise. Aircraft which utilize upper surface blowing should have greater areas of application for the technique since sonic fatigue requirements usually design a larger portion of the total structure.

The theory presented in this paper is applicable to flat, stiffened panels. The conclusions were derived from a study of stiffened beam models and it is hoped to extend the computation, using a range of structural data typical of skin-stringer panels used in various aircraft. Generally, takeoff conditions are most severe from sonic fatigue point of view and therefore the effect of fuselage pressurization need not be considered. This work is concerned with the percentage difference (rather than absolute values) in response of a periodic and a semi-periodic structure and the typically large radius of curvature of fuselage structures would probably have a secondary effect on that difference.

ACKNOWLEDGEMENT

This work was started while the author was spending a year as a Resident Research Associate of the National Academy of Science at the NASA-Langley Research Center, Hampton, Virginia, and was completed after he joined The Boeing Company, Seattle, Washington. The author would like to thank Dr. M. M. Mikulus and Mr. M. V. Rhodes of NASA-Langley and Mr. L. D. Jacobs and Mr. H. N. Waniez of Boeing, for their stimulating discussions on the possible areas of application of this work.

REFERENCES

1. J. W. Miles, "On Structural Fatigue under Random Loading," *J. Aeronautical Sciences*, V.21, 1954.
2. R. H. Lyon, E. Eichler, "Random Vibrations of Connected Structures," *JASA*, V. 36, n7, 1344-1359, 1964.
3. L. D. Jacobs, D. R. Lagerquist, "A Finite Element Analysis of Simple Panel Response to Turbulent Boundary Layers," AFFDL-TR-67-81, WPAFB, Dayton, Ohio, July 1967.

4. Y. K. Lin, T. J. McDaniel, "Dynamics of Beam-Type Periodic Structures," ASME Paper No. 68-Vibr-17, 1969.
5. D. J. Mead, "Vibration Response and Wave Propagation in Periodic Structures, ASME Paper No. 70-WA/D3-3, Winter Annual Meeting of ASME, N.Y., Nov. 29 - Dec. 3, 1970.
6. Agardograph 162, "Acoustic Fatigue Design Data," Parts I and II, 1972.
7. J. F. Wilby, F. L. Gloyna, "Vibration Measurements of an Airplane Fuselage Structure; I. Turbulent Boundary Layer Excitation; II. Jet Noise Excitation," J. Sound & Vibration, V. 23, n4, 443-486, 1972.
8. D. J. Mead, "Free Wave Propagation in Periodically Supported Infinite Beams," J. Sound & Vib., V. 11, n2, 1970.
9. G. Sen Gupta, "Natural Frequencies of Skin-Stringer Structures Using a Wave Approach," J. Sound & Vib., V. 16, n4, 1971.
10. G. Sen Gupta, "Dynamics of Periodically-Stiffened Structures, Using a Wave Approach," Ph.D. Thesis, Univ. of Southampton, July 1970. Also available as: AFML-TR-71-99, Wright Patterson AFB, Ohio, May 1971.
11. G. Sen Gupta, D. J. Mead, "Wave-Group Theory Applied to the Analysis of Forced Vibration of Rib-Skin Structures," Paper D-3, Proceedings of the Symposium on Structural Dynamics, Univ. of Loughborough, 1970.
12. D. J. Mead, "A General Theory of Harmonic Wave Propagation in Linear Periodic Structures with Multiple Coupling," J. Sound & Vib., V. 27, n.2, 235-260, 1973.
13. R. D. Ford, "The Response to Noise of a Beam Pinned at Three Points and Allowed to Vibrate in the First Two Modes," A.A.S.U. Report No. 198, Univ. of Southampton, 1961.
14. Y. K. Lin, "Free Vibration of Continuous Skin-Stringer Panels with Non-Uniform Stringer Spacing and Panel Thickness," AFML-TR-64-347, Part I, Wright-Patterson AFB, Ohio, Feb. 1965.
15. Y. K. Lin, J. N. Yang, "Free Vibration of a Disordered Periodic Beam," J. Applied Mechanics June 1974.
16. G. Sen Gupta, "Natural Flexural Waves and Normal Modes of Periodically Supported Beams and Plates," J. Sound & Vib., V. 13, n.1, 89-101, 1970.

APPENDIX I: ANALYTICS

INTRODUCTION

The analysis uses the simplified model shown in Fig. 1. In this model the skin edges along the frames are considered to be simply supported. The stringers are placed at distances of l_1 and l_2 as shown in the figure. The whole structure therefore consists of an assembly of two panels of unequal length repeated indefinitely.

OUTLINE OF THE RANDOM RESPONSE ANALYSIS

In this paper, we consider the response of this structure to random acoustic plane waves simulating jet noise, traveling with a trace-velocity C_t . The spectral density of the

acoustic pressure at any point on the structure is denoted by $S_p(\omega)$. The cross-spectral density of the pressure at two points on the structure, separated in the x-direction by ξ , is

$$S_p(\xi, \omega) = S_p(\omega) e^{-i \frac{\omega}{C_t} \xi}$$

where ω is the frequency.

The power spectral density (PSD) of skin stress response $S_\sigma(\omega)$ is related to that of the excitation $S_p(\omega)$, in the following manner:

$$S_\sigma(\omega) = |Y_\sigma(\omega)|^2 S_p(\omega) \quad (A1)$$

where, $Y_\sigma(\omega)$ is the stress response admittance function, i.e., stress response of the skin due to a traveling sinusoidal pressure field $p_0 e^{i(\omega t - \frac{\omega}{C_t} x)}$ of unit amplitude. The next section describes how $Y_\sigma(\omega)$ is determined. It is assumed (for simplicity in this presentation) that the pressure and associated responses vary across the plate in proportion to $\sin(\frac{\pi y}{b})$. The analysis is then carried out in terms of the "chordwise" amplitudes of the pressure and responses.

RESPONSE TO AN ACOUSTIC PLANE WAVE

A harmonic pressure field of frequency ω and wave number $k = \frac{\omega}{C_t}$ convected along the structure, exerts pressures of equal magnitude at all points, but at points separated by " $2l$ " (the periodic length) in the x-direction, the pressures have the phase difference $k \cdot 2l$. The responses of the skin-stringer structure at these two points are also equal in magnitude and also have the same phase difference if the structure is infinitely long. It follows, therefore, that the deflections (w), slopes (θ), bending moments (M) and shear forces (S) at the points 1 and 5 must be related by

$$\begin{aligned} w_5 &= w_1 e^{-ik 2l} \\ \theta_5 &= \theta_1 e^{-ik 2l} \\ M_5 &= M_1 e^{-ik 2l} \\ S_5 &= S_1 e^{-ik 2l} \end{aligned} \quad (A2)$$

Let us now consider the equation of motion of the skin panel

$$\nabla^4 w + \frac{\rho_{sk} h}{D_{sk}} w = \frac{p(x, y, t)}{D_{sk}} \quad (A3)$$

Since the skin edges at the frames are simply supported, the solution of this equation is given by

$$\begin{aligned} w &= A e^{\lambda_1 x} + B e^{-\lambda_1 x} + C e^{\lambda_2 x} \\ &+ D e^{-\lambda_2 x} + \frac{R e^{-ikx}}{D_{sk} (k^2 + \lambda_1^2)(k^2 - \lambda_2^2)} \end{aligned} \quad (A4)$$

From this equation for the deflection, the equations for the slope, bending moment, and shear force at any point in the panel can be derived. Expressed in a matrix form,

$$\{Z(x)\} = [E_\lambda(x)] \{A\} + P e^{-ikx} \{K\} \quad (A5)$$

Let us choose the location of stringer 1 as the origin of the x-co-ordinate. Then for panel 1

$$\{Z_1\} = \{Z(-L_1)\} = [E_\lambda(-L_1)] \{A_1\} + P e^{ikL_1} \{K\} \quad (A6)$$

$$\{Z_2\} = \{Z(0)\} = [E_\lambda(0)] \{A_1\} + P \{K\} \quad (A7)$$

and for panel 2

$$\{Z_3\} = \{Z(0)\} = [E_\lambda(0)] \{A_2\} + P \{K\} \quad (A8)$$

$$\{Z_4\} = \{Z(L_2)\} = [E_\lambda(L_2)] \{A_2\} + P e^{-ikL_2} \{K\} \quad (A9)$$

Now considering continuity of deflection and slope at the stringer 1

$$\begin{aligned} w_3 &= w_2 \\ \theta_3 &= \theta_2 \end{aligned} \quad (A10)$$

And considering the equilibrium of the stringer,

$$\begin{aligned} M_3 - M_2 &= K_{R1} \theta_2 \\ S_3 - S_2 &= -K_{T1} w_2 \end{aligned} \quad (A11)$$

Expressing in matrix form,

$$\{Z_3\} = [S_1] \{Z_2\} \quad (A12)$$

Similarly,

$$\{Z_5\} = [S_2] \{Z_4\} \quad (A13)$$

Substituting for $\{Z_2\}$ and $\{Z_3\}$ from equations (A7) and (A8) in equation (A12)

$$[E_\lambda(0)] \{A_2\} + P \{K\} = [S_1] [E_\lambda(0)] \{A_1\} + P [S_1] \{K\}$$

Therefore

$$\begin{aligned} \{A_2\} &= [E_\lambda(0)]^{-1} [S_1] [E_\lambda(0)] \{A_1\} \\ &+ P [E_\lambda(0)]^{-1} ([S_1] - [I]) \{K\} \end{aligned} \quad (A14)$$

Substituting for $\{A_2\}$ in equation (A9)

$$\begin{aligned} \{Z_4\} &= [E_\lambda(L_2)] [E_\lambda(0)]^{-1} [S_1] [E_\lambda(0)] \{A_1\} \\ &+ P \left\{ [E_\lambda(L_2)] [E_\lambda(0)]^{-1} ([S_1] - [I]) \right. \\ &\quad \left. + e^{-ikL_2} \right\} \{K\} \end{aligned} \quad (A15)$$

Therefore, from equations (A13) and (A15)

$$\begin{aligned} \{Z_5\} &= [S_2] [E_\lambda(L_2)] [E_\lambda(0)]^{-1} [S_1] [E_\lambda(0)] \{A_1\} \\ &+ P [S_2] \left\{ [E_\lambda(L_2)] [E_\lambda(0)]^{-1} ([S_1] \right. \\ &\quad \left. - [I]) + e^{-ikL_2} \right\} \{K\} \end{aligned} \quad (A16)$$

From equation (A2)

$$\{Z_5\} = e^{-ikL_2} \{Z_1\}$$

Therefore from equations (A6) and (A16)

$$\begin{aligned} [S_2] [E_\lambda(L_2)] [E_\lambda(0)]^{-1} [S_1] [E_\lambda(0)] \{A_1\} \\ + P [S_2] \left\{ [E_\lambda(L_2)] [E_\lambda(0)]^{-1} ([S_1] - [I]) + e^{-ikL_2} \right\} \{K\} \\ = e^{-ikL_2} [E_\lambda(-L_1)] \{A_1\} + P e^{-ikL_2} \{K\} \\ \text{or, } \left\{ [S_2] [E_\lambda(L_2)] [E_\lambda(0)]^{-1} [S_1] [E_\lambda(0)] \right. \\ \quad \left. - e^{-ikL_2} [E_\lambda(-L_1)] \right\} \{A_1\} \\ = -P \left\{ e^{-ikL_2} ([S_2] - [I]) + [S_2] [E_\lambda(L_2)] \right. \\ \quad \left. [E_\lambda(0)]^{-1} ([S_1] - [I]) \right\} \{K\} \end{aligned} \quad (A17)$$

Equation (A17) can now be solved for $\{A_1\}$, and equation (A14) can then be used to solve for $\{A_2\}$. Utilizing equation (A5) any of the response quantities at any point in the structure can be computed. The stress response function $Y_\sigma(\omega)$ can be directly calculated from the bending moment response function.

APPENDIX II: LIST OF SYMBOLS

A, B, C, D Coefficients used in equation (A4)
 $[A_i] = [A_i \ B_i \ C_i \ D_i]$, $i = 1$ for panel 1
 $i = 2$ for panel 2

b Panel width or frame spacing

c_t Trace-or convection velocity of the fluctuating pressure field

D_{SK}^* Skin panel flexural rigidity

$$[E_\lambda(x)] = \begin{bmatrix} e^{\lambda_1 x} & e^{-\lambda_1 x} & e^{\lambda_2 x} & e^{-\lambda_2 x} \\ \lambda_1 e^{\lambda_1 x} & -\lambda_1 e^{-\lambda_1 x} & \lambda_2 e^{\lambda_2 x} & -\lambda_2 e^{-\lambda_2 x} \\ \lambda_1^2 e^{\lambda_1 x} D_{sk}^* & \lambda_1^2 e^{-\lambda_1 x} D_{sk}^* & \lambda_2^2 e^{\lambda_2 x} D_{sk}^* & \lambda_2^2 e^{-\lambda_2 x} D_{sk}^* \\ \lambda_1^3 e^{\lambda_1 x} D_{sk}^* & -\lambda_1^3 e^{-\lambda_1 x} D_{sk}^* & \lambda_2^3 e^{\lambda_2 x} D_{sk}^* & -\lambda_2^3 e^{-\lambda_2 x} D_{sk}^* \end{bmatrix}$$

h Skin panel thickness

f Frequency

f_s Fundamental frequency of a simply-supported beam of length l

$[I]$ A unit matrix of order 4×4

$i = \sqrt{-1}$

K_{R1}, K_{R2} Rotational stiffnesses of stringers see Figure 1

K_{T1}, K_{T2} Translational stiffnesses of stringers, see Figure 1

$[K] = \begin{bmatrix} 1 & -ik & -k^2 D_{SK}^* & ik^3 D_{SK}^* \end{bmatrix}$

k Wave number

l, l_1, l_2 Stringer spacings as defined in Figure 1

M Bending moment

$P = p_0 / \gamma$

p_0 Amplitude of pressure fluctuation

$p(x, y, t)$ Pressure field distribution in x, y, t co-ordinates

S Shear force

$S_p(\omega)$ Power spectral density of the random pressure field

$S_p(\xi, \omega)$ Cross power spectral density of the pressure field at two points separated by ξ

$S_\sigma(\omega)$ Power spectral density of stress response

$$[S_i] = \begin{bmatrix} 1 & 0 & 0 & 0 \\ 0 & 1 & 0 & 0 \\ 0 & K_{Ri} & 1 & 0 \\ -K_{Ti} & 0 & 0 & 1 \end{bmatrix}$$

t Time co-ordinates

w Skin panel deflection

x, y Space co-ordinates

$\gamma_\sigma(\omega)$ Stress response admittance function as defined in equation (A1)

$\gamma = D_{sk}^* (\lambda^2 + \lambda_1^2) (\lambda^2 - \lambda_2^2)$

$z = l_1 / l_2$, the span ratio

$[Z_i] = [w_i \ \theta_i \ M_i \ S_i]$

θ Skin panel slope

$\lambda = \left(\frac{Q_{sk} h}{D_{sk}^*} \right)^{1/4} \omega^{1/2}$

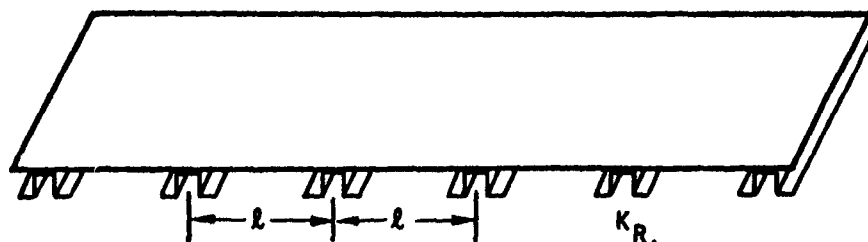
$\lambda_1^2 = \lambda^2 + \left(\frac{\pi}{b} \right)^2$

$\lambda_2^2 = \lambda^2 - \left(\frac{\pi}{b} \right)^2$

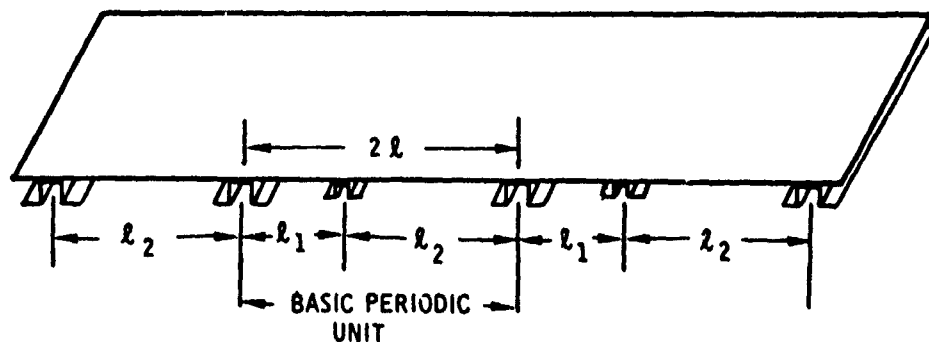
ρ_{sk} Density of skin panel material

ξ Separation distance

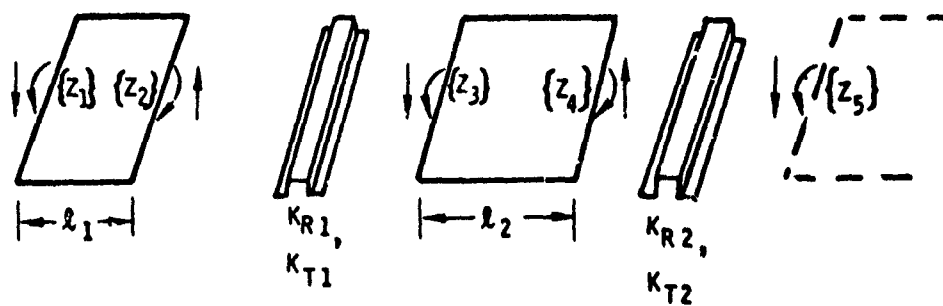
ω Circular frequency



A PERIODIC STRUCTURE



A SEMI-PERIODIC STRUCTURE



THE ELEMENTS OF THE BASIC PERIODIC UNIT

FIGURE 1. THE STRUCTURAL MODEL

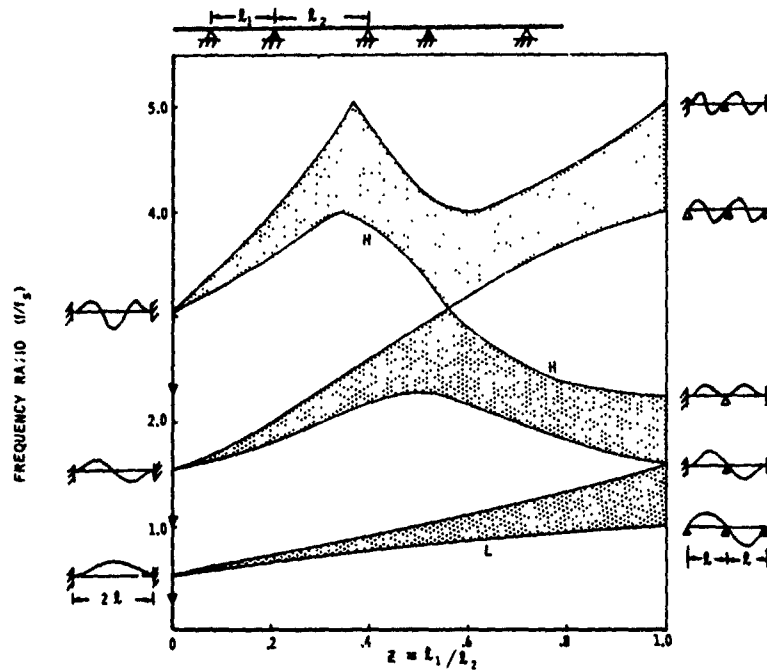


FIGURE 2. VARIATION OF THE NATURAL FREQUENCY BANDS OF A SEMI-PERIODICALLY SUPPORTED BEAM WITH THE SPAN RATIO

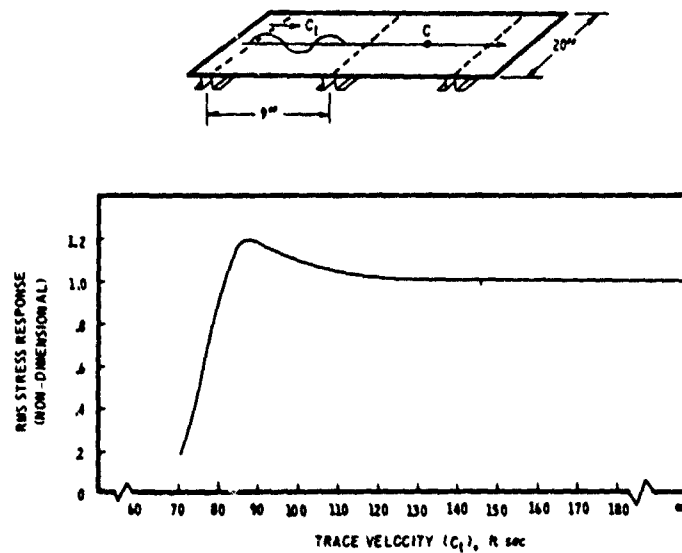


FIGURE 3. VARIATION OF R.M.S. RESPONSE AT EACH PANEL CENTER OF AN INFINITELY LONG SKIN-STRINGER ARRAY, WITH CONVECTION VELOCITY

DISCUSSION

Mr. Henderson: (Air Force Materials Lab.)
Could you clarify how you handled your forcing function in your analytical work? Was that a discrete forcing function at various points or was it a distributed forcing function over the structure?

Mr. Sen Gupta: It was a distributed forcing function which was in theory, a distributed forcing being convected down the structure. So it was a distributed force convecting at some particular speed. In the computation I put the speed at infinity which corresponded to white noise at normal incidence.

Mr. Henderson: Do your assumptions or the conclusions from this depend upon the spatial correlation or the pressure being the same over several panels? How good is this assumption?

Mr. Sen Gupta: We assume that the excitation is highly correlated over the large number of panels. In practice you don't get that strong a correlation over a long distance, but as we saw in the curve where I plotted the stress response against stress velocity, we also have some data which compared the same sort of curve for a different decay parameter of the correlation. I found for a high stress velocity or a high convection velocity that the decay parameter does not have an important effect on the RMS stresses in the skin panels.